Ingrid Domingos Pelisoli

White Dwarf and Subdwarf Stars in the *Sloan Digital Sky Survey*

(Estrelas Anãs Brancas e Subanãs no *Sloan Digital Sky Survey*)

Porto Alegre
2018

Ingrid Domingos Pelisoli

White Dwarf and Subdwarf Stars in the *Sloan Digital Sky Survey*[1]

(Estrelas Anãs Brancas e Subanãs no *Sloan Digital Sky Survey*)

Thesis submitted to *Programa de Pós-Graduação em Física* at *Universidade Federal do Rio Grande do Sul* as a partial requirement for the degree of Doctor of Sciences.

Universidade Federal do Rio Grande do Sul
Instituto de Física
Programa de Pós-Graduação em Física

Supervisor: Prof. Dr. Kepler de Souza Oliveira Filho

Porto Alegre
2018

[1] This work was financially supported by *Conselho Nacional de Desenvolvimento Científico e Tecnológico* (CNPq) and *Coordenação de Aperfeiçoamento de Pessoal de Nível Superior* (CAPES).

To every little girl who has ever dreamt of the stars.

Acknowledgements

Once upon a time, there was a little girl who liked to ask *why*. She was fascinated with the idea of learning more and more and dreamed of a PhD even before she could really understand what it was. This little girl's family never questioned her choices. They always told her she could be whatever she wanted, as long as it made her happy. She had no idea at the time of how lucky she was to be surrounded by such a supportive family. Now she has grown up and made her PhD dream come true, and looking back she understands how essential the support of her family was. Thank you all, this is as much your victory as it is mine.

The support of my family might have come to nothing if I had not found the proper guidance. Since my first week as an undergraduate student, I have taken profit of an inspiring atmosphere in the research group lead by my supervisor, Kepler. I learned to ask the right questions, and to use different tools to answer these questions, from simple physics to temperamental software (cough... IRAF... cough...). I learned everything I needed to become the independent researcher that a PhD title would imply that I am. I am deeply thankful not only to Kepler, but to all the people who were part of his group. Fabi and Ale, you know both of you are on the top of the list.

As part of the learning process of becoming an independent researcher, I have also ventured in foreign lands. I spent six months at the University of Warwick, thanks to the support of my supervisor there, Boris Gänsicke, who had all the necessary patience with Brazilian bureaucracies. Boris has also encouraged me to apply for post-doctoral positions I would have thought were way out of my league, and made me feel I was a much better researcher than Impostor Syndrome made me believe. Working on these applications made me reflect on what I wanted for myself as a researcher, and I surely learned a lot in the process. Boris, thanks for pushing me.

Stress and anxiety are unfortunately commonplace in the life of a PhD student. We do our best to deal with it, but it is very hard to cope alone. I had many friends who made that easy for me. Guto, Débs, Gui, Arthur and all of my friends from undergrad, thank you for the countless moments of laughter. My AstroFriends (Lari, Marina, ...) thank you for always sharing beer and Uber. Astro&TheoryClimbers (Tim, Odette, Sam, Edu, ...), thank you for cheering me to the top. Tom, thank you for being my tour-guide in the UK, for helping me figure out which tiny dot on the screen was my star in more than one occasion, for helping me write formal emails when I only felt like ranting, and for the countless occasions when you did your best to remind me that every little thing was going to be alright.

There's something that doesn't make sense. Let's go and poke it with a stick.
– The Doctor

Abstract

White dwarf stars are the final observable evolutionary state of over 95% of stars and also a common outcome in binary evolution. Therefore, studying white dwarfs is a powerful tool to understand both single and binary stellar evolution, local initial mass function, and post-main sequence mass loss, leading us to a better comprehension of the history of stellar formation and evolution of different stellar populations. In order to make this type of studies possible, a large and preferably complete sample of white dwarf stars, covering the whole range of physical parameters, is required. The simplest way to achieve that is to take advantage of data provided by large surveys. The *Sloan Digital Sky Survey* has already allowed the increase of the number of known white dwarf stars fivefold up to its data release 10. In this work, we extended the search for white dwarfs to the new objects in the data release 12, discovering 3 157 new white dwarfs and 1 349 new subdwarfs. For the first time, we have extended this search to $\log\ g < 6.5$, corresponding to $M < 0.3\ M_{\odot}$. White dwarfs below this mass limit cannot be formed through single evolution within a Hubble time; however, if the star is part of a close binary system, the mass loss of the system may be so intense that the resulting white dwarf has mass below the single evolution limit. These objects are known as extremely-low mass white dwarfs (ELMs). They show $T_{\rm eff} < 20\,000$ K and $5.0 \lesssim \log\ g \lesssim 6.5$ and spectra very similar to main sequence A stars. Less than a hundred of them are known, and most objects were discovered relying on biased selection criteria, that excluded cool ($T_{\rm eff} < 9\,000$ K), lower-mass ($M \lesssim 0.15\ M_{\odot}$) ELMs, making it difficult to validate the models and comprehend the properties of the ELMs as a class. We have identified thousands of objects whose physical properties, effective temperature and surface gravity, place them in the range of by-products of binary interaction such as the ELMs. We have called them sdAs, referring to their sub-main sequence $\log\ g$ and hydrogen dominated spectra. They seem to be composed of overlapping stellar populations, and we found that at least 7% are more likely ELMs or their precursors, the pre-ELMs, than main sequence stars. Obtaining time-resolved spectroscopy for 26 objects, we could confirm 15 to be in close binaries. One of them is also an eclipsing system, while another is a pulsator — the eighth member of the pulsating ELM class. Other six new pulsators were found as part of our follow-up, five of them in the vicinity of the ELM instability strip. With these results, we increase the population of ELMs by 20%, raising the fraction of cool ELMs from 4 to 20%, which is consistent with the predictions from the evolutionary models.

Keywords: stars, stellar evolution, white dwarfs, subdwarfs, main sequence.

Resumo

Estrelas anãs brancas são o último estágio evolutivo observável de mais de 95% das estrelas e também um resultado comum na evolução de estrelas binárias. O estudo de anãs brancas é, portanto, uma ferramenta poderosa na compreensão da evolução de estrelas simples e binárias, da função de massa inicial local, e da perda de massa após a sequência principal, levando-nos a uma melhor compreensão do histórico de formação e evolução estelar de diferentes populações. Para que esses estudos sejam possíveis, é necessária uma amostra grande e preferencialmente completa de anãs brancas, cobrindo todo o intervalo de parâmetros físicos. A maneira mais simples de obter isso é utilizando dados de grandes projetos de mapeamento. O *Sloan Digital Sky Survey* já permitiu o aumento do número de anãs brancas conhecidas em cinco vezes até o *data release* 10. Neste trabalho, estendemos a busca por anãs brancas aos novos objetos no *data release* 12, descobrindo 3 157 novas anãs brancas e 1 349 novas subanãs. Pela primeira vez, estendemos essa busca para $\log\ g < 6.5$, correspondente a $M < 0.3\ M_{\odot}$. Anãs brancas abaixo desse limite de massa não podem formar-se em um tempo de Hubble; contudo, se a estrela é parte de um sistema de binárias próximas, a perda de massa pode ser tão intensa que a anã branca resultante tem massa inferior ao limite por evolução simples. Esses objetos são chamados anãs brancas de massa extremamente-baixa (ELMs, do inglês *extremely-low mass white dwarfs*). Elas têm $T_{\rm eff} < 20\,000$ K e $5.0 \lesssim \log\ g \lesssim 6.5$ e espectros muito similares a estrelas A de sequência principal. Menos de cem são conhecidas, e a maioria dos objetos foi descoberta tendo em conta um critério de seleção tendencioso, que excluiu ELMs frias ($T_{\rm eff} < 9\,000$ K) e com mais baixa massa ($M \lesssim 0.15\ M_{\odot}$), tornando difícil verificar modelos e compreender as propriedades das ELMs como classe. Nós identificamos milhares de objetos cujas propriedades físicas, temperatura efetiva e $\log\ g$, estão no intervalo de produtos de evolução binária, como as ELMs. Nós os chamamos de sdAs, referindo-nos ao seu $\log\ g$ que as coloca abaixo da sequência principal e seu espectro dominado por hidrogênio. As sdAs parecem conter populações estelares sobrepostas, e encontramos que 7% são mais compatíveis com (pre-)ELMs do que com objetos de sequência principal. Obtivemos espectroscopia resolvida temporalmente para 26 objetos e pudemos confirmar que 15 estão em binárias. Um objeto faz parte de um sistema eclipsante, enquanto outro é pulsante — o oitavo membro da classe de ELMs pulsantes. Outros seis objetos também apresentaram pulsações em nossas observações, cinco desses estão na vizinhança da faixa de instabilidade das ELMs. Com estes resultados, aumentamos a população de ELMs por um fator de 20%, elevando a fração de ELMs de 4 para 20%, um valor que é consistente com as previsões de modelos evolucionários.

Palavras-chave: estrelas, evolução estelar, anãs brancas, subanãs, sequência principal.

Contents

1 Introduction

1.1 Stellar Evolution

1.1.1 Single Stars

An object is classified as a star if it stably burned hydrogen into helium in its core at some point during its evolution. This will occur for objects with initial mass higher than about 0.08 $M_\odot$, depending on metallicity[1]. Above this threshold mass, the objects are able to reach hydrogen fusion temperature ($\sim 8 \cdot 10^6$ K) in their cores. Below this minimal mass are the brown dwarfs, which cannot sustain stable hydrogen fusion in the core, and only fade away with time. Before a star exhausts the core fuel and becomes a degenerate object, most of its lifetime is spent fusing four hydrogen atoms into one helium atom in the so-called "main sequence" (MS). A rough estimate of the time spent in the main sequence is given by

$$t_{\mathrm{MS}} \approx 10^{10} \left(\frac{M}{M_\odot} \right)^{-2} \text{years.} \tag{1.1}$$

This holds for low-mass stars (up to $\sim 3\ M_\odot$), but it is still a good estimate up to $\sim 60\ M_\odot$, if the effects of metallicity are ignored — the higher the metallicity, the longer the time spent in the main sequence, because the increase in opacity decreases the luminosity of the star.

In stars with masses up to approximately 1.25 $M_\odot$, the dominant fusion channel is the proton-proton ($p-p$) chain reaction, in which protons are directly combined to form helium. On the other hand, if the star is more massive than that and has non-zero metallicity[2], the energy comes mainly from the carbon-nitrogen-oxygen (CNO) cycle, in which these three heavier elements act as catalysts in the fusion reaction.

The hydrogen fusion stops when the star has converted 10% of its initial hydrogen mass into helium. When this so-called Schoenberg-Chandrasekhar limit (Schönberg; Chandrasekhar, 1942) is reached, the internal pressure will not be enough to avoid gravitational collapse, hence the core of the star can no longer sustain hydrostatic equilibrium. It starts to contract, releasing half of the energy, according to the virial theorem, which then causes the exterior layers of the star to expand. It leaves the main sequence, becoming a red giant when the H^- opacity dominates — a more luminous

[1] in Astronomy, all elements heavier than helium are historically referred to as metals.

[2] I.e., it is not a Population III object, the pristine stars that formed before the universe was chemically enhanced by stellar evolution.

and cooler object, which fuses hydrogen into helium only in a shell surrounding the helium core. Because of the cooler temperatures, radiation transport alone cannot maintain radiative equilibrium, and the star becomes almost fully convective, approaching the so-called Hayashi limit, where it would be fully convective (Hayashi; Hoshi, 1961; Hayashi, 1961). As the H^- ions increase the opacity, the radius of the star becomes larger, increasing the luminosity and making the star climb up the Hayashi strip. The convective layer reaches the nucleus bringing heavier elements (mainly C and N) to the surface, in the event known as first dredge-up.

Meanwhile, the temperature in the contracting core is increasing. Objects lighter than $\sim 0.45\ M_\odot$, a limit which depends on metallicity, will never reach helium fusion temperature (approximately 10^8 K); therefore, after ejecting their external layers, they evolve directly from the red giant branch to their last observable evolutionary phase: He-core white dwarf stars. These objects are sometimes called AGB-*manqué*, in the sense that they skip the asymptotic giant branch (AGB) phase. The white dwarfs formed through this channel are less massive than $0.45\ M_\odot$ and have helium core and hydrogen atmosphere. Considering the evolutionary time scales, only objects with final masses above $\sim 0.3\ M_\odot$ could have been formed through this channel within the approximate age of the Galaxy. Producing white dwarfs with masses below $\sim 0.3\ M_\odot$ most likely requires interacting binary systems (e.g. Marsh; Dhillon; Duck, 1995; Brown et al., 2010). Theory suggests that low-mass single systems could be explained by other mass-loss enhancing mechanisms, such as high metallicity (D'Cruz et al., 1996) or supernova stripping (Wang; Han, 2009), or by mass ejection caused by a massive planet (Nelemans; Tauris, 1998). It is also possible for single objects to be formed as a result of merger events (Zhang; Jeffery, 2012; Zhang et al., 2017). Toonen et al. (2017) estimated that 10–30% of all single white dwarfs are a result of a merger. Still, as the merger triggers core fusion, it is unlikely that the resulting object will have a He-core and usually the predicted result is a canonical mass white dwarf (e.g. Brown et al., 2016).

If the initial mass of the star is up to $1.8 - 2.3\ M_\odot$ (depending on the efficiency of overshooting from the convective layers), the nucleus will contract to a point in which the core helium becomes degenerate before fusion temperature is reached. The burning process will thus start in a degenerate nucleus, resulting on a runaway combustion called helium-flash. When the degeneracy is lifted after the flash, the luminosity decreases, and the star goes through a brief phase called subgiant. For masses higher than the $1.8 - 2.3\ M_\odot$ lower limit, fusion temperature is reached faster, and the burning occurs in a stable manner — the star goes through the horizontal branch (HB), which is similar to the main sequence, but helium is burnt in the core, instead of hydrogen.

When the helium fuel in the core is exhausted, the core will again start to contract, releasing energy. A scenario similar to the one preceding the red giant phase occurs: the

exterior of the star expands, it becomes more luminous, and the convective layer extends down to the nuclear burnt region, bringing heavier elements to the surface (second dredge-up). The star reaches the supergiant phase and has a degenerate core composed mainly by carbon and oxygen, with alternate external layers burning helium into carbon and oxygen (closer to the core) and hydrogen into helium, under a hydrogen envelope. This configuration makes the star very unstable: helium burns until there is not enough fuel, then the hydrogen burning layer produces more helium and the burning restarts, releasing energy and making the star expand, cooling the exterior and stopping the hydrogen fusion, so the helium finishes again and the star cools down and contracts, reigniting the hydrogen and restarting the cycle. This sequence of processes is known as thermal pulses; the number of pulses varies for each star, but more massive and metallic stars have more thermal pulses as a rule.

As the thermal pulses occur, the star will eject the mass in its external layers, potentially forming a planetary nebula. All stars that have masses up to $7.0 - 10.6\ M_\odot$ (e.g., Woosley; Heger, 2015), depending on metallicity, will finish their evolution as a white dwarf star, in this case with a C/O (for white dwarfs up to $\sim 1.06\ M_\odot$) or O/Ne/Mg core (for the more massive ones). If the star is more massive than the $7.0 - 10.6\ M_\odot$ limit, the contraction of the core will be enough for it to reach the temperature of carbon fusion ($\sim 10^9$ K). In this case, the star evolves relatively quick, burning all the elements heavier than carbon until iron is synthesised. The binding energy of iron is maximal, therefore it is no longer possible to extract energy from fusion processes and the star collapses into a neutron star, if neutron degeneracy pressure is enough to maintain hydrostatic equilibrium (the mass of the object is smaller than $\sim 3.0\ M_\odot$, the non-rotating, non-magnetic Tolman-Oppenheimer-Volkoff limit), or otherwise into a black-hole. It is important to emphasise that all these mass limits depend on rotation, magnetic fields, and strong force repulsion.

In short, stars have initial mass higher than $0.08\ M_\odot$. If the initial mass is up to $\sim 0.45\ M_\odot$, the star will evolve into a white dwarf with helium core. Considering the age of the Universe as a limit on the evolutionary time, the lower mass of an observable white dwarf which formed through this channel is within $0.30 - 0.45\ M_\odot$ (e.g. Kilic; Stanek; Pinsonneault, 2007). When the star has initial mass between $0.45\ M_\odot$ and $7.0 - 10.6\ M_\odot$, its final observable stage is a white dwarf with C/O or O/Ne/Mg core. Above such limit, the star collapses into a neutron star (typically for initial masses up to around $25\ M_\odot$) or a black hole (above $25\ M_\odot$).

1.1.2 Binary Stars

The processes described in Section 1.1.1 are only valid if the star evolves without interacting with a binary companion. Stellar multiplicity is a function of mass, increasing

from about 46% for G-stars (Tokovinin, 2014) to over 70% for A stars (De Rosa et al., 2014), but most stars with initial mass larger than 1.0 $M_\odot$ are in multiple systems (Duchêne; Kraus, 2013). When the distance between the two stars is small enough for them to exchange mass (typically, smaller than 10 $R_\odot$), which is the case for about 25% of binaries (Willems; Kolb, 2004), their evolutionary processes cannot be treated independently. These objects are called close binaries.

One very important concept in the study of binary stars is the Roche lobe. It is the maximum radius a star can have before mass transfer starts to occur due to overflow. In other words, it is the first equipotential involving both stars (see Fig. 1), so when the radius of one of the stars is larger than its Roche radius, mass will flow from this star to the other (e.g. Paczyński, 1971; Iben; Livio, 1993; Podsiadlowski, 2008).

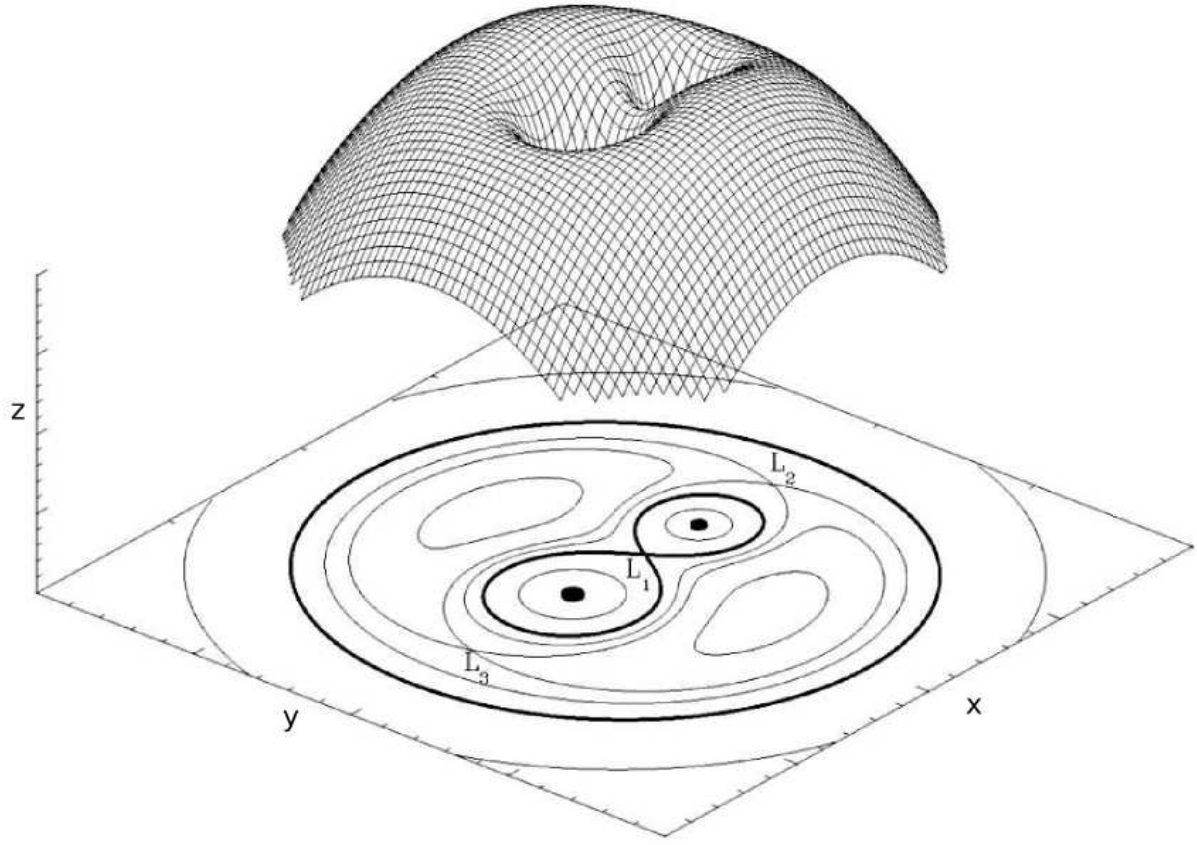

Figure 1 – Three-dimensional representation of the Roche potential in a binary star. The inner equipotential in bold, the first to involve both stars, is the Roche lobe. The points L_1, L_2, and L_3 are Lagrangian points, where an object would be in a stable orbit relative to the two bodies.
(Original figure by Marc van der Sluys, available at Wikimedia Commons.)

There are three types of close binaries, which correspond to different possible stages in the evolution. The first is a detached binary, when the radii of both stars are smaller than their Roche radii. When one of the stars fills its Roche lobe, the binary is

semi-detached. The last possibility is when both stars fill their lobes, and the binary is said to be an overcontact binary.

As the time spent in the main sequence is inversely proportional to the mass of the star (see Eq. 1.1), the more massive star in a binary — sometimes called the primary — will leave the main sequence first. It will become a red giant and, depending on the distance between the stars, might fill in the Roche lobe, resulting in mass transfer. If the secondary star does not effectively accrete all the transferred material, an accretion disk may be formed. Mass transfer can also occur due to stellar winds, which make the red giants lose mass. Hence, either way, the evolution of the secondary star is altered by the presence of the primary, as its mass will be changed. That is why they cannot be treated separately.

When the primary fills its Roche lobe, the binary goes through a semi-detached phase. If they are close enough, there might be a common envelope phase. Because of the friction between the stars and the envelope, their distance is going to decrease. The released orbital energy will cause the ejection of most of the envelope. This is one of the formation channels of subdwarf stars (sds, e.g. Heber, 2016), also called extreme-horizontal branch stars, because they burn helium in their nucleus as well, but appear hotter than ordinary horizontal branch stars, given that their external layers were lost.

When the mass of the primary star is smaller than the supernova limit, it will become a white dwarf and the system will be detached again. This can also happen if the primary becomes a neutron star, but the secondary might be ejected by the supernova event and become a so-called runaway star, showing velocity that can be comparable to the escape velocity of the Galaxy. When the mass of the two stars is similar, they will evolve simultaneously, so both will fill the Roche lobe at the same time, forming an overcontact binary.

As the secondary evolves, again the binary may go through a semi-detached phase. In this situation, mass will be accreted by a degenerate object, what may result in a supernova type Ia if the degenerate object exceeds its limiting mass (the Chandrasekhar limit for white dwarfs or the Tolman-Oppenheimer-Volkoff for neutron stars), ejecting away the companion star. If this does not happen, the remnant will be a binary millisecond pulsar (neutron star plus white dwarf) or double-degenerate system (two white dwarfs). A binary with two pulsars is also possible, but a very rare outcome (Tauris; Langer; Podsiadlowski, 2015; Rueda et al., 2018).

Another possible outcome of interacting binary systems are extremely-low mass white dwarfs (ELMs). The intense mass-loss due to the binary interaction allows the formation of these white dwarfs with masses below the single evolution limit of 0.3 $M_{\odot}$, typically still found in orbit with their binary companions. The formation channel is similar to the one leading to hot subdwarfs, but in this case the common envelope happens

before helium is ignited in the core, hence the objects effectively skip the horizontal branch, evolving directly to the cooling white dwarf branch with a helium core.

The evolution henceforth depends on the mass of the resulting ELM and on the occurrence of element diffusion processes (Althaus; Serenelli; Benvenuto, 2001; Panei et al., 2007; Althaus; Miller Bertolami; Córsico, 2013; Córsico; Althaus, 2014; Córsico; Althaus, 2016; Córsico et al., 2016; Istrate et al., 2016). Diffusion leads to a dichotomy in the thickness of the H envelope, resulting on a dichotomy in the cooling ages. In the theoretical models, stars with $M \gtrsim 0.18 - 0.20\ M_{\odot}$ experience multiple diffusion-induced CNO thermonuclear flashes which consume most of the H in the envelope (see Fig. 2), so that the remnant enters the final cooling track with a very thin H envelope, being unable to sustain stable nuclear burning as it cools. As a result, the evolutionary time scale is quite short ($\sim 10^7$ yr). When $M \lesssim 0.18 - 0.20\ M_{\odot}$, on the other hand, H flashes are not experienced, and the remnant enters the cooling branch with an envelope thick enough to have residual H burning as the main energy source. This slows down the evolution, so that the cooling time scale is of about $\sim 10^9$ yr (Córsico; Althaus, 2014; Córsico; Althaus, 2016; Córsico et al., 2016). In addition, rotational mixing plays a significant role in the evolution of these ELMs that experience hydrogen shell flashes (Istrate et al., 2016) — it can effectively counteract diffusion, thus playing a key role in the surface chemical abundances of ELMs.

It is worth mentioning that the evolutionary models of Córsico & Althaus (2014), Córsico & Althaus (2016), Córsico et al. (2016) and Istrate et al. (2016) assume an initial binary consisting of a main sequence star with initial mass $\sim 1\ M_{\odot}$ and a $\sim 1.4\ M_{\odot}$ neutron star. As will be discussed in Section 1.2.2, most ELMs seem to actually have white dwarf companions. Hence these models must be considered as only an initial attempt to describe the formation and evolution of ELMs, which must be even more complex than the models indicate. Moreover, less than a hundred ELMs are known so far, since they were only recently discovered (see e.g. the ELM Survey: Brown et al., 2010; Kilic et al., 2011; Brown et al., 2012; Kilic et al., 2012; Brown et al., 2013; Gianninas et al., 2015; Brown et al., 2016). This calls for a more thoroughly search for these stars, so that meaningful comparisons with binary evolution models can be done in order to improve the input physics.

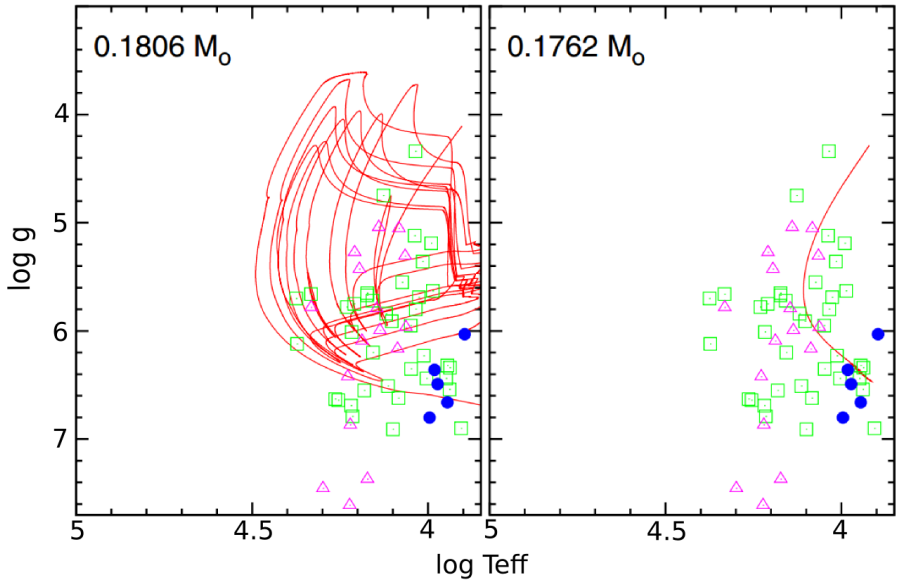

Figure 2 – log $T_{\rm eff}$ – log g diagrams for two He-core WD sequences computed by Althaus, Miller Bertolami & Córsico (2013). The sequence with $M > 0.18\ M_{\odot}$ undergoes CNO flashes during the early-cooling phase, showing complex loops in the diagram, while the lower mass sequence has no complex structure. Green squares and magenta triangles correspond to the observed post-RGB low-mass stars from Silvotti et al. (2012) and Brown et al. (2013). Filled blue circles correspond to five pulsating low-mass white dwarfs detected at the time (Hermes et al., 2013). Adapted from Córsico & Althaus (2014).

1.2 White Dwarf Stars

As can be inferred from the previous sections, the study of white dwarf stars is essential to understand stellar evolution, both for single and binary stars. In the single evolution case, the fraction of stars that become white dwarfs is believed to be over 97% (Fontaine; Brassard; Bergeron, 2001). That can be easily verified describing the mass distribution of stars formed in a cloud by an initial mass function. The first suggested, and still commonly assumed, is the Salpeter function (Salpeter, 1955):

$$\xi(m)dm \;=\; \xi_0 \left(\frac{m}{M_{\odot}}\right)^{-2.35} \frac{dm}{M_{\odot}}, \tag{1.2}$$

where m is the mass of the formed stars and ξ_0 is a normalisation constant. Integrating Eq. 1.2 from the minimum mass of a star, to the upper mass limit for a star to become a white dwarf, one obtains a fraction larger than 0.99. Even when other initial mass functions, with different exponents, or smaller superior limits are assumed, one obtains that at least 95% of the formed stars will evolve to white dwarfs.

Most white dwarfs do not generate energy by nuclear fusion, except for the initial states in their evolution where the hydrogen layer might be thick and hot enough for residual burning to occur. That happens for ELMs, as previously mentioned. However,

after that and for the rest of their evolution, they will only radiate energy due to residual gravitational contraction. The radius of a white dwarf star is usually similar to the Earth's radius, hence they have small surface area, resulting in very large cooling times (it takes around 10^{10} years for the effective temperature of a canonical mass white dwarf to decrease from 100 000 K to 5 000 K). Therefore cool white dwarfs are some of the oldest objects in the Galaxy, and studying them helps to understand the history of stellar formation and evolution in the Milky Way (e.g. Winget et al., 1987; Bergeron; Saffer; Liebert, 1992; Liebert; Bergeron; Holberg, 2005; Moehler; Bono, 2008; Tremblay et al., 2014).

The structure of white dwarfs in general is relatively simple when compared to stars in other evolutionary stages. The core is composed by helium for masses lower than around 0.45 $M_{\odot}$, depending on metallicity, which includes the ELMs. For masses above this limit and $\lesssim 1.06\ M_{\odot}$, the core is a mixture of carbon and oxygen. Above $\sim 1.06\ M_{\odot}$, the core is probably composed by oxygen, neon, and magnesium. The maximum mass of a white dwarf, above which the electron degeneracy pressure is no longer sufficient to counteract gravitational force, is known as Chandrasekhar mass and is equal to $\sim 1.40\ M_{\odot}$, when magnetic fields are not strong (i.e. not comparable to the electric field). Such limit is theoretical, not being confirmed observationally so far. These masses, close to solar, within a radius of approximately the size of Earth, give the white dwarfs very large densities (of the order of 1 ton/cm^3) and likewise strong gravitational fields.

The atmosphere of close to 80% of the white dwarfs is composed solely by hydrogen, because the heavier elements are diffused to the nucleus due to the strong gravity. This process is known as gravitational settling. Such stars are classified as *DA*, where the *D* refers to the degenerate nature of the core of the white dwarf and the *A* indicates the hydrogen composition of the atmosphere, similar to the main sequence classification scheme. Most remaining objects have helium atmosphere, because all the hydrogen was burned or lost in the initial phase of the white dwarf evolution, and visible He lines, being called *DB*. When the star is hot enough that the helium is ionised (effective temperature higher than $\sim$ 40 000 K), the classification is *DO*. For temperatures above $\sim$ 65 000 K, radiative levitation still plays a significant role, and heavier elements such as carbon and oxygen can still be detected in the atmosphere; these stars are called PG1159 (e.g. Werner et al., 1996). Recently, a few objects showing strong oxygen lines at lower $T_{\rm eff}$ ($<$ 40 000 K), where radiative levitation is negligible, have been found. They can only be explained as bare oxygen-neon cores; the proposed classification is *Dox* (Kepler; Koester; Ourique, 2016). If the white dwarf has cooled down below the excitation limit of any element in the atmosphere ($T_{\rm eff} \sim 5\,000$ K for hydrogen atmospheres, and $T_{\rm eff} \sim 12\,000$ K for helium atmospheres), there are no visible lines, and it is classified as *DC*. In some cases, carbon can be brought from the core to the surface by a convective layer and be detected in the atmosphere, situation in which the star is called a *DQ*. When a magnetic field is detected in the spectrum due to Zeeman splitting of the lines, an *H* is added to the classification.

If the magnetic field is detected by polarisation, a p is added. When metals are observed in the atmosphere despite gravitational settling, what is believed to be caused by ongoing accretion of disrupting planetesimals orbiting the white dwarf (Jura, 2008), a Z is added. Examples of these spectra can be seen in Fig. 3.

This simple structure, with limited atmosphere compositions, yet presenting temperature and pressure conditions difficult, and even impossible, to replicate on Earth, makes white dwarfs very rich laboratories to test physical models (e.g Winget et al., 2009; Córsico et al., 2012; Bainbridge et al., 2017). Adding that to all the possibilities they offer to study single and binary star evolution as well as Galaxy formation and evolution, one might say they are the most amazing astrophysical objects.

1.2.1 White Dwarf Stars in the SDSS

The number of known white dwarfs has largely increased thanks to the Sloan Digital Sky Survey (SDSS). SDSS is an ongoing project of mapping the sky which started in 1998. It is currently in its fourth phase (SDSS-IV), which started in 2014 and consists of three different projects: eBOSS (*e*xtended *B*aryon *O*scillation *S*pectroscopic *S*urvey), a cosmological survey with subprograms to survey variable objects and X-Ray sources; APOGEE-2 (*A*pache *P*oint *O*bservatory *G*alactic *E*volution *E*xperiment), a infrared spectroscopic survey of the Galaxy, and MaNGA (*Ma*pping *N*earby *G*alaxies at *A*pache Point Observatory), which intends to make spatially resolved maps of individual galaxies.

SDSS-III (2008–2014), on the other hand, had four projects: APOGEE, the previous version of APOGEE-2; BOSS, which proceeded eBOSS and focused on mapping the large scale structure of the Universe; MARVELS (*M*ulti-Object *A*PO *R*adial *V*elocity *E*xoplanet *L*arge-area *S*urvey), which searched for exoplanet evidence on nearby stars, and SEGUE-2 (*S*loan *E*xtension for *G*alactic *U*nderstanding and *E*xploration), focused on the structure and evolution the Milky Way.

SDSS prior surveys, SDSS-I/II (2000–2008), carried out the SDSS Supernova Survey, which repeatedly imaged along the celestial equator allowing the discovery of over 500 type Ia supernovae, and SEGUE-1, which started the Milky Way mapping continued by SEGUE-2. White dwarf stars were targeted by the SEGUE projects, but they were also observed by the BOSS projects, because white dwarfs are blue objects, with colours resembling quasars, and the targets are selected based on preliminary photometry. Still, Gentile Fusillo, Gänsicke & Greiss (2015) estimate that only 40% of white dwarfs with photometric measurements by the SDSS had follow-up spectroscopy.

SDSS has obtained almost five million spectra across about a third of the sky, including nearly a million observation of stars in our Galaxy. SDSS-I/II spectra were taken with the SDSS spectrograph, which covered $3800 - 9200$ Å. More recent data was

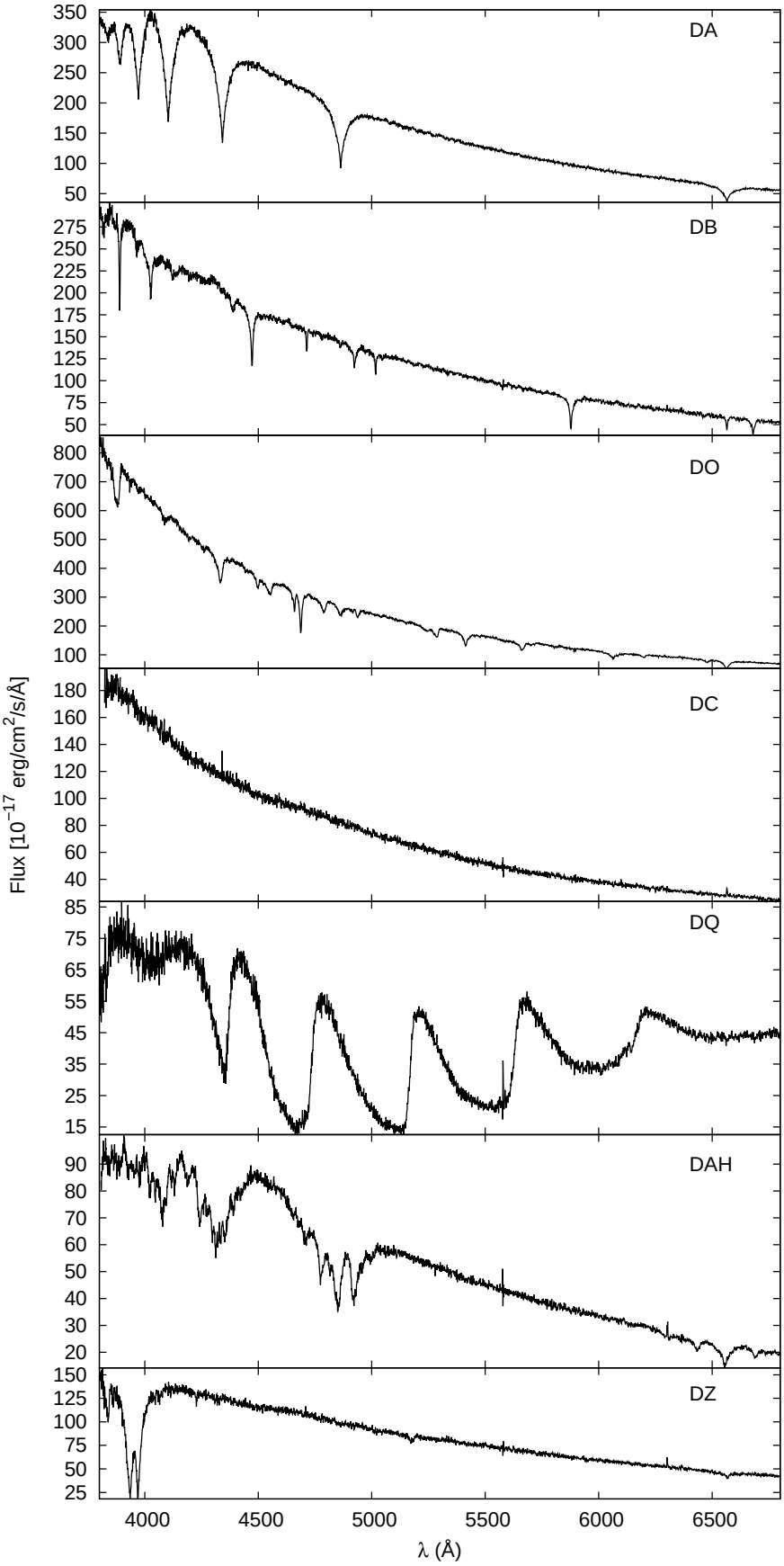

Figure 3 – Spectra of white dwarf stars with different atmosphere compositions.

taken with the BOSS spectrograph, which has a larger spectral coverage of $3650-10400$Å. The resolution $R = \lambda/\Delta\lambda$ is the same for both spectrographs: from 1500 at 3800 Å to 2500 at 9000 Å. SDSS has also imaged its footprint in five filters: u, g, r, i, and z. The detection limits are about [22.3, 23.3, 23.1, 22.3, 20.8] in these five filters, for an airmasss of 1.4, whereas the saturation limits are [13, 14, 14, 14, 12].

The first white dwarf catalogue compiled from SDSS data (Kleinman et al., 2004) was based on SDSS Data Release 1 (DR1, Abazajian et al., 2003). The next catalogue (Eisenstein et al., 2006), using the SDSS Data Release 4 (DR4, Adelman-McCarthy et al., 2006), roughly doubled the number of spectroscopically confirmed white dwarf stars. With the white dwarf catalogue based on the SDSS Data Release 7 (DR7, Abazajian et al., 2009), Kleinman et al. (2013) increased the total number of white dwarf stars by more than a factor of two compared to the catalogue based on DR4 data and also (re)analysed all stars from previous releases. I started my work in white dwarf classification with this catalogue. In Kepler et al. (2015) we reported over 8 000 new spectroscopically confirmed white dwarf stars after analysing SDSS Data Release 10 (DR10, Ahn et al., 2014). There we also implemented an automated search algorithm to search for objects missed by standard selection criteria, improving the candidate selection compared to previous catalogues. This was also the first white dwarf catalogue based on SDSS data to fit not only DA and DB stars, but also DZ, DQ, and pairs of a DA with a main sequence M star. More details concerning these catalogues are presented in Table 1.

Table 1 – Number of objects and the main classifications in the previous white dwarf catalogues published based on SDSS data releases.

Catalogue	Objects	Main classifications
DR1[a]	2 551 WDs	1 888 DA
	240 sds	171 DB
DR4[b]	9 316 WDs	8 000 DA
	928 sds	731 DB
DR7[c]	19 713 WDs	12 831 DA
		922 DB
DR10[d]	8 441 WDs	6 887 DA
	647 sds	450 DB

[a]Kleinman et al. (2004). [b]Eisenstein et al. (2006). [c]Kleinman et al. (2013), includes the (re)analysis of stars from previous releases, but does not include subdwarfs. [d]Kepler et al. (2015).

This large increase in the number of known white dwarfs made many other works possible, not only concerning the characteristics of the white dwarfs in the sample, but also

some of its implications to more general properties. In Kepler et al. (2013), for example, we studied the magnetic white dwarfs in the DR7 sample and found fields as high as 700 MG. The explanation for the existence of such high fields is still an open issue, but Kepler et al. (2013) found an increase in the mean field for lower $T_{\rm eff}$, in excess of a simple statistical increase in number from cooling. Kilic et al. (2013) suggested many of the objects in the SDSS sample should be observed as an alternate mission for the Kepler spacecraft, after it was damaged, what has been done since in the K2 mission (e.g. Hermes et al., 2014, Hermes et al., 2015, Bell et al., 2016). Tremblay et al. (2013) used the sample to test improved 3D atmosphere models, in an attempt to fix inaccuracies in the 1D mixing-length approach which caused apparent higher log g at temperatures where convection is the main energy transport. Another relevant work using this sample was done by Andrews et al. (2015), who used the binaries in the sample to constrain the initial–final mass relation in the solar neighbourhood.

All this progress was possible despite the fact that *all* of these works have used an artificial cut in log g, excluding all objects with log $g < 6.5$. This was based on the fact that the minimum mass of a white dwarf generated by the evolution of a single star corresponds to this log g. As a consequence, white dwarf stars coming from the evolution of interacting binaries, the already mentioned extremely-low mass white dwarfs, were excluded from all catalogues. Therefore, to understand the ELM class, it is necessary to search for other members by extending white dwarf searches to lower log g.

1.2.2 Extremely-low Mass White Dwarf Stars

Extremely-low mass white dwarfs were first found in searches for merging white dwarfs that could lead to type Ia supernovae. These white dwarfs in close binary systems are useful for providing constraints to the poorly understood common-envelope phase of binary evolution (Iben; Livio, 1993). Several unsuccessful surveys were carried out searching for such systems (e.g. Robinson; Shafter, 1987, Foss; Wade; Green, 1991). The first one to obtain considerable success was carried by Marsh, Dhillon & Duck (1995). It followed the work of Bergeron, Saffer & Liebert (1992), who found 14 white dwarfs with masses below 0.45 $M_{\odot}$ — too low to be explained by single evolution within the age of the Galaxy. Marsh, Dhillon & Duck (1995) proposed that their evolution was cut short by mass loss in binary interaction, and thus these stars should be members of close binary systems.

To test this hypothesis, they carried out time-resolved spectroscopy searching for radial velocity variations consistent with a close orbital configuration. Out of seven targets, they have found five to be in detached close systems, interpreting that as a confirmation that binary interaction is needed to produce low-mass white dwarfs. They were able to

determine the orbital period P and the radial velocity semi-amplitude K, which allow the calculation of the so-called mass function $f(M_1, M_2)$ for the binary, given by

$$f(M_1, M_2) = \frac{M_2^3 \sin^3 i}{(M_1 + M_2)^2} = \frac{PK^3}{2\pi G}, \tag{1.3}$$

where i is the orbital inclination and M_1 and M_2 are the masses of the component stars. The convention for defining M_1 and M_2 depends on the authors. Marsh, Dhillon & Duck (1995) called M_1 the mass of the brightest star, and M_2 the mass of the unseen companion. I will use this same nomenclature in this work.

The mass function sets a lower limit to the mass of the companion M_2, reached when the system is edge-on with $i = 90°$ and taking the limit $M_1 \to 0$. In this case, M_1 can be estimated from the spectrum, setting a larger lower limit to M_2. Marsh, Dhillon & Duck (1995) obtained lower limits above 0.1 $M_\odot$, implying that the companions cannot be main sequence dwarfs, since any M dwarf would have to have a mass below 0.1 $M_\odot$ to remain undetectable in the spectra or colours. The only alternative is that the companions are also compact stars, probably cooler white dwarfs.

Similar results were obtained in the more recent ELM Survey (Brown et al., 2010; Kilic et al., 2011; Brown et al., 2012; Kilic et al., 2012; Brown et al., 2013; Gianninas et al., 2015; Brown et al., 2016). They have so-far published 88 objects, out of which 76 are confirmed binaries. Analysing the velocity amplitudes, they conclude that the binary companions have a normal distribution of mass with a 0.76 $M_\odot$ mean and 0.25 $M_\odot$ dispersion, thus they are probably white dwarfs, since almost all are also usually undetectable in the spectra or colours. The orbital periods seem to follow a lognormal distribution with a median period of 5.4 h. The timescale τ for the distance between the stars to shrink so that they begin mass transfer via Roche-lobe overflow is given by the gravitational wave merger time,

$$\tau = 47925 \frac{(M_1 + M_2)^{1/3}}{M_1 M_2} P^{8/3} \text{ Myr}, \tag{1.4}$$

where the masses are in $M_\odot$ and the period P is in days (Kraft; Mathews; Greenstein, 1962). Half of the observed binaries will merge in less than 6 Gyr due to the gravitational wave radiation, which causes the system to lose angular momentum J at a rate given by

$$\frac{\dot{J}}{J} = -\frac{32}{5} \frac{G^3}{c^5} \frac{M_1 M_2 (M_1 + M_2)}{a^4}, \tag{1.5}$$

where a is the orbital separation (Landau; Lifshitz, 1958). The amplitude of their gravitational strain is too low to be detected by the Laser Interferometer Gravitational-Wave Observatory (LIGO), but, as shown by Nelemans, Yungelson & Portegies Zwart (2001), merging white dwarfs are predicted to be one of the dominant sources for the upcoming Laser Interferometer Space Antena (LISA). It is important to notice that, statistically,

95% of the ELMs have a total mass below the Chandrasekhar mass, hence they are not type Ia supernova progenitors. The outcomes of these merger events are single massive white dwarfs, stable mass transfer AM CVn binaries, and R Coronae Borealis stars (Brown et al., 2016). In AM CVn binaries, a white dwarf accretes helium-rich material from a companion, which can also be a white dwarf. They have very short orbital periods, usually less than 65 min, and spectra dominated by helium with hydrogen absent or extremely weak (e.g. Solheim, 2010). R Coronae Borealis (RCB) stars are hydrogen-deficient objects of varying spectral classes. Their brightness can decline by 8 magnitudes in a few weeks, due to dust formation episodes whose cause is still unknown (e.g. Clayton, 1996). Brown et al. (2016) noticed that the merger rate of ELMs is statistically identical to the formation rate of these stars.

The ELM Survey started within a hypervelocity star survey (see the MMT Hypervelocity Star Survey: Brown; Geller; Kenyon, 2009; 2012; 2014), which targeted objects with the colours of late-B type stars. The targets were selected from the SDSS photometric catalogue using calibrated, de-reddened PSF magnitudes (Adelman-McCarthy et al., 2008). Their colour selection (Fig. 4) was designed to exclude normal mass white dwarfs, but fortuitously includes low mass white dwarfs. Spectroscopy revealed that 15% of the HVS Survey targets were actually white dwarfs, amounting to 589 objects and motivating the ELM Survey. They did a spectroscopic follow-up to the ELM candidates, searching for radial velocity variations in the same fashion as Marsh, Dhillon & Duck (1995). Currently, they have obtained spectra for 80% of the stars in the ELM Survey over the magnitude range $15 < g_0 < 20$. The multi-epoch follow-up is less complete, resulting in a completeness of about 60% for the ELM Survey so far (Brown et al., 2016).

However, as the target selection was developed for B-type stars, it favours the detection of hot ELMs ($T_{\rm eff} \gtrsim 12\,000$ K). Cooler objects ($T_{\rm eff} \lesssim 10\,000$ K) were targeted by Brown et al. (2012). Yet, less than 5% of the objects in the ELM Survey show $T_{\rm eff} \lesssim 9\,000$ K, while evolutionary models (Althaus; Miller Bertolami; Córsico, 2013; Córsico; Althaus, 2014; Córsico et al., 2016; Istrate et al., 2016) predict the same amount of time to be spent above and below $T_{\rm eff} = 9\,000$ K. As there are many uncertainties in the models, concerning e.g. assumptions on element diffusion, progenitor initial mass and metallicity, and rotation, the cooling time scale between models can vary by more than a factor of two. Brown; Kilic; Gianninas (2017) estimated a 1:2 ratio of ELMs in the ranges $6500 < T_{\rm eff} < 9000$ K to $10\,000 < T_{\rm eff} < 15\,000$ K. Propagating the factor of two uncertainty in the cooling time scale, this ratio can be from 1:4 to 1:1, so 20–50 % of the ELMs should show $T_{\rm eff} < 9\,000$ K; however, as a systematic effect of the search criteria, only three (4%) of the published ELMs are in this range.

Moreover, the ELM Survey selection criteria also favoured higher log g objects. The low-log g phases happen before the object reaches the white dwarf cooling track (the

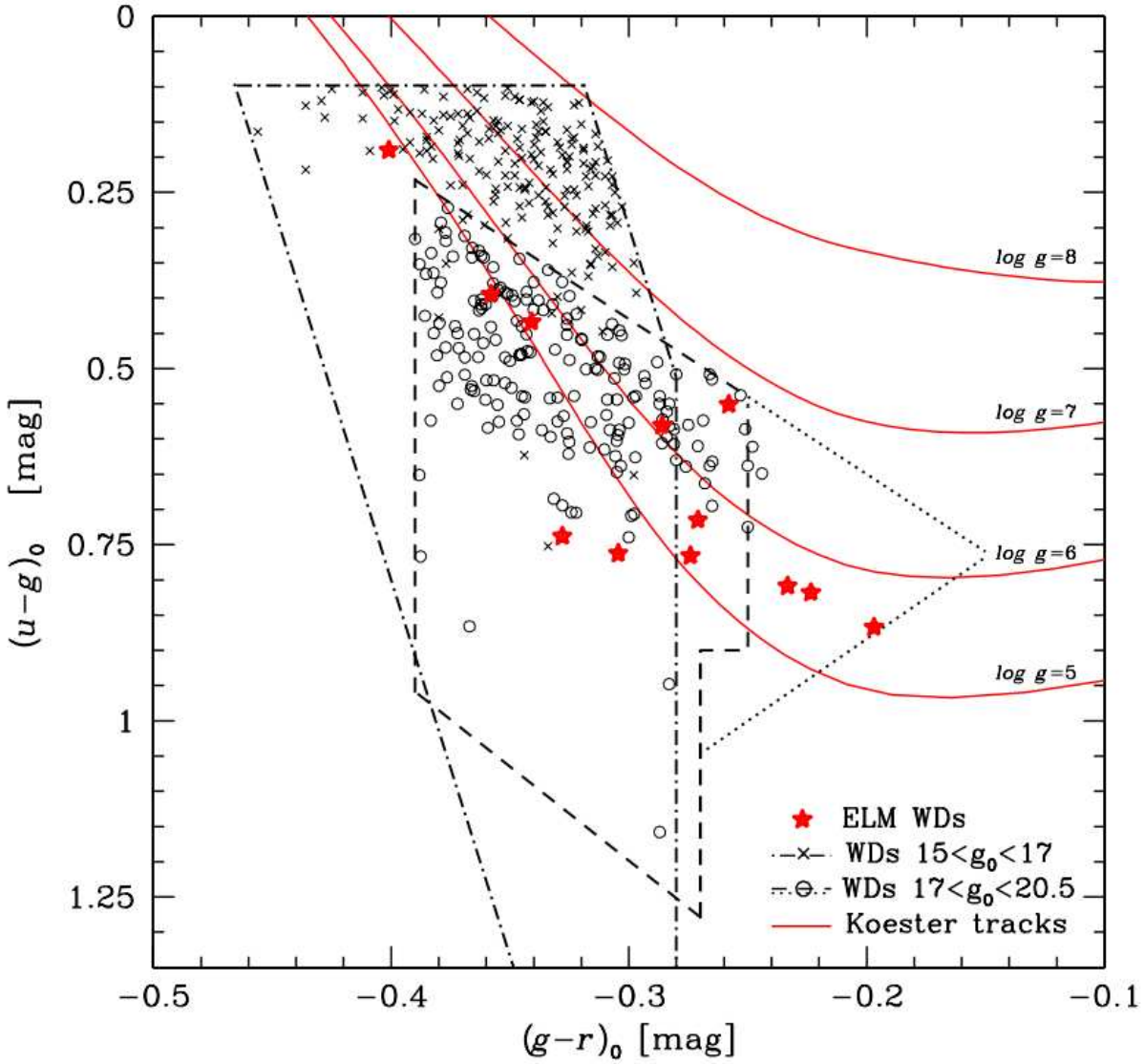

Figure 4 – Colour-colour diagram with the observed ELMs (solid stars) and other WDs (crosses, circles) within the HVS Survey. The colour selections are different depending on magnitude: $15 < g_0 < 17$ dot-dashed line, $17 < g_0 < 19.5$ dashed line, and $19.5 < g_0 < 20.5$ dotted line. The solid lines are synthetic photometry for white dwarf models with fixed log g and varying $T_{\rm eff}$ following Koester (2010) [Adapted from Brown et al. (2010)].

objects are hence known as pre-ELMs, e.g. Maxted et al., 2011; Maxted et al., 2014) and are relatively quick. The time spent with $\log g = 5 - 6$ is ten times smaller than with $\log g = 6-7$ in the models of Istrate et al. (2016). However, the average luminosity is about a hundred times higher in the $\log = 5 - 6$ range, hence the objects are five magnitudes brighter. Assuming a spherical distribution, and limiting magnitudes of $g = 14.5$ (bright saturation in the SDSS) and $g = 20$ (faint limit detection), the detection volume for $\log = 5 - 6$ is a thousand times larger than the volume for $\log = 6 - 7$. Combining these two factors, one should expect to find a hundred objects with $\log g = 5-6$ for each object with $\log g = 6 - 7$ in a magnitude-limited survey. There are 31 objects with $\log g = 6 - 7$ in the ELM Survey, but only 44 with $\log g = 5 - 6$, about 85% less than this estimate predicts, which is a consequence of their biased selection criteria. Hence there is clearly a missing population of cool, low-mass ELMs yet to be found, as evidenced in Fig. 5.

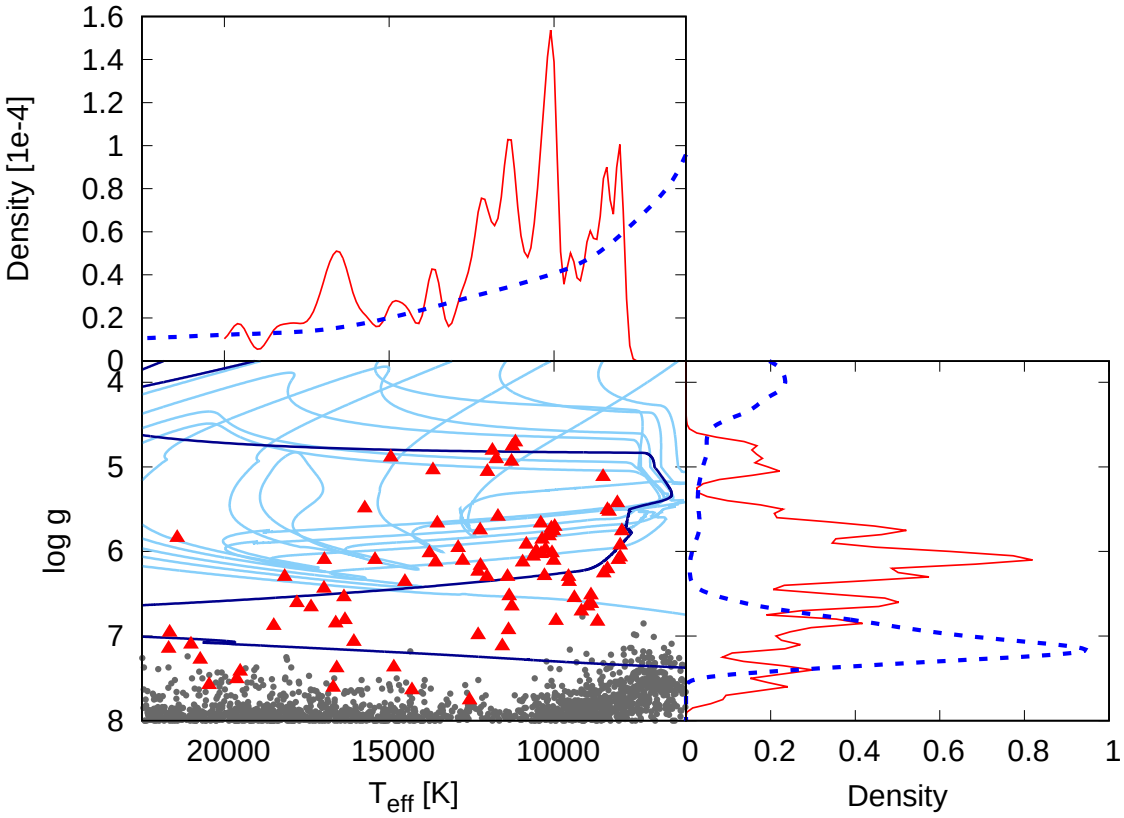

Figure 5 – Bottom-left panel shows the $T_{\rm eff} - \log g$ diagram for the objects in the ELM Survey, shown as red triangles, compared to two binary evolution models of Istrate et al. (2016), resulting on ELMs of masses 0.182 (light blue) and 0.324 $M_{\odot}$ (dark blue). Canonical mass white dwarfs are shown as grey dots for comparison. The top panel shows the distributions in $T_{\rm eff}$, both for the observed ELMs (red continuous line) and obtained from the models (blue dashed line). The bottom-right panel shows the distributions for log g. The distributions for the models were obtained taking into account the time spent at each bin of $T_{\rm eff}$ or log g compared to the total evolutionary time, with a spherical volume correction to account for difference in brightness. Note that there is a lack of known ELMs in the low $T_{\rm eff}$ and low log g ends of the distribution. There are also missing objects around log $g \sim 7.0$. As the distributions are normalized, the fact that there are very few observed ELMs at log $g \simeq 7.0$ moves the observed peak to log $g \simeq 6.0$, range that was prioritized in the ELM Survey selection, because log $g \approx 7.0$ can also be reached through single evolution.

1.3 Variable Stars

There exists a limitation to the study of most stars: we can only obtain information concerning the external layers, from which the light we analyse is emitted — the internal structure can usually only be inferred from evolutionary models. The only exception, apart from the ineffective study of neutrino emissions, are pulsating stars, in which case the measured periods are normal modes determined by the internal structure. Pulsations occur in many phases during the evolutionary process (see Fig. 6), and are one of five types of observed variability: (i) eclipsing binaries, (ii) rotating stars, (iii) cataclysmic variables, (iv) eruptive variables, and (v) pulsating variables. The first two are *extrinsic* variables, meaning there is no change in the star itself, but the presence of a companion or the rotation of the star affects the detected flux. The last three types, on the other hand, are *intrinsic* variables. This means the detected variation is due to a change in the physical properties of the star or stellar system itself.

(i) Eclipsing binaries are multiple stellar systems whose orbital plane is in an angle with the line of sight so that one star will partially or completely cover the other at some point during the orbit. This will cause a periodic variation in the observed magnitude of the system (example in Fig. 7). When the observed magnitude is at its maximum, the stars are seen side by side. When it reaches a minimum, one star is eclipsing the other. The depth of the eclipses depends on the effective temperatures of the stars, on the ratio between their radii, on the orbital inclination, and on the semi-major axis of the orbit. As the temperatures can be obtained through spectroscopy and the semi-major axis of the orbit can be calculated using the period and an estimated mass ratio $q = M_2/M_1$, the masses of the stars can be obtained combining the spectroscopic $\log\ g$ and the radius estimated from the light curve. This is one of the most precise ways of obtaining the physical parameters of a star. The other would be to measure its luminosity and temperature, and obtain the distance from parallax — which has been available only for a few white dwarfs.

(ii) Rotating stars sometimes show small variations due to dark or bright spots, as is the case for the Sun. Stars that have ellipsoidal shape, as close binaries, will also show variation as they rotate, since the area seen by the observer will change, altering their brightness. Very fast rotation can also flatten the star, giving it an ellipsoidal shape and causing variations with rotation. Another example of variation due to rotation are pulsars: neutron stars with high magnetic fields which emit beams of electromagnetic radiation in the direction of their magnetic poles, causing peaks in detected energy when the beam points towards the observer.

(iii) Cataclysmic variables are interacting binary stars and show sudden variations due to thermonuclear processes either in their interior or on their surface layers (example in Fig. 8). They are in binary systems, usually close, implying each component has strong

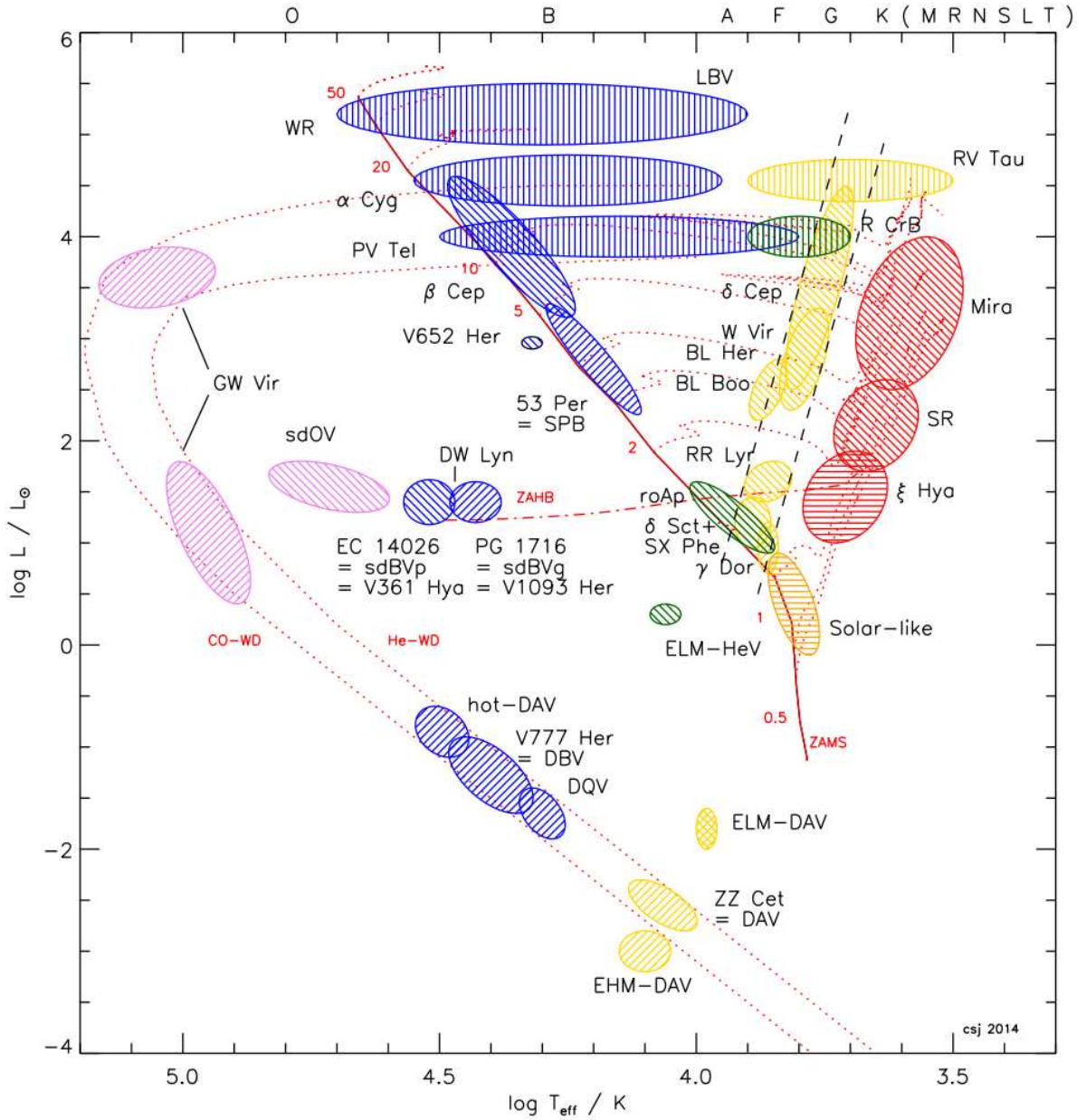

Figure 6 – Luminosity–effective temperature (or HR) diagram showing the approximate location of different classes of pulsating variables, coloured roughly by spectral type. The zero-age main sequence (ZAMS) and horizontal branch (HB), the Cepheid instability strip, and evolution tracks for model stars of various masses, indicated by small numbers in $M_\odot$, are shown. Shadings represent p-modes (\\\\), g modes (///), strange modes (|||) and acoustically driven modes (≡). Approximate spectral types are indicated on the top axis.
[Adapted from Jeffery & Saio (2016)].

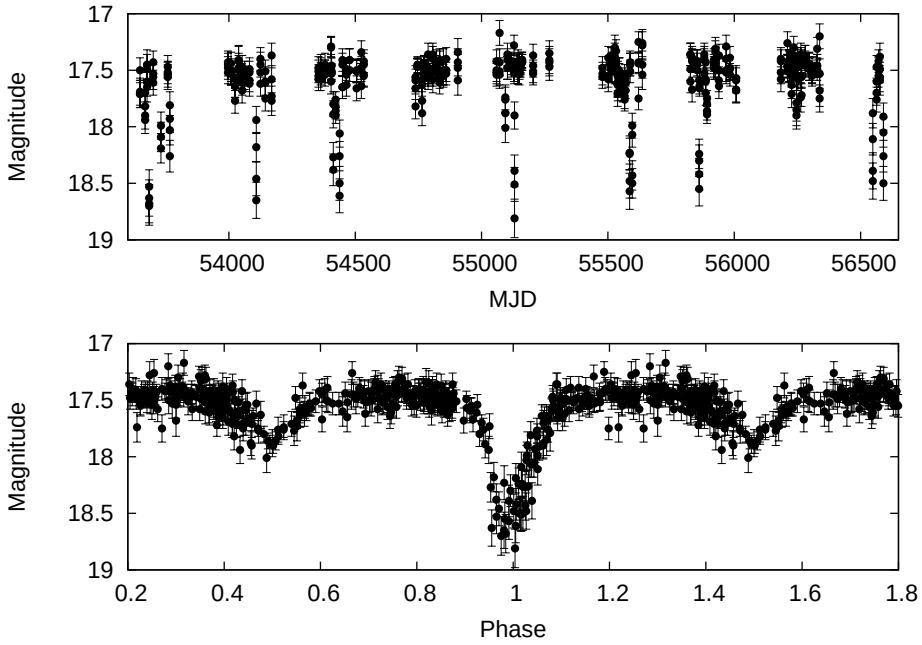

Figure 7 – Light curve in days (top panel) and in phase (bottom), folded to the estimated period of 1.34 days, of the eclipsing A-type star SDSS J035144.78+112502.5. The companion is unseen on the spectra, implying it is probably a cooler star of similar spectral type. Data from the Catalina Real-Time Transient Survey (CRTS, Drake et al., 2009).

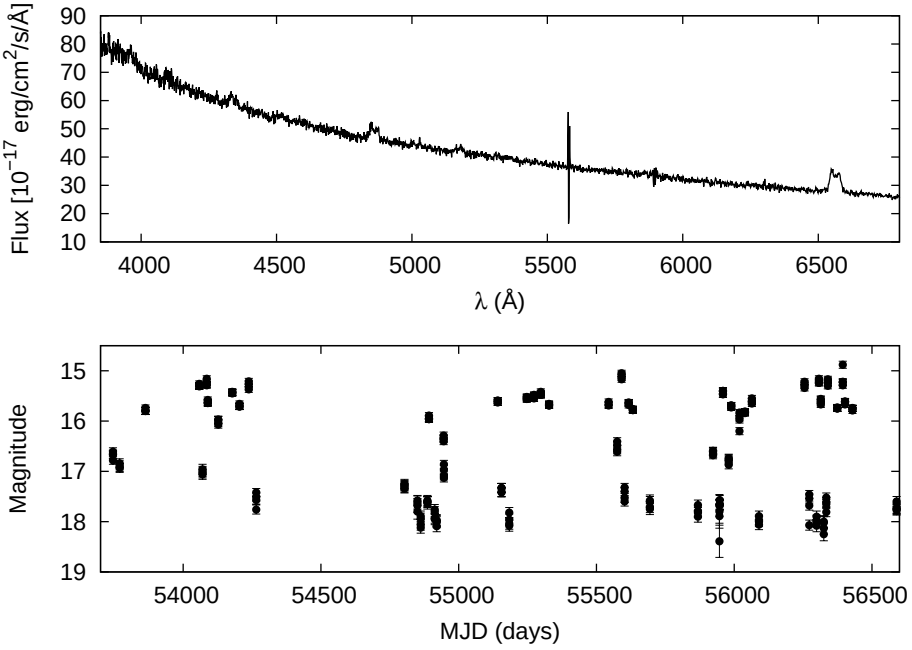

Figure 8 – SDSS spectrum (top panel) and light curve in days (bottom) of the cataclysmic variable SDSS J091216.19+505353.8. One can see that the hydrogen lines are in emission, due to the high-temperature on the burning external layers. The light curve, obtained from CRTS (Drake et al., 2009), shows that the magnitude can vary by as much as three orders because of these burning events.

influence in the evolution of the other. Many observations show that most of them are surrounded by an accretion disk formed by material lost by the binary companion. The variations occur when part of this material falls on the star and reaches a layer in which the temperature is high enough for it to ignite. Supernovae Ia, novae and recurrent novae are examples of cataclysmic variables. In most cases the accreting star is a white dwarf, which burns the accreted matter on its surface when the critical mass is reached.

(iv) Eruptive stars show variations, usually irregular, because of material being accreted to the star or else being lost by it. These events concentrate in their chromospheres and coronae and are not explosive, like in cataclysmic variables. Classical examples are protostars, which are still contracting inside a gas nebula to form the star, and pre-main sequence stars, as Herbig objects, which are usually still embedded in envelopes of gas and dust and commonly present circumstellar disks. Giants and supergiants also present this type of variation, since in these phases the star is losing mass through stellar winds. Another rather common eruptive event are flares, when a star undergoes a large increase in magnitude for a few minutes or hours and goes back to its original state. These events, which occur also for the Sun, are believed to be related to local variations in the magnetic energy.

(v) Pulsating variables, on the other hand, are not in perfect hydrostatic equilibrium, so there are, locally, accelerations causing movement of the fluid in the star, hence it shows periodic expansion and contraction of its surface layers. There are many types of pulsating variables (see Fig. 6). The pulsations may be radial, in which case spherical symmetry is preserved, or non-radial. The main modes of non-radial pulsations are g-modes (gravitational modes) and p-modes (pressure modes), each associated with one restoring force: gravitational or pressure force, respectively.

The characteristic frequency of the g-modes is the Brunt-Väisälä or buoyancy frequency η:

$$\eta = -g\left[\frac{d\ln\rho}{dr} - \frac{1}{\Gamma_1}\frac{d\ln P}{dr}\right], \tag{1.6}$$

where g is the local gravitational acceleration, r is the distance from the centre, ρ and P are local density and pressure, which are related through the coefficient Γ_1 by

$$\Gamma_1 = \left(\frac{\partial\ln P}{\partial\ln\rho}\right). \tag{1.7}$$

On the other hand, the characteristic frequency of the p-modes is the Lamb or sound frequency, given by

$$S_\ell = \sqrt{\frac{\ell(\ell+1)}{r^2}\frac{\Gamma_1 P}{\rho}} \tag{1.8}$$

$$= \sqrt{\frac{\ell(\ell+1)}{r^2}}\, v_s, \tag{1.9}$$

where ℓ is the degree of the harmonic describing the oscillation, and v_s is the sound speed at the given conditions. These frequencies are important because, in an adiabatic and perturbative theory, the radial wave number k_r follows the dispersion relation

$$k_r^2 = \frac{k_t^2}{\omega S_\ell^2}(\omega^2 - \eta^2)(\omega^2 - S_\ell^2), \tag{1.10}$$

where k_t is the transversal wave number, given by

$$k_t = \frac{\ell(\ell+1)}{r^2} = \frac{S_\ell^2}{v_s^2}, \tag{1.11}$$

and ω is the angular frequency of the pulsation. Therefore k_r^2 is positive if ω is either greater than both or smaller than both η and S_ℓ, in which case k_r is real and the waves propagate. On the other hand, if ω has a value between η and S_ℓ, k_r is imaginary and the waves are evanescent. Thus the frequencies η and S_ℓ define the range of possible propagating waves in a pulsating star.

Finally, assuming a constant density $\langle\rho\rangle$ over the star, radial pulsations show a period

$$\Pi = \frac{2\pi}{\sqrt{(3\Gamma_1 - 4)\langle\rho\rangle 4\pi G/3}}. \tag{1.12}$$

Examples of radial pulsating variables are the classical Cepheids, which are yellow supergiants with masses in the range $4 - 20\ M_\odot$ and luminosities up to $10^5\ L_\odot$. They have periods ranging from a few days to months, which present a well established relation with their luminosity. Such period-luminosity relationship, discovered in 1908 by the astronomer Henrietta Swan Leavitt, was used to estimate the distance between the Milky Way and the (at the time) Andromeda Nebula, allowing to conclude it was too far away to be part of the Milky Way, being in fact another galaxy. This discovery solved once and for all the "Great Debate", showing the Milky Way does not represent the entire Universe, and is a classical example of the relevance of variable stars. Other types of radial pulsating stars, also showing period-luminosity relationships, are RR Lyrae and some δ-Scuti stars. However, the relation is not so straightforward for the latter case because δ-Scuti can be multiperiodic, showing both radial and non-radial oscillations.

White dwarfs, already described as good laboratories to study stellar evolution, are a common type of nonradial pulsators. Carbon/oxygen core white dwarfs present g-mode pulsations related to the size of the convective layer in their atmospheres, with periods of hundreds to thousands of seconds. There are multiple instability strips in their evolution as they cool down. The pulsations are a result of an increase in opacity due to the existence of a partially ionised zone, most commonly of hydrogen. This effectively traps the photons, causing the pulsation. This is known as $\kappa - \gamma$ mechanism. As the convection responds to the pulsations, storing energy, the driving is also called convective

blocking. The most common type of variable white dwarf is DAV, or ZZ Ceti (bottom of Fig. 6). As the excited modes of pulsation depend on the physical properties of the *interior* of the star, measuring its observed frequencies and comparing them to theoretical models allows one to infer properties of the stellar interior, and not only of its external layers, as is the case for non-pulsating stars. ELM white dwarfs were also discovered to present pulsations (Hermes et al., 2012, 2012; Hermes et al., 2013; Hermes et al., 2013; Kilic et al., 2015; Bell et al., 2015), in what seems to be an extension of the ZZ Ceti instability strip (Van Grootel et al., 2013; Córsico; Althaus, 2014; Córsico; Althaus, 2016; Córsico et al., 2016). However, besides presenting the g-modes characteristic of regular ZZ Ceti stars, they may also present p-modes, with short periods of even a few seconds (Hermes et al., 2013). Less than ten pulsating ELM are known to date, making it difficult to comprehend their characteristics as a class. Thus in our search for new ELMs, we will also study their variability to search for new variables.

2 Aims and Scope

In the Introduction, we hinted about the impact of white dwarf stars in many areas of astronomy and physics. We can summarise some of the main potential applications of white dwarfs as follows:

- Constrain the formation history, initial mass function (e.g. Tremblay et al., 2014), initial-to-final mass relation (e.g. Romero; Campos; Kepler, 2015), and post-main sequence mass loss (e.g. Cummings et al., 2016) for different stellar populations, through the analysis of white dwarf mass and age distributions.
- Calibrate stellar ages by observing binary systems including white dwarfs (e.g. Fouesneau et al., 2018).
- Constrain binary evolution models (e.g. Zorotovic et al., 2010), understand the pathways towards supernovae Ia explosions (e.g. Badenes; Maoz, 2012) and also the low-frequency gravitational waves detectable with future space-based missions such as LISA (e.g. Nelemans, 2009).
- Derive the bulk composition of extra-solar planets and assess the frequency of planetary systems as a function of initial stellar mass and lookback time, by observing polluted white dwarfs (e.g. Gänsicke et al., 2012).
- Serve as laboratories for extreme physics, such as atomic and molecular physics in strong magnetic fields (Guan, 2006), high-density plasmas (Kowalski, 2006), and crystallisation (Winget et al., 2009).
- Test new physics theories, such as variations of the gravitational constant (Bainbridge et al., 2017), the mass of the axion (e.g. Córsico et al., 2012), and modified gravity theories (e.g .Saltas; Sawicki; Lopes, 2018).

In order to make this meaningful studies possible, one needs the white dwarf sample to be large, so that it offers a statistically significant representation of the whole space of physical parameters, especially throughout $T_{\rm eff}$ and log g. The easiest way to achieve that is to make use of available large surveys.

In this work, we search for white dwarfs in the *Sloan Digital Sky Survey* (SDSS) in order to improve the statistics of the white dwarf population. The reason behind this choice is simple: the SDSS is designed to observe quasars, which have colours very similar to white dwarfs. Therefore, as mentioned in Sec. 1.2.1, many white dwarfs are observed by this survey, both intentionally and due to being mistaken for quasars. Bearing in mind

the fact that very few ELMs are known, and that there were many biases in the search for these objects, we further extend our search to lower log g and cooler temperatures, with the additional goal of finding the missing population of ELMs.

In Chapter 3, I describe the methods employed in our search for new white dwarfs, from the candidate selection to subsequent data analysis and follow-up observations. Chapter 4 describes the results, which are split in two sections. Section 4.1 is dedicated to the new white dwarfs in SDSS. I discuss their classification, physical properties, and important results regarding mass and abundance estimates. In Section 4.2, I discuss the nature of the objects showing lower log g, unveiled in our search for new ELMs. I analyse photometric and kinematic properties to determine possible evolutionary origins, perform a probabilist analysis, and finally show results of follow-up observations revealing new (pre-)ELMs. Chapter 5 summarises the main results and draws conclusive remarks.

3 Methods

3.1 Candidate selection

We first searched white dwarfs using three different methods: a colour selection (done by me), a query for objects which the SDSS pipeline targeted or identified as a white dwarf (done by my supervisor, S. O. Kepler), and finally an automated search to find objects missed by previous searches (designed by Gustavo Ourique, now a Masters student). This automated search assumes the spectra of two objects with same composition, effective temperature, and surface gravity differ only in flux (normalization), due to different distances, and in slope, due to reddening and calibration issues. The developed code determines a polynomial of order between zero and two which minimises the difference between each spectrum and a sample of white dwarf templates, returning objects similar to other known white dwarfs.

The colour selection is illustrated in Fig. 9. It selects objects containing spectra with colours in the region where

$$(u-g) < 0.70 \text{ or } (u-g) < 2.5(g-r) - 0.5, \text{ if } 0.20 < (g-r) < 1.00 \tag{3.1}$$

$$-2.00 < (u-g) < 0.83 - 0.67(g-r), \text{ if } -2.00 < (g-r) < 0.20 \tag{3.2}$$

as already done in Kleinman et al. (2013) and Kepler et al. (2015), considering those are the regions populated by canonical white dwarfs ($\log\ g > 6.5$ and $T_{\rm eff} > 8\,000$ K) according to models.

Next, we selected objects labelled as O, B or A-type by the SDSS pipeline. These spectral types all show hydrogen dominated spectra, as observed for most (80%) white dwarfs and, importantly, for all known ELMs. The SDSS bright saturation is $g \sim 14.5$, hence main sequence stars with spectral type O, B, and A ($M_g \lesssim 0$) would have a distance modulus implying $d \gtrsim 8$ kpc. As the SDSS observes mostly outside of the Galactic disk ($|b| > 30^\circ$), a large population of OBA-type stars in the SDSS would imply an unexpectedly high population of early-type main sequence stars, whose main sequence lifetime is shorter than 1.5 Gyr, spread in the halo, which is older than 10 Gyr. Therefore, we anticipated a large population of ELMs within this sample, given their spectral type and the smaller radius, placing them within the disk for the SDSS saturation magnitudes.

I visually inspected all the selected objects to eliminate contamination, mainly by quasars, and to classify the found white dwarfs following the spectral classification described in Section 1.2. The features which guide this classification are described in Table 2. The selected O, B, and A-type stars were also inspected to confirm their hydrogen-

rich atmospheres.

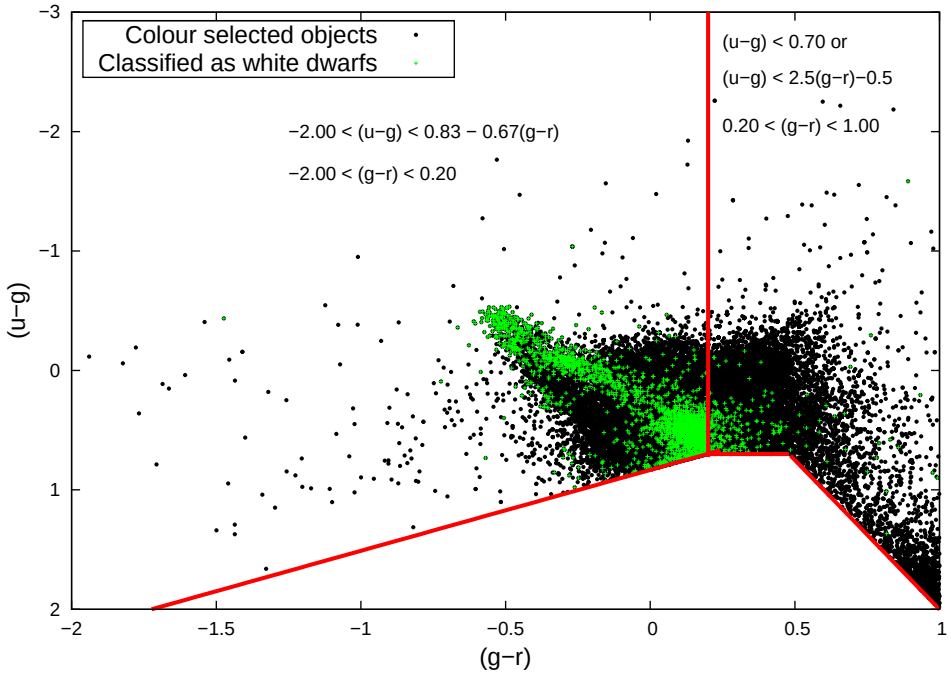

Figure 9 – Colour-colour diagram showing the region where objects were considered as white dwarf candidates.

Table 2 – Features which aid in the white dwarf classification. If more than one of the features are present in the spectrum, the representative letters are written side-by-side, starting with the most prominent feature (e.g. DAZ, DBA, DAH).

Feature	Classification(s)
Balmer lines	DA and sdB
HeI 4471Å	DB and sdB
HeII 4686Å	DO and sdO
Featureless spectrum	DC
C2 Swan bands or CI atomic lines	DQ
CaII H & K	DZ
CII 4367Å	hotDQ
Zeeman splitting	DH

3.2 Spectral modelling

After the visual confirmation of the spectra as white dwarfs, we fitted DAs, DBs, DQs and DZs to a grid of local thermodynamic equilibrium (LTE) synthetic non-magnetic spectra derived from model atmospheres (Koester, 2010) to obtain their $T_{\rm eff}$, log g (DAs and DBs), and abundances (DQs and DZs).

The DA grid covers the ranges $3.75 \leq \log\ g \leq 10.00$ for $6\,000\ \mathrm{K} \leq T_{\mathrm{eff}} < 25\,000\ \mathrm{K}$, and $5.00 \leq \log\ g \leq 10.00$ for $25\,000\ \mathrm{K} \leq T_{\mathrm{eff}} \leq 100\,000\ \mathrm{K}$. Non-LTE effects are neglected. The grid was extended to $\log\ g = 3.75$ to facilitate the separation of white dwarfs and main sequence stars ($\log\ g \lesssim 4.75$). However, this extension was not meant to be used for a full-fledged analysis of main sequence stars. It rather serves as an indicator of the luminosity class, given the external uncertainties of 5–10% in T_{eff} and 0.25 dex in $\log g$.

The DB model grid, on the other hand, covered $6.50 < \log\ g < 10.00$ and $12\,000\ \mathrm{K} < T_{\mathrm{eff}} < 50\,000\ \mathrm{K}$. Convection was treated using mixing-length theory, with coefficients ML2/α = 0.6 for DAs and ML2/α = 1.25 for DBs, to be consistent with Kleinman et al. (2013) and Kepler et al. (2015). For the DZs and DQs, it is not possible to obtain the $\log\ g$ from the spectra, because the line broadening is poorly known, hence there is a degeneracy between gravity and abundance concerning the width of the lines. They were thus fitted with models assuming $\log\ g = 8.00$ to determine their T_{eff} and the abundances of $[Ca/He]$ and $[C/He]$, respectively.

We classified all objects with $\log\ g \geq 6.50$ as common white dwarfs. Objects with lower $\log\ g$ which were not classified as hot subdwarfs (i.e., cooler than 20 000 K) were kept for further analysis. This resulted on about 50 000 spectra. As many of the remaining objects showed metal lines, our collaborator Detlev Koester calculated another model grid assuming solar abundances. The grid covers $6\,000\ \mathrm{K} \leq T_{\mathrm{eff}} \leq 40\,000\ \mathrm{K}$ and $3.5 \leq \log g \leq 8.0$. The models include metals up to $Z = 30$ with solar abundances in the equation of state, and include also the H_2 molecules. This ensures that the number densities of neutral and ionised particles are reasonable, which is important for the line broadening, in particular the Balmer lines. The tables of Tremblay & Bergeron (2009), which include nonideal effects, are used to describe the Stark broadening of the Balmer lines. The occupation probability formalism of Hummer & Mihalas (1988) is taken into account for all levels of all elements. Absorption from metals is not included. We have tested that the addition of the photo-ionisation cross sections of metals with the highest abundances does not result in significant changes in the A star region. Line blanketing for the atmospheric structure uses only the hydrogen lines. The synthetic spectra, however, include approximately the 2400 strongest lines of all elements included in the range 1500–10000 Å.

To choose between hot and cool solutions with similar χ^2, that arise given to the fact that these solutions give similar equivalent width for the lines, we have relied on SDSS *ugriz* photometry, and *fuv* and *nuv* magnitudes from the Galaxy Evolution Explorer (GALEX, Martin et al., 2005) when available. Specifically, we have chosen the solution which gave a T_{eff} consistent with the one obtained from a fit to the spectral energy distributions (SED) when the $\log\ g$ was fixed at 4.5, the average value for the sample in the spectroscopic fit. Full reddening correction was applied following Schlegel, Finkbeiner & Davis

(1998) for the SDSS *ugriz* magnitudes. For GALEX magnitudes, extinction correction was applied using the $E(B-V)$ value given in the GALEX catalogue, which was derived from the dust maps of Schlegel, Finkbeiner & Davis (1998), and the relative extinction of Yuan, Liu & Xiang (2013), $R_{fuv} = 4.89$ and $R_{nuv} = 7.24$, given that such values are not present in the catalogue of Schlegel, Finkbeiner & Davis (1998). Yuan, Liu & Xiang (2013) caution, however, that the *fuv* and *nuv* coefficients have relatively large measurement uncertainties.

To estimate internal uncertainties of our model grid, we have compared our estimates for objects with duplicate spectra. We have found the average difference to be 0.55% in $T_{\rm eff}$, with a standard deviation of 2.8%, and of 0.047 dex in $\log g$, with a standard deviation of 0.133 dex. Interestingly, these values are not significantly dependent on S/N for $S/N > 15$. We have also found no variation in these internal uncertainties when excluding objects cooler than 8 000 K from the sample. Hence the behaviour of the internal uncertainty does not seem to depend on either $T_{\rm eff}$ or S/N for the ranges considered here — for the O, B, and A type objects in particular, we have only considered objects with $S/N \geq 15$. The external uncertainty is higher for lower $T_{\rm eff}$, due to the decreasing strength of the lines, making them less sensitive as gravity indicators. That is, however, hard to quantify.

As a test for the validity of the solar metallicity models, we fitted a selection of known A stars. These include some of the objects with $\log g > 3.75$ from Allende Prieto & del Burgo (2016), as well as Vega from Bohlin (2007). As Fig. 10 shows, the average differences between our obtained values and the values from the literature are 4% in $T_{\rm eff}$ and -0.06 dex in $\log g$, with no great discrepancies or systematic differences. Moreover, some of the published ELMs were part of our sample, and both the $T_{\rm eff}$ and $\log\ g$ obtained by us agree with the values published by Brown et al. (2016), as can be seen in Fig. 11. The average difference was 6% in $T_{\rm eff}$ and and 0.001 dex in $\log g$, also with no apparent discrepancies or systematic differences. These average differences can be easily explained by the dominant external errors. In Appendix A, we compare our estimates to those of the SDSS pipelines, whose grids have much smaller coverage than our own.

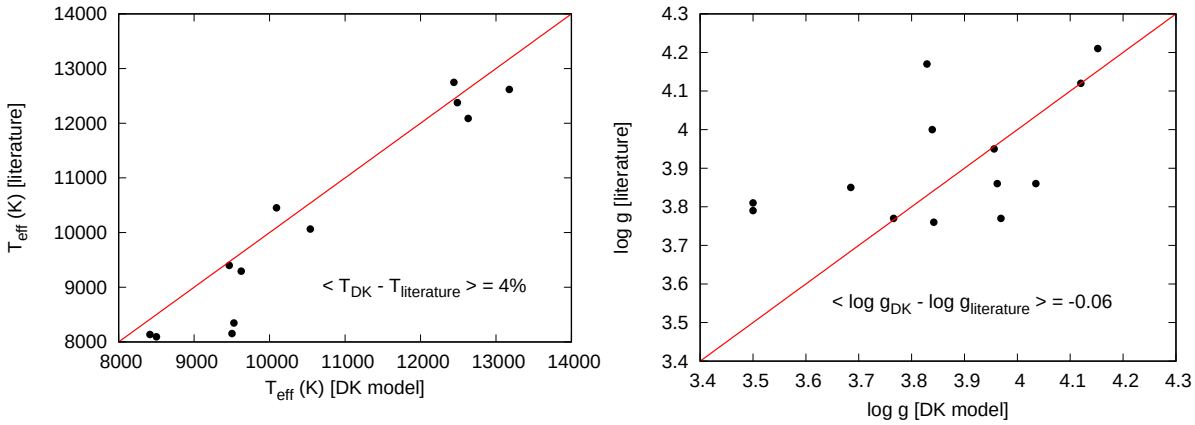

Figure 10 – Left panel shows the comparison between the $T_{\rm eff}$ obtained with our models (DK), and values from the literature. Right panel shows the same comparison for log g. The average difference is of about 4% in $T_{\rm eff}$, and of -0.06 in log g, which is even lower than the external error. The continuous red line in both panels shows where both determinations would be equal.

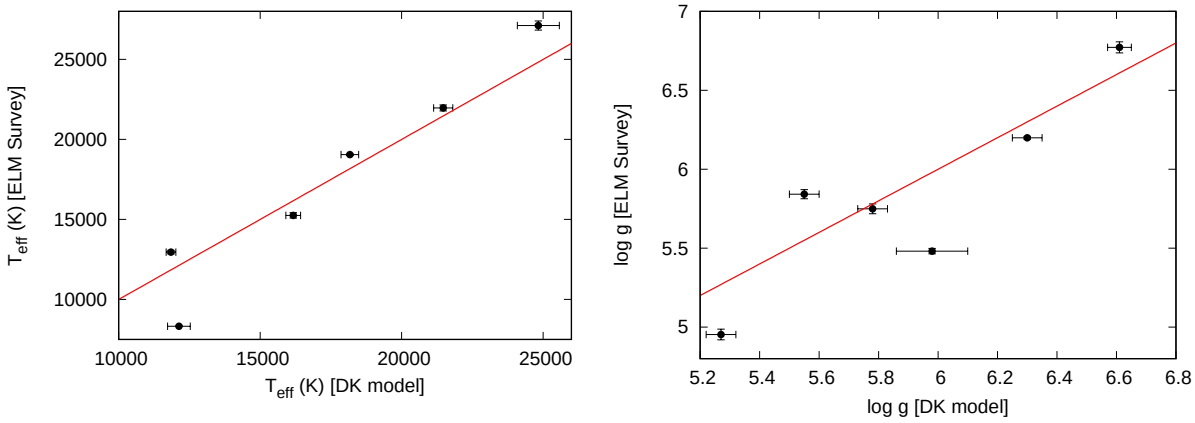

Figure 11 – Left panel: our estimated $T_{\rm eff}$ compared with the $T_{\rm eff}$ from the ELM Survey, for known ELMs in our sample. There is obviously a good agreement, with an average difference of less than 6%. Right panel: The log g estimated by us compared with the results from the ELM Survey. The agreement is not as obvious as for the $T_{\rm eff}$ case, but the average difference is 0.001 dex, and the average of the squared differece is 0.18 dex, still smaller than the external error.

I have also performed an analysis to estimate whether the metallicity would play a significant role in the gravity estimate. In order to do that, I verified if the difference in log g between our determination and that of the SEGUE Stellar Parameter Pipeline (SSPP, Lee et al., 2008) was dependent on the value of $[Fe/H]$ given by SSPP. There were 10 120 objects in our sample with SSPP determinations. I ordered them by $[Fe/H]$, and calculated the average of the absolute difference in $\log g$, $\sqrt{(\log g_{\rm DK} - \log g_{\rm SSPP})^2}$, as well as the standard deviation of this average, every 100 points. Fig. 12 suggests that the metallicity is not a dominant uncertainty factor in the gravity estimate, since there is no dependence of the difference between determinations on $[Fe/H]$.

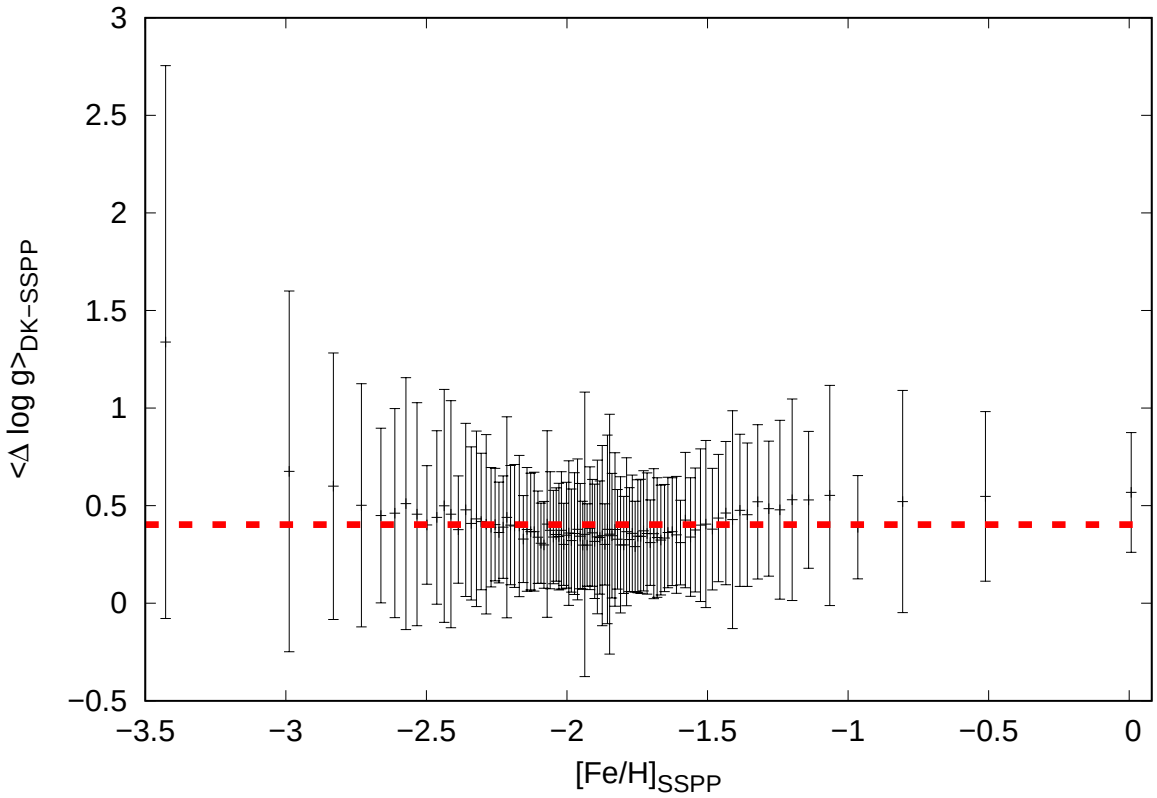

Figure 12 – Absolute difference in log g between our models and the SSPP determination, averaged every 100 points, as a function of the metallicity $[Fe/H]$ given by SSPP. The red dashed line shows the overall average. There seems to be no strong dependence of the difference between surface gravity on the metallicity.

3.3 Analysis of time-resolved survey data

Besides inspecting SDSS spectra for the selected O, B, and A-type stars, I also analysed light curves from open surveys, namely the Catalina Real-Time Transient Survey (CRTS, Drake et al., 2009), the Lincoln Near Earth Asteroid Research (LINEAR, Stokes et al., 2000), and the Palomar Transient Factory (PTF, Law et al., 2009; Rau et al.,

2009). I calculated the Fourier transform of the light curves for all O, B, and A-type stars available in the CRTS database, covering the whole range of accessible frequencies considering the time span and spacing of observations [from $f = 2/T$ to $f = 1/(2\,dt)$ with steps of $1/(10\,T)$, where T is the full span of the light curve and dt the minimal spacing]. This, of course, limits the range of periods that can be detected depending on the cadence of the survey. In general, only periods of the order of 0.1–100 days could be detected. When an object was not available in CRTS, I searched for it in the LINEAR and PTF databases. The amplitude in the Fourier transform for a given frequency f was calculated as

$$A(f) = 2\sqrt{C_r^2(f) + C_i^2(f)} \tag{3.3}$$

where the coefficients $C_r(f)$ and $C_i(f)$ are given by

$$C_r(f) = \frac{1}{N}\sum_{i=1}^{N} F(i)\cos\left[2\pi\, f\, t(i)\right] \tag{3.4}$$

$$C_i(f) = \frac{1}{N}\sum_{i=1}^{N} F(i)\sin\left[2\pi\, f\, t(i)\right] \tag{3.5}$$

and N is the number of observations, $F(i)$ is the normalised flux, and $t(i)$ the time of the observation.

The light curves were folded to the period corresponding to the maximum peak of the amplitude spectrum and I visually inspected them for signs of variability. It is worth mentioning that the data are not equally spaced, on the contrary: observations are spread through a number of years with very uneven spacings. Consequently, it is important to take into account the spectral window when analysing the data. To do that, one can calculate, for the same observation times as the analysed light curve, a synthetic light curve with the form

$$F(t) = \sin(2\pi f_{\mathrm{peak}} t + \pi/2) \tag{3.6}$$

where f_{peak} is the frequency of a chosen peak in the Fourier transform of the data. The Fourier transform of this synthetic light curve can be compared to the Fourier transform of the data, to estimate the effects of the uneven spacing on the amplitude spectrum, and verify if the detected peak is real or an artefact of the data acquisition. As a general rule, the main effect is the separation of the peaks in multiplets.

Taking into account that ELMs are the outcome of binary star evolution, I searched for signs of eclipses in the phase-folded light curves. The known ELMs show periods between 12 min and 36 h (Brown et al., 2016); theoretical models suggest the periods can be up to several days (Sun; Arras, 2017). I also searched for variability with periods in the range predicted for the ELMs, which is of up to a couple of hours to g-modes (Althaus; Miller Bertolami; Córsico, 2013; Istrate et al., 2014). The p-modes show periods of the order of a few seconds, which cannot be detected with the cadence of these surveys.

I also inspected the SDSS subspectra for each object to search for radial velocity variations between them. Each final SDSS spectrum is composed by multiple spectra, usually three, with ~ 15 min exposure time. The S/N of the subspectra is almost always below ten, so while conclusions can rarely be made based solely on the SDSS subspectra, they can be used to probe for possible variations suggesting the need for a follow-up. My approach was similar to that of Badenes & Maoz (2012) and Hermes, Gänsicke & Breedt (2017) for searching double degenerate binaries. I normalised each subspectrum by the continuum, which was estimated by fitting a linear function between each of the Balmer lines, and then fitted each of the lines (up to H8) to a Gaussian profile. The obtained shift of the line centre in relation to the rest wavelength was used to estimate a radial velocity for each line. The final radial velocity for the given subspectrum was assumed to be the average velocity, with the error estimated by the standard deviation. I used this simple approach as a practical way to analyse such a large sample; the more formal cross-correlation technique was used to followed up spectra, as described in Section 3.4.1.

I was able to obtain a fit to 80% of the spectra in the O, B, A sample. I then evaluated the ΔV between the maximal and the minimal estimated radial velocities, considering only estimates with an error smaller than 100 km/s. Badenes & Maoz (2012) suggest that follow-up is needed to reach conclusions on objects that show $\Delta V < 200$ km/s, hence I restricted further analysis to 14 objects showing $\Delta V > 200$ km/s. I used the Period04 software (Lenz; Breger, 2005) to estimate the orbital period by doing a Fourier transform and finding the orbital solution with the smallest residuals.

3.4 Follow-up observations

To confirm the nature of identified ELM candidates, I obtained time-resolved spectroscopy to search for radial velocity (RV) variations indicating the presence of a close binary companion, and time-series photometry to look for eclipses, ellipsoidal variations, or pulsations typical of ELMs.

Our observing campaign for a small subsample targeted bright objects with $T_{\rm eff}$ and log g in the range predicted by the evolutionary models shown in Fig. 5. Targets with high proper motion and/or high radial velocities and ELM-like colours were prioritized. I also gave priority to objects showing radial velocity variations in the subspectra taken by the SDSS. I obtained time-resolved spectroscopy for 26 targets. I have also obtained time-series photometry for 21 targets in the vicinity of the instability strip by Tremblay et al. (2015) and Gianninas et al. (2015), which was empirically obtained taking into account 3D corrections to $T_{\rm eff}$ and log g.

I carried out spectroscopy mainly with the Goodman Spectrograph

(Clemens; Crain; Anderson, 2004) on the 4.1 m Southern Astrophysical Research (SOAR) Telescope. All exposures were taken with a 1.0" slit, and binned by a factor of two in both dimensions to improve S/N. The width of the slit was chosen based on the average seeing ($0.8 - 1.5$"), so that we could obtain good resolution without losing too much light. I used a 1200 l/m grating, with a camera angle of 30.00° and grating angle of 16.30°, obtaining a wavelength coverage of 3600–4950 Å with a resolution of ~ 2 Å.

I also obtained spectroscopy with the GMOS spectrographs (Hook et al., 2004; Gimeno et al., 2016) on both Gemini North and Gemini South 8.1 m telescopes. The exposures were taken with a 0.75" slit. As with SOAR, the CCD was binned by a factor of two in both dimensions and I used a 1200 l/mm grating. Exposures centred at both 4400 Å and 4450 Å were taken at each semester, to dislocate the position of the two gaps between the CCDs in GMOS, covering wavelengths 3580–5190 Å and 3630–5240 Å, respectively. The data was partially affected by the bright columns issue developed by GMOS-S CCD2 and CCD3 during September 30, 2016 – February 21, 2017.

I also observed five $\log g > 5.5$ objects with the medium resolution echelle spectrograph X-shooter (Vernet et al., 2011), mounted on VLT-UT2 at Paranal, Chile. X-shooter covers the spectral range from the atmospheric cut-off in the UV to the near-infrared with three separate arms: UVB (3000 – 5600 Å), VIS (5600 – 10100 Å) and NIR (10100 – 24000 Å). The data were taken in stare mode, using slits of 1.0", 0.9", and 1.2" for UVB, VIS, and NIR arms, respectively, which allows a resolution of ~ 1 Å. X-shooter has the advantage of also allowing to search for red companions, that could appear as an excess in the NIR arm spectra.

For all instruments, arc-lamp exposures were taken before and after each science exposure to verify the stability. For the wavelength calibration, a CuHeAr lamp was taken after each round of exposures, at the same position of the science frames. Due to the faintness of the objects and the need for multiple spectra, the exposure time was estimated aiming at a median signal-to-noise ratio (S/N) of 10–15 per exposure. One radial velocity standard was observed at each semester to verify the reliability of the method, and a spectrophotometric standard star was observed every night for the flux calibration, except for Gemini observations, which observed one spectrophotometric standard star per semester.

Time-series photometry was obtained with the 1.6 m Perkin-Elmer telescope at Observatório do Pico dos Dias (OPD, Brazil), with an Andor iXon CCD and a red-blocking filter (BG40) to reduce sky noise. I have also used the imaging mode in Goodman at SOAR for photometry, with the S8612 red-blocking filter. The integration time varied from 10 to 30 s, depending on the brightness of the target, with typical readout of 1-3 s.

3.4.1 Data analysis

I reduced the SOAR spectroscopic data reduced using IRAF's NOAO package. The frames were first bias-subtracted, and flattened with a quartz lamp flat. I then extracted the spectra and did the wavelength calibration with a CuHeAr lamp spectrum extracted with the same aperture. Finally, flux and extinction calibration were applied. I used the GEMINI IRAF package for data from these telescopes, and the X-shooter pipeline for the VLT data, with equivalent steps in the reduction.

I did the radial velocity estimates with the XCSAO task from the RVSAO package (Kurtz; Mink, 1998), after verifying that the intercalated HeAr lamps presented no shift, which was always the case. I cross-correlated the spectral region covering all visible Balmer lines (typically from 3750 to 4900 Å) to spectral templates from our model grid. The values of RV were corrected to the Solar System barycentre given the time of observations and the telescope location.

I performed a Shapiro-Wilk normality test (Shapiro; Wilk, 1965) on the estimated radial velocities using the STATS package in R. This test checks the validity of the null-hypothesis that a sample of values came from a Gaussian distribution, and was proven to be more reliable than other normality tests such as Kolmogorov-Smirnov (Razali; Wah, 2011). The test statistic W compares the observed values with expected values from a Gaussian distribution. Comparing the value of W with its probability distribution, we can obtain the p-value. The p-value gives the probability that the statistical properties of the two compared groups (here the sample of RVs and a Gaussian distribution) are compatible when the null-hypothesis is true. The null-hypothesis is rejected when the p-value is smaller than a chosen α level, which we discuss below. In this case, there is evidence that the data are not from a Gaussian distributed population — in other words, the detected variability cannot be explained by Gaussian uncertainties.

Next, I calculated the Lomb-Scargle periodogram (Lomb, 1976; Scargle, 1982) using the NASA Exoplanet Archive tool[1] for the obtained RVs of all objects. This periodogram is similar to a Fourier transform, but it is designed to detect periodic signals in unevenly-spaced observations. For each of the highest fifty peaks in the periodogram, I calculated an orbital solution of the form

$$RV(t) = RV_0 + K \sin(2\pi t/T + \phi), \tag{3.7}$$

where RV_0 is the systemic velocity, K is the semi-amplitude of the RV variation, T is the period, and ϕ the phase. I selected as the best solution the one with the highest reduced R^2, defined as

$$R^2 \equiv 1 - \frac{\sum_i (y_i - f_i)^2}{\sum_i (y_i - \bar{y})^2}, \tag{3.8}$$

[1] <https://exoplanetarchive.ipac.caltech.edu/cgi-bin/Pgram/nph-pgram>

where y_i are the observed values, $\bar{y}$ is their mean, and f_i are the adjusted values. This is equivalent to selecting the solution with the smallest reduced χ^2. I have also verified whether the difference in R^2 between the dominant solution and the next best was significant. In case there was a small difference in R^2 ($\lesssim 10\%$), both solutions are shown.

The results of the Shapiro-Wilk test and of the orbital fit were interpreted independently. I have assumed a 95% confidence level ($\alpha = 0.05$) in the Shapiro-Wilk test to flag an object as RV variable, and $R^2 > 0.75$ to flag the orbital solution as reliable. In some cases, a very good solution ($R^2 > 0.80$) was obtained even though the Shapiro-Wilk test presented $p > 0.05$. This is probably related with the low sampling of the RV curve, hence we also consider these objects as probable binaries. It is important to emphasise that obtaining $p > 0.05$ in the Shapiro-Wilk test does not prove that the sample is Gaussian, only that we cannot reject that based on the observed sample.

I later Doppler-corrected each individual spectrum considering the estimated velocities, and combined all spectra of each object to obtain a $S/N \gtrsim 30$ spectrum (the average for the whole sample was $S/N = 45$). Considering the lack of strong metal lines, we fitted these spectra to a grid of models assuming metallicity $Z = 0.1\ Z_{\odot}$, with the same input physics as described in Section 3.2. The SDSS spectra of the objects were also fit to this same grid to allow a comparison.

All photometry images were bias-subtracted, and flat-field corrected using dome flats. I performed photometry with the DAOPHOT package. As all the targets were resolved, I did aperture photometry, which consists in counting the detections inside a circle around each star and subtracting the sky counts, estimated on a ring around the object. To eliminate the effect of random sky variations and extinction, I did differential photometry, i.e. subtracted the magnitude of a neighbouring comparison star of similar brightness or brighter from the target magnitude. I also rescaled the whole light curve to vary around zero by subtracting the average, according to

$$m = m_{target} - m_{comparison} - \frac{1}{N}\sum_{1}^{N}(m_{target} - m_{comparison}), \tag{3.9}$$

were m is the target's differential magnitude, m_{target} and $m_{comparison}$ are the magnitude estimated from the counts for the object and the comparison star, and the last term is the subtraction of the average to rescale the light curves to zero. I analysed the resulting light curve with PERIOD04 (Lenz; Breger, 2005), in search of pulsations with amplitude at least four times larger than the average amplitude of the Fourier transform (false alarm probability smaller than 1 in a 1000). PERIOD04 was also used to fit the light curve and perform pre-whitening when pulsations were found.

4 Results

4.1 White Dwarf Stars in SDSS DR12

4.1.1 Identification and Classification

The spectra obtained by SDSS are cross-correlated by their pipeline with many stellar templates, covering all spectral types for the main sequence and the giant branch (O, B, A, F, G, K, M), brown dwarfs (L, T), carbon stars, and some types of white dwarfs (DA, DAH, DQ, and cataclysmic variables). The template which gives the smallest chi-square,

$$\chi^2 \;=\; \sum_{i=1}^{n} \frac{(F_{obs_i} - F_{model_i})^2}{\sigma^2_{F_{obs_i}}}, \tag{4.1}$$

where n is the number of points in the flux curve, F_{obs} is the observed flux, F_{model} is the flux of the model, and $\sigma_{F_{obs}}$ is the uncertainty in the observed flux, is used to estimate the redshift and to determine the class of the object. By this method, 3 687 objects in the DR12 were classified by their pipeline as white dwarf stars. These spectra were inspected to check for wrong identifications. We identified 8 quasars and 1 BL Lac object, which were removed from the sample. The remaining objects were white dwarfs or subdwarfs. We also removed those which had already been identified and published by previous catalogues (Kleinman et al., 2004; Eisenstein et al., 2006; Kleinman et al., 2013; Kepler et al., 2015). This left 2 016 new white dwarfs and 219 new subdwarfs, whose classifications are shown in Table 3. Among these subdwarfs, almost all (216) are objects showing only hydrogen lines (spectral classification A), with log g in the range 5.5–6.5, but temperature below 20 000 K. Therefore, they do not have all the characteristics of any evolutionary class: the log g is too high for main sequence, but too low for canonical white dwarfs, and the temperature is too low for hot subdwarfs. We attributed the classification *sdA* to these objects, but this is merely an spectral classification; we know nothing yet about the true nature of these objects or their evolutionary origin. One possibility is that they are extremely-low mass white dwarfs, what shall be left for discussion in Section 4.2.

Next, we searched for objects missed by the SDSS pipeline using colours. The colour selection described in Section 3 by Eqs. 3.1 and 3.2, and used before by Kleinman et al. (2013) and Kepler et al. (2016), returned 68 836 objects. We first eliminated those which had already been identified by the SDSS pipeline, and were therefore in the previous sample, being left with 66 270 objects. They were all visually inspected to identify and classify the white dwarfs and subdwarfs. Visual inspection is our preferred method because it also

allows to identify new classes and peculiar objects (e.g. Kepler; Koester; Ourique, 2016), which would not be straight-forward with machine learning algorithms. Most objects turned out to be quasars, which have colours very similar to white dwarfs, as mentioned before, but show easily identifiable highly redshifted emission lines in the spectra. There remained 1 371 white dwarfs and subdwarfs which were missed by the SDSS pipeline. Their classification is shown in Table 4. It is important to notice that, while most DA and DZ-type objects are recovered by the pipeline, other white dwarf types are almost completely missed, mainly because there are no templates for them in the SDSS pipeline. Therefore, the colour query is crucial to obtain a complete white dwarf sample.

Table 3 – Classification of the new white dwarfs identified in DR12 by SDSS's pipeline.

Classification	Number of objects
DA	1 840
sdA	216
DZ	166
DC	6
DB	3
sdB	3
CV	1
Total	2 016 WDs
	219 sds

Table 4 – Classification of the new white dwarfs identified in DR12 by colour selection.

Classification	Number of objects
DA	623
sdA	277
DZ	12
DC	245
DB	99
sdB	35
CV	10
sdO	28
DQ	28
DO	11
PG1159	2
AMCVn	1
Total	1 031 WDs
	340 sds

Finally, the automated search described in Section 3 was done in the *whole* 4.5 M spectra database of the SDSS DR12. This had the intention of not only finding objects

missed be the previous searches, but also check if there were white dwarfs missed by the previous catalogues. Additional 1 180 new white dwarfs and subdwarfs were recovered (Table 5), besides 170 white dwarfs missed by previous catalogues. Most of these objects are relatively cool, which explains why they were missed. The cooler the object, the closer it is to the main sequence. The SDSS pipeline usually misclassifies such cool objects as belonging to the main sequence, while our colour selection avoids them in order not to increase even more its number of false positives. The automated search does not make cuts in colour, being capable of recovering these objects. However, cuts in S/N must be made to limit the number of identifications, since they are also visually inspected to exclude the numerous false positives. Therefore it cannot substitute the colour selection, which is independent of the spectra's S/N, and can be used to find DCs, which show no spectral lines.

Table 5 – Classification of the new white dwarfs recovered in DR12 by our automated search.

Classification	Number of objects
DA	312
sdA	787
DZ	37
DC	29
sdB	3
DQ	11
Dox	1
Total	390 WDs
	790 sds

The total number of identified objects is given in Table 6. In short, the SDSS pipeline is efficient in recovering DAs (66%) and DZs (77%), but the colour selection is essential to recover other dominant classes, especially DBs (97%), DCs (87.5%), and DOs (100%). Hot DAs are also better recovered by the colour selection, because the pipeline usually misclassifies them as main sequence O stars, since the continuum is dominant over the lines in the fit. Many low-S/N objects are also missed by the pipeline since the noise reduces the quality of the fit, increasing the probability of obtaining a wrong solution. On the other hand, both the pipeline and the colour search miss some cool ($T_{\rm eff} \lesssim 10\,000$ K) objects, especially of low-log g, which in turn are recovered by the automated search. That is illustrated in Fig. 13 for the DAs. Therefore the three methods complement each other, being all necessary to recover most white dwarfs. Unfortunately, none of these methods is able to recover really cool ($T_{\rm eff} \lesssim 6000$ K) white dwarfs, because they have no spectral lines, are faint ($M \sim 15$ for $T_{\rm eff} = 5000$ K and log $g = 8$), and show low S/N.

We fitted white dwarfs and subdwarfs showing atmosphere composed either by

hydrogen or by helium to local thermodynamic equilibrium (LTE) grids of synthetic non-magnetic spectra derived from model atmospheres (Koester, 2010). Our DA grid extends up to $T_{\rm eff} = 100\,000$ K, but non-local thermodynamic equilibrium (NLTE) effects are not included. Napiwotzki (1997) concluded pure hydrogen atmospheres of DA white dwarfs are well represented by LTE calculations for effective temperatures up to 80 000 K, but, when traces of helium are present, NLTE effects on the Balmer lines occur down to effective temperatures of 40 000K. He concluded LTE models should exclude traces of helium for the analysis of DA white dwarfs, as is done here. We fitted the spectral lines and photometry separately (Koester, 2010), selecting between the hot and cool solutions using photometry as an indicator.

Table 6 – Classification of all the new white dwarfs in DR12. The number in parentheses indicates the percentage of the WD or sd sample corresponding to that class. CV and AMCVn objects, which are binaries containing a white dwarf, are included in the WD statistic.

Classification	Number of objects
DA	2 775
	(87.90%)
sdA	1 280
	(95%)
DZ	215
	(6.81%)
DC	280
	(8.87%)
DB	102
	(3.23%)
sdB	41
	(3%)
CV	11
	(0.35%)
sdO	28
	(2%)
DQ	39
	(1.23%)
DO	11
	(0.35%)
PG1159	2
	(0.06%)
AMCVn	1
	(0.03%)
Dox	1
	(0.03%)
Total	3 157 WDs
	1 349 sds

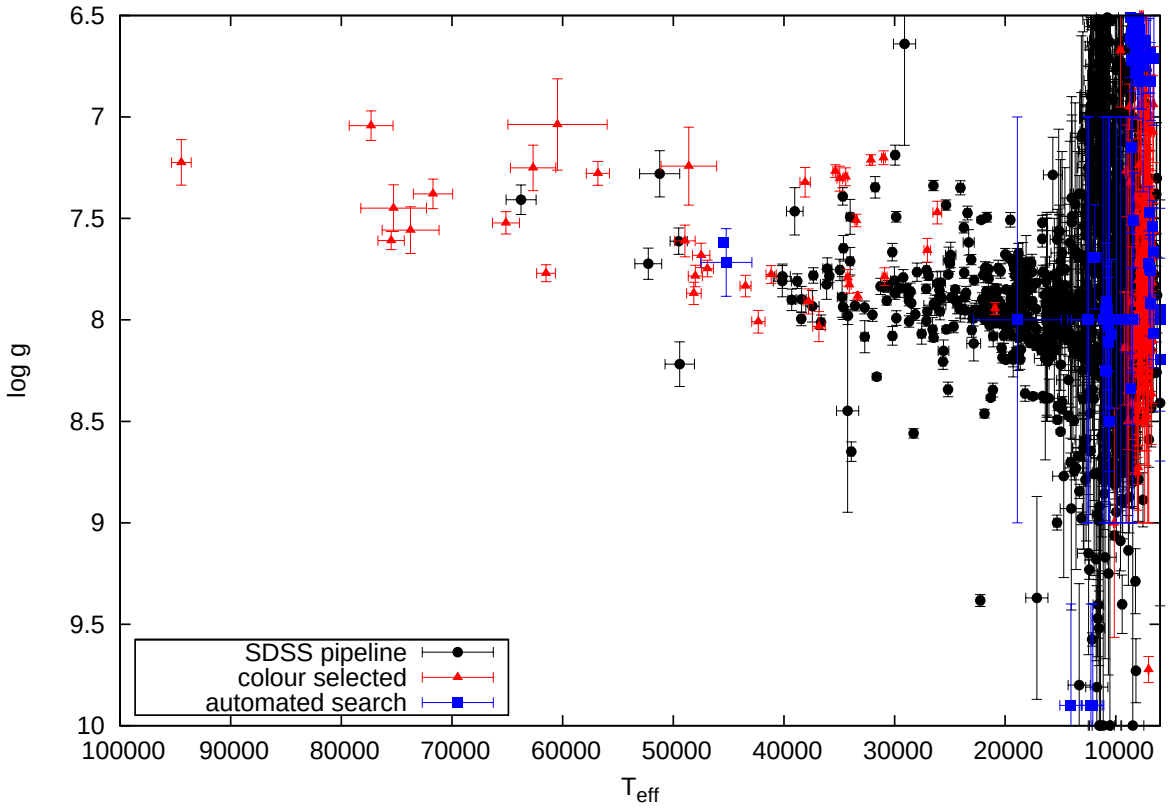

Figure 13 – $T_{\rm eff}$–log g diagram for the DA white dwarfs in the catalogue. Black circles were identified by the SDSS pipeline, red triangles by the colour selection, and blue squares recovered by the automated search. One can note that most cool and hot objects are not recovered by the SDSS pipeline, being identified only by the colour selection. Some of the cool objects, especially of low-log g, are only recovered by the automated search.

The SDSS spectra we classified as white dwarfs or subdwarfs have a g-band signal–to–noise ratio $3 \leq S/N(g) \leq 85$, with an average of 12. The lowest S/N in the g-band occurs for stars cooler than 7 000 K, but they have significant S/N in the red part of the spectrum. A $T_{\rm eff}$–log g diagram for all fitted white dwarfs and subdwarfs with simple classification (i.e. no mixed composition as DAB, no magnetic fields, no visible companion) is shown in Fig. 14. The values were corrected from unidimensional mixing-length theory to 3D convection using the calculations from Tremblay et al. (2013). The separation between sdAs and DAs that can be noted in the plot at $T_{\rm eff} \lesssim 15\,000$ K is imposed: objects with log g lower than 6.5 were classified as sdA, leaving their true nature to be further investigated later. They can either be ELM white dwarfs, or binaries of a subdwarf with a main sequence star, or A stars with an overestimated log g, as shall be discussed in Section 4.2. The zero-age horizontal branch (ZAHB) calculated for models with solar composition by A. D. Romero with the LPCODE (Althaus et al., 2003) is also shown in Fig. 14. Hot subdwarfs are burning helium in their cores, so they should lie above the ZAHB. However, for hot subdwarfs, He abundances affect the NLTE atmosphere structure and,

to some extent, CNO and Fe abundances are also important in deriving accurate temperatures and gravities (Nemeth et al., 2014b; Rauch et al., 2014). As we took none of these effects into account, our determinations of $T_{\rm eff}$ and log g serve only as a rough estimate. Thus the cloud containing both sdAs and sdBs around log $g \sim 6.0$ and $T_{\rm eff} \sim 20\,000$ K was also imposed: objects below $T_{\rm eff} = 20\,000$ K and with log $g < 6.5$ were denominated sdAs, while objects with $T_{\rm eff} > 20\,000$ K and log g in such range were classified as sdBs. This cloud may be dominated by NLTE and metallicity effects. Models calculated for subdwarfs should be used to better separate these objects. There are very few NLTE determinations in the literature, given the increased complexity of the models. In Fig. 15, we show the comparison of our determination with NLTE values listed in Geier et al. (2017). The effective temperature shows only a 4.1% average difference. The log g, however, shows an average difference of 0.24 dex, evidencing the importance of NLTE effects in its determination.

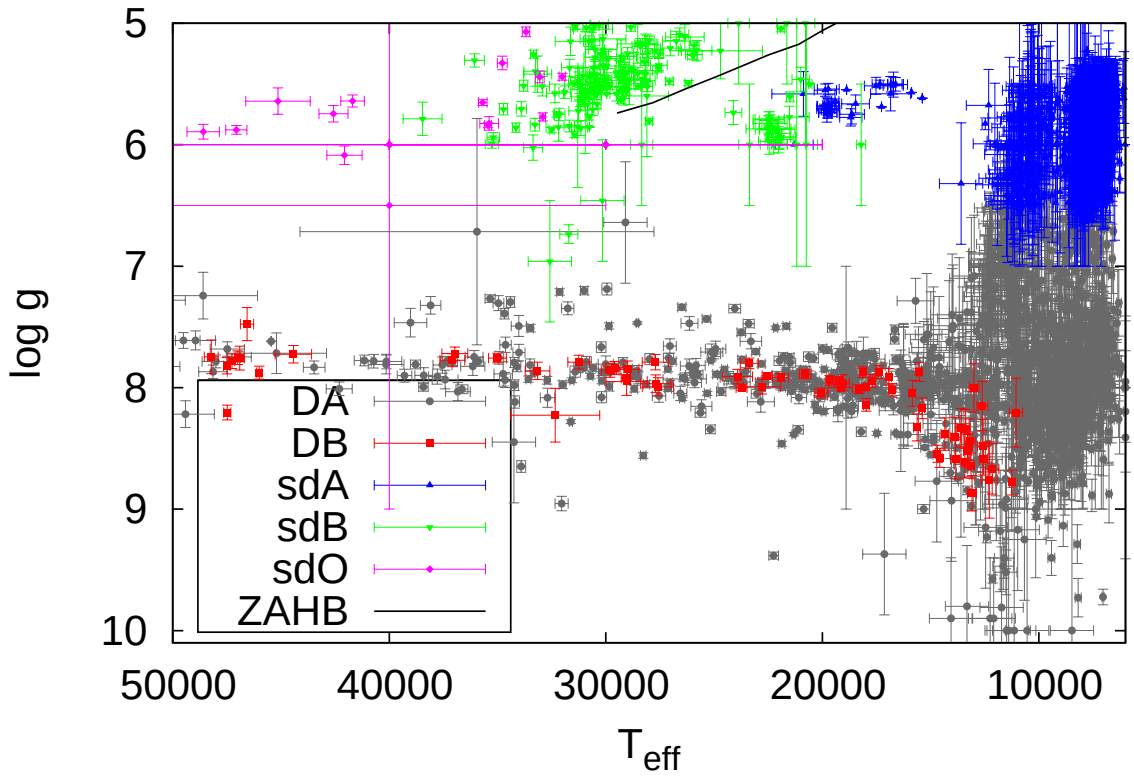

Figure 14 – $T_{\rm eff}$–log g diagram for all fitted white dwarfs and subdwarfs with simple classification. DAs (grey circles) and DBs (red squares) occupy similar regions, but show different spectrum. DAs were separated from the sdAs (blue triangles) at log g=6.5. Objects below this limit were named sdA, but require further investigation (see Section 4.2). O and B subdwarfs (magenta diamonds and green inverted triangles, respectively) should lay above the ZAHB, shown in black. As our models are not designed to properly fit subdwarfs, taking into account NLTE effects and metal content, this does not happen.

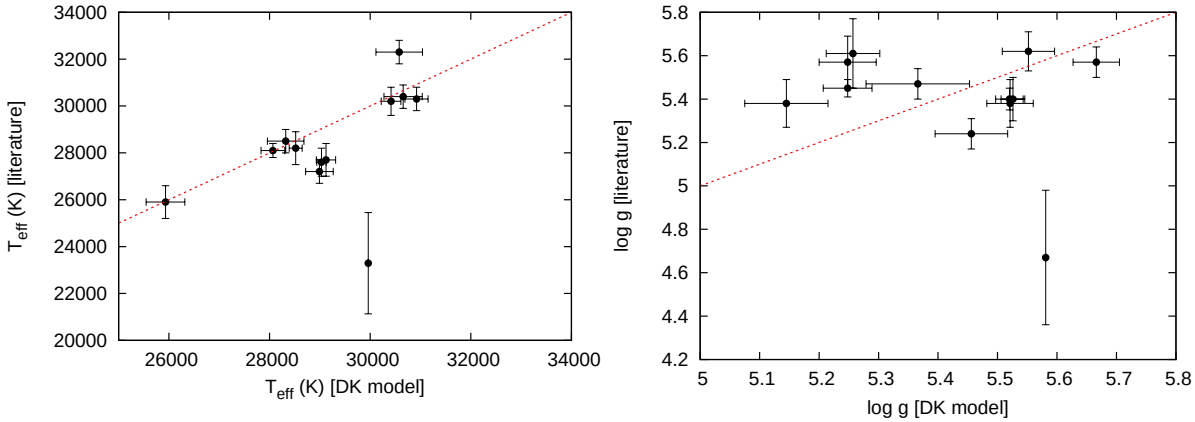

Figure 15 – Comparison between our LTE determination of $T_{\rm eff}$ (left panel) and log g (right panel) to NLTE values given by Geier et al. (2017). The dashed red lines show were determinations would be equal. The average difference in $T_{\rm eff}$ is about 4%, while the log g shows a large average difference of 0.24 dex.

4.1.2 Mass Distributions for DAs and DBs

We estimated the masses of our identified DA stars from the $T_{\rm eff}$ and log g values, which were obtained from our fits and then corrected to 3D convection, using the mass–radius relations of Renedo et al. (2010) and Romero, Campos & Kepler (2015) for carbon–oxygen DA white dwarfs whose progenitors had solar metallicities. These mass–radius relations are based on full evolutionary calculations appropriate for the study of hydrogen-rich DA white dwarfs which take into account the whole evolution of progenitor stars. The sequences were computed from the zero-age main sequence, through the hydrogen and helium central burning stages, thermal pulsations and mass-loss in the asymptotic giant branch phase and finally the planetary nebula domain. The white dwarf masses for the resulting sequences range from 0.525 to 1.024 $M_{\odot}$, covering the stellar mass range for C–O core DAs. For high-gravity white dwarf stars, we used the mass–radius relations for O–Ne core white dwarfs given in Althaus et al. (2015) in the mass range from 1.06 to 1.30 $M_{\odot}$. For the low-gravity white dwarf and cool subdwarf stars, we used the evolutionary calculations of Althaus, Miller Bertolami & Córsico (2013) for helium-core white dwarfs with stellar mass between 0.155 and 0.435 $M_{\odot}$, supplemented by sequences of 0.452 and 0.521 $M_{\odot}$ calculated in Althaus et al. (2009b). A normalised histogram with the masses for all fitted pure DAs is shown in Fig. 16, discriminating between the whole sample and objects selected by colour. While most massive objects were already identified as white dwarfs by the SDSS pipeline, being therefore removed from the initially selected colour sample, many white dwarfs with lower masses were recovered only by their colours.

The DB masses were calculated relying on the evolutionary calculations of hydrogen-deficient white dwarf stars with stellar masses between 0.515 and 0.870 $M_{\odot}$ computed by Althaus et al. (2009a). These sequences have been derived from the born-again episode

responsible for the hydrogen-deficient white dwarfs. For high- and low-gravity DBs, we used the same O–Ne and helium evolutionary sequences mentioned before. The normalised mass histogram is shown in Fig. 17 for the whole sample and only the objects selected by their colours. As almost all DBs were only identified by the colour selection, the distributions are very similar.

These histograms are illustrative of the resulting obtained sample; however, to obtain a reliable mass distribution, one should limit the sample to high-S/N, where a reliable fit can be obtained. The histogram considering only DAs with $S/N \geq 15$ is shown in Fig. 18. The mean S/N for the total DR12 sample (519 objects) is 26.4. The solely colour selected sample (39 objects) has a mean S/N of 28.5. The mean mass for the total high-S/N sample is $0.607 \pm 0.006\ M_{\odot}$. The colour-selected objects have, in average, mass smaller than that, since the selection includes lower log g objects mistakenly identified as main sequence stars by the SDSS pipeline. The obtained mean mass value is significantly smaller than the ones we obtained in Kleinman et al. (2013) and Kepler et al. (2015) considering the whole samples.

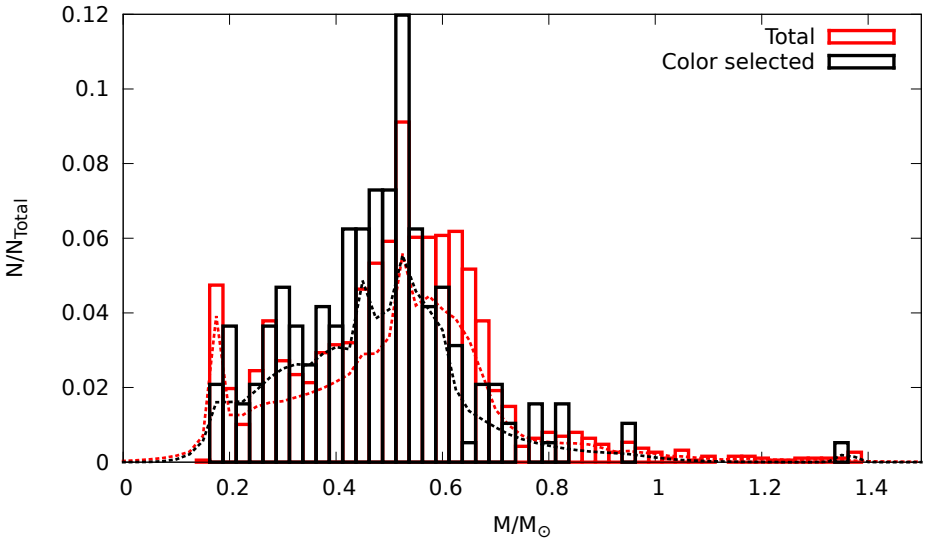

Figure 16 – Normalised mass histogram for all fitted DA white dwarfs (red) and the ones from the colour-selected sample (black). The dotted lines are the distributions obtained assuming the mass for each DA white dwarf follows a Gaussian distribution, with the mean value given by the estimated mass and the standard deviation given by the uncertainty — this dissolves the peaks, because the uncertainty implies the objects can be in other bins. Massive objects are easily identified as white dwarfs by the SDSS pipeline, because their broad lines cannot be fitted with main sequence models. Less-massive objects, on the other hand, can be mistaken with O/B/A main sequence stars, therefore are better recovered by our colour selection.

In Kleinman et al. (2013), we also did an estimate disregarding objects with $T_{\rm eff}$ smaller than 13 000 K, because there was an apparent increase in log g for objects below

such temperature when the 3D correction was not taken into account. In this case we obtained a smaller $\langle M_{\rm DA} \rangle = 0.593 \pm 0.002\ M_{\odot}$, which is closer to the value obtained for DR12. This apparent increase in log g below $T_{\rm eff} = 13\,000$ K was believed to be an artefact of the models, which make use of a 1D mixing-length approximation to model the convection that happens at these lower temperatures. However, in Kepler et al. (2015), the 3D corrections calculated by Tremblay et al. (2013) were already implemented, and we obtained a *higher* mean mass of $0.662 \pm 0.003\ M_{\odot}$ when excluding objects cooler than 10 000 K from the sample. For the DR12 sample alone, we obtain $\langle M_{\rm DA}^{T_{\rm eff}>10\,000{\rm K}} \rangle = 0.615 \pm 0.005\ M_{\odot}$, which is also higher than the value considering the whole sample (see Table 7). This apparent increase in mean mass when lower $T_{\rm eff}$ objects are disregarded may indicate that the 3D corrections are not well determined, implementing overcorrections at least in some cases. Lower $T_{\rm eff}$ white dwarfs may actually have smaller masses, if they have larger ages, what is expected if they come from single-evolving progenitors of low masses ($\lesssim 2.0\ M_{\odot}$).

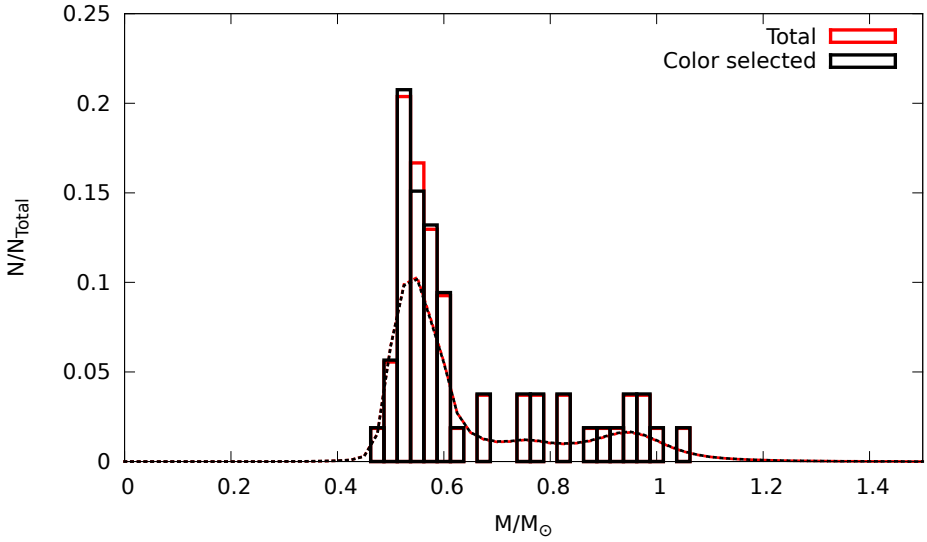

Figure 17 – Normalised mass histogram for all fitted DB white dwarfs (red) and those recovered in the colour selection (black). The distributions shown as dotted lines were obtained in the same way as for the DAs, spreading each point as a Gaussian taking into account the uncertainties. As mentioned earlier, 97% of the DBs were not identified by the SDSS pipeline, being only recovered by our colour sample; therefore, the complete sample and the colour selected are the same but for a few objects.

The mean value considering objects with $S/N \geq 15$ in the aggregate sample — DR7, DR10, and DR12 — is $0.608 \pm 0.002\ M_{\odot}$, with the 3D corrections implemented. This sample contains 5884 pure DAs. No difference in mean mass is found between objects lower and hotter than the convection limit. Determinations of the mean mass have also been made by other authors with models independent of the line profiles, therefore

not affected by the convection. Falcon et al. (2010) determined the mean ensemble mass of a sample of 449 DAs observed in the ESO SN Ia progenitor survey (SPY) project using their mean gravitational redshift and found $0.647 \pm 0.014\ M_{\odot}$. They also did not find any significant difference between the mean masses for objects cooler or hotter than 12 000 K. Romero et al. (2012) determined the masses of 44 DAV, or ZZ Ceti stars, using asteroseismology and obtained a mean mass of $0.630 \pm 0.028\ M_{\odot}$. ZZ Ceti stars have temperatures precisely on the region where convection happens. These two values agree with each other, and are significantly higher than the values obtained with spectral fits in DR7 and DR12. The higher values obtained in the DR10 are higher and just marginally agree with the values of Falcon et al. (2010) and Romero et al. (2012). These discrepancies are an indication that the atmosphere and spectral models are still incomplete. One possible reason besides the convection theory is the poorly modelled broadening by collisions between neutral hydrogen atoms, which can be disregarded at higher temperatures, when the hydrogen is mostly ionised, but becomes important for $T_{\rm eff} \lesssim 10\,000$ K.

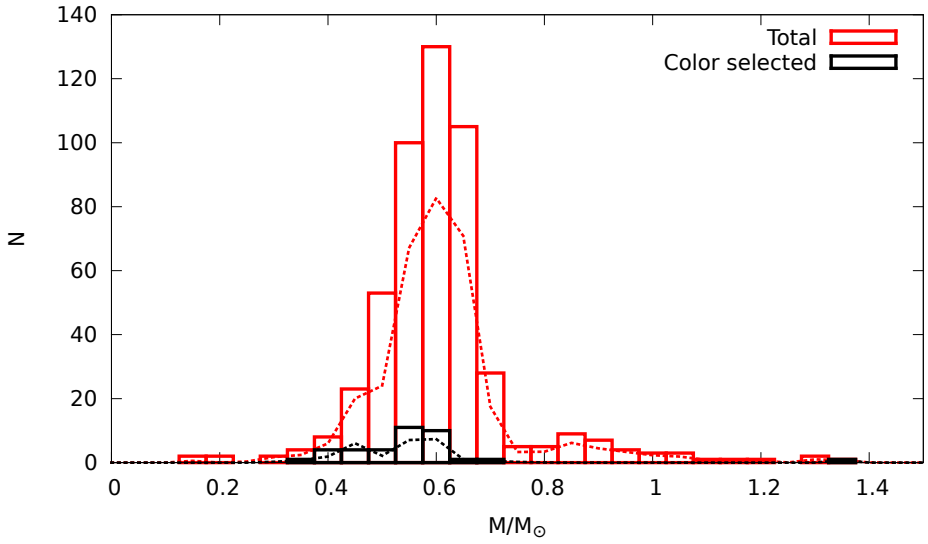

Figure 18 – Mass histogram for pure DAs with $S/N \geq 15$ in DR12, with the distribution obtained from the summed up Gaussians shown as dotted lines. The distribution peaks around 0.6 $M_{\odot}$, which is also the mean mass. The colour selected objects represent only a small portion of the total sample, mainly at masses smaller than the mean mass.

We also calculated the mass distribution corrected to the observed volume. The histogram can be seen in Fig. 19. We can note an increase at the density of higher mass white dwarfs when compared to the uncorrected histogram. This reflects the fact that more massive white dwarfs have smaller radius, so they are fainter and observable only when close (at most 500 pc for the SDSS), implying that our sample is limited to a smaller volume. Less-massive white dwarfs, on the other hand, are brighter and can be observed further away (up to a few kpc even with the SDSS), so their density is smaller when

compared with the uncorrected histogram. Besides the main peak at 0.6 $M_{\odot}$, two smaller peaks can be identified, at $\sim$ 0.9 $M_{\odot}$ and around 1.2 $M_{\odot}$. The existence of multiple peaks reflects a difference in formation channel or in internal structure. The peak at $\sim$ 0.9 $M_{\odot}$ can be explained by white dwarfs formed by merger events in multiple systems (Kilic et al., 2018), although a change in the slope of the initial-to-final mass relation between progenitor and white dwarf (e.g. Romero; Campos; Kepler, 2015) is also present at these masses, suggesting single evolution itself can also contribute to the bimodality. The peak at 1.2 $M_{\odot}$ reflects the existence of O–Ne core white dwarfs, which follow a different distribution than the more common C–O core white dwarfs.

Table 7 – Mean mass obtained for pure DAs in the latest SDSS white dwarf catalogues and with two methods independent of the model atmospheres. There is still disagreement between the spectroscopic method and the others, even after the 3D corrections to convection, suggesting the models ares still incomplete.

Catalogue	$\langle M_{\rm DA}\rangle(M_{\odot})$	$\langle M_{\rm DA}^{T_{\rm eff}>10\,000{\rm K}}\rangle(M_{\odot})$
DR7[a]	0.623±0.002	0.593±0.002
DR10[b]	0.656±0.004	0.662±0.003
DR12[c]	0.607±0.006	0.615±0.005
DR7–12[c]	0.608±0.002	–
Gravitational Redshift[d]	0.647±0.014	–
Asteroseismology[e]	0.630±0.028	–

[a]Kleinman et al. (2013), before the implementation of 3D corrections. [b]Kepler et al. (2015). [c]Kepler et al. (2016). [d]Falcon et al. (2010). [e]Romero et al. (2012).

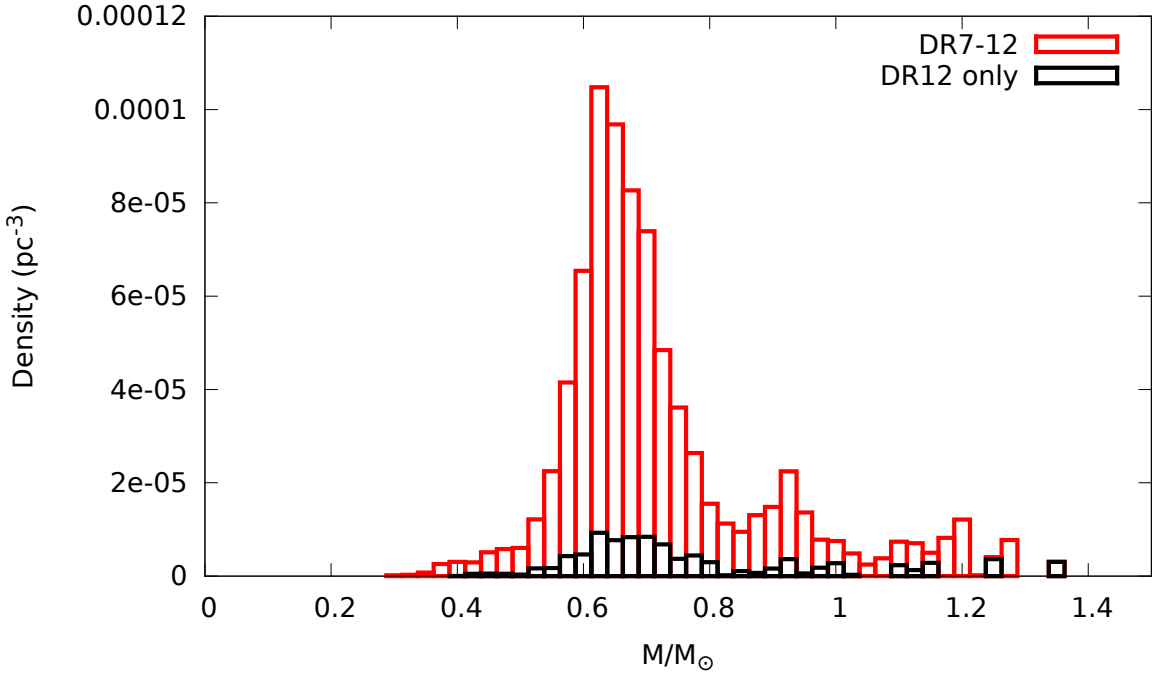

Figure 19 – Mass distribution corrected to the observed volume for DA white dwarfs with $S/N \geq 15$. The correction takes into account the shape of the galactic disk, and minimum and maximum magnitudes of detection of 14.5 and 19.0, respectively. The main peak is at 0.6 $M_{\odot}$, with two smaller peaks around 0.9 and 1.2 $M_{\odot}$, which reflect the outcomes of distinct formation mechanisms, as single star formation, accretion, and mergers. As our DR12 catalogue does not include stars from previous catalogues, the density is comparatively smaller, despite the similar area coverage.

The applied volume correction follows Schmidt (1968), Schmidt (1975), Green (1980), Stobie, Ishida & Peacock (1989), Kepler et al. (2007), Limoges & Bergeron (2010) and Rebassa-Mansergas et al. (2015). It takes into account the shape of the galactic disk, so that the volume $V_{\rm WD}$ in which each white dwarf would have been detected given the magnitude limits of the SDSS survey is given by:

$$V_{\rm WD} = V_{\rm max} - V_{\rm min} = \frac{\omega}{4\pi} \int_{d_{\rm min}}^{d_{\rm max}} {\rm e}^{-z/z_0}\, 4\pi r^2 {\rm d}r \tag{4.2}$$

$$= -\frac{\omega z_0}{|\sin(b)|} \left[\left(r^2 + \frac{2z_0 r}{|\sin(b)|} + \frac{2z_0^2}{|\sin(b)|^2} \right) {\rm e}^{-\frac{r|\sin(b)|}{z_0}} \right]_{d_{\rm min}}^{d_{\rm max}}, \tag{4.3}$$

where ω is the fraction of white dwarfs in the SDSS footprint for which a spectrum was obtained [which is around 40%, according to Gentile Fusillo, Gänsicke & Greiss (2015) and Girven et al. (2011)], $d_{\rm min}$ is the distance where the star would saturate and therefore not be observed (around g=14.5 for the SDSS), $d_{\rm max}$ is the maximum distance where a good S/N could be obtained for the star (we estimated a limit of $g = 19$ for $S/N \geq 15$), z_0 is the scaleheight of the old thin disk, assumed as 250 pc, and b is the galactic latitude of the white dwarf.

Green (1980) proposed that completeness can be estimated from the value of $\langle V/V_{\rm max}\rangle$. $V_{\rm max}$ corresponds to the maximum volume over which the source could be observed, while V is the actual volume given its estimated distance, hence $V/V_{\rm max}$ measures the position of the source within the observable volume. For a complete sample, this should be a uniform distribution from 0 to 1, therefore $\langle V/V_{\rm max}\rangle$ should be equal to 0.5 for a complete sample. This value is equal to 0.47 for the DA white dwarfs with $S/N \geq 15$ in DR12, indicating the sample is close to being complete in the covered area. For the sample comprising DR7–12, the value is 0.48.

The number of DBs with $S/N \geq 15$ is substantially lower than the number of DAs. The complete DR12 sample has 55 objects, with mean S/N of 22.5, while the colour selected sample has 48 objects and mean S/N equal to 22.9. The mass histogram for the objects is shown in Fig. 20. The mean mass for this limited simple is $0.66\pm0.03\ M_{\odot}$, which agrees within errors with the value of $0.696\pm0.010\ M_{\odot}$ we obtained in Kepler et al. (2015) for DR10 alone. It is also in agreement with the value of $0.74^{+0.08}_{-0.09}\ M_{\odot}$ from gravitational redshift by Falcon et al. (2012) and with the value we obtained in Kleinman et al. (2013) of $0.685\pm0.013\ M_{\odot}$. However, our temperatures and surface gravities were estimated with pure DB models, disregarding hydrogen contamination. Koester & Kepler (2015), on the other hand, took this contamination into account and re-analysed 1107 helium-rich objects from the SDSS, so their sample is more significant and their values are more accurate. They obtained a mean value of $0.606 \pm 0.004\ M_{\odot}$, smaller than previous determinations, but very similar to the determination for DAs.

We also calculated the volume corrected distribution for pure DBs with $S/N \geq 15$, shown in Fig. 21, compared to the distribution of the complete sample of DBs in the DR7–12 published by Koester & Kepler (2015). Our sample is small, but the value of $\langle V/V_{\rm max}\rangle$ is 0.53, indicating it should be complete in the sampled region. The value for DR7–12 is 0.48, also suggesting that the sample is close to completion. It is worth mentioning that no DBs below 0.4 $M_{\odot}$ or above 1.0 $M_{\odot}$ were found.

Finally, in Fig. 22, we compare the volume corrected distributions for DAs and DBs in the DR7–12 with $S/N \geq 15$. It is clear that the DBs have a narrower distribution, as mentioned before. They are also less numerous, with pure DBs representing less than 10% of the whole white dwarf sample, while pure DAs represent about 80%. Moreover, we can note that the DA distribution has a positive skewness (i.e., a tail extended to larger masses), while the DB distribution has negative skewness (its tail extends to lower masses). This may reflect an intrinsic difference between the masses of the progenitors that may originate DAs or DBs. Currently, the models do not predict that the probability of a very-late thermal pulse may depend on the mass of the star, as it only depends on the thickness of the external hydrogen layer, which usually comprises less than 0.01% of the mass. Hence this significant difference in the shape of the distributions, not predicted

by the evolutionary models, suggests that there is still missing physics in the models describing the formation of white dwarfs. This difference might be partially explained by the fact that the DA distribution shows a larger contribution of objects resulting from multiple evolution, which explain both the DAs at $M \lesssim 0.4\ M_{\odot}$ and at $M \gtrsim 0.8\ M_{\odot}$.

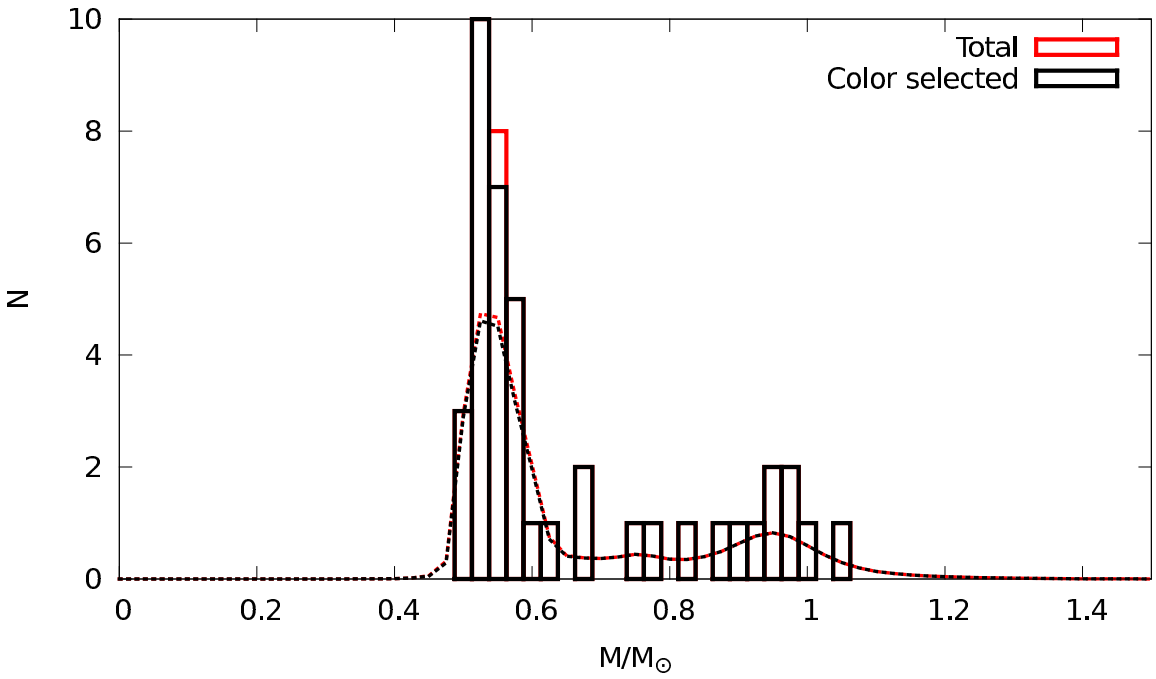

Figure 20 – Mass histogram for pure DBs with $S/N \geq 15$ in DR12, with the distribution obtained from the summed up Gaussians shown as dotted lines. The distribution peak is around 0.6 $M_{\odot}$, as for the DAs, but the distribution is much less broader than that of the DAs, a result that is known in the literature (e.g. Bergeron et al., 2011). Almost all objects were colour selected.

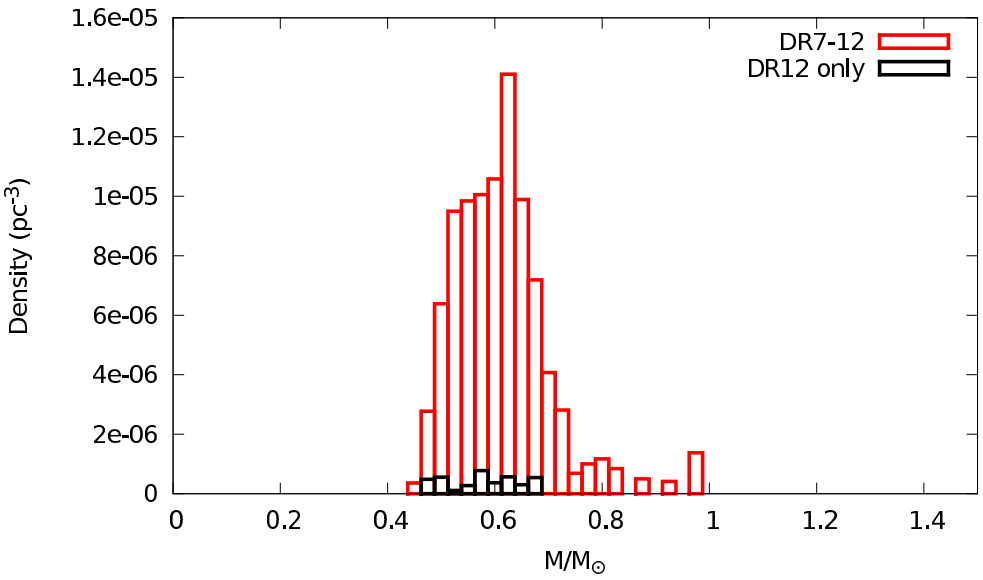

Figure 21 – Mass distribution corrected to the observed volume for DB white dwarfs with $S/N \geq 15$. Again the shape of the galactic disk, with a scaleheight of 250 pc, and minimum and maximum magnitudes of detection of 14.5 and 19.0 are assumed. No DBs below 0.4 $M_{\odot}$ or above 1.0 $M_{\odot}$ are found. This may imply that there are yet unknown the constraints on the very-late thermal pulse phase precluding the formation of DBs with lower or higher masses.

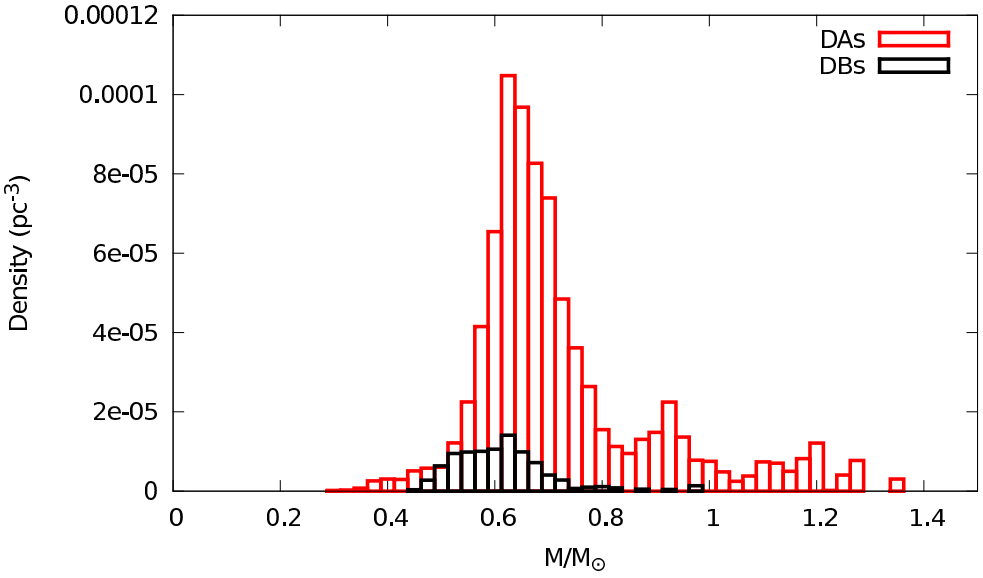

Figure 22 – Comparison between the volume corrected distributions for DAs and DBs in the DR7–12 with $S/N \geq 15$. DBs are less numerous, but the main difference is in the skewness of the distributions: the tail of the DB distribution extends to lower masses, while the DA distribution favours higher masses. Such difference cannot be explained by current evolutionary models.

4.1.3 Magnetic Fields

The visual inspection of each spectrum allows the identification of otherwise unnoticed features which can affect the fit of a model. One such feature are Zeeman splittings, an indication of a magnetic field. The magnetic field lifts the degeneracy on the quantum number m_j, related to the magnetic moment $\vec{m}$, splitting the line into components (see Figs. 23 and 24) with different energies (and, consequently, wavelengths).

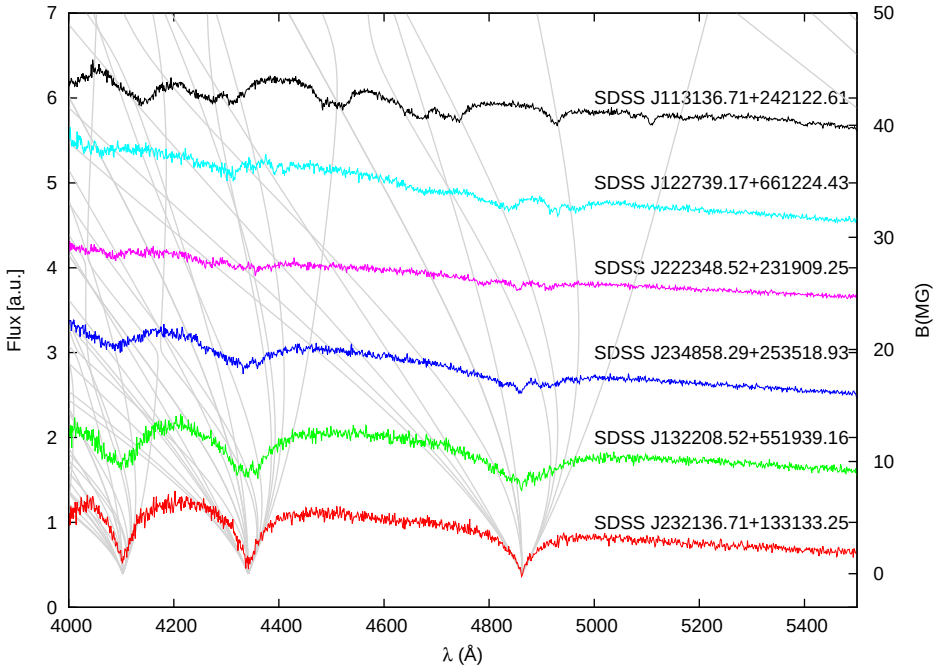

Figure 23 – Six identified DAHs, with increasing fields from about 3 MG (bottom spectrum) to about 50 MG (upper spectrum). The spectra are normalised at 4600 Å and shifted vertically for clarity. The grey lines indicate the positions of each theoretical Zeeman split Balmer line subcomponent, assuming a dipole magnetic field of strength indicated in the right axis. These theoretical models are from Schimeczek et al. (2013), Schimeczek & Wunner (2014a), and Schimeczek & Wunner (2014b)

.

In DR12 we have found 34 stars with Zeeman splittings indicating magnetic fields above 2 MG — below this limit, the line splitting becomes too small to be identified at the SDSS spectral resolution. The percentage is similar to our findings reported for DR7 in Kepler et al. (2013) and Kepler et al. (2015). If the line splitting and magnetic fields were not identified, the spectral fittings of DA and DB models would have rendered too high log g determinations due to magnetic broadening being misinterpreted as pressure broadening. For DZ, splitting may affect the estimate of abundances, if not all the components of the line are taken into account.

We estimated the mean fields for the new DAHs as being from 3 to 80 MG. Fig. 23 shows some examples, with increasing fields from about 3 MG (bottom spectrum) to

about 50 MG (upper spectrum). We estimated the fields following Külebi et al. (2009). They have calculated a grid of theoretical optical spectra of DAHs with magnetic field strengths between 1 and 1200 MG for different angles between the magnetic field vector and the line of sight, and for effective temperatures between 7 000 and 50 000 K. A least-squares minimisation scheme is used in order to find the magnetic field geometry best fitting the observed data. We assumed a dipole as the geometry, being either centred or shifted along the dipole axis.

It is important to caution that stars with large fields are hard to identify, because fields above around 30 MG, depending on effective temperature and signal-to-noise, intermix subcomponents of different lines so much that it becomes difficult to identify the star as containing hydrogen or helium at all. That also affects the colours significantly, so that none of our three methods of search might be able to identify the spectrum as of a white dwarf candidate, hence highly-magnetic white dwarfs are possibly under-represented in our sample.

We also identified seven cool DZH, similar to those identified by Hollands, Gänsicke & Koester (2015). An example is shown in Fig. 24, where one can easily note that the lines are splitted into components, especially the magnesium line at 5175 Å and the blended Na lines at 5889 and 5895 Å. The estimated fields for the seven DZHs identified by us are shown in Table 8. The field estimate follows the approach of Hollands, Gänsicke & Koester (2015), which is to fit each component of the Mg and Na triplets with a Gaussian, after normalising by the continuum, and calculate the average surface magnetic field strength B_S from

$$B_S = \frac{\Delta(1/\lambda)}{46.686}\ \mathrm{MG}, \tag{4.4}$$

where $\Delta(1/\lambda)$ is the inverse wavelength separation in cm^{-1} between the components of the triplet (Reid; Liebert; Schmidt, 2001).

Table 8 – Magnetic field for the seven identified DZs, estimated following Eq. 4.4. This is the mean field obtained from the different lines, with the respective σ.

SDSS J	T_{eff} (K)	B (MG)	σ_B (MG)
003708.42−052532.80	5700(18)	7.2	0.2
010728.47+265019.94	5509(21)	3.4	0.1
110644.27+673708.64	6075(44)	3.3	0.1
111330.27+275131.41	5706(37)	3.0	0.1
114333.46+661532.01	5260(1000)	9.0	1.5
225448.83+303107.15	5900(13)	2.5	0.1
233056.81+295652.68	6945(36)	3.4	0.3

The origin of such intense magnetic fields is still an open issue. One possible explanation is simply magnetic flux conservation. The magnetic field in the white dwarf

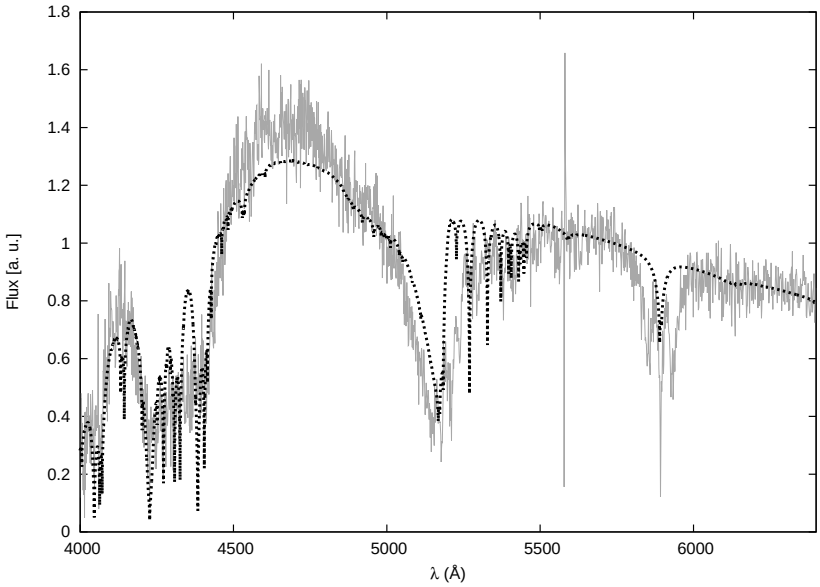

Figure 24 – The grey continuous line shows the spectrum of a DZH with an estimated field of 2.5±0.1 MG. The dashed black line shows a non-magnetic model with similar effective temperature and abundance. One can note that the observed spectrum has the lines splitted in components when compared to the model spectrum.

will be amplified in order to conserve the flux due to the field of its progenitor, which is explained by the dynamo effect — i.e., generation of a magnetic field because of the movement of ionised particles. For low-mass main sequence stars ($M \lesssim 2.0\ M_{\odot}$), mainly the external layers will show convection and hence will be magnetic. This implies that most of the magnetic flux will be lost when the external layers are ejected before the white dwarf phase. However, for massive progenitors, when the hydrogen fusion occurs primarily by the CNO-cycle, the high temperature gradient will make the core convective, and it thus concentrates most of the magnetic flux. In this case, the magnetic flux is not lost with the external layers, but conserved in the core, causing the magnetic field to be amplified when the white dwarf forms. This would imply that magnetic white dwarfs show higher masses (because they come from massive progenitors) and lower temperatures (massive progenitors evolve faster, hence the white dwarf has had longer to cool down). We reported detection of such trends in Kepler et al. (2013) analysing DR7 data, and this trend seems to be maintained in DR12, although the low number of magnetic objects does not allow an independent analysis.

4.1.4 Abundances for DZs

About 8% of the new white dwarfs in our DR12 sample show metal lines, similar to what we found in Kleinman et al. (2013) and Kepler et al. (2015). This contamination is probably due to accretion of rocky material around the stars (e.g. Graham et al., 1990;

Jura, 2003; Koester; Gänsicke; Farihi, 2014). The measured abundance patterns in these metal polluted stars are overall similar to those of the terrestrial planets in the solar system, i.e. dominated by the major rock-forming elements (Si, Fe, Mg, and O) and depleted on volatile elements (Jura et al., 2012; Gänsicke et al., 2012).

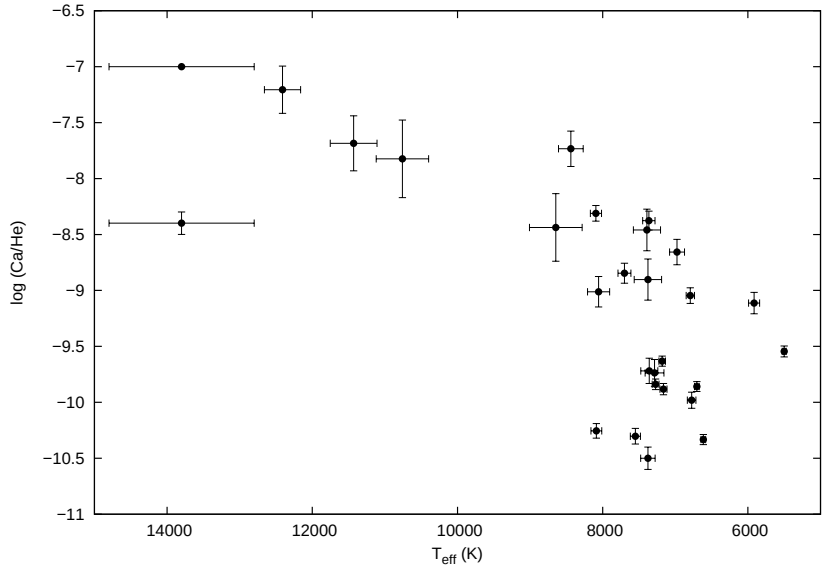

Figure 25 – Abundances of Ca/He for DZs identified here, when a good fit could be obtained. The log (Ca/He) abundance varies between -7.0 and -10.5 and appears to decrease as effective temperature decreases. This could be a reflex of the increase of the convective layer as the star cools down, what might dilute the accreted material.

We identified 62 DAZ, 1 DBZ, and 236 DZ. We fitted the spectra of each of the 236 DZs to a grid of models with Mg, Ca, and Fe ratios equal to the averages from the cool DZs in Koester et al. (2011), and added Si with the same abundance as Mg (Koester; Gänsicke; Farihi, 2014). These models have a fixed surface gravity of log $g = 8.0$, as it is not possible to otherwise obtain it from the spectra, as there are no available complete calculations of line broadening profiles for metals, and we would be introducing an extra parameter that would lead to degenerate solutions. The values for log (Ca/He) range from -7.00 to -10.50. Fig. 25 shows the calcium/helium abundance for the DZs identified in DR12 for which we could obtain a good fit. There seems to be a decrease of Ca/He abundances at lower temperatures. This trend might be explained if all stars had the same accretion rate of metal-rich material, but the material becomes more diluted at cooler temperatures due to the increasing size of the convective layer as the star cools down.

4.1.5 Abundances for DQs

Only about 1% of the newly identified spectra in our sample are dominated by carbon lines. The carbon is believed to be dredged up from the underlying carbon-oxygen core through the expanding He convection zone (e.g. Koester; Weidemann; Zeidler, 1982, Pelletier et al., 1986, Koester; Knist, 2006, Dufour et al., 2007). These stars are in general cooler than $T_{\rm eff}$ = 12 000 K. A few ($\sim$ 50) hot DQs are known above this temperature (Dufour et al., 2008; Kleinman et al., 2013), but none was found in DR12.

We fitted the spectra of the cool DQs to a grid of models reported in Koester & Knist (2006). The models have fixed log $g = 8.0$, because it is not possible to estimate it from the spectra, as there are no available complete calculations of line broadening profiles for carbon. Moreover, adding the extra fitting parameter would introduce a degeneracy between abundance and log g. The values of log (C/He) range from -8 to -4, and of effective temperatures vary between 4 400 and 13 000 K. Fig. 26 shows the carbon/helium abundance for the new cool DQs identified here for which we could obtain a good fit. Similar to what happens with the Ca/He abundance for DZs, there is a decrease of C/He abundances at lower temperatures, again probably caused by the deepening of the convection zone, which could dilute any surface carbon.

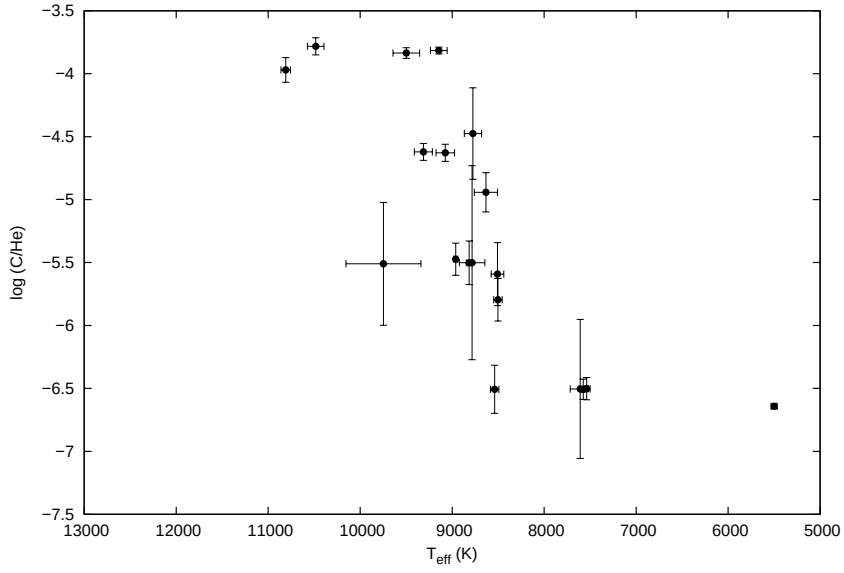

Figure 26 – Abundances of C/He for DQs identified here, in the cases a good fit was obtained. The log (C/He) abundance ranges from -4.0 to -7.0. The formal error bars for the object at $T_{\rm eff} \sim$ 5 500 K are of the order of the symbol size. Similar to the behaviour of Ca/He in the DZs, the abundance of the C/He seems to decrease with decreasing effective temperature. This could be explained by the deepening of the convection zone, diluting any surface carbon.

4.1.6 Subdwarfs

Hot subdwarfs are core helium burning stars. As described in the Introduction, their main channel of formation involves a binary companion stripping away the external hydrogen layer (about 50% of hot subdwarfs are found to be in binaries, see Heber, 2016), in such a way that the star appears hotter and, consequently, bluer. Therefore, subdwarfs are also called extreme-horizontal branch stars (EHB). Following Németh, Kawka & Vennes (2012), Drilling et al. (2013), Nemeth et al. (2014a) and Nemeth et al. (2014b), we have classified stars with $\log\ g < 6.5$ and $T_{\rm eff} > 20\,000$ K as hot subdwarfs: sdOs if He II lines were visible, and sdBs otherwise. If helium lines were dominant over hydrogen lines, the classifications are He-sdB and He-sdO. Nemeth et al. (2014b) and Rauch et al. (2014) discuss how the He abundances typical for sdB stars affect the Non-Local Thermodynamical Equilibrium (NLTE) atmosphere structure. To a lower extent, CNO and Fe abundances are also important in deriving accurate temperatures and gravities. As previously mentioned, our determinations of $T_{\rm eff}$ and $\log\ g$ do not include NLTE effects or mixed compositions, hence they serve only as a rough estimate. We classified 28 new sdOs and 41 new sdBs in the DR12 sample.

In Fig. 27 we show the comparison between a subdwarf and white dwarf of type B (sdB and DB, respectively) of similar S/N. They can be quite easily told apart: the sdB is dominated by hydrogen lines, commonly with traces of helium, while the DB shows only helium lines. A similar plot compares an sdO and a DO with similar S/N in Fig. 28. These two objects can also be easily distinguished: the sdO is dominated by hydrogen, with traces of helium I and II, while the DO shows mainly He II lines, significantly broadened by pressure.

In contrast, we have found a significant number of objects which do not fall in any of the mentioned classifications. They show only hydrogen lines, usually with traces of metals, mainly Ca and Mg, but their $\log\ g$ is too low to be classified as DA (see Fig. 29). At the same time, their $\log\ g$ is above the estimated limit for main sequence A stars, even for very low metallicity. Moreover, their temperature is well below 20 000 K so they are not hot subdwarf stars (Heber, 2016). As already mentioned, we have classified these hydrogen dominated spectra with $4.5 \lesssim \log\ g < 6.5$ and $T_{\rm eff} < 20\,000$ K as sdAs. This classification is a postponement of the problem: as we have mentioned before, they are *not* normal known types of subdwarfs, which are either hot sdOs and sdBs, or cool metal-weak sdFs and sdGs. We have chosen this classification merely to stress that they lie below the main sequence in an HR-diagram as the subdwarfs and have spectra similar to main sequence A stars.

Some of these stars have been classified previously as horizontal branch stars, but, to our knowledge, this is the first analysis with model spectra covering the range of

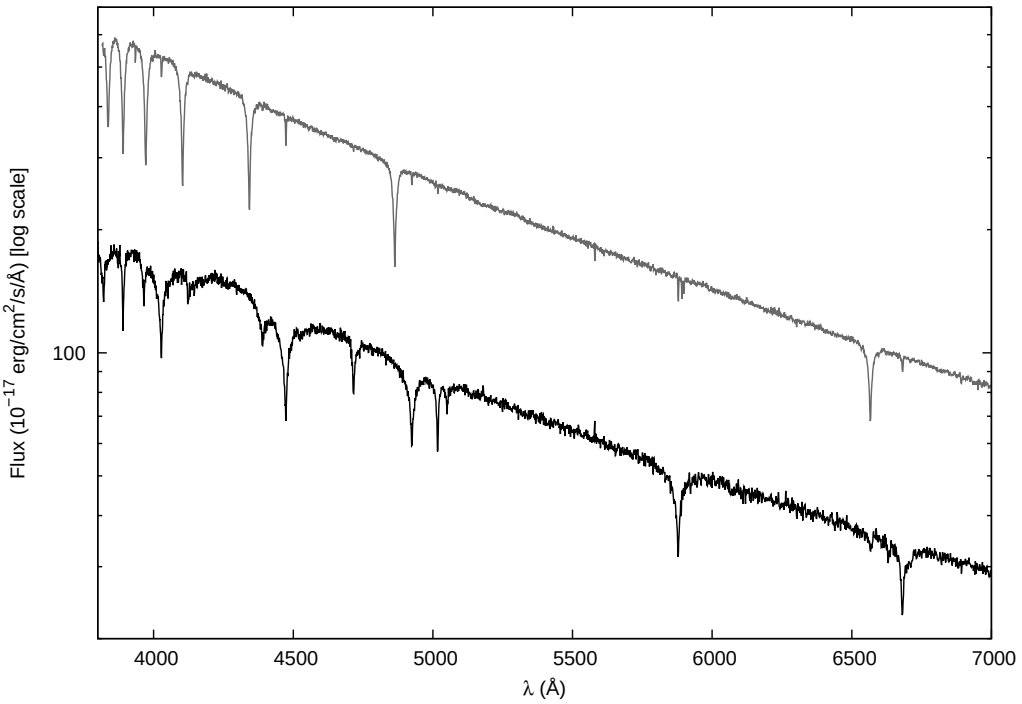

Figure 27 – Spectra of an sdB (grey) and a DB (black). Despite both being of type B, their features are fairly different. Moreover, sdBs have lower log g, below 6.5.

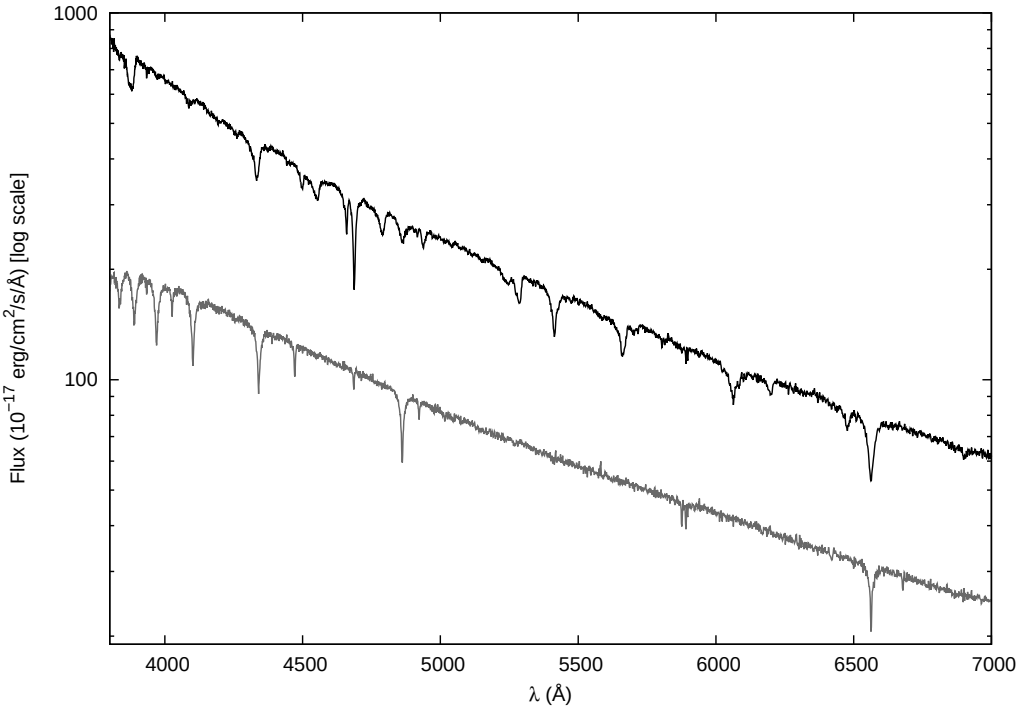

Figure 28 – Spectra of a subdwarf (grey) and a white dwarf (black) of type O. They show very different features, with the sdO being dominated by hydrogen, and the DO, by ionised helium. The width of the lines is also different, reflecting the fact that the subdwarfs have lower log g.

surface gravities $3.75 < \log\ g < 10$. Of these sdAs, 3954 have estimated proper motions larger than 15 mas/yr, and 607 larger than 30 mas/yr, considering only objects with $ppm > 3\ \sigma_{ppm}$. If main sequence stars, the distance modulus suggest they would be several kpc away — otherwise they would saturate in the SDSS. These proper motions suggest distances smaller than ~ 1.5 kpc. As a reference, the proper motion of the globular cluster NGC 6396, which is about 2.3 kpc away, was estimated to be 17.70±0.06 mas/yr by Kalirai et al. (2007). We propose many of these objects are ELMs instead, and will investigate their nature in the next Section.

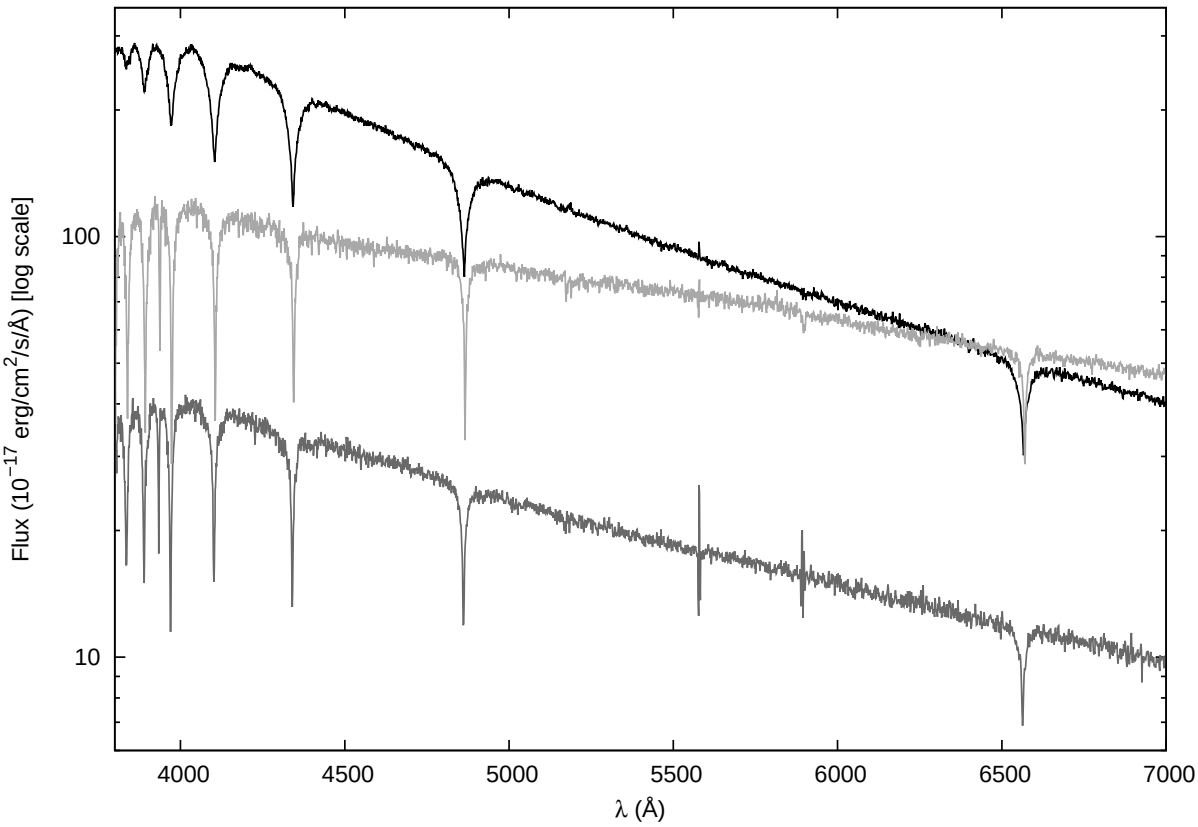

Figure 29 – Spectra of three hydrogen dominated objects, therefore type A, with different estimates of log g. The black spectrum belongs to an object with log $g = 7.468 \pm 0.010$ and $T_{\rm eff} = 28500 \pm 1500$ K, therefore a DA white dwarf. The light grey resulted on log $g = 4.351 \pm 0.064$ and $T_{\rm eff} = 7750 \pm 400$ K and belongs to a main sequence A star. The dark grey spectrum, on the other hand, gives log $g = 5.636 \pm 0.049$ and $T_{\rm eff} = 7900 \pm 400$ K, so the object cannot be classified as either DA, A, or sdB. We have defined the spectral classification of objects of this type as sdA.

4.2 Unveiling the nature of the sdA stars

The population of sdA stars was discovered when we mined the SDSS DR12 for pre-ELMs and ELMs, as described in Section 4.1.6. They were believed to belong to either of these classes because of the log g estimated from their SDSS spectra. ELMs show $\log g$ in the range $5.0 \lesssim \log\ g \leq 7.0$ and $T_{\rm eff} \leq 18\,000 - 20\,000$, filling in the region between the main sequence and the white dwarfs resulting from single evolution in a $T_{\rm eff} - \log g$ diagram. However, they also show other particular properties. While their colours might be similar to main sequence stars, ELM radii are at least ten times smaller, so they are significantly less luminous than main sequence stars, and thus need to be nearer to be detected at same magnitude. As a consequence, they show higher proper motions than main sequence stars with similar properties. Moreover, they are expected to be encountered still with the close binary companion which led to their mass loss. Most will merge within a Hubble time (Brown et al., 2016), implying detectable radial velocity variation.

The properties of the precursors of the ELMs, the pre-ELMs, are more difficult to establish, as they have not reached the white dwarf cooling branch yet. If the time-scale for mass loss from the white dwarf progenitor is longer than the thermal time-scale, a thick layer of hydrogen will be surrounding the degenerate helium core. This can lead to residual p–p chain reaction which can last for several million years (Maxted et al., 2014). Moreover, instead of a smooth transition from pre-ELM to ELM, the star can undergo episodes of unstable CNO burning, or shell flashes. These flashes can shorten the cooling time-scale, by reducing the hydrogen mass on the surface, and can significantly alter the radius and effective temperature of a pre-ELM, making it very difficult to distinguish them from main sequence or even giant branch stars. Pietrzyński et al. (2012a), for example, found a 0.26 $M_{\odot}$ pre-ELM showing RR Lyrae-type pulsations — the flashes caused the object to reach the RR Lyrae instability strip. Its identification was possible because the system is eclipsing, with an orbital period of 15.2 days, which allowed for an estimate of the mass. Greenstein (1973) and Schönberner (1978) discuss an interesting example of a post-common envelope binary mimicking a main sequence B star. Hence pre-ELMs can show log g, $T_{\rm eff}$ and colours in the same range as main sequence or even giant stars, being even as bright as them. Their ages are more consistent with the halo population than single main sequence stars of similar properties though, since they are at a later stage of evolution.

If found in the halo without a close binary companion inducing enhanced mass loss, an sdA could also be explained as a metal-poor star of type A–F. This explanation was suggested by Brown, Kilic & Gianninas (2017). They have, however, based this conclusion on the fact that their fit of pure hydrogen models to metal abundant models seemed to indicate an overestimate in log g of about 1 dex. As we will show, the change in $\log g$ with the addition of metals to the modelled spectra is actually *not* a constant systematic

effect. Moreover, they have overlooked the possibility that the sdAs are pre-ELMs, which do show log g in the same range as main sequence stars, but are older and thus should be found in abundance in the halo, whose age is over 10 Gyr — close to 10 times the expected lifetime in the main sequence of A stars. Main sequence A stars in the halo can only be explained if blue stragglers, where mass transfer from a companion can extend their lifetime in the main sequence by a factor of up to ten (Schneider et al., 2015), or by rare events of star formation induced by matter accreted to the Galaxy (Lance, 1988; Camargo et al., 2015), allowing the existence of early-type stars in the outer halo. Main sequence F stars might still be approaching the turn-off point in the halo: Thévenin et al. (2001), for example, finds $T_{\rm eff}$ up to 6300 K for the turn-off stars in the globular cluster NGC6397, which is about 13 Gyr old (Campos et al., 2016). Hence F and other late-type main sequence stars could explain cooler sdAs ($T_{\rm eff} \lesssim 8000$ K). A key-way to analyse the feasibility of this scenario is analysing the spatial velocities of the sdAs given a main sequence radius, as we will show in Section 4.2.4. This would also be possible if we knew their distances from parallax, for example.

Finally, another possibility that might explain some sdA is that they are binaries of a hot subdwarf with a main sequence companion of type F, G or K, as found by Barlow et al. (2012). In this kind of binary systems, the flux contribution of both components is similar, so the spectra appear to show only one object, with the lines of the main sequence star broadened by the presence of the subdwarf, explaining the higher values of $\log g$ obtained. However, due to the presence of the subdwarf, which shows $T_{\rm eff} \geq 20\,000$ K, a higher flux contribution on the UV is expected when compared to main sequence or ELM stars, allowing for telling these objects apart.

In summary, the sdAs physical properties are consistent with basically four different possibilities: (i) pre-ELMs or ELMs; (ii) blue stragglers; (iii) metal-poor late-type main sequence stars; (iv) hot subdwarf plus main sequence F, G, K binary. Estimated log g and $T_{\rm eff}$ should be similar between all possibilities. Colours are similar for pre-ELMs, ELMs and metal-poor main sequence stars, but hot subdwarfs with a main sequence companion should have higher UV flux. ELMs and pre-ELMs should show a close binary companion leading to high radial velocity variations and orbital periods lower than 36 h, according to the empirical determinations of Brown et al. (2016), or up to several days, according to the theoretical calculations of Sun & Arras (2017). Main sequence binaries showing physical parameters in the sdA range, on the other hand, should have orbital periods above $\sim$ 9 h (Brown; Kilic; Gianninas, 2017). ELMs and pre-ELMs have long evolutionary timescales, so they can be detected with ages above 10 Gyr, while main sequence stars of A-type have main sequence life times lower than $\sim$ 1.5 Gyr (which is the main sequence life time of a 1.5 $M_{\odot}$, $Z = 10^{-4}$, F0 star with the LPCode, described in Althaus et al., 2003), although a companion might delay the evolution by transferring mass as occurs for blue straggler stars.

In the next sections, I will analyse properties of the sdAs in order to assess their possible nature. The physical parameters we obtained are compared to both single evolution and binary evolution models to assess if they can be explained by these scenarios. Based on these findings, I estimate a probability of being a (pre-)ELM and a probability of being a main sequence star for each object in the sample. Selected sdAs were followed-up to probe their binarity with the aim of extending the population of known (pre-)ELMs to all the space of physical parameters predicted by the evolutionary models. I obtained time-resolved spectroscopy to search for radial velocity variations indicating the presence of a close binary companion, and time-series photometry to look for eclipses, ellipsoidal variations, or pulsations typical of ELMs for a small sample of objects.

4.2.1 Spectral fits with solar abundance models

With our solar metallicity grid, we were able to obtain a good fit to 39 756 spectra out of the initial sample of 56 262 spectra. The remaining objects were mostly close to the border of the grid, either in $T_{\rm eff}$ or in $\log\ g$, and are probably giant stars. 723 objects fitted $T_{\rm eff} > 20\,000$ K and were later excluded from the sdA sample — 49 show $\log g > 6.5$ and are canonical mass white dwarfs, while 674 show $\log g < 6.5$ and are most likely hot subdwarfs. All the white dwarfs were known with the exception of two new DA white dwarfs (SDSS J152959.39+482242.4 and SDSS J223354.70+054706.6). 66 out of the 674 possible sdBs were not in the catalogue of Geier et al. (2017) and were marked as probable new subdwarfs.

Next, we removed from the sample contaminations from other SDSS pipeline possible classifications that contained our keywords, such as G0V**a**, F8I**b**v**a**r and Calcium**WD**. Those were only 182 objects, leaving a sample of 38 850 narrow hydrogen line objects with a good solar abundance fit and $T_{\rm eff} < 20\,000$ K. This sample will be referred to as *sample A* throughout the text.

When we rely on spatial velocity estimates to analyse our sample, only objects with a reliable proper motion are taken into account. Unfortunately, our objects are too faint to be featured in the DR1 of Gaia[1], so we used the proper motions of Tian et al. (2017), which combine Gaia DR1, Pan-STARRS1, SDSS and 2MASS astrometry to obtain proper motions. To flag a proper motion as good, we required that the distance to nearest neighbour with $g > 22.0$ was larger than 5", that the proper motion was at least three times larger than its uncertainty, and that the reduced χ-squared from the evaluation of proper motions in right ascension and declination was smaller than 5.0. This left 16 656 objects with a reliable proper motion, with an average uncertainty of 2.0 mas/yr, to be referred to as *sample B* in the text.

[1] This thesis was submitted on April 11 2018, prior to Gaia DR2. After the Gaia DR2 release, on April 25 2018, we verified that the GPS1 proper motions agree with Gaia for over 98% of our sample.

In order to estimate the contamination by outliers, we have compared GPS1 proper motions to both the Hot Stuff for One Year (HSOY, Altmann et al., 2017) catalogue and the catalogues by Munn et al. (2004) and Munn et al. (2014), directly available at the SDSS tables. HSOY combines positions from Gaia DR1 and the PPXML catalogue (Roeser; Demleitner; Schilbach, 2010), while Munn et al. combine SDSS and USNO-B data. Hence they are not completely independent, but nevertheless useful to find possible outliers. We find only 69 objects whose proper motions differ by more than 3-σ when comparing GPS1 and HSOY, and 110 objects when comparing to Munn et al. They represent less than 1% of the sample, so we decided to keep them as part of sample B, since it does not affect the analysis, and GPS1 is regarded as the best proper motion catalogue available for our objects.

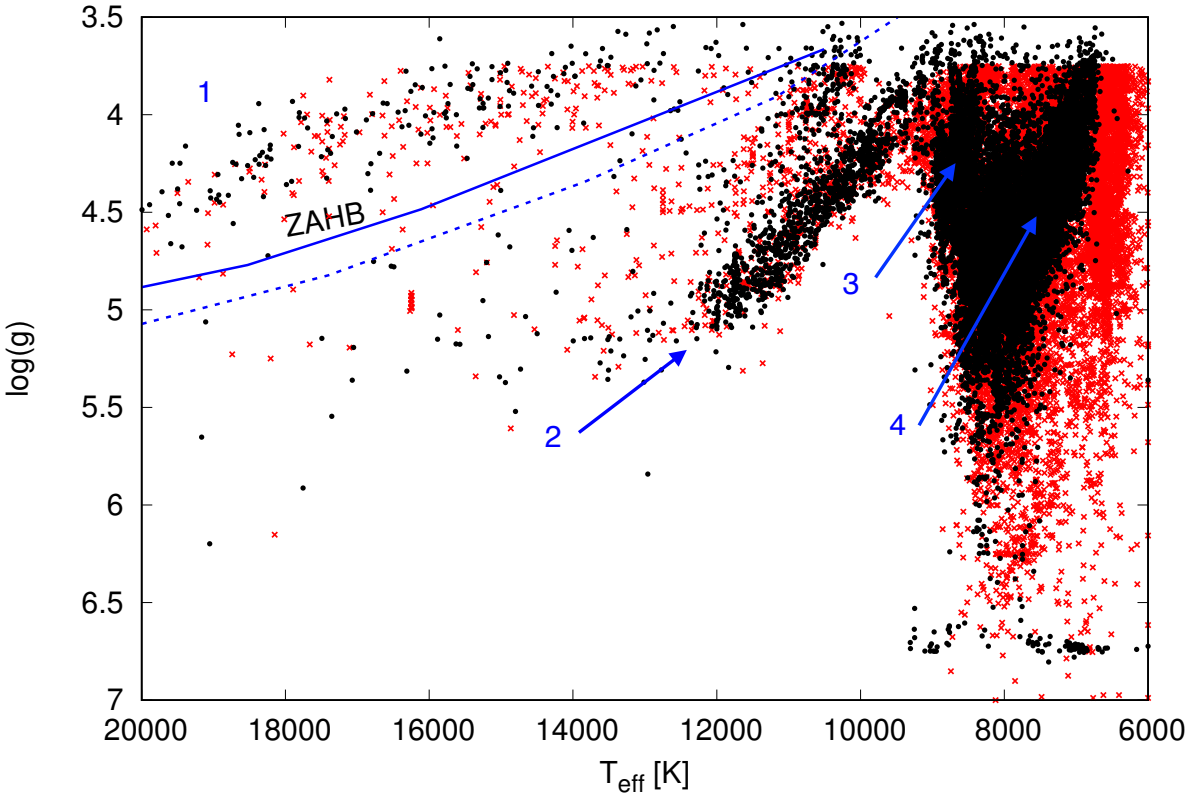

Figure 30 – $T_{\rm eff} - \log g$ diagram showing the results of our pure hydrogen spectral fits as red crosses, and the updated result with metals added in solar abundance as black dots. The two distributions are shifted due to the changes in $T_{\rm eff}$ and $\log g$ for individual objects. The continuous blue line indicates the ZAHB, above which stars might be burning He in the core. Its position depends on metallicity; the continuous line assumes $Z = 0.0001$, the dashed line is for solar metallicity. Different sequences are labelled as 1, 2, 3, and 4. They reflect different temperature regimes described in the text.

Fig. 30 shows the $T_{\rm eff} - \log g$ diagram with the comparison between values obtained from our pure hydrogen fit and the solar abundance values, for objects with good fit in

both cases. It can be noted that the distribution shifts as a whole with the addition of metals to the models. Four sequences can be distinguished. At the hot low gravity end, some objects (labelled as sequence 1 in Fig. 30) are above the ZAHB; they could hence be blue horizontal branch stars. They are kept in the sample because, as we will show later, this region of the diagram can also be reached through binary evolution. There are a few hot objects between 10 000–12 000 K (sequence 2), and the bulk of the distribution is between 7 000–10 000 K. Careful inspection, especially at the low log g end, suggests this region can also be split in two regimes around 8 000 K (sequences 3 and 4).

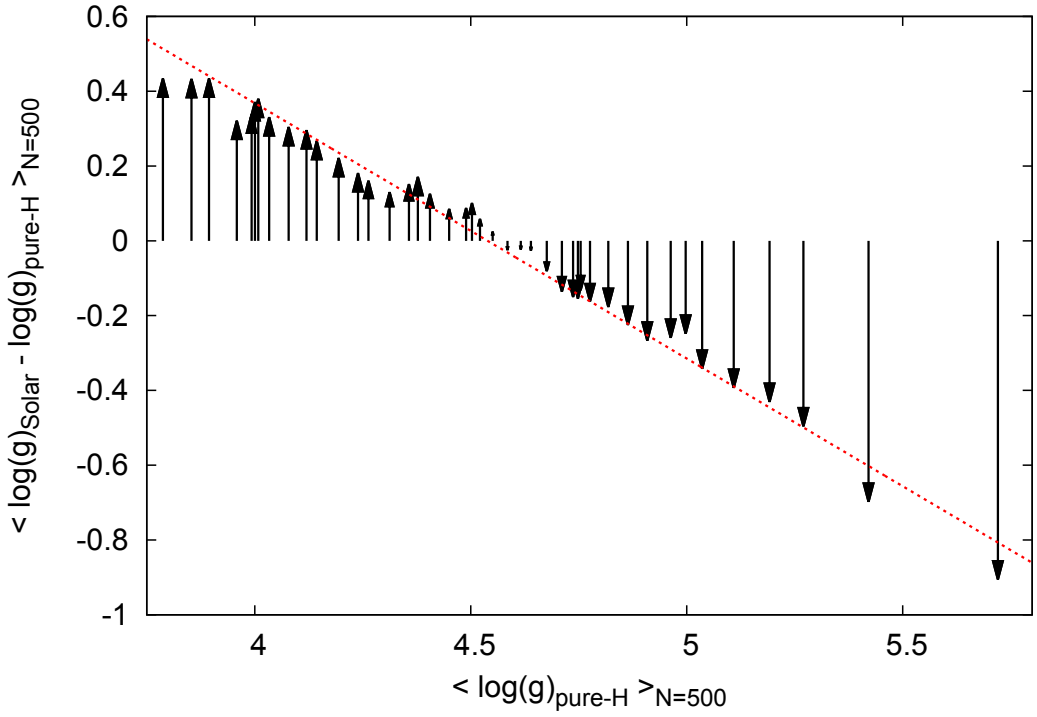

Figure 31 – Shift in $\log g$ with the addition of metals in solar abundances as a function of the $\log g$ given by the pure-H models. Values were averaged over 500 objects sorted by $\log g$. The shifts are well described by a linear fit

$$\Delta \log g = -0.68(0.01)\ \log g_{\text{pure-H}} + 3.10(0.06)$$

with the pure-H values being larger by almost 1.0 dex above $\log g = 5.5$. This is a similar result to the obtained by Brown, Kilic & Gianninas (2017) when fitting pure hydrogen model to synthetic main-sequence spectra.

I analysed the change in log g for objects in sample A as a function of the pure hydrogen T_{eff} and log g values. I took into account only objects whose two estimated T_{eff} values differed by less than 500 K, to avoid solutions conflicting due to the hot-cold degeneracy. I found a clear trend when plotting log g_{Solar} − log $g_{\text{pure-H}}$ as a function of log $g_{\text{pure-H}}$, as can be seen in Fig. 31. The larger the $\log g_{\text{pure-H}}$, the smaller is the log g obtained from solar abundance models compared to pure hydrogen models. The shift,

however, is not a constant value of ~ 1.0 dex as suggested by Brown, Kilic & Gianninas (2017), but it rather behaves as a linear function of log $g_{\text{pure-H}}$. Above log $g \sim 5.5$, the solar abundance log g is in fact about 1 dex smaller than the value obtained from pure hydrogen models, as they have found. This explains their conclusion and that of Hermes, Gänsicke & Breedt (2017) when analysing the log $g \geq 5.5$ DR12 sdAs: they are exactly in this range where the difference between these two values is maximal. However, it is important to emphasise that the solar abundance model is not necessarily the correct one; while many sdAs do show clear signs of metals in their spectra, others seem to be almost free of metals (see two examples in Fig. 32).

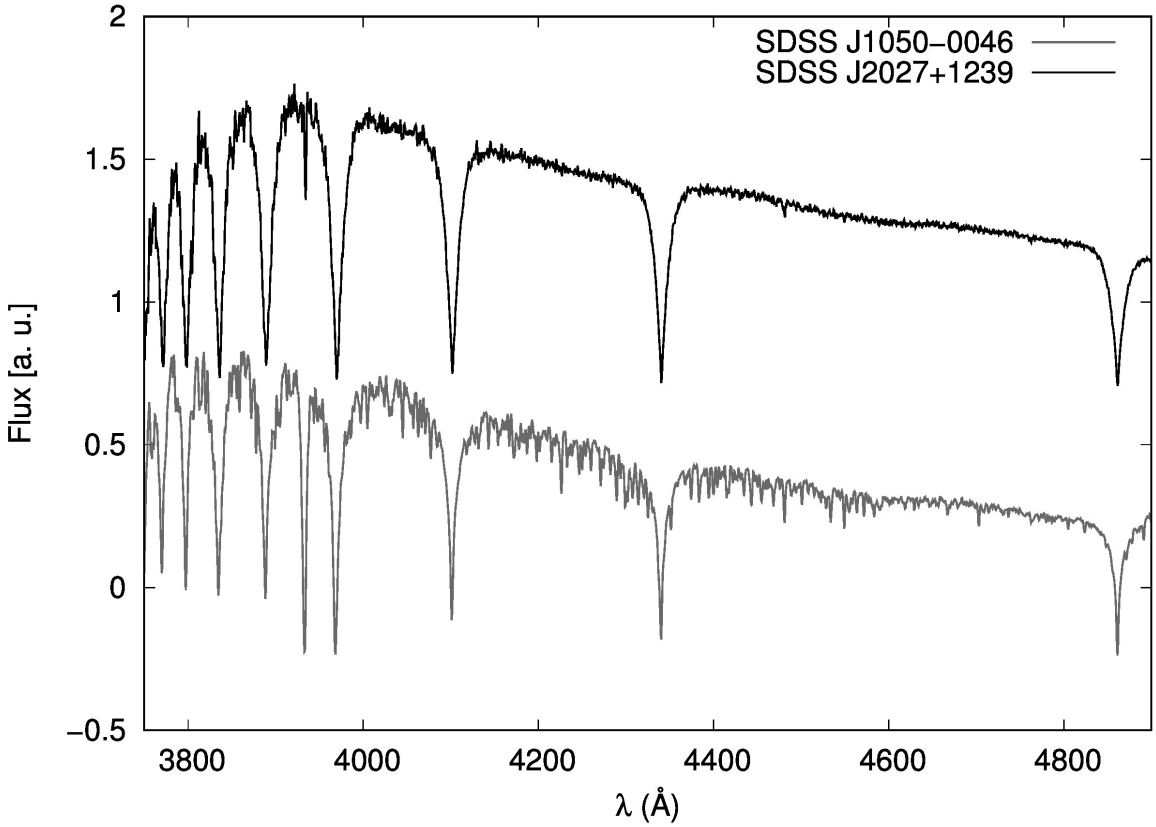

Figure 32 – Two sdA stars, SDSS J105025.94-004655.5 (bottom) and SDSS J202721.77+123942.7 (top). While SDSS J1050-0046 shows lots of metallic lines, SDSS J2027+1239 appears to have only a small amount of Ca and Mg.

This systematic trend also reflects on the dependence of the log g change with T_{eff}, shown in Fig. 33. At $T_{\text{eff}} \sim 8\,500$ K, there are objects spanning all the log g range (sequence 3 in Fig. 30), but a prevalence of objects with lower log g, which have an upward correction, i.e. in the direction of log $g_{\text{pure-H}} <$ log g_{Solar}. Hence the same upward correction is seen in this T_{eff} range. Between $7\,500-8\,000$ K, a gap in the lower log g objects can be seen in Fig. 30, which moves the correction downwards (log $g_{\text{pure-H}} >$ log g_{Solar}). Finally, below $T_{\text{eff}} \sim 7\,500$ K (sequence 4), most objects show log $g \leq 4.5$, so the correction

moves upwards again. Close to the cool border of $T_{\rm eff}$, most objects are also close to the lower border of the log g grid, which is 3.75 for the pure-hydrogen models and 3.5 for the solar abundance models, implying on an average difference of 0.25. There can of course be differences in metallicity and errors in the determination, so individual objects can somewhat obscure these trends.

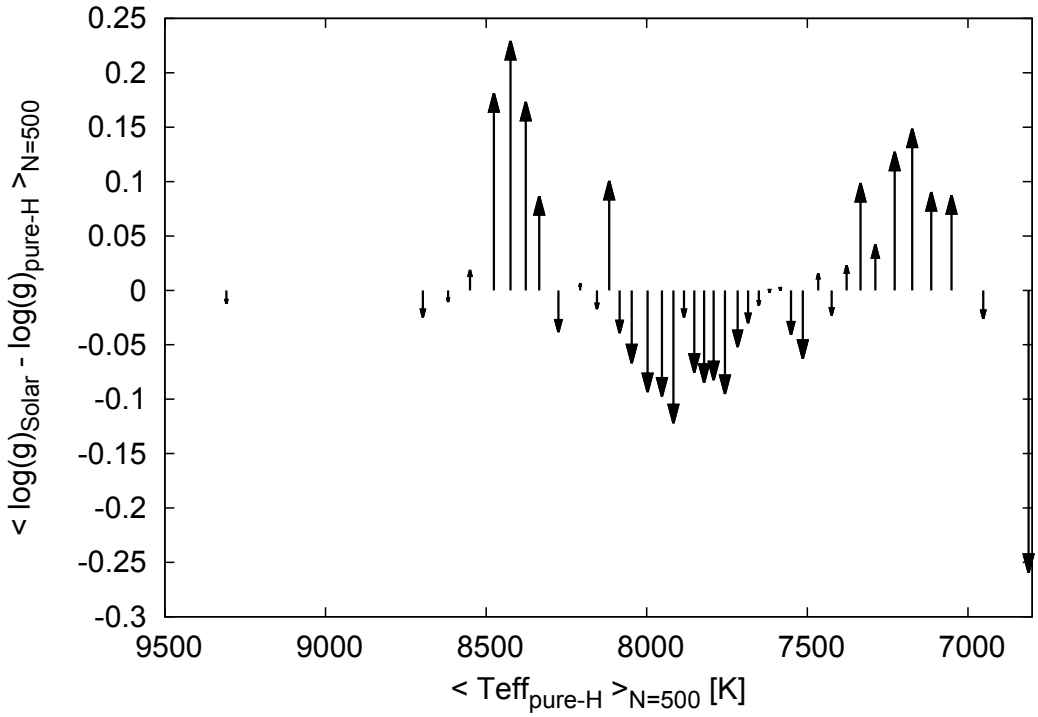

Figure 33 – Change in log g when metals were added to the models as a function of the effective temperature of the pure-H models. The $T_{\rm eff}$ and the change in log g were averaged over 500 objects, sorted by $T_{\rm eff}$. The systematic effect found as a function of log $g_{\rm pure\text{-}H}$ implies on a correlation also in $T_{\rm eff}$, depending on how each range of $\log g$ is sampled in each bin of $T_{\rm eff}$. Around 7 000 K, for example, most objects have log $g < 4.5$, where the shift in log g points upwards in Fig. 31, what is also seen here.

The solar abundance solutions put most of the 2 443 sdAs we found to show log $g >$ 5.5 with pure-H models in Section 4.1.6 in the main sequence range, with the exception of 39 objects which still show log $g \geq 5.0$. Only seven out of these maintain log $g \geq 5.5$ in the solar abundance models. It is important to notice, however, that these higher values of log g can rise from statistics alone given an external uncertainty of about 0.25 dex even if the correct log g for these objects is about 4.5, therefore they should be analysed with caution.

Two of the log $g > 5.0$ objects were published in the ELM Survey, SDSS J074615.83+392203.1 (Brown et al., 2012) and SDSS J091709.55+463821.7 (Gianninas et al., 2015). SDSS J0746+3922 was not confirmed as a binary; the pub-

lished solution of $T_{\rm eff} = 12\,130 \pm 400$ K and log $g = 5.98 \pm 0.12$ agrees in $\log g$ with our pure hydrogen solution, $T_{\rm eff} = 8\,300$ K and log $g = 5.85$, but there is a discrepancy in $T_{\rm eff}$, which cannot be explained by the hot-cool duality because the equivalent widths are significantly different between these two sets of solutions. The UV colours favour the hotter solution. Our solar metallicity solution gives a slightly lower log g of 5.481 ± 0.017 and $T_{\rm eff} = 8\,326 \pm 9$ K[2]. SDSS J0917+4638 was confirmed as a binary with period of 7.6 h and amplitude of 150 km/s. The solution published in Gianninas et al. (2015), $T_{\rm eff} = 12240 \pm 180$ and log $g = 5.75 \pm 0.04$, agrees with our solar metallicity values of $T_{\rm eff} = 12\,958 \pm 111$ and log $g = 5.842 \pm 0.029$. Our pure hydrogen fit indicates $T_{\rm eff} = 9\,600$ K and log $g = 5.00$.

Another object which maintained log $g > 5.0$ is SDSS J075017.35+400441.2, an eclipsing binary analysed in Brown, Kilic & Gianninas (2017). Our solar metallicity fit gives $T_{\rm eff} = 8\,071 \pm 15$ K and log $g = 5.019 \pm 0.038$, a log g significantly lower than the pure-hydrogen value of 5.619. Brown, Kilic & Gianninas (2017) point out that the SEGUE stellar parameter pipeline (SSPP) gives a much lower log g of 4.229 ± 0.155. However, the SSPP grid has no model above log $g = 5.0$. The obtained period from their radial velocity orbital fit agrees with the photometric period of 28 h. They obtain a radial velocity amplitude of 36.2 km/s and conclude the star is best explained by a metal-poor main-sequence binary, which is consistent with our solar metallicity solution given the external uncertainties. The star's detected proper motion is not significant (2.03 ± 1.96 mas/yr), but the distance obtained from its distance modulus is over 14 kpc — in the Galactic halo. If indeed a main sequence A star, it can only be explained as blue straggler whose main sequence lifetime was significantly extended due to mass accreted from the companion. It could alternatively be a pre-ELM at 225 pc, a much lower distance given that compact objects have smaller radius and are intrinsically fainter.

SDSS J014442.66-003741.7, which was classified as δ-Scuti by Bhatti et al. (2010) given its Stripe 82 SDSS data, also has log $g > 5.0$ in both our models. Bhatti et al. (2010) obtained a period of 1.5 h, which could also be explained as a g-mode pulsation of a pre-ELM star, given our solar metallicity fit of $T_{\rm eff} = 7\,949 \pm 35$ K and log $g = 5.18 \pm 0.11$ (the pure-H fit gives a similar solution, $T_{\rm eff} = 7\,900$ K, log $g = 5.0$). The object's proper motion in the GPS1 proper motion table, 8.48 ± 3.59 mas/yr has too high uncertainty to allow any further conclusions on the object's nature. The object is relatively faint, $g = 19.8$, so the SDSS subspectra have too low S/N to allow good estimates of radial velocity. Better data are needed in order to establish the nature of this star. Evolutionary models suggest that period spacing and rate of period change can be used to tell pre-ELMs and δ-Scuti stars apart (Sánchez-Arias et al., *submitted to A&A*). However, with the current available data, this technique cannot be applied, because the data do not

[2] Quoted uncertainties in our values of $T_{\rm eff}$ and $\log g$ are formal fit errors. The external uncertainties in the models are much larger, as discussed in Section 3.2.

allow the estimate of the rate of period change, and only one period was detected.

4.2.2 Colours

While spectra are considered the most reliable way to estimate the physical properties of a star, the colours of an object alone can still tell us something about its nature and be used as a complement to spectral results, especially when the colours include the ultraviolet region, not included in most spectra. This method relies notably on the $(u-g)\times(g-r)$ diagram, where models can be significantly dependent on $\log g$. Most known white dwarfs are hot objects, because they are brighter and easier to detect than cool white dwarfs, and they appear bluer than the main sequence. However, the cooler the white dwarf, the closer its colours are to the main sequence. When the log g is low, this is aggravated: for pre-ELMs and ELMs, the low log g gives them colours very similar to main sequence stars, making this method less effective. This is very clear on Figs. 34 and 35: the main sequence model for log $g = 4$ and $[M/H] = -5.0$ [3] overlaps with the DA model in many regions, making it difficult to rely on colours for selecting ELMs.

In Fig. 34, I show the $(u-g)_0 \times (g-r)_0$ diagram for samples A (all) and B (proper motion selected) of sdAs. Full reddening correction is applied following Schlegel; Finkbeiner; Davis (1998), given that, if main sequence stars, the sdAs are tens of kiloparsecs away, and, if subdwarfs, they are a few hundred parsecs away. For comparison, we also show the confirmed ELMs from the ELM Survey as published in Brown et al. (2016). Objects that were placed in the ELM range, $T_{\rm eff} \leq 20\,000$ K and $5.0 \leq \log g \leq 7.0$, when fitted with our solar metallicity models, are marked with orange circles. They could be interpreted as extending the ELM strip to cooler temperature, but remarkably most of them lie below the $\log g = 5.0$ model line in this colour-colour diagram, despite the fact that spectroscopy indicates $\log g > 5.0$. This might suggest that there is still some missing physics in our spectral models: the addition of metals alone does not solve the discrepancy. Possibly some opacity included in the models needs better calculations, as might be the case for broadening of the Balmer lines by neutral hydrogen atoms. Contamination by He through deep convection may also play a role. A possibility that cannot be discarded is that the extinction correction is not accurate due to reasons such as variations on dust type and size, or the object being within the Galactic disk. The fact that the other colour-colour diagrams, $(g-r)_0$ versus $(r-i)_0$ and $(r-i)_0$ versus $(i-z)_0$, shown in Fig. 35, do not seem to indicate an overestimate of the spectroscopic log g may be seen as an indication for this underestimate of the extinction correction.

I have also analysed the GALEX UV magnitudes, far-ultraviolet (fuv) and near-

[3] $[M/H] = \log\left(\frac{Z/X}{Z_\odot/X_\odot}\right)$, where Z and X are the metal and hydrogen mass fractions of the star, respectively.

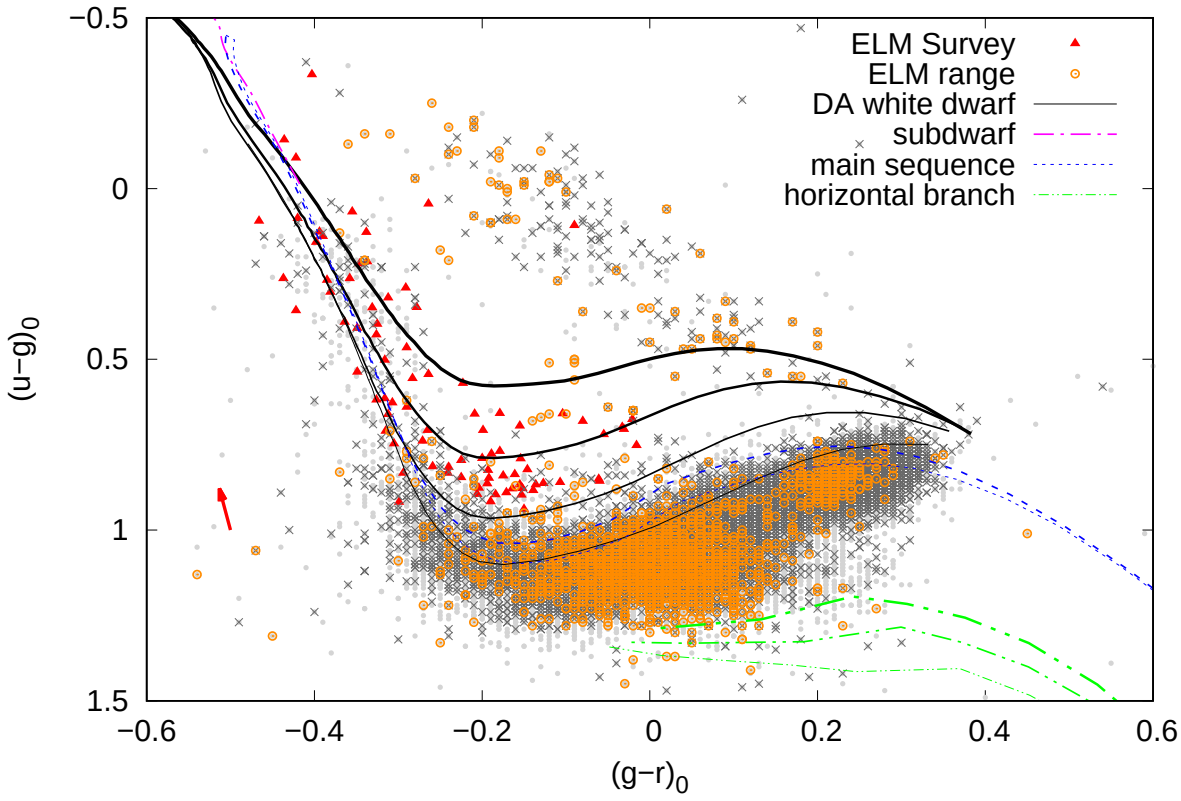

Figure 34 – Colour-colour diagram showing sample A as dots in light grey, sample B as dark grey crosses, and the known ELMs from Brown et al. (2016) as red triangles. Objects whose obtained spectral fit places them in the ELM range $T_{\rm eff} \leq 20\,000$ K and $5.0 \leq \log g \leq 7.0$ are marked with orange circles. The red arrow indicates the average vector of the reddening correction. Some theoretical models are included to guide the eye; the increasing thickness of the lines reflects an increasing $\log g$. The DA white dwarf models in black are obtained from our pure-hydrogen spectral models by convolving them with the SDSS filters. They span $\log g$ 4.0–7.0 in steps of 1.0 from bottom to top. Subdwarf, main sequence, and horizontal branch models are from Lenz et al. (1998). The subdwarf model assumes $\log g = 5.00$ and $[M/H] = 0.0$, and covers 20 000 K$\leq T_{\rm eff} \leq 50\,000$ K. The selected main sequence models have fixed $[M/H] = -5.0$, with $\log g = 4.0, 4.5$ and 4 250 K$\leq T_{\rm eff} \leq 40\,000$ K. Finally, horizontal branch models have $[M/H] = -1.0$, $\log g = 1.0, 1.5, 2.0$ and span the theoretical limits of the HB phase, 3 500 K$\leq T_{\rm eff} \leq 26\,000$ K.

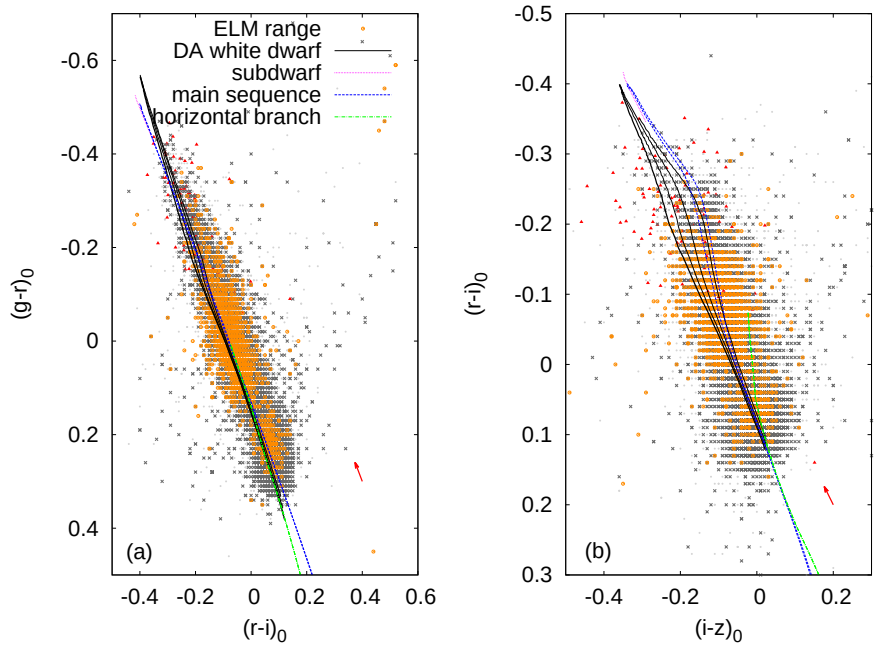

Figure 35 – Panel (a) shows the $(g-r)_0$ versus $(r-i)_0$ colour-colour diagram, while (b) shows the diagram for $(r-i)_0$ versus $(i-z)_0$. Labels and plotted models are the same as in Fig. 34.

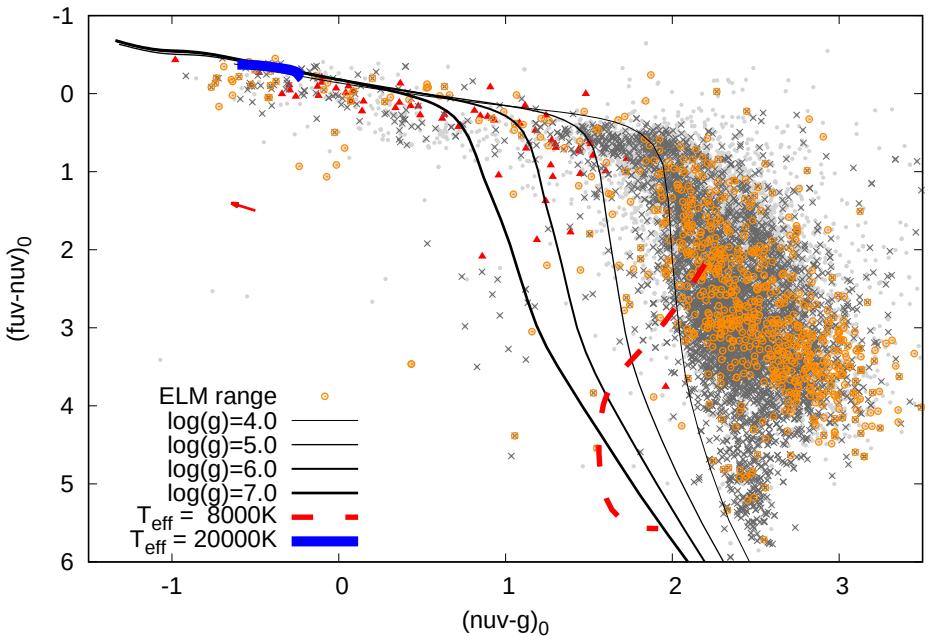

Figure 36 – Diagram showing the $(fuv-nuv)_0$ and $(nuv-g)_0$ colours. The colours of each sample are the same as in Fig. 34. The red arrow indicates the average reddening correction vector. The indicated models were obtained from our pure-hydrogen spectral models. Despite the reddening correction, the data still seems dislocated in relation to the models, suggesting this correction might be underestimated.

ultraviolet (nuv), when available. Fig. 36 shows a $(fuv - nuv)_0 \times (nuv - g)_0$ diagram for samples A and B; the objects for which we have obtained $T_{\rm eff} \leq 20\,000$ K and $5.0 \leq \log g \leq 7.0$ are marked as orange circles. Extinction correction was applied using the $E(B-V)$ value given in the GALEX catalogue, $R_{fuv} = 4.89$ and $R_{nuv} = 7.24$ (Yuan; Liu; Xiang, 2013). The colours suggest again log g lower than the estimated spectroscopically. However, extinction correction is even more uncertain in the ultraviolet than in the visible region, so again it should not be discarded that the correction is underestimated.

This diagram is especially useful in identifying sdB + FGK binaries, which should have significant flux in the UV due to the hot subdwarf component showing $T_{\rm eff} \gtrsim 20\,000\ K$. In Fig. 36, there is a clustering of objects with $(nuv - g)_0 < -0.4$. I noticed that many of them show radial velocity differences larger than 100 km/s in the SDSS subspectra that compose the final spectrum. About half of the sdBs are found to be in close binary systems (e.g. Heber, 2016), with many showing radial velocity amplitudes in this range (e.g. Copperwheat et al., 2011). This considered, we suggest that sdAs showing $(nuv - g)_0 < -0.4$ — 153 objects, or 0.5% of the objects with GALEX colours — can be explained as sdB + FGK binaries.

Notably, two published ELMs are in this colour range: SDSS J234536.46-010204.9 and SDSS J162542.10+363219.1. SDSS J2345-0102 was analysed in Kilic et al. (2011). They obtained $T_{\rm eff} = 33\,130 \pm 450$ and $\log g = 7.20 \pm 0.04$ and found no evidence of radial velocity variations, suggesting this object is 0.42 $M_\odot$ white dwarf — therefore a low-mass white dwarf, which are often found to be single, rather than an ELM. The obtained $T_{\rm eff} > 20\,000$ K and $\log g > 7.0$ make it easier to distinguish this object from the sdAs, so it is not affected by our $(nuv - g)_0 < -0.4$ criterion. On the other hand, SDSS J1625+3632 which was also analysed in Kilic et al. (2011), has its estimated parameters, $T_{\rm eff} = 23\,570 \pm 440$ K and $\log g = 6.12 \pm 0.03$, close to the log g range where we put the sdAs. Kilic et al. (2011) found it to present a small semi-amplitude of $K = 58.4$ km/s and a period of 5.6 h, suggesting it to be a 0.20 $M_\odot$ ELM with most likely another white dwarf as a companion. However, they point out that their obtained physical parameters are very similar to the sdB star HD 188112 (Heber et al., 2003), and mention that the 4471 Å line, a common feature of sdB stars, can be detected in the spectrum of the object. All this combined suggests that this object is not an ELM, but an sdB, fitting the $(nuv - g)_0 < -0.4$ criterion. As previously mentioned, sdBs are also commonly found in binaries, often with a canonical mass white dwarf. The canonical mass for sdBs is usually quoted as 0.45 $M_\odot$; however, objects with a lower mass such as this one are known (e.g. Latour et al., 2016).

Finally, I searched for infrared excess due to a cool companion star using data from the Wide-field Infrared Survey (WISE, Wright et al., 2010) and the Two Micron All Sky Survey (2MASS, Skrutskie et al., 2006). I followed the approach of Hoard et al.

(2013), who searched for candidate white dwarfs with infrared excess by examining a $(J-W1)\times(W1-W2)$ diagram, suggesting $(W1-W2) > 0.3$ as an indication of possible excess. As both white dwarfs and sdAs show hydrogen-dominated spectra, with very few lines in the infrared, the infrared flux in both cases depends basically on $T_{\rm eff}$, thus the method is suitable for analysing the sdAs. Hoard et al. (2013) restrict their analysis to objects with $S/N > 7$ at both W1 and W2. Using this same criterion, I found only about 1.3% of sample A (376 objects) to possibly show infrared excess. The percentage is similar when I consider only objects brighter than $W1 = 14$ or than $W1 = 15$, as illustrated in Fig. 37.

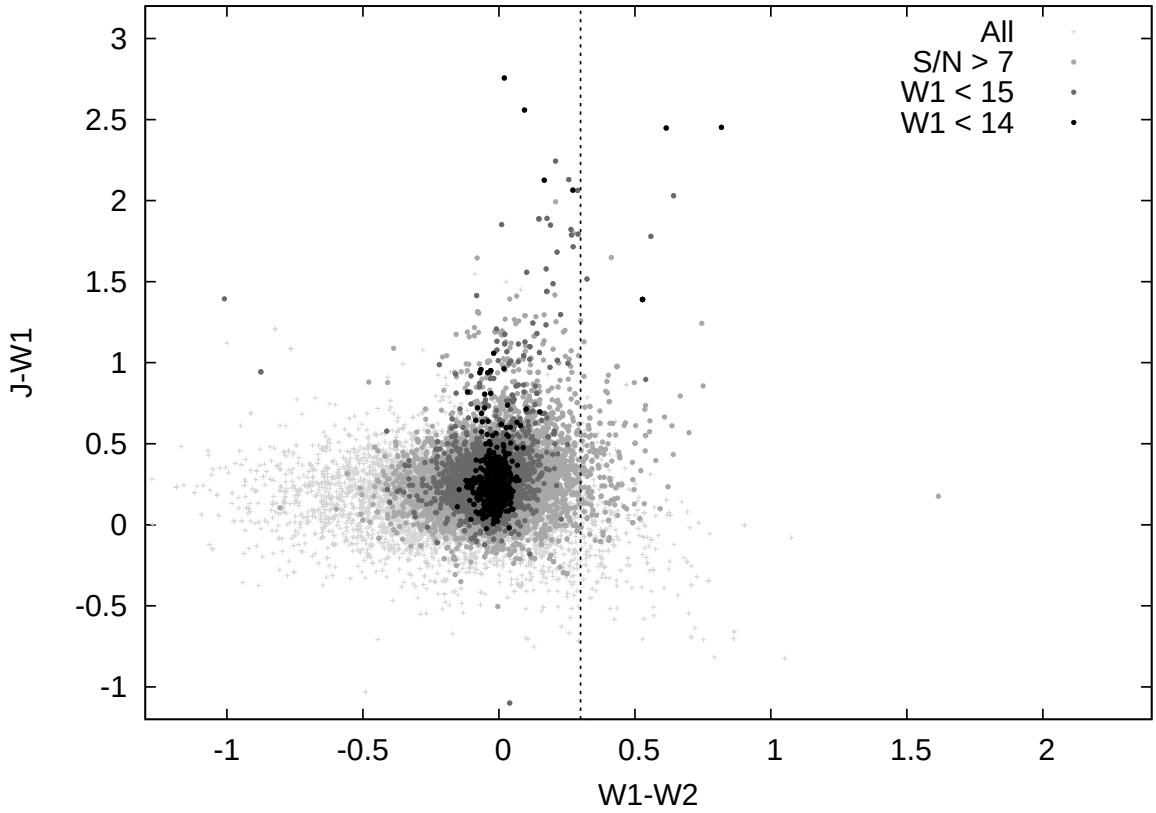

Figure 37 – $(J-W1)\times(W1-W2)$ colour-colour diagram for sample A. The whole sample is shown as light grey crosses, objects with $S/N > 7$ at both $W1$ and $W2$ filters are shown as grey dots. The dark grey dots indicate objects brighter than $W1 = 15$, and the black dots are those brighter than $W1 = 14$. The dashed vertical line is the $(W1 - W2) = 0.3$ limit, above which the objects might have infrared excess as suggested by Hoard et al. (2013).

In summary the sdA colours are consistent with a cooler ELM population, especially considering that the extinction corrections are uncertain for the ultraviolet region. The hypothesis that they are far-away young main sequence A stars with an overestimated log g cannot, however, be ruled out, as they do occupy the same region as most main sequence stars in all colour-colour diagrams. An sdB+FGK binary, on the other hand, is

ruled out for most objects (over 99%) by the GALEX colours, as are cool companions given the infra-red data, with very few exceptions.

4.2.3 Galactic coordinates and velocities

I have also analysed the distribution of the sdAs across the sky and estimated their distances and velocities. In Fig. 38, I show the galactic coordinates latitude b and longitude l of sample A, with objects in the ELM range shown in black, using an Aitoff projection. One can notice that they are spread all over the footprint of SDSS, there are no streams which would justify the presence of young stars in the halo of the Milk Way. Moreover, there seems to be no difference between the regions occupied by the whole sample and by objects with log $g > 5.0$.

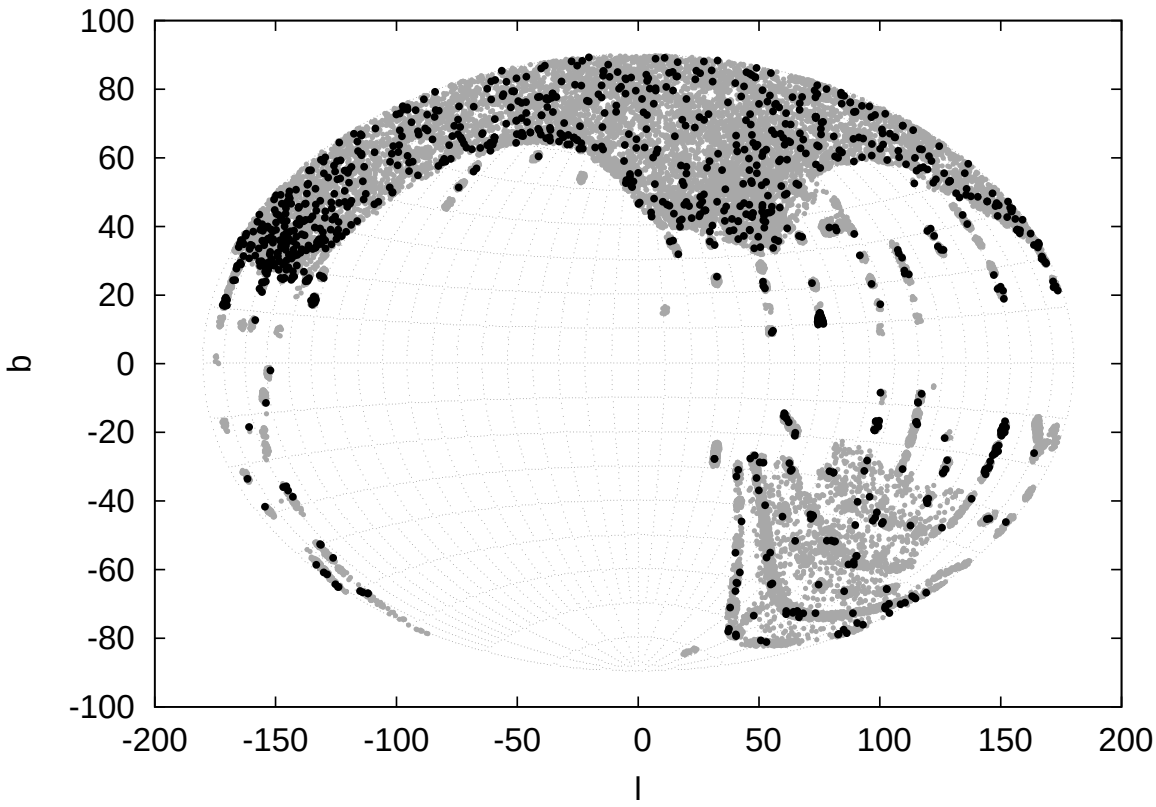

Figure 38 – Aitoff projection showing the galactic latitude (b) and longitude l for the sdAs and the main sequence objects. No streams can be identified; both samples seem to be distributed all over the SDSS's footprint.

Using the coordinates b and l and an estimated distance d, one can obtain the galactic Cartesian coordinates, X, Y and Z:

$$X = d\cos(b)\cos(l) \quad (4.5)$$

$$Y = d\cos(b)\sin(l) \quad (4.6)$$

$$Z = d\sin(b). \quad (4.7)$$

With three more estimates, namely the proper motions along declination and right ascension (μ_δ and μ_α, which can be obtained from proper motion catalogues), and the radial velocity (RV, estimated as part of the spectral fit), one can also obtain the Galactic spatial velocities U, V, and W (e.g. Johnson; Soderblom, 1987).

From our photometric fits to the objects, that relate the observed flux with the expected flux given a modelled luminosity, we obtained the solid angle

$$\Omega = \pi \frac{R^2}{d^2}. \tag{4.8}$$

Assuming the sdAs with log $g_{\rm Solar} > 5$ are ELMs, we have used the evolutionary models of Althaus, Miller Bertolami & Córsico (2013) to obtain their radius R, allowing to estimate d. Similarly, we have estimated the distances for the objects with log $g_{\rm Solar} < 5.0$ assuming main sequence radii, which were interpolated from solar-abundance values given the $T_{\rm eff}$ of the object. Combining that with the coordinates b and l, we obtained their coordinates X, Y and Z. Fig. 39 shows the projections in the planes XY and XZ. Apparently, if the sdAs are ELMs, they are constrained to the galactic disk ($d \lesssim 2$ kpc). In contrast, assuming a main sequence radius for the log $g < 5.0$ objects, they seem to extend to larger distances, up to the galactic halo or even farther, some with distances which imply they could be located in nearby galaxies

A histogram of the height above the galactic plane Z, shown in Fig. 40, leads to similar conclusion. Exponential functions describing a thin and thick disk with the scaleheights given by Bland-Hawthorn & Gerhard (2016) are shown as a comparison. Assuming main sequence radii, the sdA distribution extends much further than the disk, to distances up to 10 kpc.

The velocities U, V, and W, which I estimated for the objects in sample B (reliable proper motion) only, show that, when the main sequence radius is assumed, about 38% of all objects in the sample show velocities out of the 3-σ ellipsoid for the halo — implying a 1% chance that they actually belong to the Galactic halo (Fig. 41). When the (pre-)ELM radius is assumed, on the other hand, the objects show a distribution consistent with a disk population (Fig. 42).

The fact that many objects seem to belong to the halo, or even appear not to be bounded to the Galaxy when a main sequence radius is assumed, is confirmed by their orbits. Using a code provided by our collaborators Drs. Uli Heber and Stephan Geier, I calculated the orbits for objects in sample B. The code computes the orbit assuming the potential given by the mass distribution of Allen & Santillan (1991), having as input the distance, radial velocity, and proper motions in right ascension and declination in the present. Given these initial conditions, I calculated the orbits for a period of 5 Gyr, with steps of 1 Myr. Analysing a randomly selected sub-sample with 6000 objects, I found only 35% to show an orbit constrained to $|z| < 10$ kpc, which is about twice as much

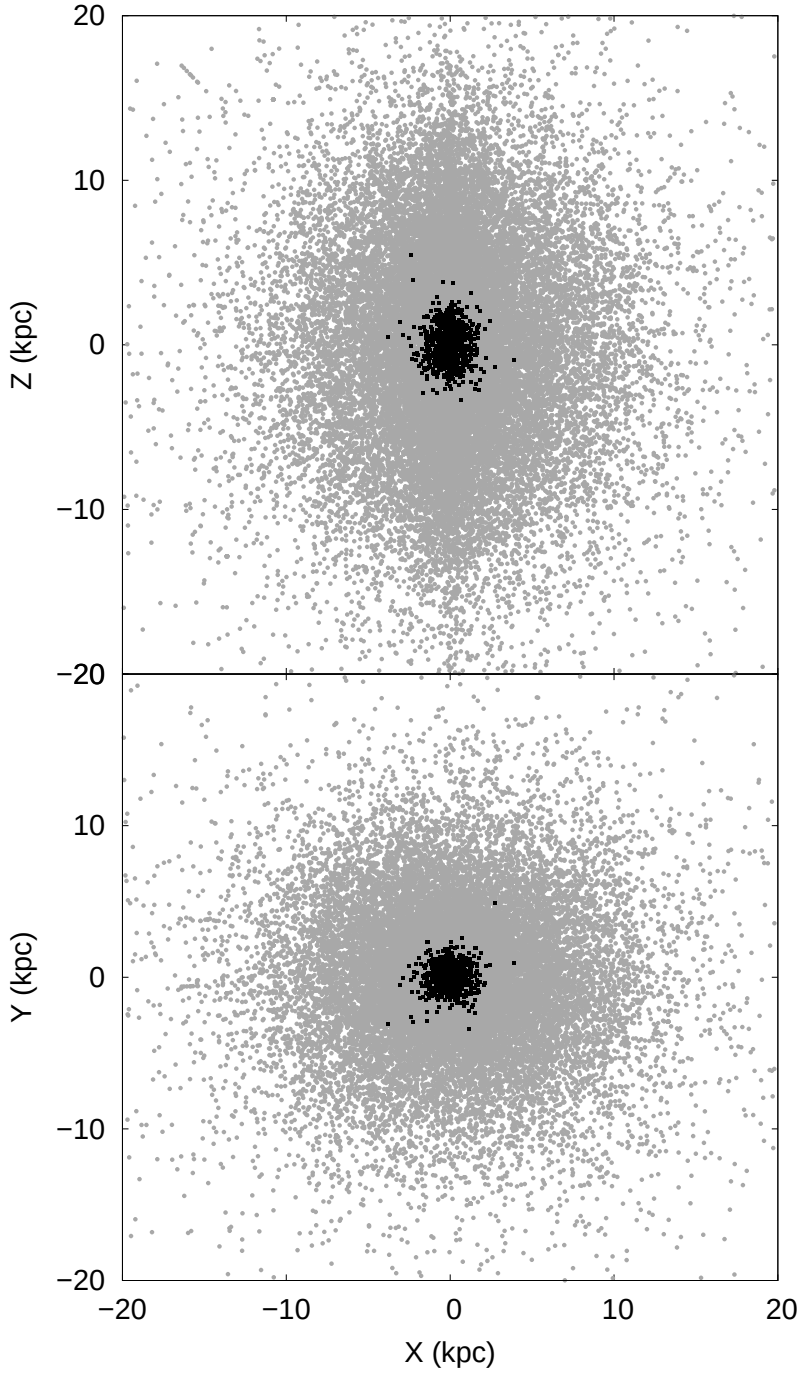

Figure 39 – Distances projected in the XY and XZ planes for the objects in sample A in the ELM range (log $g > 5.0$, black), assuming ELM radii, and for objects with estimated log $g < 5.0$ (grey), assuming main sequence radii. As all objects have similar magnitudes, the difference in radius makes the sdAs constrained to the disk if they are ELMs, while they seem to extend up to the halo, if we assume main sequence radius.

as the thick disk extends considering the exponential models shown in Fig 40 — i.e., not even relaxing the limits of the disk by a factor of two the sdAs would be constrained to it given a MS radius. About 20% are unbounded given the main sequence radius and current estimates of proper motion and radial velocity. Fig. 43 shows the orbits for a few objects as illustration.

We have found very unexpected that all these A-type objects seem to be in the halo or even beyond. According to models, the halo should be at least 10 Gyr old (e.g. Krauss; Chaboyer, 2003), while stars of O, B, A type, which are the ones we have retrieved, stay less than ~ 1.5 Gyr in the main sequence. Hence if they were formed with the halo, they should have already evolved off the main sequence. Considering their velocities, it also does not seem plausible that they migrated from the disk to the halo within their evolutionary time. This seems a strong suggestion that these objects have actually smaller radii, as the (pre-)ELMs, which gives them a distribution consistent with the disk.

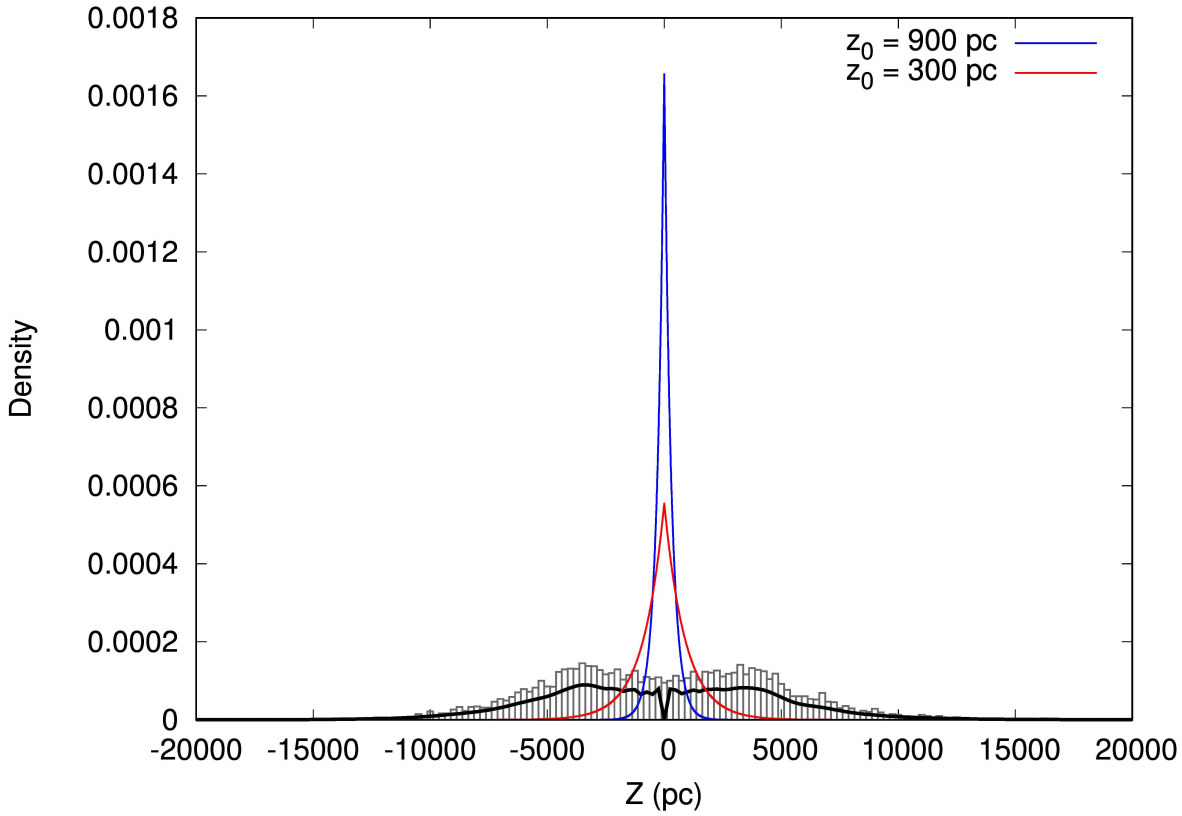

Figure 40 – The distance to the disk of the stars classified as O, B and A, assuming a main sequence radius. The histogram is given as N/N_{total}; the solid black line is calculated assuming each point as a Gaussian with standard deviation of 0.1 Z. The red line is an exponential thin disk model assuming $Z_0 = 300$ pc, while the blue line is a thick disk model with $Z_0 = 900$ pc. All functions are normalised. It is clear that, if indeed main sequence objects, these stars are not consistent with a disk distribution, but would rather have to be in the halo.

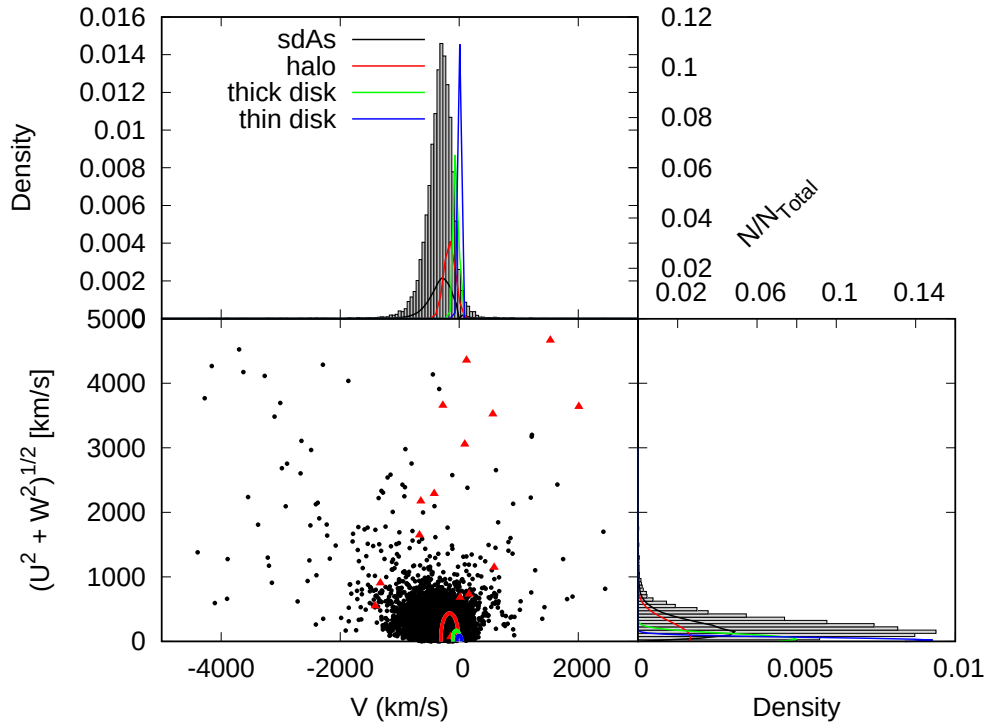

Figure 41 – Toomre velocity diagram of the objects in sample B, assuming a main sequence radius. Density plots are shown to left and on top. The ellipsoids indicate the 3-σ values for halo (red), thick disk (green) and thin disk (blue) according to Kordopatis et al. (2011).

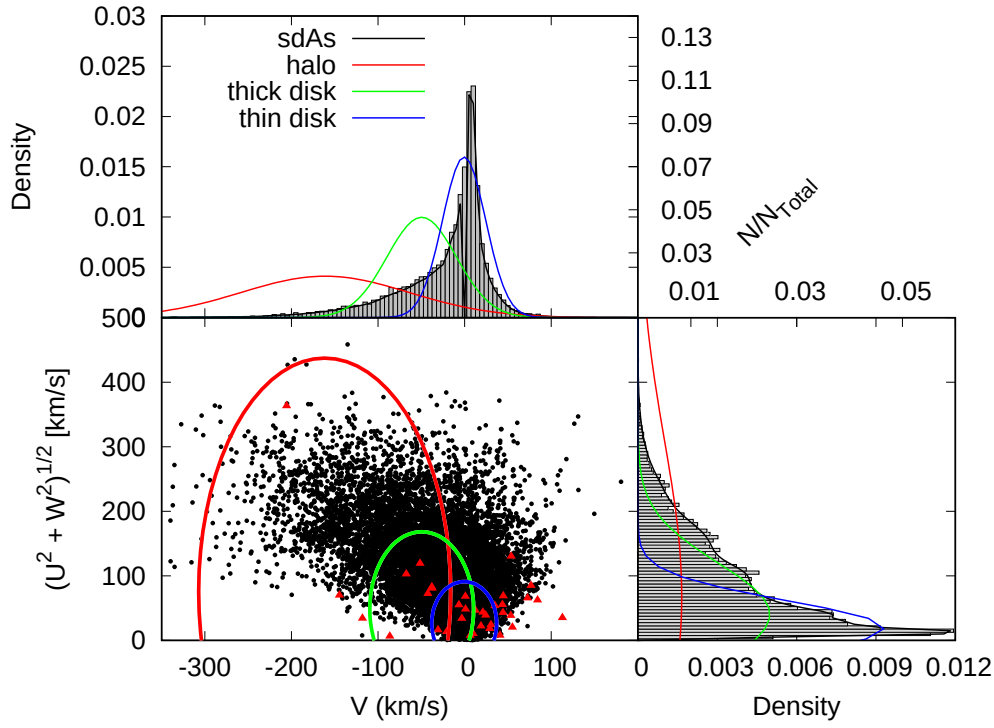

Figure 42 – Same as Fig. 41, but assuming a (pre-)ELM radius.

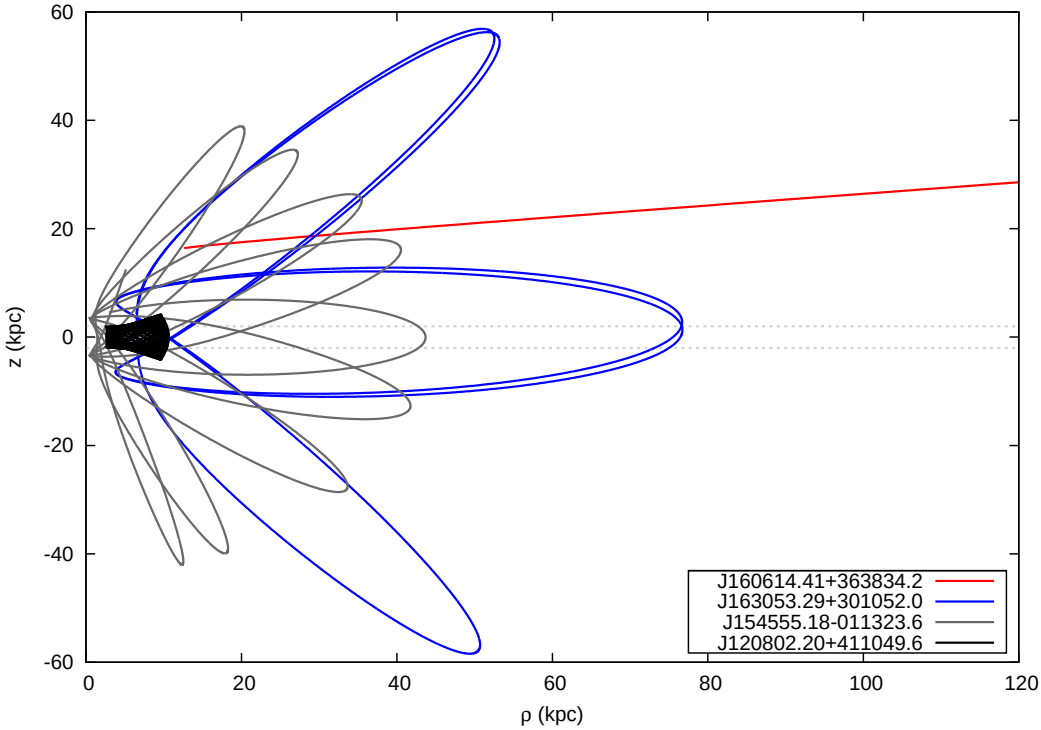

Figure 43 – Orbits for four sdAs: J1208+4110 seems to be disk-bounded, J1630+3010 and J1545-0113 extend to the halo, and J1606+3638 is unbounded when a main sequence radius is assumed.

4.2.4 Proper motion

One further step in the separation of white dwarfs from main sequence objects is taking into account measured proper motions (e.g. Gentile Fusillo; Gänsicke; Greiss, 2015). As white dwarfs are compact objects, they have smaller radius and therefore are fainter than main sequence stars with same temperature. Due to their degenerate nuclei, white dwarfs have a mass-radius relationship $R \sim M^{-1/3}$, implying that the smaller the mass, the larger the radius. Thus ELMs have larger radius and are brighter than common mass white dwarfs. Still, their radii are of the order of 0.1 $R_{\odot}$, so they should be about 10 times closer than main sequence stars with similar $T_{\rm eff}$ to be seen at similar apparent magnitude, showing higher proper motion. The picture is more complicated when the pre-ELMs are considered. Mostly because of the CNO flashes, they can be as bright as main sequence stars, so proper motion cannot be used as a criterion to tell these objects apart, because the pre-ELMs can be detected at distances as large as main sequence stars. Fig. 44 shows a reduced proper motion (H_g) versus $(g-z)_0$ diagram. Only sample B, containing objects with reliable proper motion, is shown. Here the reduced proper motion is evaluated as

$$H_g = g_0 + 5\log(\mu[''/yr]) + 5. \quad (4.9)$$

It can be interpreted as a proxy for the absolute magnitude: the higher the reduced proper motion, the fainter the object. The objects are colour coded by their Mahalonobis distance D_M (e.g. Kilic et al., 2012) to the halo when a main sequence radius is assumed. The Mahalonobis distance is given by

$$D_M = \sqrt{\frac{(U - \langle U \rangle)^2}{\sigma_U^2} + \frac{(V - \langle V \rangle)^2}{\sigma_V^2} + \frac{(W - \langle W \rangle)^2}{\sigma_W^2}}, \tag{4.10}$$

where I have assumed the values of Kordopatis et al. (2011) for the halo mean velocities and dispersions. The Mahalonobis distance measures the distance from the center of the distributions in units of standard deviations; hence considering the size of our sample and assuming a Gaussian behaviour, all objects should show $D_M < 4.0$. Nonetheless, when a main sequence radius is assumed, about 74% of the objects show $D_M > 4.0$. When we assume an ELM radius for these objects, this number falls to less than 2%. The logic conclusion is that most of the sdAs have radii smaller than the main sequence.

Fig. 44 suggests that most of the objects with $T_{\rm eff}$ and $\log g$ in the ELM range have, on average, H_g lower than the estimated value for known ELMs. This, combined with the fact that they seem to be in the same region of the diagram as the $\log g < 5.0$ objects, could again be seen as an indication of missing physics in the models leading to an overestimate of the $\log g$. However, their reduced proper motion is consistent with a tentative limit that I estimated based on Gentile Fusillo, Gänsicke & Greiss (2015), but including all ELMs. This limit is given by

$$H_g = 2.72(g - z)_0 + 16.09. \tag{4.11}$$

The diagram in Fig. 44 is very enlightening when we look at the density of objects. It is evident that there are two different populations within the sdAs: one to the red limit of the diagram and another in an intermediate region. While the distribution of the red population has no intersection with the known ELMs, the distribution resulting from the blue population shares colour properties with the known ELMs. Most of the ELMs in the blue distribution show $T_{\rm eff} > 8\,000$ K (comprising sequences 1, 2, and 3 from Fig. 30), while the red distribution contains objects mainly cooler than that (sequence 4 in Fig. 30), explaining the two regimes which could be glimpsed in Fig. 30. I will use these distributions to study the nature of the sdAs in terms of probabilities in Section 4.2.5. I believe the red distribution ($\sim 60\%$ of stars) is dominated by main sequence late-type stars with low metallicity, which can be found in the halo and show spectra mimicking A-type stars due to the lack of metals, with some possible contamination of cooler (pre-)ELMs, since there is an intersection with the blue distribution. The blue distribution, on the other hand, should contain the missing cool (pre-)ELM population, which is under-represented in the literature.

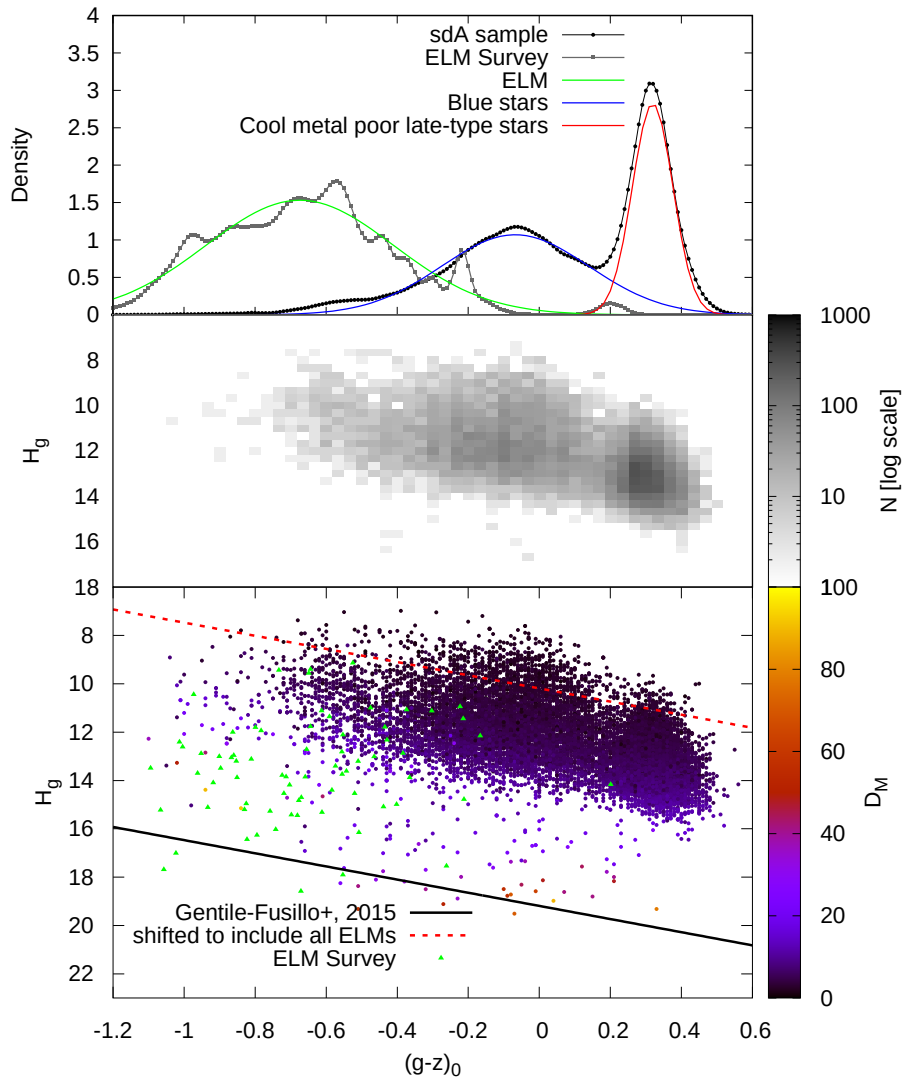

Figure 44 – The bottom panel shows the $H_g \times (g - z)_0$ diagram (see e.g. Gentile Fusillo; Gänsicke; Greiss, 2015), with the objects in sample B (i.e., proper motion selected) colour coded according to their Mahalonobis distance to the halo given a main sequence radius. Known ELMs are shown as green triangles for comparison. Middle panel shows the same diagram as a bidimensional histogram. The top panel shows the densities assuming each object as a Gaussian to account for the uncertainty; it becomes clear that there are two populations of objects within the sdA sample. The suggested limit for white dwarf detection with probability equal to 1.0 given by Gentile Fusillo, Gänsicke & Greiss (2015) is indicated as a black solid line. Most known ELMs, due to their larger radius implying a smaller reduced proper motion, since they can be detected at larger distances, are not below the white dwarf limit. A reference line, defined arbitrarily shifting the estimate of Gentile Fusillo, Gänsicke & Greiss (2015) to include all known ELMs is shown as a red dashed line. Most sdAs are also below such line.

4.2.5 Probabilistic analysis

Considering the previous analyses, it is clear that the observable properties of the sdAs are consistent with more than one evolutionary channel, since there is overlap between evolutionary paths. The only physical parameter that would allow an unique classification for the sdAs would be the radius, which, combined with log g estimates, would allow us to tell whether the objects have a degenerate nucleus. As there is no parallax measured for the sdAs, this will not be possible at least until Gaia's data release 2, scheduled for the 25th of April, 2018[4]. In the meantime, we can analyse the sdAs in terms of probability: do they have a higher probability of belonging to the main sequence, or can they be more easily explained by (pre-)ELMs?

Based on the estimated log g compared to evolutionary models, on the reduced proper motion diagram distributions, and on the spatial velocities given either a (pre-)ELM radius or a main sequence radius, I estimated for each object in sample B a probability of belonging to the main sequence and a probability of being a (pre-)ELM star. My intention was to provide a basis for future follow-up projects, such as time resolved spectroscopy, impossible with the present size of the samples, and to understand the sdA population as a whole.

The main sequence probability was evaluated taking into account three probabilities:

i) probability of being explained by a single-evolution model (see Fig. 5) given the estimated solar abundance $\log g$: $p_{\rm MS1}$;

ii) probability of belonging to the red distribution in Fig. 44 given the $(g-z)_0$ colour: $p_{\rm MS2}$;

iii) probability of belonging to the halo, thick or thin disk of the Galaxy given the U, V, W velocities estimated with a main sequence radius (Fig. 41): $p_{\rm MS3}$.

The final probability was calculated as the complementary probability of the object *not* belonging to the main sequence, so that the final probability increases when p_1, p_2, and p_3 are larger. Assuming the intermediary probabilities listed above are independent, we thus calculated it as:

$$p_{\rm MS} \;=\; 1-(1-p_{\rm MS1})\times(1-p_{\rm MS2})\times(1-p_{\rm MS3}). \qquad (4.12)$$

The (pre-)ELM probability on the other hand takes into account:

[4] The analysis presented in this Section was published in online form by MNRAS on the 9th of January, 2018. Following Gaia DR2, we verified that over 70% of the sdA sample has unreliable parallax ($\pi < 3\ \sigma_\pi$). Moreover, due to the asymmetric uncertainties in distance and hence radius, over 90% of the objects with $\pi > 3\ \sigma_\pi$ show inconclusive radii estimates, consistent with both main sequence and (pre-)ELM.

i) probability of being explained by binary evolution models (Fig. 5) given their estimated solar abundance $\log g$: $p_{\rm ELM1}$;

ii) probability of belonging to the blue distribution in Fig. 44 given the $(g-z)_0$ colour: $p_{\rm ELM2}$;

iii) probability of belonging to the halo, thick or thin disk of the Galaxy given the U, V, W velocities estimated with a (pre-)ELM radius (Fig. 42): $p_{\rm ELM3}$.

This gives a final probability, again assuming the intermediary probabilities are independent, of

$$p_{\rm ELM} = 1 - (1 - p_{\rm ELM1}) \times (1 - p_{\rm ELM2}) \times (1 - p_{\rm ELM3}). \quad (4.13)$$

As previously mentioned, there are intersections between the properties of the two populations, therefore the two probabilities are not independent and *do not* sum up to one. Fig. 45 shows the obtained results for the objects in sample B. If we analyse these results in terms of an average, a random sdA has 68% probability of belonging to the main sequence, and a 46% probability of being a (pre-)ELM. Doing the ratio between the two probabilities, we can select the objects which are more likely (pre-)ELMs in the sample. Fig. 46 shows the (pre-)ELM probability over the main sequence probability. 1 150 objects in sample B, or 7%, have a higher probability of being (pre-)ELMs. 170 of these objects show $\log g > 5.0$ — implying they would be ELMs rather than pre-ELMs. Out of those, 146 also show $T_{\rm eff} < 8\,500$ K.

Assuming all these objects have their nature correctly predicted, this would raise the number of ELMs with $T_{\rm eff} > 8\,500$ K in the SDSS footprint to 97 (73 confirmed binaries of Brown et al., 2016 in this range + 24 sdAs), while the number of objects with $T_{\rm eff} < 8\,500$ K would be 149 (3 confirmed binaries of Brown et al., 2016 in this range + 146 sdAs), making the cool ELM population about 50% larger. The evolutionary models predict the same amount of time to be spent in both ranges, but shell flashes can reduce the hydrogen in the atmosphere, speeding up the cooling process and making it possible that the time spent at lower temperatures be higher by a factor of two, as our findings seem to suggest. However, the circumstances where these shell flashes occur are still unclear. Follow-up of these objects to detect the true cool ELMs, allowing for an observational estimate of the rate of objects in the two $T_{\rm eff}$ ranges, should be acquired to help calibrate the evolutionary models. I will discuss the current state of my follow-up in Section 4.2.8.

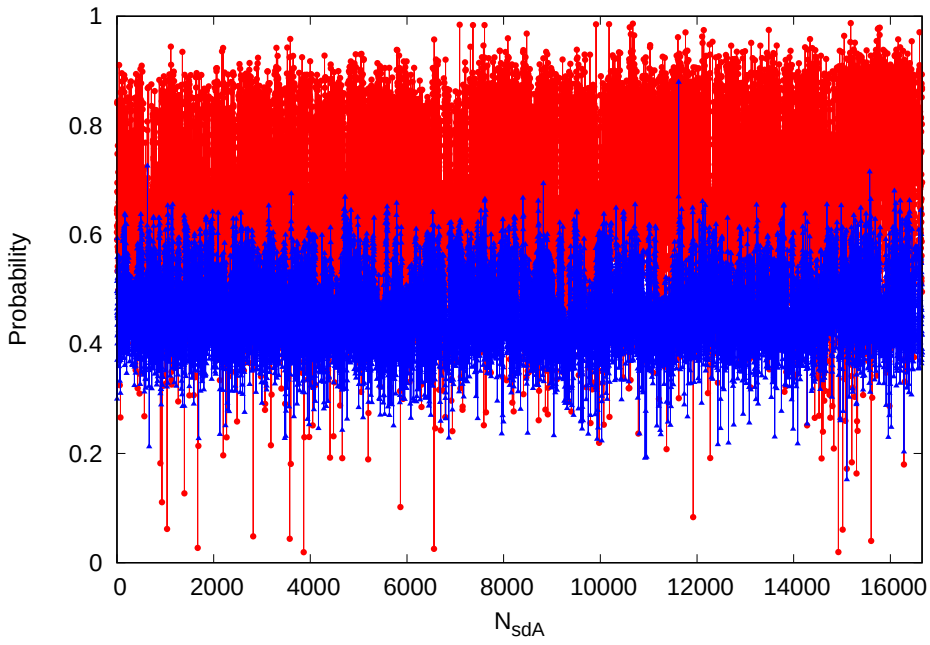

Figure 45 – Circles in red show the probability of belonging to the main sequence, while triangles in blue show the resulting probability of being a (pre-)ELM object according to our evaluated distributions. The x-axis is simply a count of sdAs in sample B.

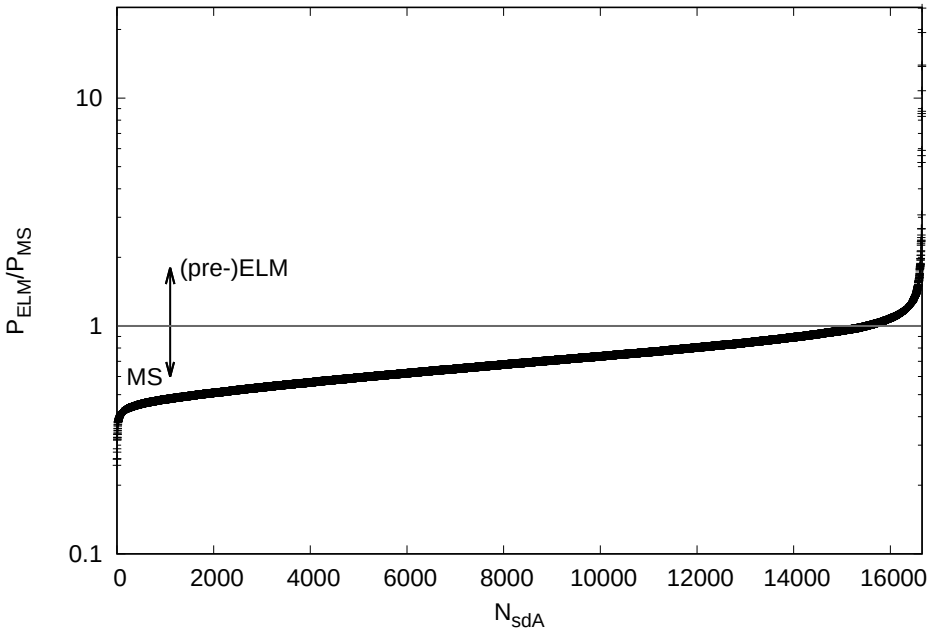

Figure 46 – Probability of (pre-)ELM over probability of main sequence, ordered from smallest to largest. The y-axis is shown in log scale. Most objects do show a larger probability of belonging to the main sequence, but 1 150 objects in sample B (about 7%) are most probably (pre-)ELMs.

4.2.6 Radial Velocity Variations from SDSS

Fig. 47 shows a histogram of the estimated radial velocity amplitude ΔV from the SDSS subspectra. Most spectra show $\Delta V < 100$ km/s, with 334 having $\Delta V > 100$ km/s. Out of those, 14 show $\Delta V > 200$ km/s. Two of these objects were previously published in the ELM Survey, namely SDSS J123800.09+194631.4 (Brown et al., 2013) and SDSS J082511.90+115236.4 (Kilic et al., 2012). Three are hot subdwarf stars showing $T_{\rm eff} > 20\,000$ K, which are also commonly found in binaries (SDSS J141558.19-022714.3, SDSS J163205.75+172241.3, and SDSS J211651.95-003328.5). Another one is a known CV (SDSS J152020.40-000948.3) identified by its colours by Gentile Fusillo, Gänsicke & Greiss (2015). Two others show $\log\ g > 7.0$ and are probably double degenerate systems, given that the companion is unseen in the spectra (SDSS J095157.78+290341.5 and SDSS J132232.12+641545.8, see Figs. 48 and 49). SDSS J132232.12+641545.8 (also known as PG 1320+645) was previously flagged as probable binary by Brown et al. (2011), but they were unable to constrain the orbital period. The SDSS data are good enough to allow that, given that there are ten subspectra over two nights with relatively good $S/N \approx 10$. The data fit a period of 2.207 ± 0.004 h and $K = 109 \pm 5$ km/s (Fig. 50), which implies a minimal companion mass of 0.15 $M_\odot$ and a merging time shorter than 1 Gyr. For SDSS J095157.78+290341.5, the S/N of the subspectra is much lower and we could not determine an orbit.

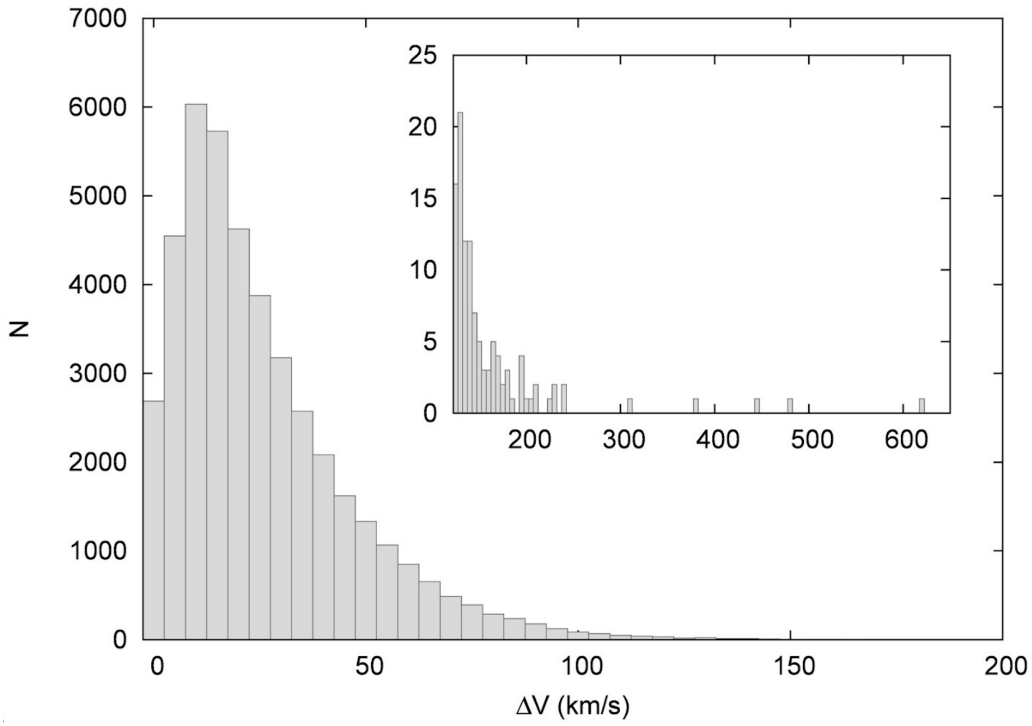

Figure 47 – Histogram showing the obtained amplitude for all analysed SDSS spectra. Most show no significant amplitude, but over 300 indicate an amplitude between subspectra larger than 100 km/s, 14 larger than 200 km/s.

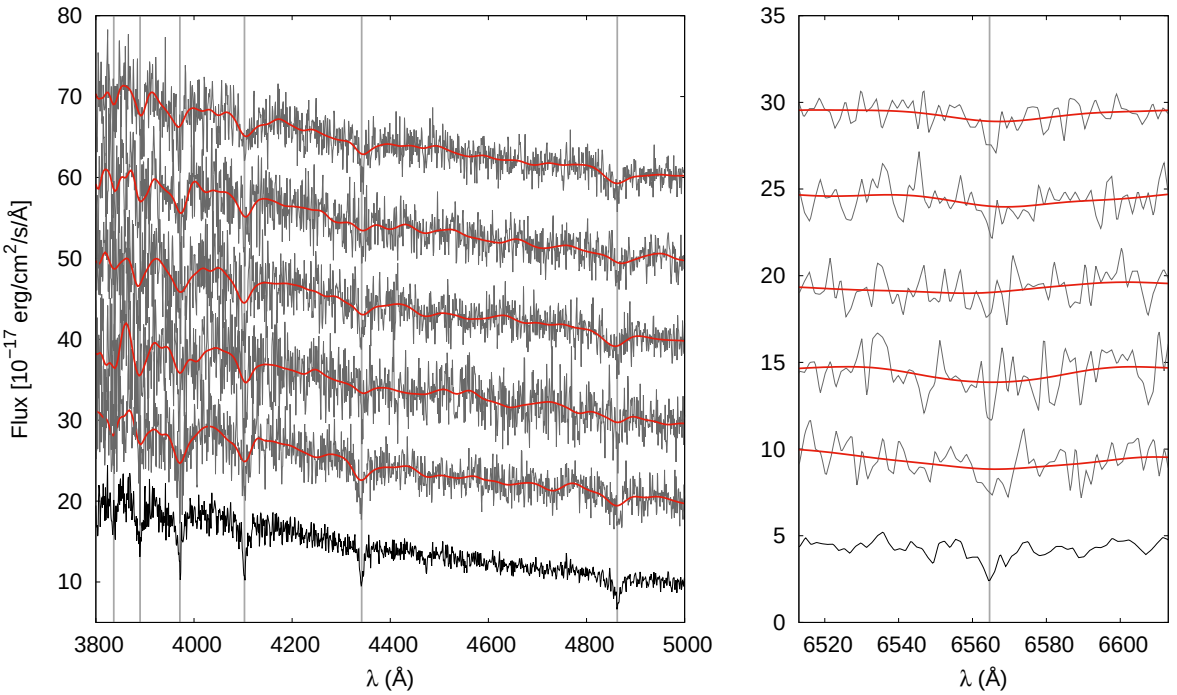

Figure 48 – The black lines show the composite spectra for SDSS J095157.78+290341.5. The grey lines show the subspectra, dislocated to facilitate visualization. The red overplotted lines are smoothed spectra. The vertical grey lines are the rest position of the hydrogen Balmer lines.

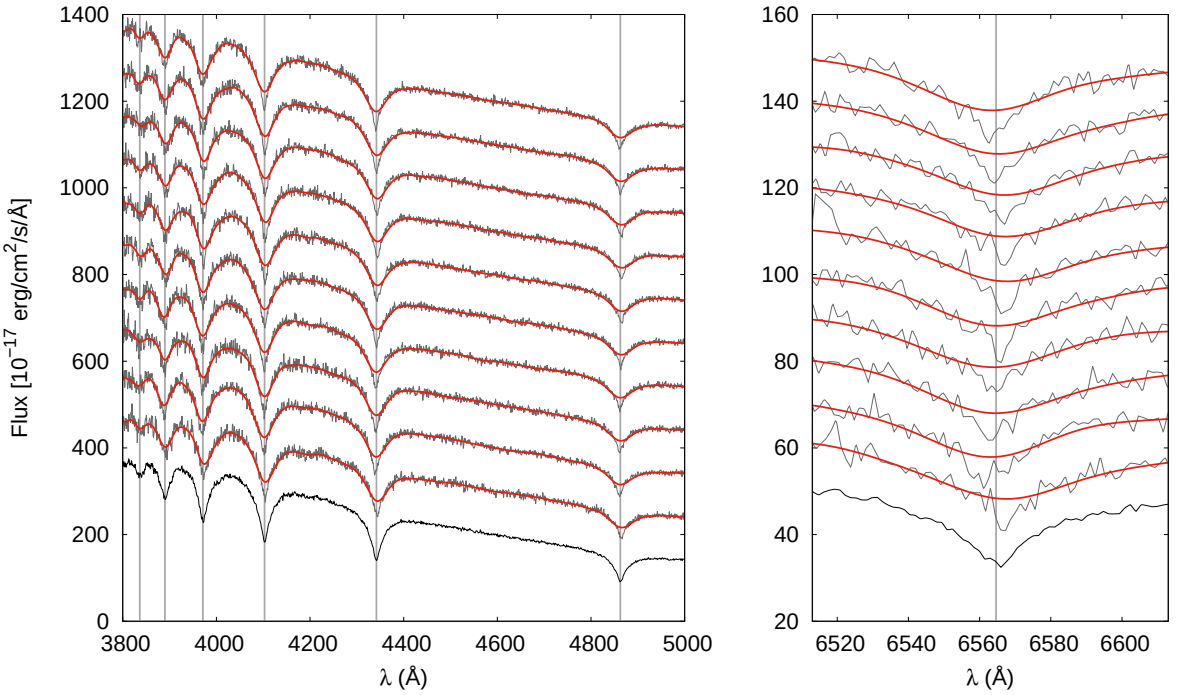

Figure 49 – Same as Fig. 48, but for SDSS J132232.12+641545.8.

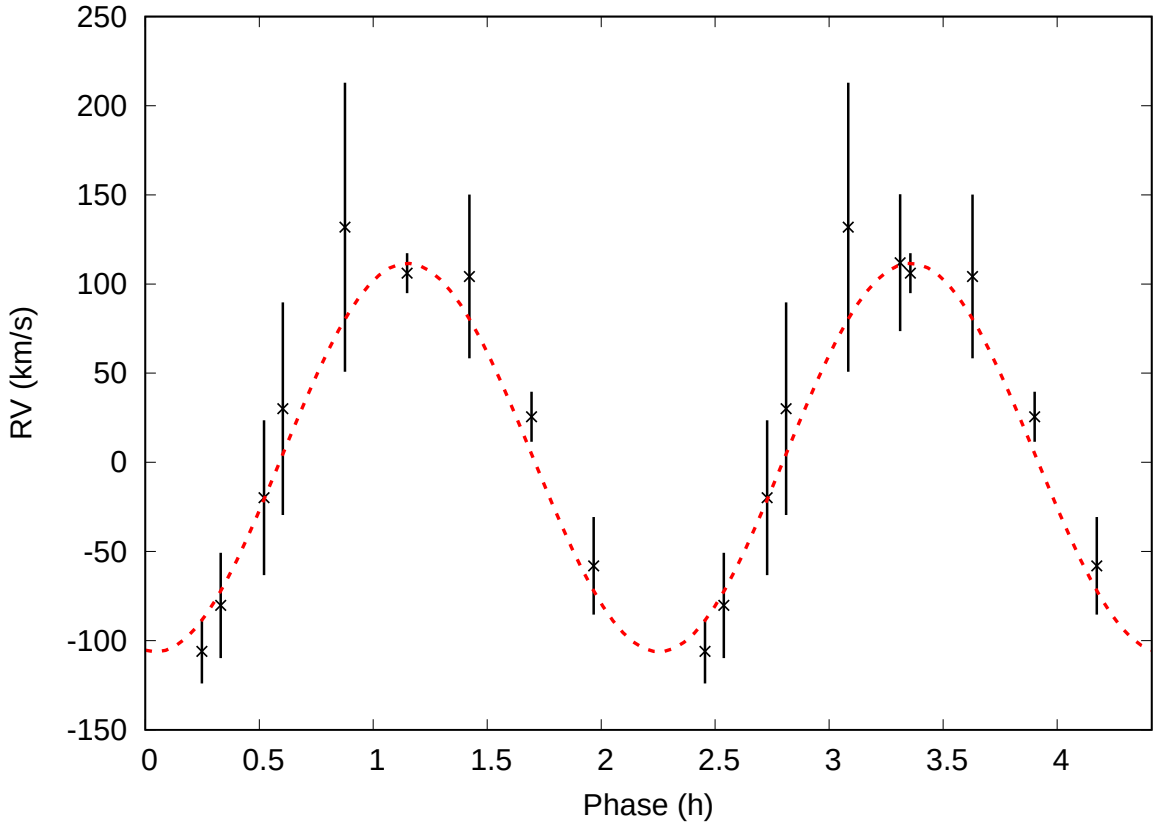

Figure 50 – The orbital solution obtained for SDSS J132232.12+641545.8 using the velocities obtained from SDSS subspectra.

The remaining six spectra showing $\Delta V > 200$ km/s belong to five objects. The spectra are shown in Fig. 51. Their atmospheric parameters are shown in Table 9, for both solar abundance models and pure-hydrogen atmosphere models. Using the radial velocities estimated from the SDSS spectra of these objects, I attempted to obtain their orbital parameters. The best fit results are shown in Table 10. The best orbital solutions are shown in Fig. 52. SDSS J104826.86-000056.7 has nineteen subspectra, which were enough to constrain the period and obtain a good orbital solution. SDSS J120616.93+115936.2 has only seven subspectra, but its light curve on CRTS shows variability with a period which was consistent with the highest peak on the Fourier transform of the velocities. The phase-folded light curve is shown in Fig. 53. SDSS J045947.40-040035.2 has ten subspectra, but the spacing is such that many aliases arise in the Fourier transform, and in fact periods ranging from 10 h to 60 h had orbital solutions with similar residuals; follow-up is needed to study the nature of this object. SDSS J171906.23+254142.3 has five subspectra, but less aliasing than SDSS J045947.40-040035.2, suggesting a period between 8 h and 14 h. We were not able to find a good solution for SDSS J122911.49-003814.4, which has six subspectra; follow-up was obtained with SOAR and is described in Section 4.2.8.

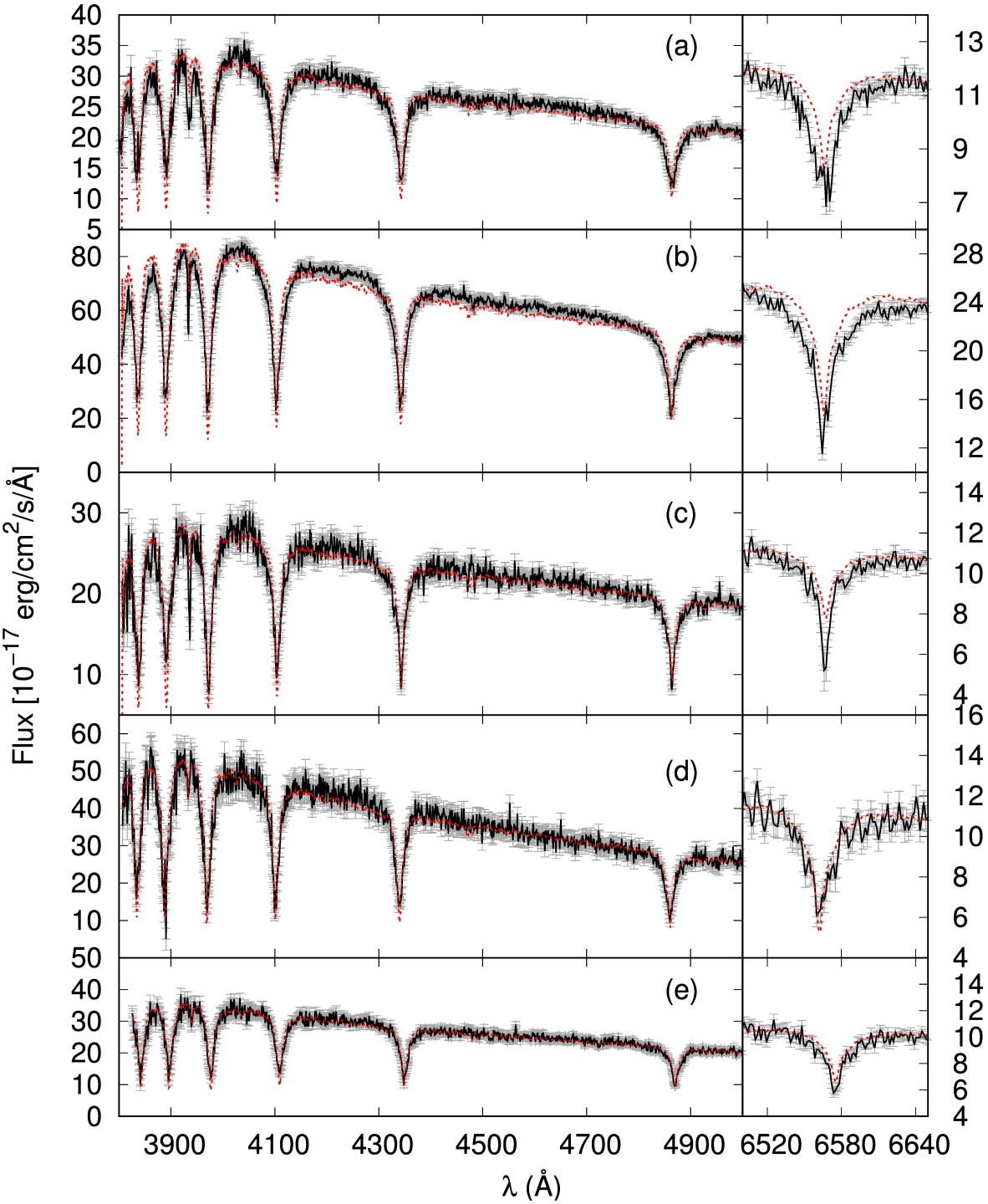

Figure 51 – Spectra for the five objects showing $\Delta V > 200$ km/s (solid black line). The SDSS template is shown as a dashed red line for comparison. For the object with two spectra, the highest S/N spectrum is shown.

Table 9 – Solar abundances and pure-hydrogen atmosphere spectral parameters for the objects shown in in Figs. 51 and 52. Quoted uncertainties in our values of $T_{\rm eff}$ and log g for solar abundances are formal fit errors. The external uncertainties in the models are much larger, of about 5% in $T_{\rm eff}$ and 0.25 dex in log g.

	SDSS J	g	$T_{\rm eff}$	log g	$T_{\rm eff}$	log g
			Solar		Pure-H	
(a)	104826.86-000056.7	18.39	8 508(17)	5.861(0.068)	8571	6.269
(b)	120616.93+115936.2	17.37	8 869(12)	5.092(0.050)	8861	5.308
(c)	045947.40-040035.2	19.62	8 182(21)	4.804(0.113)	8153	4.815
(d)	171906.23+254142.3	19.13	8 566(41)	4.126(0.128)	11288	4.500
(e)	122911.49-003814.4	18.27	8 020(22)	4.657(0.128)	8083	5.339

Table 10 – Orbital parameters obtained for the objects shown in Figs. 51 and 52, assuming the best solution. Some objects might need follow-up (see text for discussion). The secondary mass M_2 is the minimal mass assuming an edge-on orbit.

	SDSS J	P (h)	K (km/s)	R^2	M_2 ($M_\odot$)	$\mathcal{T}_{\rm merge}$ (Gyr)
(a)	104826.86-000056.7	2.9	246	0.88	0.32	2.7
(b)	120616.93+115936.2	6.4	220	1.00	0.50	16
(c)	045947.40-040035.2	61	53	0.82	0.18	11280
(d)	171906.23+254142.3	13	197	1.00	0.75	69

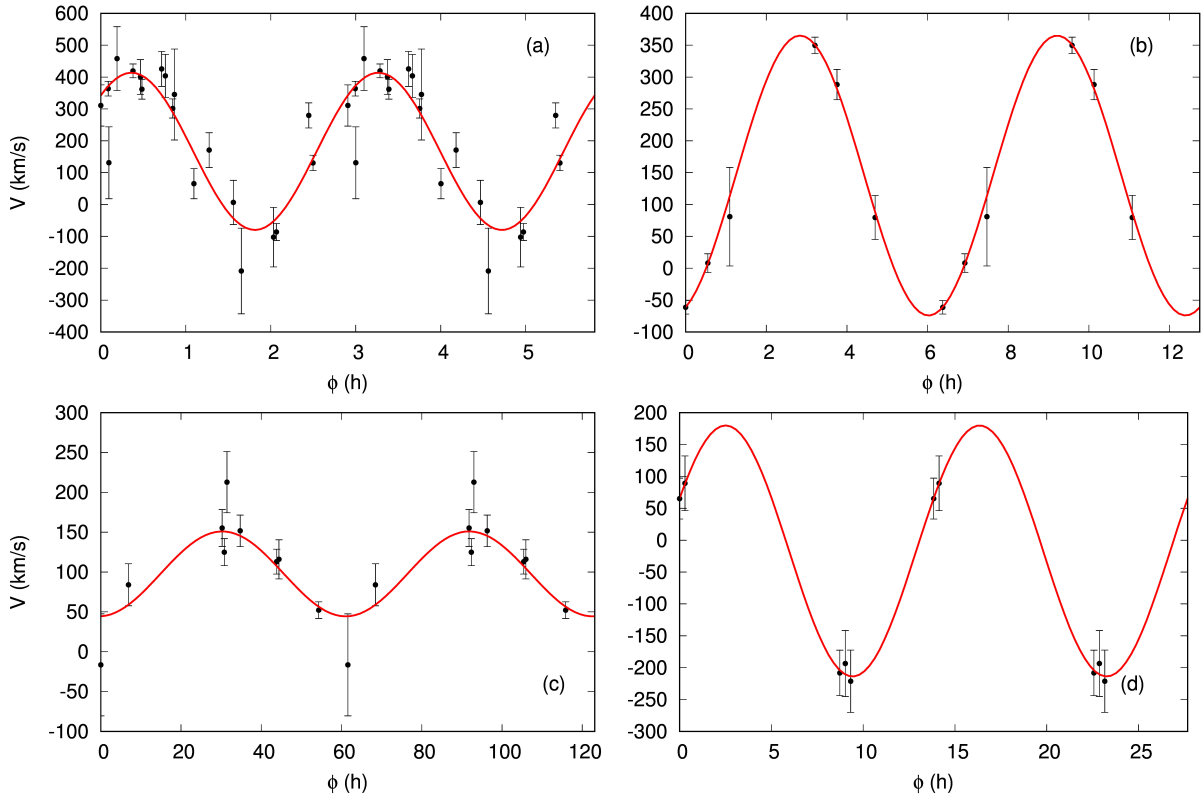

Figure 52 – Best orbital solutions for the four objects for which we were able to constrain the period.

Out of these five objects, we concluded that SDSS J104826.86-000056.7 and SDSS J120616.93+115936.2 are unarguably new ELMs, given that both their atmospheric and orbital parameters are consistent with the class. The three remaining objects show the solar abundance $\log g < 5.0$. SDSS J122911.49-003814.4, however, has $\log g > 5.0$ when the pure-hydrogen models are used. Its spectrum does not show strong metal lines, hence it is a good ELM candidate and follow-up was obtained. SDSS J171906.23+254142.3 still shows $\log g < 5.0$ with the pure-hydrogen models, but the obtained radial velocity amplitude (197 km/s) can only be explained if the object is in a close binary, requiring it to be compact, therefore it is most likely an ELM. The most uncertain object is SDSS J045947.40-040035.2, which has $\log g$ in the threshold between main sequence and ELM assuming both models. The estimated distance assuming a main sequence radius is 16 kpc, and its velocities are consistent with the halo. The obtained period and amplitude are also consistent with a main sequence object. Given all that, SDSS J045947.40-040035.2 is probably a blue straggler star in the halo.

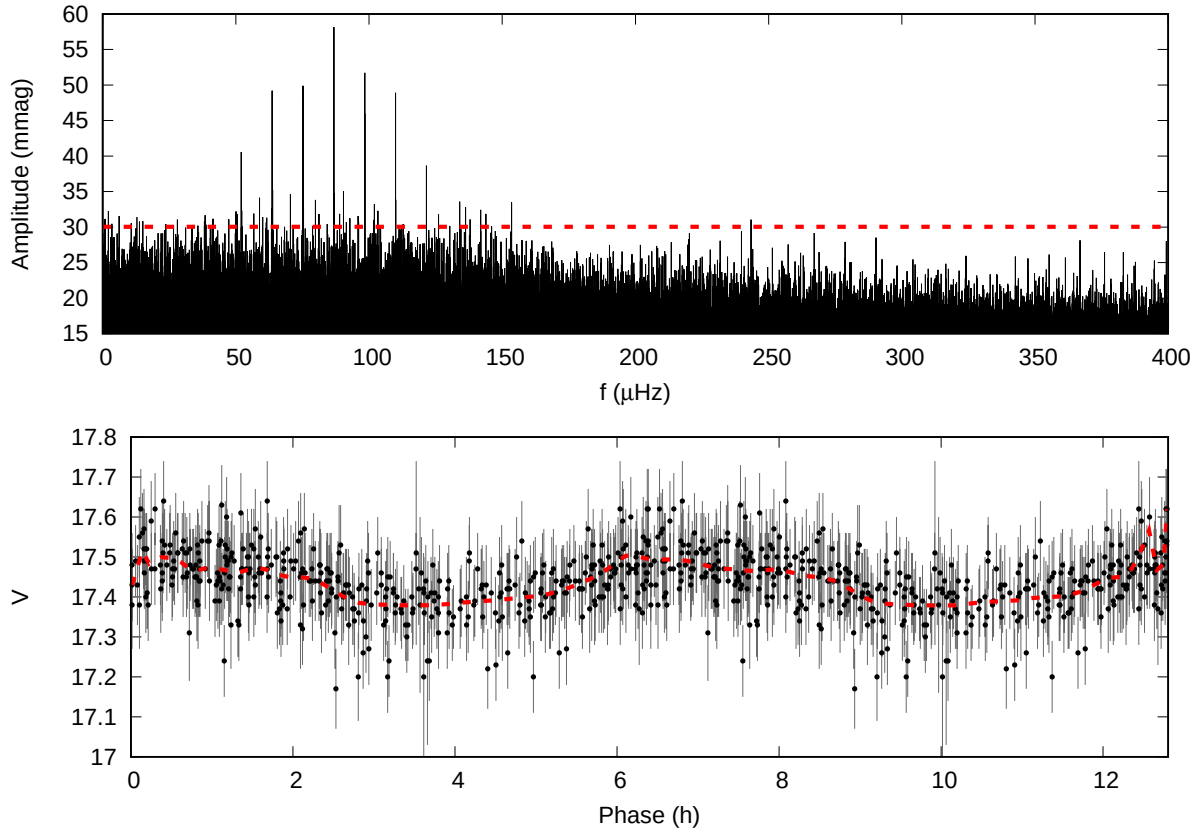

Figure 53 – Top panel shows the Fourier transform for CRTS light curve of SDSS J120616.93+115936.2. The dashed lines shows the detection limit of 4 $\langle A \rangle$. For binary stars, the main peak corresponds to half the orbital period, here of 3.2 h (86 μHz) . Bottom panel shows the light curve phase-folded to the 6.4 h orbital period, which is the same obtained analysing the velocities, suggesting the variability is due to either eclipses or ellipsoidal variation. The dashed line shows the smoothed data.

4.2.7 Light Curves from Public Databases

As described in Section 3, I have searched for time-resolved photometric data for the sdAs in the CRTS database. When I found no data in this database or the data were inconclusive, I have searched also in the PTF and in the LINEAR databases. The CRTS was given priority because it is more easily accessible and has published more reliable photometry. Analysing the light curves folded to the highest amplitude peak in the Fourier transform, I found 59 sdAs with $\log g > 5.0$ to be variable: 29 eclipsing, 8 with a light curve similar to δ Scuti stars, one similar to an RR Lyra, and 21 with variations of unknown type. These objects, as well as their periods, are listed in Table 11.

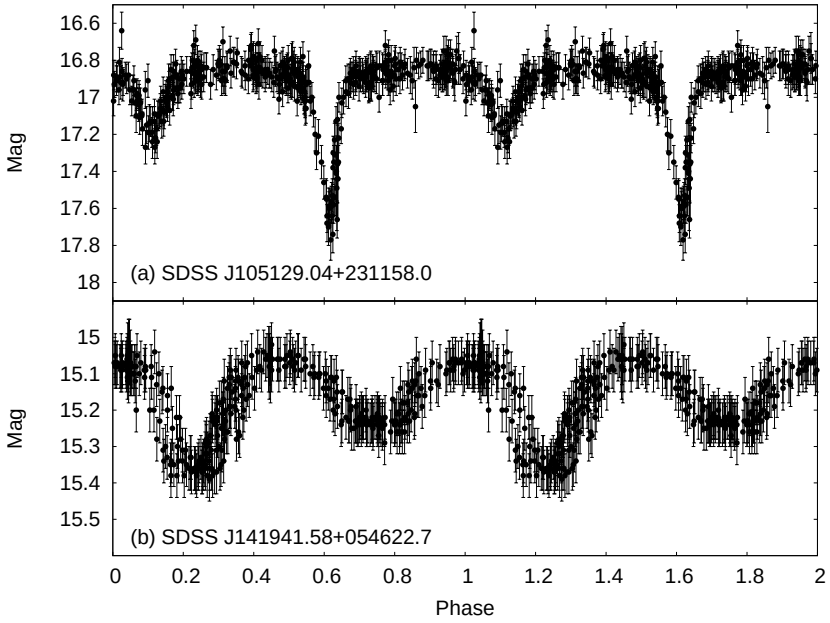

Figure 54 – Phase-folded light curves for two sdAs identified as eclipsing binaries. (a) SDSS J105129.04+231158.0, which has a period of 12.5 h. It was identified by Drake et al. (2014) as an eclipsing binary of Algol type. We have estimated $T_{\rm eff} = 8\,225 \pm 10$ K and $\log\ g = 5.019 \pm 0.044$ for this object. (b) SDSS J141941.58+054622.7, classified as W Uma by Drake et al. (2014). We have estimated a period of about 10 h, $T_{\rm eff} = 8077 \pm 10$ K and $\log\ g = 5.140 \pm 0.040$.

Most objects identified as eclipsing show an orbital period below 36 h, as is empirically expected for ELMs (Brown et al., 2016). Two examples are shown in Fig. 54. However, the median period is of about 18 h, which is significantly larger than the median of 5.4 h obtained for the known ELMs. Their SDSS subspectra do not show significant radial velocity variation (Fig. 55), but have a short baseline of less than 2 h. SDSS J105129.04+231158.0 has a proper motion of 9.1±3.7 mas/yr, which would be considerably small for a compact object, while SDSS J141941.58+054622.7 has a reliable proper motion of 26.4±3.5 mas/y. Moreover, this range of periods is the same for bina-

Table 11 – sdAs found to be photometrically variable in public databases. First column is the object's name, second column its period in days, third column indicates whether it was previously known to vary (1=yes, 0=no), and the last column states the type of variation, followed by a colon when it is uncertain.

Object	Period (days)	Known?	Type
SDSS J170518.49+242412.4	1.2048	0	eclipsing
SDSS J163248.37+282057.6	0.4406	1	eclipsing
SDSS J160755.31+332342.9	0.3572	1	eclipsing
SDSS J152617.92+180638.6	1.4704	1	eclipsing
SDSS J152146.37+164251.4	0.3260	0	eclipsing
SDSS J151823.31+453944.1	0.3510	1	eclipsing
SDSS J145325.53+120225.0	0.6296	1	eclipsing
SDSS J141941.58+054622.7	0.4234	1	eclipsing
SDSS J134639.42+242023.7	10.461	1	eclipsing
SDSS J134438.26+280216.4	0.3504	1	eclipsing
SDSS J134127.41+230705.6	0.3608	1	eclipsing
SDSS J133951.05+051948.3	0.6758	0	eclipsing
SDSS J122354.31+154420.0	0.7984	0	eclipsing
SDSS J121715.08-000928.3	0.9214	0	eclipsing
SDSS J113514.14+353601.3	0.3282	1	eclipsing
SDSS J105129.04+231158.0	0.8938	1	eclipsing
SDSS J104908.36+005744.4	0.9222	1	eclipsing
SDSS J090804.53-000208.7	0.3202	1	eclipsing
SDSS J090709.76+360205.1	0.9190	0	eclipsing
SDSS J090226.53+302022.8	0.8172	0	eclipsing
SDSS J083957.52+122002.5	0.3570	1	eclipsing
SDSS J081800.16+252545.4	0.8514	0	eclipsing
SDSS J081208.51+321418.5	0.7504	1	eclipsing
SDSS J080313.31+415740.4	1.3444	0	eclipsing
SDSS J075017.35+400441.2	1.0614	1	eclipsing
SDSS J073157.82+370437.6	1.1154	0	eclipsing
SDSS J224125.04+132945.5	0.5280	0	eclipsing:
SDSS J073714.47+372719.8	4.2782	0	eclipsing:
SDSS J072744.24+163217.2	0.3116	0	eclipsing:
SDSS J221234.50+224041.7	0.0570	0	δ Sct
SDSS J160814.91+262129.3	0.0511	0	δ Sct
SDSS J160302.63+182807.0	0.0421	0	δ Sct
SDSS J155531.32+400005.7	0.0361	0	δ Sct
SDSS J144929.44+444432.8	0.0508	0	δ Sct
SDSS J124334.25+184131.6	0.0357	0	δ Sct
SDSS J121015.84+324417.6	0.0607	0	δ Sct
SDSS J111701.77-001812.6	0.0562	0	δ Sct
SDSS J130313.61-012222.1	0.2190	1	RRLyr:
SDSS J235706.15+364617.2	0.1838	0	?
SDSS J224222.13+124723.4	0.3027	0	?
SDSS J214300.42+005507.8	0.0454	0	?
SDSS J162638.69+465026.6	0.1627	0	?
SDSS J162353.75+004718.8	0.3423	0	?
SDSS J154200.04-003814.5	0.1185	0	?
SDSS J150323.11-004827.8	0.1423	0	?
SDSS J132042.17+482105.8	0.2726	0	?
SDSS J125940.45+512234.7	0.0295	0	?
SDSS J122505.51+300923.3	0.2045	0	?
SDSS J120802.20+411049.6	0.2968	0	?
SDSS J120616.93+115936.2	0.1334	0	?
SDSS J120509.10+484933.9	0.0664	1	?
SDSS J095345.78+344906.3	0.1967	0	?
SDSS J091653.18+083302.7	0.1605	0	?
SDSS J085653.31+005035.1	0.2808	0	?
SDSS J080841.76+290558.4	0.1999	0	?
SDSS J080830.28+124611.1	0.3954	0	?
SDSS J075149.42+501925.8	0.2396	0	?
SDSS J070604.58+391659.0	-	0	?

ries of the W Ursae Majoris (W UMa) kind, which are cool binary systems in which both components fill their Roche lobes, sharing a common envelope (e.g. Binnendijk, 1970). Eclipsing binaries of the Algol type, which are similar to W Uma but detached, can also show periods in this range. Thus while the period puts most of our variables within the ELM range, we cannot rule out that at least some may be W Uma or Algol binaries of main sequence stars, which are both abundant types of binaries (e.g. Avvakumova; Malkov; Kniazev, 2013). The shape of the light curve could, in principle, constrain the ratio between the stars' radii, but it also depends on the mass ratio q, which can only be determined from the radial velocity variation curves. Hence time-resolved spectroscopy is pending to constrain these eclipsing stars' parameters. Seven of these objects were observed by our collaborator Warren Brown. The results are described in Section 4.2.8.

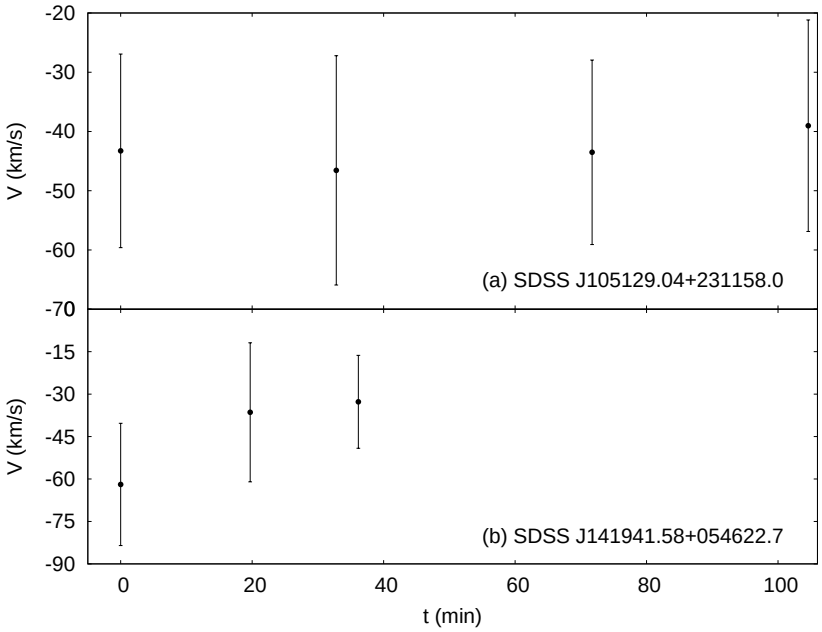

Figure 55 – Radial velocities, estimated from the SDSS subspectra, for the two eclipsing stars shown in Fig. 54, there is no significant variation, what is not surprising considering that the baseline of the observations is much shorter than the period for both stars.

There are eight objects showing light curve and period similar to what is observed for variables like δ Scuti or their low-metallicity counterparts, SX Phoenicis. One example is shown in Fig. 56. These two types of variables are main sequence stars, so the $\log\ g > 5.00$ we estimate is too large for them to be in fact δ Scuti or SX Phoenicis, unless it is overestimated. They could also be pre-ELMs, which also show pulsations (Maxted et al., 2013; Maxted et al., 2014). Moreover, ELMs show g-mode pulsations up to 6000 s, or 1.7 h, which is the same range as these other variables. Therefore we cannot reach conclusions based solely on these periods. Some ELMs are also expected to present p-modes of the order of a few to hundreds of seconds, so further observations focused on finding these

modes could help obtain a more definite classification. Besides that, ELMs are usually in close binaries, so they should also present high radial velocity variations not expected from binaries of main sequence objects, like the δ Scuti or SX Phoenicis, which have longer orbital periods. Follow-up time resolved spectroscopy is needed to test that.

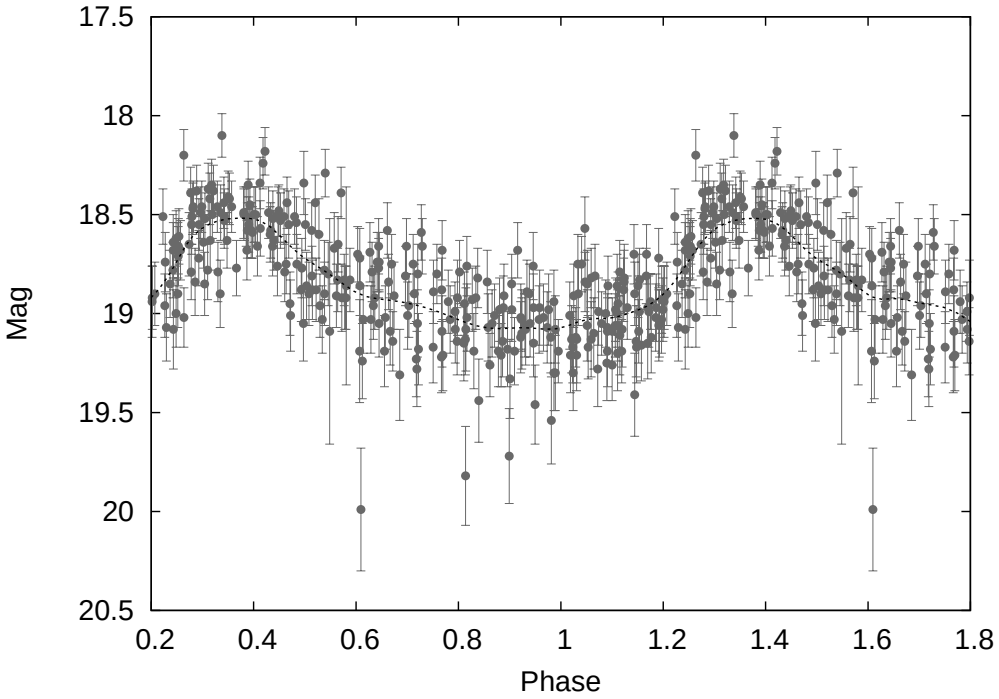

Figure 56 – SDSS J121015.84+324417.6, an sdA showing a δ Scuti-like light curve as plotted above. The dashed black line is a smoothed curve. The light curve is phased to a period of 1.5 h. We have estimated $T_{\rm eff} = 8105 \pm 400$ K and $\log\ g = 5.290 \pm 0.264$, which is too high for a main sequence object like the δ Scuti and the SX Phoenicis, but in the range of known variable ELMs. However, in four SDSS spectra no significant radial velocity variation appears, the dispersion around the average of 30 km/s being of about 0.8 σ. The proper motion is also not significant, estimated in 5 mas/yr but with uncertainty larger than 80%.

One object in our sample, whose phase-folded light curve is shown in Fig. 57, was previously classified as an RR Lyra variable by Vivas et al. (2004) and Drake et al. (2014). Normal RR Lyrae are in the horizontal branch, therefore they have already evolved off the main sequence and should show an even lower $\log\ g$ than main sequence stars due to the expansion of the external layers. However, RR Lyra-type pulsations were already observed on a pre-ELM with 0.26 $M_{\odot}$, as reported in Pietrzyński et al. (2012b). In this case, mass exchange led to the current situation, where the object is in a very short-lived phase (as the CNO flashes shown in Fig. 2) and the physical properties of the pulsator happen to place it in the same instability strip as the RR Lyrae stars. They estimate that 0.2% of RR Lyrae stars may be similar to this one, hence it would not be too surprising if we have found another example considering that thousands of RR Lyrae are known. The

binarity of this object needs to be studied in order to confirm that.

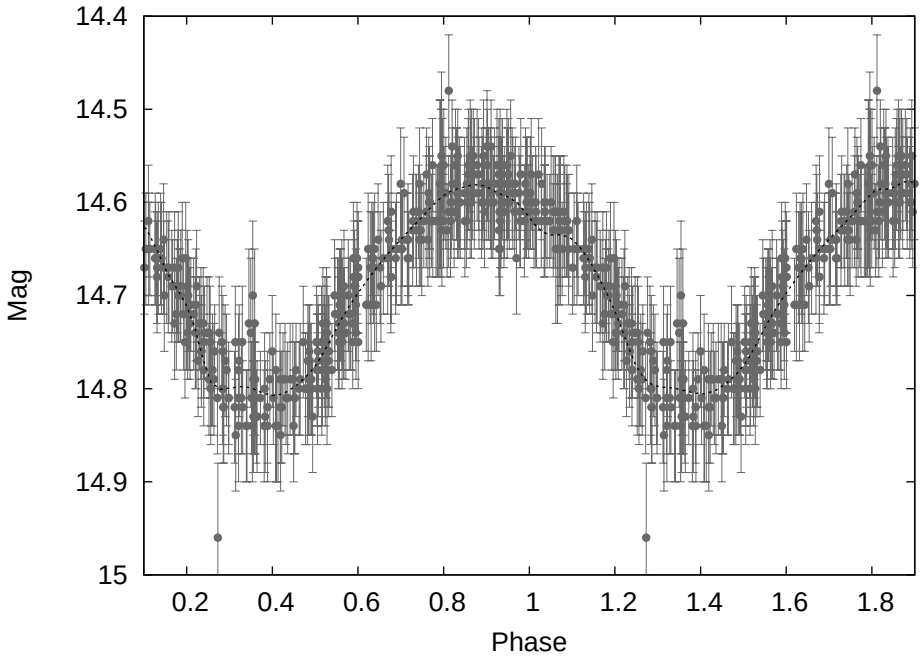

Figure 57 – The light curve of a known RR Lyra, SDSS J130313.61-012222.1, folded to the 5.25 h period. An smoothed curve is shown as a dashed black line. We have estimated $T_{\rm eff} = 8119 \pm 400$ K and log $g = 5.016 \pm 0.250$, which imply the object is not a common RR Lyra, but might be a result of binary evolution such as the pre-ELM found by Pietrzyński et al. (2012b). The SDSS subspectra cover about 1 h, showing no significant dispersion in radial velocity around the average, only about 0.12σ. Its proper motion is estimated as 10.6±4.1 mas/yr.

Finally, there were some objects whose Fourier transform and light curve suggested variability, but we could not identify the nature of the variation. In some cases, the data were too poor to allow a good determination of the shape of the light curve. In other cases the shape is well defined, but more than one mechanism could lead to it, such as ellipsoidal variations or eclipses between two stars of very similar radii. One example is shown in Fig. 58. There is clear variability, but the shape and period are not characteristic of one class of variable.

The search for variables is not conclusive in telling ELMs from main sequence stars, since they share some period intervals. It is interesting, however, to help selecting good targets for follow-up time resolved spectroscopy. Moreover, as the integration time and the time span of the public surveys do not allow the identification of the p-modes for ELMs, which are usually lower than ∼100 s, we should also obtain high-speed photometry to search for this kind of mode. These two follow-up projects will be discussed in the next Section.

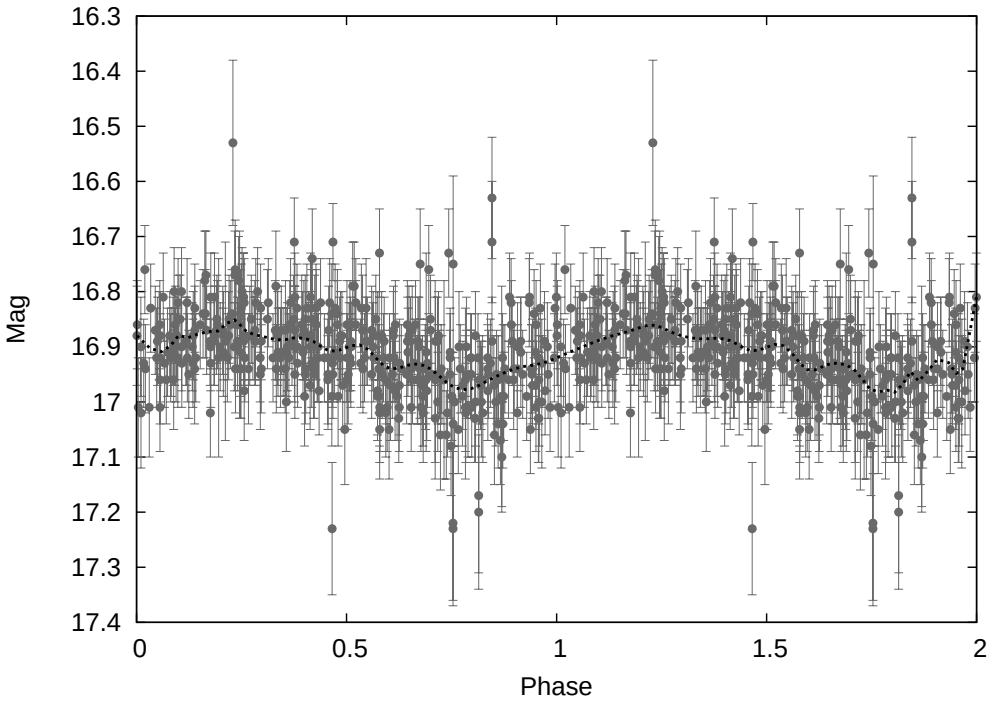

Figure 58 – SDSS J214300.42+005507.8, a variable of unknown type. It has a period of 1.1 h, which is compatible with a g-mode for an ELM. It could also be the result of eclipses or ellipsoidal variations caused by the deformation of the star if there is a close companion, or spots.

4.2.8 Follow-up Observations

We have applied for observation time in five different facilities. We have proposed photometric follow-up to targets brighter than g=18 on the 1.6 m Perkin-Elmer telescope at *Observatório do Pico dos Dias* (OPD) in Brazópolis, Brazil. Twelve nights were awarded to the project in 2016A (OP2016A-005), eleven in 2017A (OP2017A-007), and six in 2017B (OP2017B-004). The targets fainter than g=18 were proposed as photometric targets to the Southern Astrophysical Research (SOAR) 4 m Telescope on Cerro Pachón, Chile. We have been awarded 60 h in 2016A (SO2016A-006), 28 h in 2016B (SO2016B-001), 40 h in 2017A (SO2017A-001) and 8 h in 2017B (SO2017B-002). We have also applied for time-resolved spectroscopy of the targets brighter than g=18 with SOAR. We were awarded 28 h in 2016A (SO2016A-005), 33 h in 2016B (SO2016A-002), 20 h in 2017A (SO2017A-002) and 5 h in 2017B (SO2017B-007). Time-resolved spectroscopy for targets fainter than g=18 was requested at both Gemini North (Mauna Kea, Hawaii) and South (Cerro Pachón, Chile) 8 m telescopes and at the European Southern Observatory (ESO) 8 m Very Large Telescope (VLT). We were awarded a total of 9 h at Gemini North (GN-2016B-Q-54, GN-2017B-Q-72), 43.9 h at Gemini South (GS-2016B-Q-54, GS-2016B-Q-78, GS-2017A-Q-68, GS-2017B-Q-70), and 14 h at ESO's VLT in 2016B (P098.D-0068). Table 12 lists the total number of hours at each facility, as well as the percentage of hours

executed, considering hours lost to bad weather or technical issues.

I found seven objects to show radial velocity variations indicating they are in close binaries. They show p-value smaller than 0.15 for the Shapiro-Wilk test (see Section 3.4.1), implying that the variations cannot be explained by Gaussian noise to a confidence level of 85%. For six objects out of these seven, the p-value is smaller than 0.05, hence the confidence level is 95%. The orbital solution shows R^2 larger than 0.95 for all but one object. $T_{\rm eff}$ and $\log g$ suggest they are new (pre-)ELMs. Their properties are given in Section 4.2.8.1.

For six other objects, the p-value is larger than 0.15, but I obtained an orbital solution with a short period ($P \lesssim 10$ h), expected from (pre-)ELMs in the range of physical parameters for the sdAs (Brown; Kilic; Gianninas, 2017), and $R^2 \gtrsim 0.85$. Two other objects show $p < 0.05$, but their atmospheric parameters are compatible with both a pre-ELM and a main sequence star. More data are required to confirm the nature of these eight objects. Their distance modules or proper motion, and the estimated physical parameters suggest they are probably (pre-)ELMs. I discuss their properties in Section 4.2.8.2.

Table 12 – Follow-up observations approved to further study the sdAs. Numbers in parentheses indicate the percentage executed.

Facility	2016A	2016B	2017A	2017B
OPD	12 nights (50%)	-	11 nights (45%)	6 nights (0%)
SOAR	88 h (94%)	61 h (91%)	60 h (95%)	13 h (100%)
Gemini South	-	17.4 h (100%)	14 h (4%)	12 h (100%)
Gemini North	-	3 h (100%)	-	6 h (100%)
ESO VLT	-	14 h (100%)	-	-

Another six objects have twelve measurements or more (the average necessary to confirm binarity, according to Brown et al., 2016), in at least three different epochs and often multiple telescopes, but the Shapiro-Wilk test suggested no real variation. These objects are possibly single stars, or show either very short ($\lesssim$ 1.0 h) or long periods

($\gtrsim$ 200 days). I also found no RV variation or red companions for the five objects observed with X-shooter in three nights over a week. All these objects are detailed in Section 4.2.8.3. Seven objects identified by me as eclipsing stars were observed for us by our collaborator Warren Brown. They are discussed in Section 4.2.8.4.

In Section 4.2.8.5, I compare the values of $T_{\rm eff}$ and $\log g$ obtained fitting the SDSS spectra and the SOAR or X-shooter spectra for each object. We were unable to obtain a good spectral fit to the Gemini spectra. The Gemini reduction package interpolates between the CCD gaps before performing the flux calibration, and that seems to be affecting the output to a point where our models cannot fit the slope of the continuum. The issue is worse the higher the $\log\ g$, because then the lines are so wide one of them is always spanning a gap. As the position of the line centres are not affected by the flux calibration, the Gemini data can still be used to estimate radial velocities.

In addition, I found seven new pulsators among the sdAs. For other fourteen observed stars, I obtained a detection limit $\lesssim$ 10 mmag and found no pulsations. All known pulsating ELMs show a dominant mode higher than 10 mma (e.g. Hermes et al., 2013). The photometry results are discussed in Section 4.2.8.6.

4.2.8.1 New (pre-)ELMs

J032914.77+003321.8: The thirty RV estimates for J0329+0033 (g = 16.76), taken over seven non-consecutive nights at SOAR, yielded a Shapiro-Wilk p-value of 0.004, suggesting with a very high confidence level that the observed variations are not due to chance. I estimated the period to be 20.1 $\pm$ 0.1 h. The semi-amplitude is not well constrained by the data; I estimated it to be 83 $\pm$ 22 km/s. This results on an orbital fit with $R^2 = 0.78$, shown in Fig. 59, the lowest R^2 among our fits. However, when I assume a main sequence radius, the photometric parallax gives a distance larger than 20 kpc for this object, what is inconsistent with its proper motion of 11.5 ± 2.3 mas yr^{-1}(Tian et al., 2017). The systemic velocity is also relatively high, 153 $\pm$ 18 km/s. Assuming an ELM radius, the distance drops to $\sim$ 200 pc.

Our fit to the SOAR spectrum of J0329+0033 gives $T_{\rm eff}$ = 9 080 $\pm$ 10 K and $\log\ g = 5.18 \pm 0.03$. Interpolating the models of Althaus, Miller Bertolami & Córsico (2013), we obtain $M = 0.1536 \pm 0.0006\ M_{\odot}$. Given this mass and the orbital parameters, the minimal mass of the companion (for an edge-on orbit) is $M_2 = 0.17\ M_{\odot}$, implying a merging time smaller than 765 Gyr.

J073934.37+172225.5: I obtained nine spectra in three nights with SOAR for J0739+1722 (g = 18.07), whose RV variability was already suggested by its SDSS sub-spectra. The RV estimates from the SOAR spectra give $p = 0.1465$. I obtained a period of 6.64 $\pm$ 0.03 h, too short for a main sequence star in the sdA range of parameters

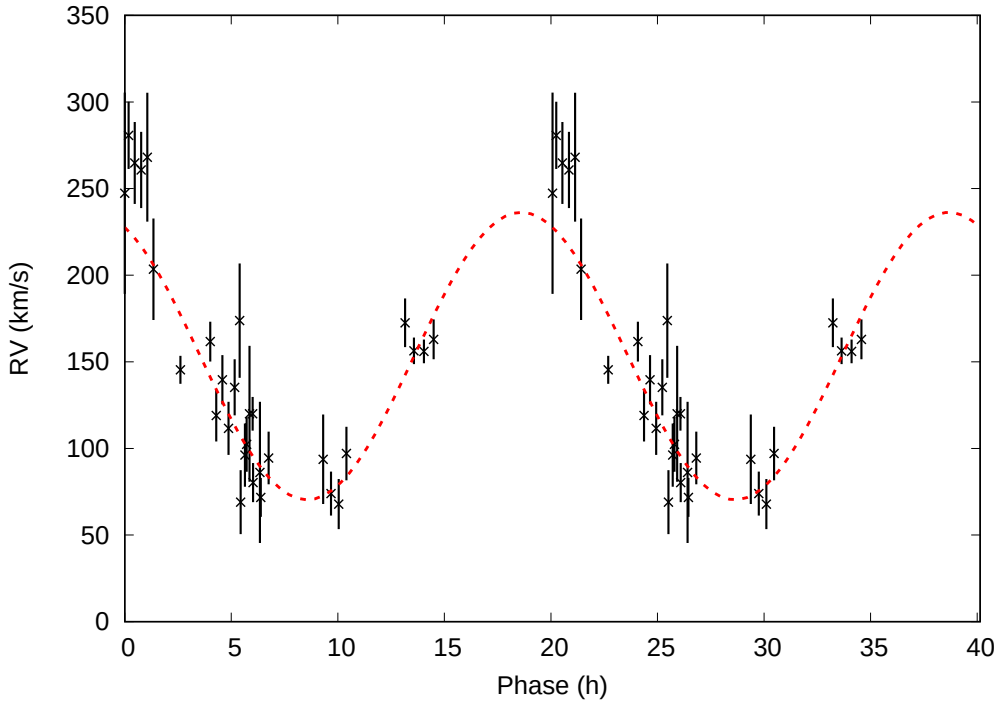

Figure 59 – Orbital solution for SDSS J032914.77+003321.8, phase-folded to the 20.1 h period. Note that in this and also in the next orbital solution plots, two cycles are shown. The semi-amplitude is 83 ± 22 km/s, and the systemic velocity is 153 ± 18 km/s.

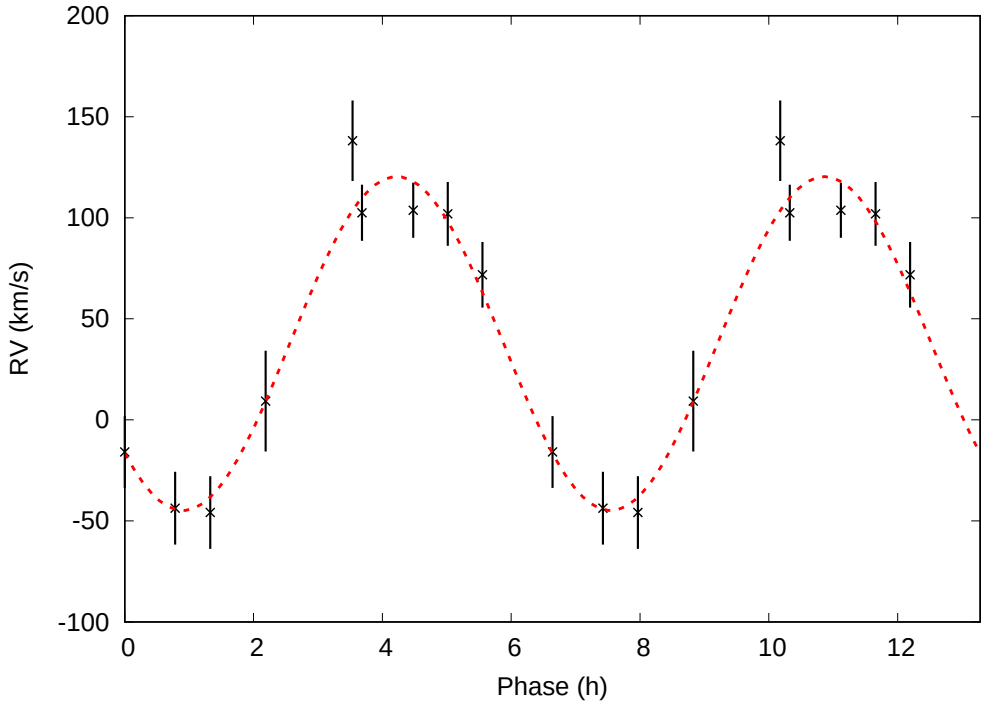

Figure 60 – Our orbital fit for J073934.37+172225.5, given the SOAR RV estimates. We obtained $T = 6.61 \pm 0.01$ h, $K = 82.6 \pm 6.8$ km/s, $RV_0 = 37.8 \pm 3.4$ km/s, and $R^2 = 0.96$.

(Brown; Kilic; Gianninas, 2017), and $K = 82.6 \pm 6.8$ km/s. The orbital solution, shown in Fig 60, has a high $R^2 = 0.96$.

We estimated the mass of the ELM primary to be 0.145 ± 0.001 $M_\odot$, given the $T_{\rm eff} = 7\,550 \pm 12$ K and the log $g = 5.06 \pm 0.05$. The minimum mass of the companion is $M_2 = 0.10$ $M_\odot$, going up to 2.1 $M_\odot$ for a 15° orbital inclination. Given the orbital parameters, the merging time is smaller than 68 Gyr.

J084034.83+045357.6: J0840+0453 ($g = 17.34$) was observed in three nights with SOAR, and I obtained nine spectra. A possible RV variability was first detected in the SDSS subspectra. The Shapiro-Wilk test performed in the SOAR RV data confirmed the variability. The best orbital solution (Fig. 61) gives $R^2 = 0.98$, with a semi-amplitude of 221.6 ± 12.8 km/s and a period of 8.13 ± 0.01 h.

Our fit to the SOAR spectra of J0840+0453 gives $T_{\rm eff} = 7\,890 \pm 32$ K and log $g = 5.07 \pm 0.09$, implying an ELM mass of $M = 0.147 \pm 0.002$ $M_\odot$. The secondary mass is $M_2 > 0.59$ $M_\odot$, hence it is probably a canonical mass white dwarf. The merging time due to gravitational wave radiation is ≤ 28 Gyr.

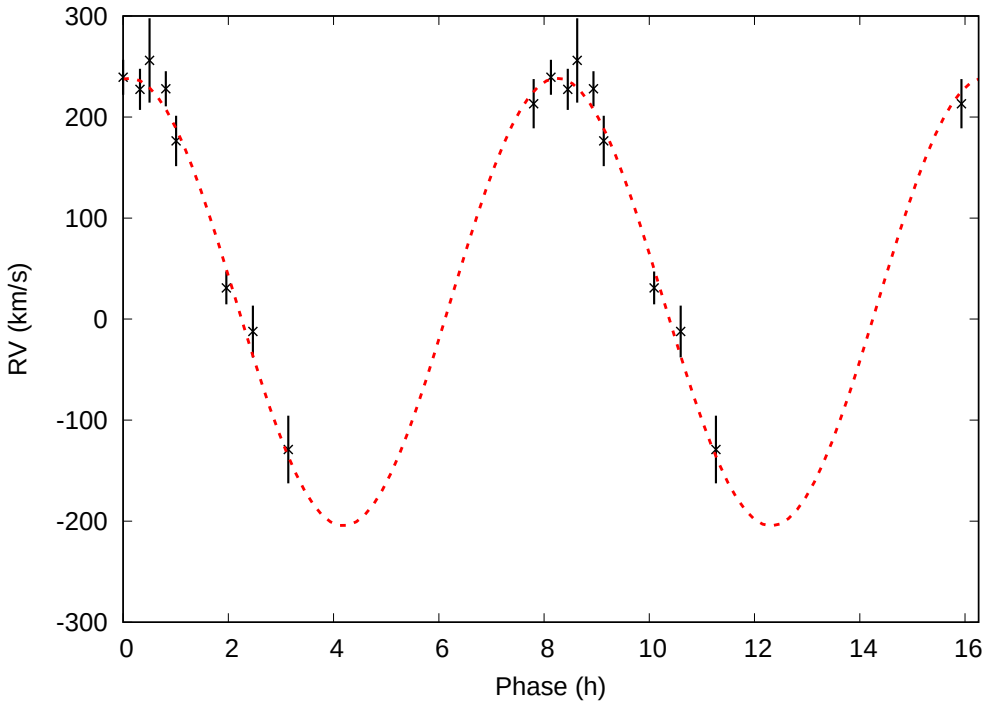

Figure 61 – The orbital solution for J084034.83+045357.6, a 0.147 $M_\odot$ pre-ELM with $T_{\rm eff} \sim 8000$ K. The RV estimates are phase-folded to the 8.13 h period, and show a semi-amplitude of $K = 221.6 \pm 12.8$ km/s and $RV_0 = 17 \pm 13$ km/s.

J134336.44+082639.4: J1343+0826 ($g = 16.34$) was found to be photometrically variable in our observations carried out with OPD (see Fig. 62). I also found it to be most likely ELM given the criteria of Section 4.2.5. I found a photometric period of about one hour, with an amplitude of 26.2 ± 2.3 mmag. This is consistent with the predicted values

of Córsico et al. (2016). Unfortunately, this is the only detected period, and therefore we cannot obtain an asteroseismological fit to this object. Spectroscopic follow-up was obtained over five nights at SOAR; twenty-eight spectra were obtained. The derived velocities give $p = 0.004$, indicating variability with a high confidence level ($> 99\%$). The dominant period was ~ 24 h, a probable alias given that four of the observed nights consisted of two sets of consecutive nights. A similar R^2 (only 0.5% smaller) is obtained with $T = 21.39 \pm 0.01$ h, which is the period I adopted for the orbital solution shown in Fig. 63. The derived semi-amplitude is 136.2 ± 7.0 km/s. The systemic velocity is remarkably high, $RV_0 = 326.0 \pm 7.2$ km/s. If the 24.7 h period is the true one, the amplitude would be 175.5 ± 6.8 km/s, and $RV_0 = 323.0 \pm 3.8$ km/s.

The log g we estimated from its SOAR spectrum is among the highest in our sample (5.97 ± 0.03), and the effective temperature is nonetheless quite low ($T_{\rm eff} = 8120 \pm 10$ K), making it a very interesting addition to the known population of pulsating ELMs. We estimate its mass to be $M = 0.153 \pm 0.001\ M_\odot$, while the companion has $M_2 > 0.43\ M_\odot$. The objects will merge in less than 449 Gyr.

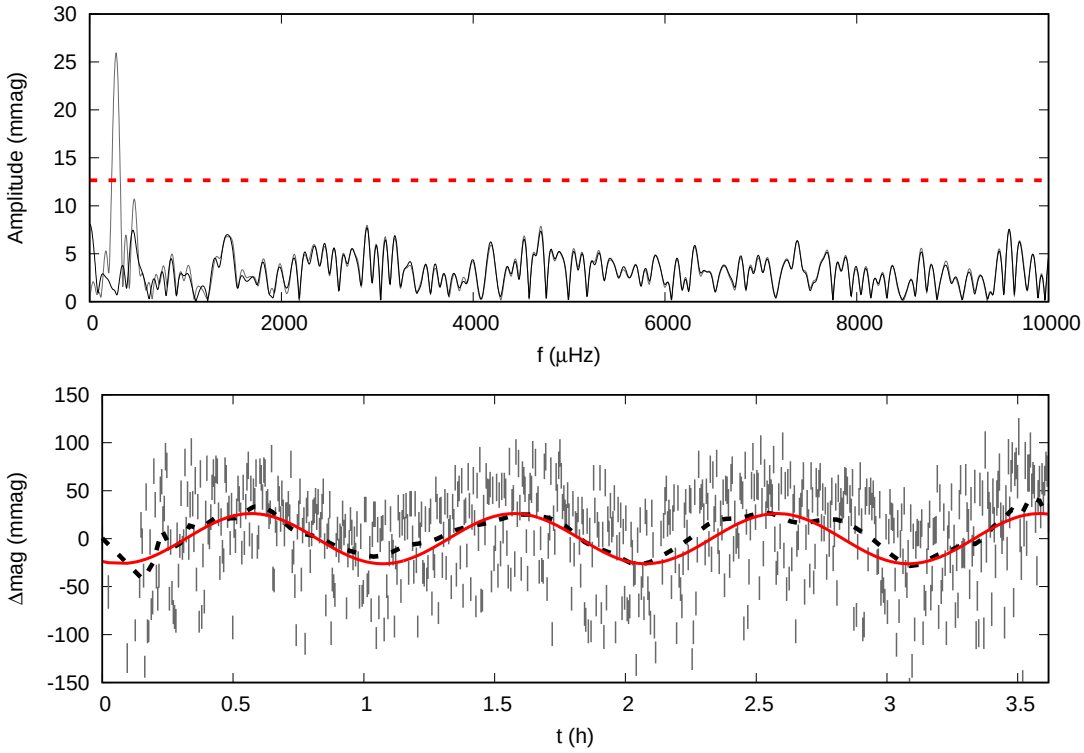

Figure 62 – Fourier transform (top) and light curve for SDSS J134336.44+082639.4, obtained at OPD. The grey line in the top panel shows the original Fourier transform, whereas the black line shows it after the main period was subtracted from the light curve. The red dashed line is the detection limit. There is a lot of spread in the data in the bottom panel due to the variation of the seeing throughout the night. The dashed black line shows the smoothed data. The red line shows the best fit obtained with PERIOD04, with a period of 3618 ± 55 s and amplitude of 26.1 ± 2.4 mmag.

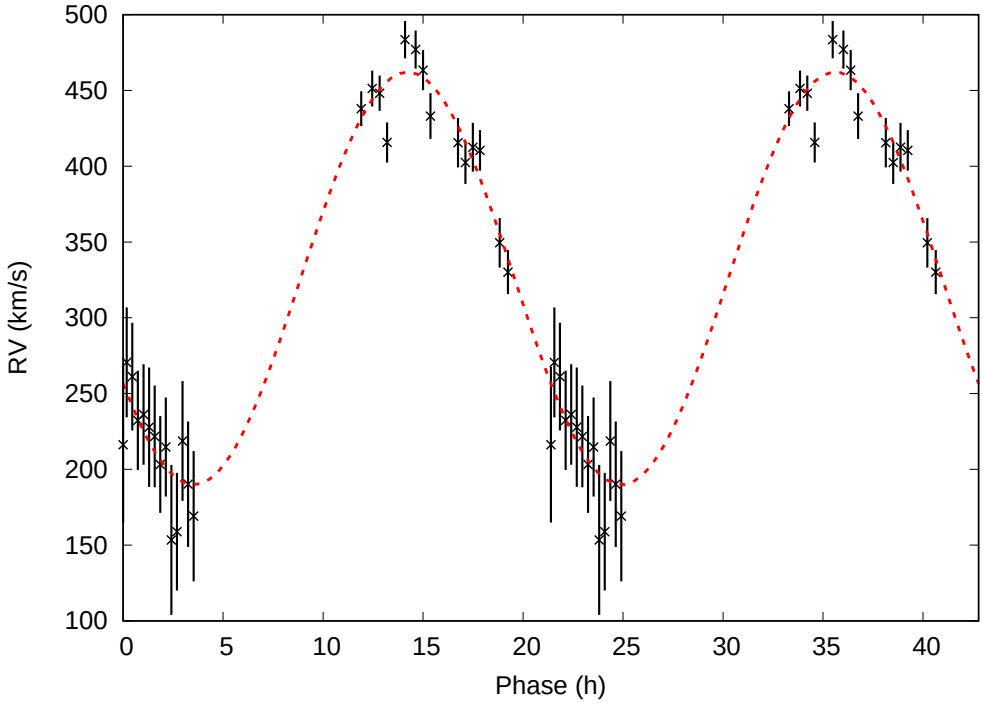

Figure 63 – Orbital solution for the photometric variable star SDSS J134336.44+082639.4, with $T = 21.39 \pm 0.01$ h, $K = 136.2 \pm 7.0$ km/s, $RV_0 = 326.0 \pm 7.2$ km/s, and $R^2 = 0.95$.

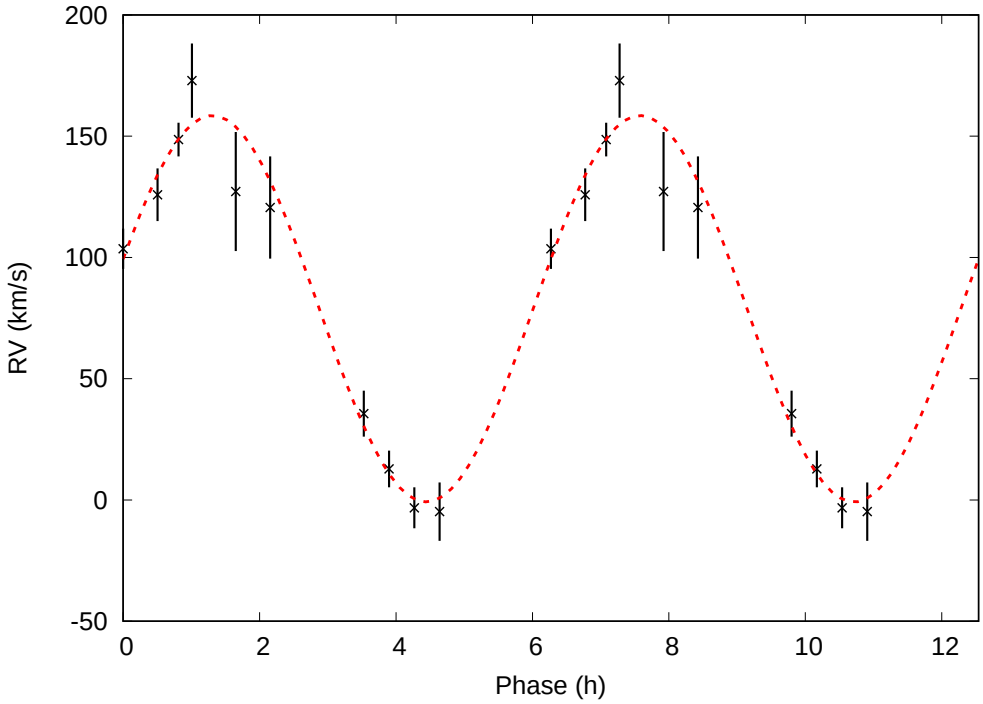

Figure 64 – The orbital solution obtained for SDSS J142421.30-021425.4, whose RV estimates indicated variability at the 85% confidence level.

J142421.30-021425.4: I followed-up on J1424-0214 ($g = 16.93$) given the RV variability suggested by its SDSS subspectra. I observed it in three nights at SOAR, obtaining ten spectra. I obtained a period of 6.3 ± 0.4 h, with a semi-amplitude of 79.7 ± 21.8 km/s. The orbital solution, shown in Fig. 64, has $R^2 = 0.988$.

We derived $T_{\rm eff} = 9\,300 \pm 11$ K and $\log\ g = 5.13 \pm 0.03$ from the SOAR spectrum assuming one tenth of the solar metallicity, obtaining $M = 0.156 \pm 0.001\ M_\odot$ from the evolutionary models of Althaus, Miller Bertolami & Córsico (2013). Slightly smaller atmospheric parameters are obtained from the SDSS spectrum, $T_{\rm eff} = 9\,090 \pm 24$ K and $\log\ g = 4.53 \pm 0.04$, resulting on $M = 0.170 \pm 0.002\ M_\odot$. Given the estimated period and semi-amplitude, and assuming the parameters derived from the SOAR spectrum are correct, the companion has $M_2 > 0.09\ M_\odot$ ($M_2 = 1.8\ M_\odot$ for $q = 15°$) and the objects will merge in less than 57 Gyr.

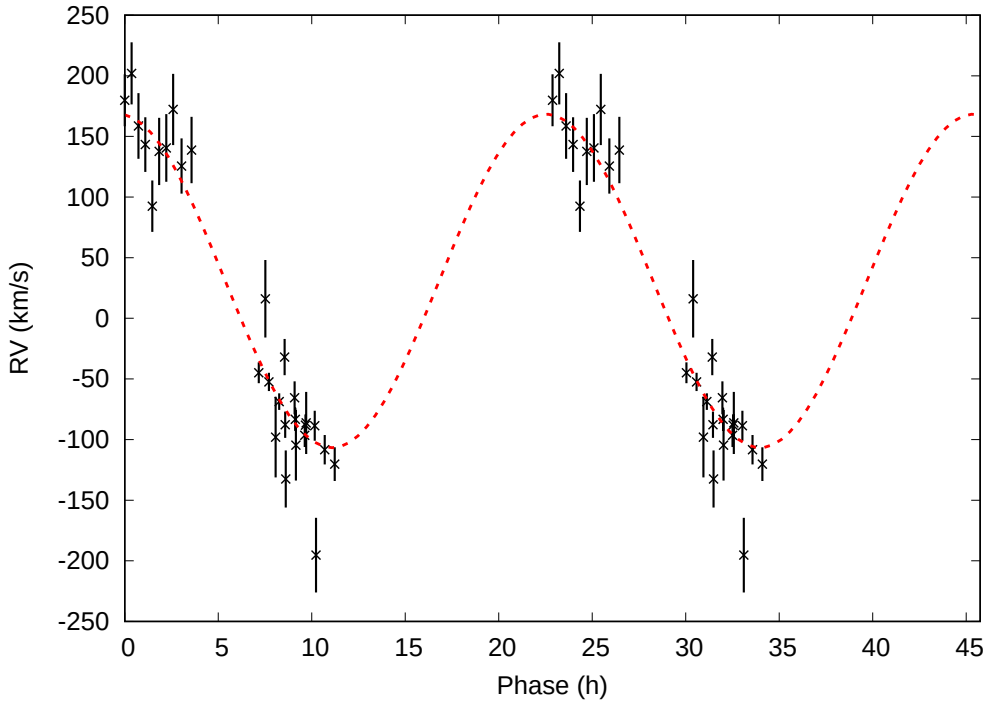

Figure 65 – Estimated RVs and orbital solution for SDSS J205120.67+014554.4, that was observed with both SOAR and Gemini. The orbital fit gives $R^2 = 0.93$.

J205120.67+014554.4: J2051+0145 ($g = 17.27$) would be at a distance of ~ 9 kpc if it had a main sequence radius; however, its proper motion of 9.0 ± 2.4 mas yr^{-1} suggests a smaller distance, compatible with a (pre-)ELM radius. Observing it for five nights at SOAR, and three nights at Gemini South, I obtained twenty-eight spectra. After obtaining a p-value of only 0.002 (variability confidence level $> 99\%$), I estimated the orbital period to be 22.9 ± 0.2 h. The semi-amplitude of the orbital solution is 137 ± 14 km/s, and the systemic velocity is $RV_0 = 31 \pm 14$ km/s. The orbital solution is shown in Fig. 65.

The estimates of $T_{\rm eff}$ and $\log\ g$ using the combined SOAR spectrum, $7\,810 \pm 13$ K

and 5.00 ± 0.05, give $M = 0.148 \pm 0.001\ M_\odot$. The minimal mass of the secondary is $M_2 = 0.45\ M_\odot$, and the merging time due to the emission of gravitational waves is shorter than 533 Gyr.

J092056.09+013114.8 – An eclipsing binary: J0920+0131 ($g = 16.53$) is an eclipsing binary identified independently by Palaversa et al. (2013) and Drake et al. (2014), but whose nature was not further analysed. Using data from CRTS, we estimated the orbital period to be 15.742 ± 0.003 h. The phase-folded light curve is shown in Fig. 66. I obtained thirteen spectra in five nights at SOAR. Fixing the period to the photometric estimate, we obtained an orbital solution with $R^2 = 0.95$ (see Fig. 67) and $K = 76 \pm 11$ km/s.

I fitted the photometry using JKTEBOP (Southworth; Maxted; Smalley, 2004), and obtained an orbital inclination of $82.7 \pm 0.4°$ and $R_2/R_1 = 0.80 \pm 0.03$. Given this inclination, we obtain $M_2/M_1 = 0.894$ from the RV fit. Our spectroscopic fit to the spectrum of the primary gives $T_{\rm eff} = 7\,480 \pm 13$ K and $\log\ g = 4.80 \pm 0.06$, implying $M_1 = 0.149 \pm 0.002\ M_\odot$ and $R_1 = 0.25\ R_\odot$. Therefore the secondary mass seems to be an even lower mass ELM with $M_2 = 0.133 \pm 0.002\ M_\odot$ and $R_2 = 0.20\ R_\odot$. The external uncertainty in the radius, given the 0.25 dex uncertainty in $\log\ g$, is about $0.07\ R_\odot$ (assuming a fixed mass of $0.15\ M_\odot$). Thus the radius of the secondary might be larger, as it would be expected from a lower mass white dwarf given the mass-radius relation. I estimated the secondary to show $T_{\rm eff} \sim 4\,000$ K, given the ratio between fluxes estimated from the light curve.

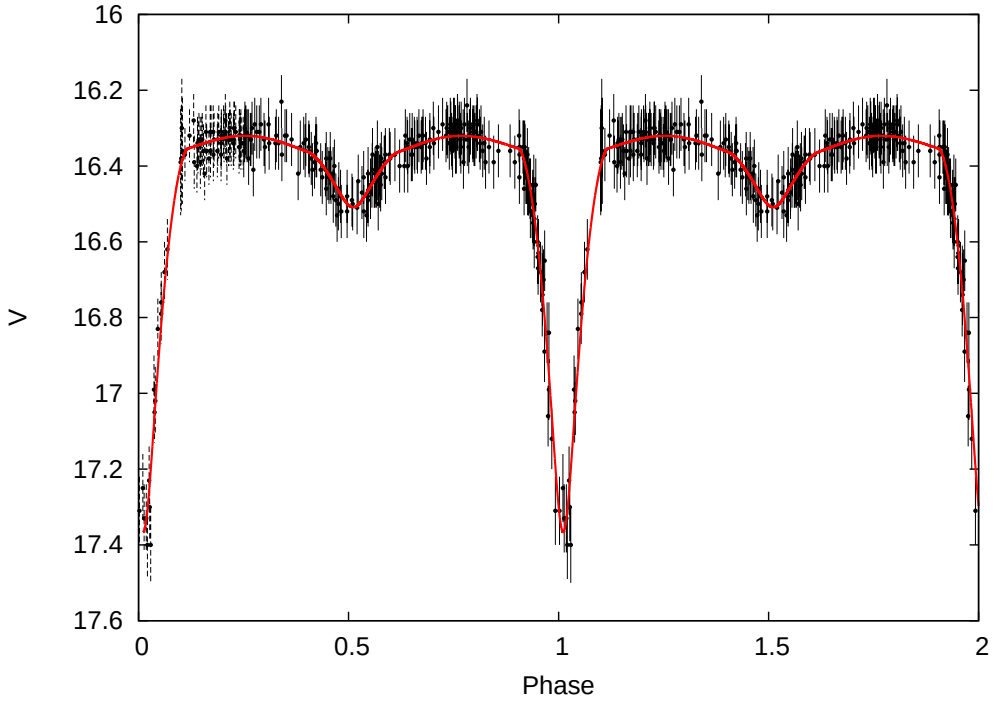

Figure 66 – Light curve of J0920+0131, phase-folded to the 15.7 h period. The best fit to the light curve, calculated with JKTEBOP, is shown as a red line.

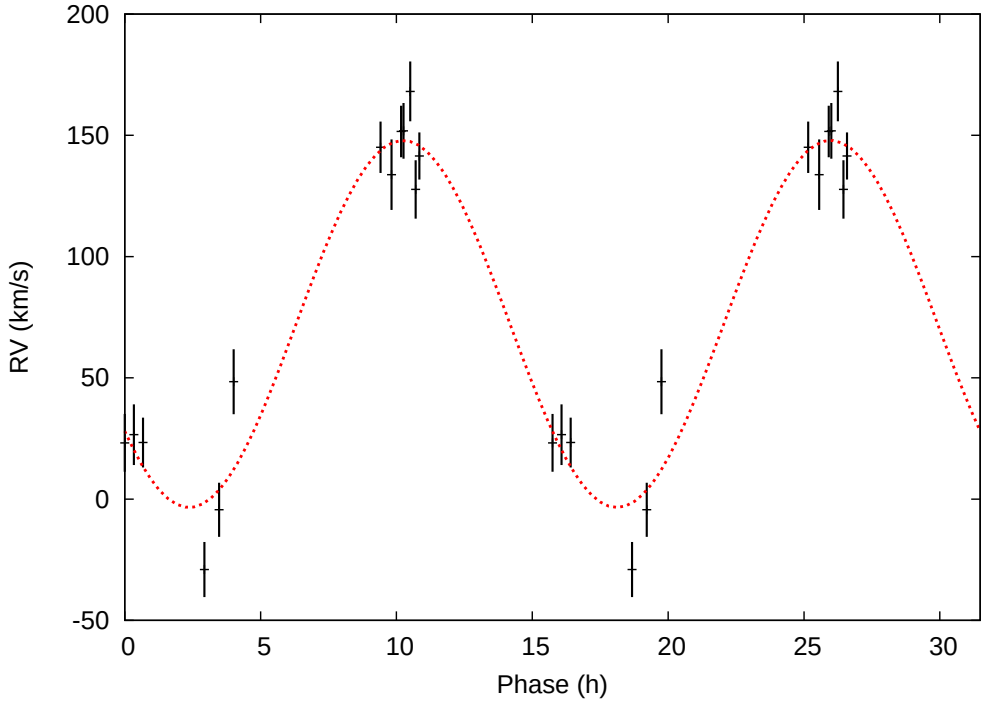

Figure 67 – RV data and the obtained orbital solution for SDSS J092056.09+013114.8. The RV data are phase-folded to the photometric 15.7 h period.

4.2.8.2 Probable (pre-)ELMs

J004227.73-010634.9: J0042-0106 ($g = 18.63$) was followed up because of the $\log g > 5.5$ that we obtained by fitting its SDSS spectrum to solar abundance models. Moreover, assuming the object has a main sequence radius, we obtain a distance of over 15 kpc. It was observed in three nights with Gemini South; two spectra were obtained at each night. Although the observed variations are consistent with Gaussian errors, I obtained an orbital solution with $R^2 = 0.993$ (Fig. 68). The estimated amplitude is 48 km/s, and the period is quite low, of only 91 min. Further observations are required to confirm these findings.

The mass of the primary, given the fit to the SDSS spectrum which resulted on $T_{\rm eff} = 8\,050 \pm 24$ K and $\log\ g = 5.51 \pm 0.08$, is $M = 0.1449 \pm 0.0003\ M_\odot$. Assuming the estimated orbital parameters, we obtained the secondary to show $M_2 > 0.03\ M_\odot$ (for an inclination of 15°, $M_2 = 0.22\ M_\odot$). Given the short period, the system would merge in less than a Hubble time ($\tau_{\rm merge} < 4.2$ Gyr).

J011508.65+005346.1: J0115+0053 ($g = 18.07$) also shows $\log g > 5.5$ in our solar abundance fits to its SDSS spectrum, and $d > 15$ kpc when a main sequence radius is assumed. Moreover, I found it to be more likely ELM in the analysis of Section 4.2.5. Six spectra were obtained on three nights with Gemini. The obtained RVs show real variability only at a 70 per cent confidence level, but I obtained $R^2 = 0.97$ for the best

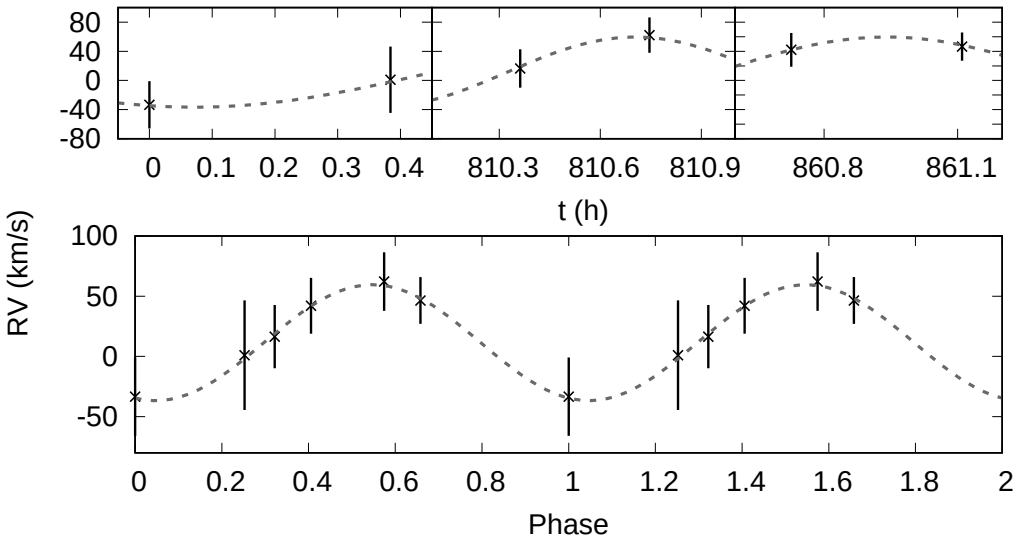

Figure 68 – Top panel shows the estimated RVs in the three observed epochs for SDSS J004227.73-010634.9. The bottom panel shows a tentative orbital solution, with a 91 min period and $R^2 = 0.993$.

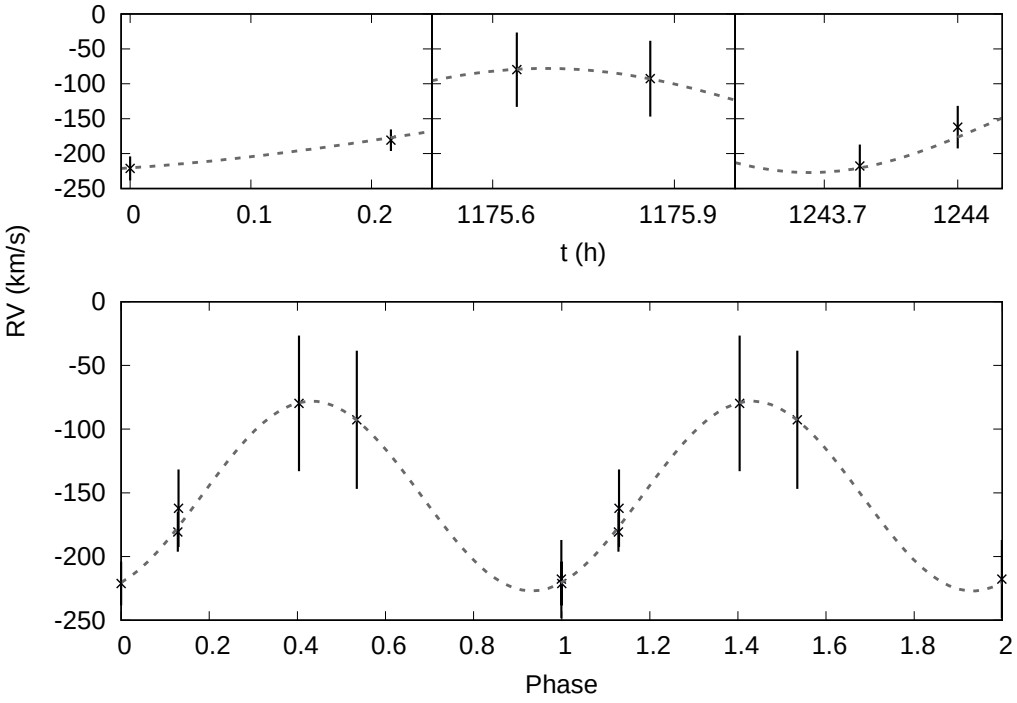

Figure 69 – Estimated RVs for SDSS J011508.65+005346.1 (top), and the best orbital solution (bottom). The average uncertainty was 33 km/s, much larger than our typical values of 10–15 km/s, due to the bias issue at GMOS South.

orbital solution, with $T = 100$ min and $K = 74$ km/s (see Fig. 69). However, all the spectra were affected by the bright columns that appeared at the Gemini South CCD during the end of 2016B, hence the uncertainties in the velocities are larger.

Given the $T_{\rm eff} = 8\,670 \pm 24$ K and the log $g = 5.64 \pm 0.08$, and the hinted RV variability, we propose J0115+0053 is a probable ELM, but we caution that more data are needed to confirm this identification. The evolutionary models give a primary mass of 0.150 ± 0.001 $M_\odot$, and, assuming the tentative orbital parameters, the minimal secondary mass is 0.05 $M_\odot$ ($M_2 = 0.54$ $M_\odot$ for $i = 15°$), and the merging time is shorter than 3.2 Gyr.

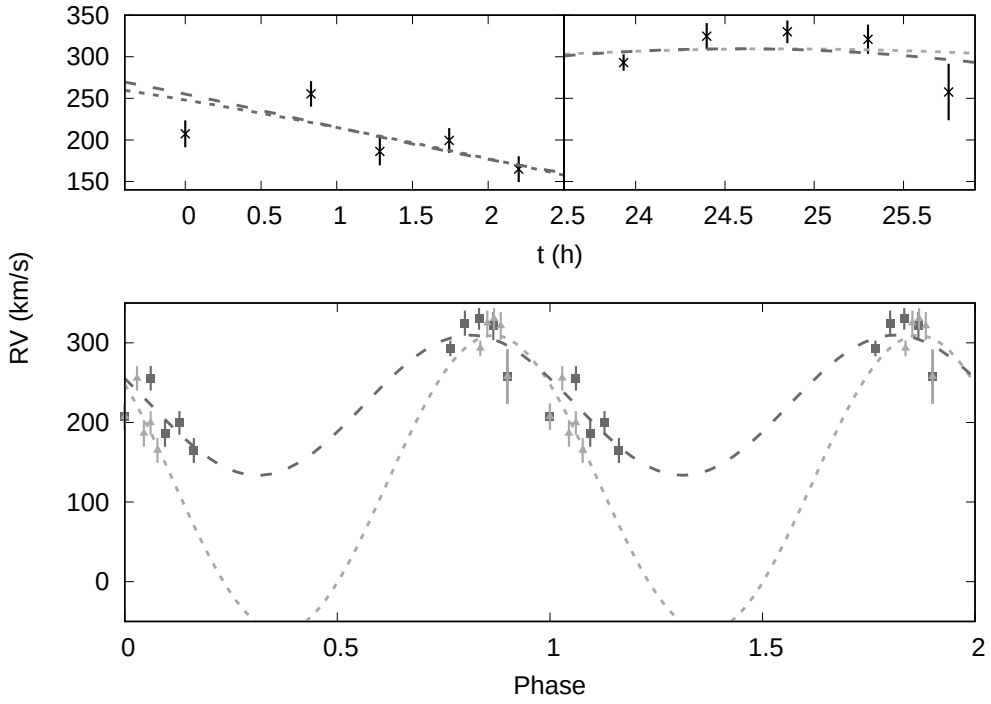

Figure 70 – The top panel shows the estimated RVs for SDSS J030608.92-001338.9 in the two observed nights. Two orbital solutions are shown: short dashed line (light grey) for the 28.1 h period, and the long dashed line (dark grey) for the 13.1 h period. In the bottom panel, the RVs are phased folded to these two periods, following the same colour code.

J030608.92-001338.9: I found J0306-0013 ($g = 16.95$) to be most likely a (pre-)ELM in the analysis of Section 4.2.5. I obtained ten spectra over two nights at SOAR. Fitting the combined spectrum to our new $Z = 0.1$ $Z_\odot$ grid, we obtain $T_{\rm eff} = 7\,770 \pm 10$ K and log $g = 5.36 \pm 0.04$, implying $M = 0.1433 \pm 0.0004$ $M_\odot$. The Shapiro-Wilk test yields $p < 0.3$, suggesting the estimated RVs vary at the 70% confidence level. With only two nights, it is hard to constrain the orbital period. I found two solutions with R^2 differing by less than 2% for $T = 28.6$ h and $T = 13.5$ h, the former with $K = 186$ km/s, and the latter with $K = 88$ km/s. Both solutions are shown in Fig. 70.

For the 28.6 h period, the secondary has a relatively high minimum mass of $\sim$ 1.0 $M_\odot$. For any inclination above 60°, the companion would have to be a neutron star. The merging time for this period is smaller than 546 Gyr. On the other hand, for the 13.5 h period, the minimal mass is $M_2 > 0.15\ M_\odot$, and the merging time is shorter than 320 Gyr.

J045515.00-043231.0: J0455-0432 ($g = 16.49$) was also found to be most likely a (pre-)ELM in Section 4.2.5. Eleven spectra were obtained over two nights at SOAR. The estimated RVs suggest variability at 65% confidence level. I obtained a dominant period of 4.1 h, but with a high uncertainty of 3.8 h. I estimated $K = 60 \pm 24$ km/s. The orbital solution assuming the 4.1 h period, shown in Fig. 71, gives $R^2 = 0.89$.

The SOAR spectrum fits $T_{\rm eff} = 8\,250 \pm 8$ K and $\log\ g = 4.15 \pm 0.03$. These values are consistent with a pre-ELM of $M = 0.180 \pm 0.001\ M_\odot$, in a binary with an object of minimal mass 0.06 $M_\odot$ (0.69 $M_\odot$ for $i = 15°$), which will merge within 25 Gyr.

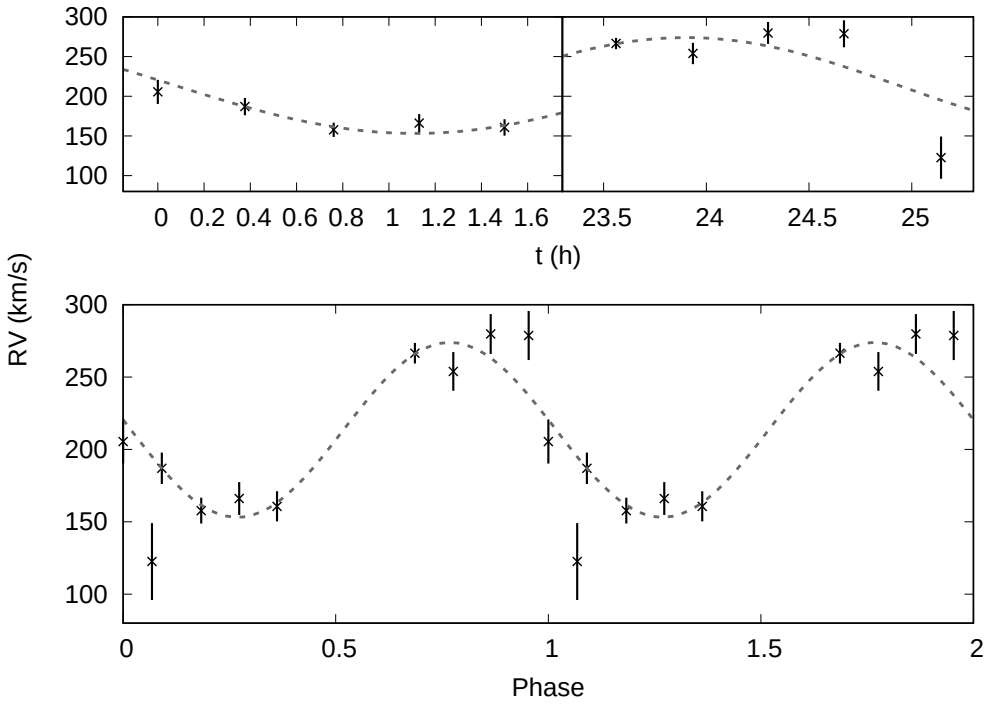

Figure 71 – Obtained RVs for SDSS J045515.00-043231.0 are shown in the top panel. Bottom panel shows the RVs phase-folded to a 4.1 h.

J122911.49-003814.4: The radial velocity we derived for J1229-0038 ($g - 18.27$) from its SDSS spectrum was 472 ± 3 km/s, consistent with the 465 ± 5 km/s given by the SDSS spectral pipeline fit and close to the escape velocity of the Galaxy. Moreover, a main sequence radius would place it at a distance close to 15 kpc, inconsistent with its proper motion of 10.2 ± 1.8 mas yr^{-1} (Tian et al., 2017). Observing it for two nights at SOAR, I obtained five spectra. Although the Shapiro-Wilk test cannot rule out that the variability is due to Gaussian noise, I found an orbital solution with $R^2 = 0.96$, $T = 3$ h,

and $K = 47$ km/s (see Fig. 72). I estimated a very high systemic velocity of 510 km/s, consistent with the SDSS spectrum, suggesting the semi-amplitude might actually be higher. More data are needed to constrain the orbit of this object

The fit to its SOAR spectrum gives $T_{\rm eff} = 8300 \pm 21$ K and $\log\ g = 5.65 \pm 0.06$, implying a mass $M = 0.1476 \pm 0.0009\ M_\odot$ in the models of Althaus, Miller Bertolami & Córsico (2013). Assuming the obtained orbital parameters are correct, the mass of the companion should be higher than $M_2 = 0.04\ M_\odot$, or $M_2 = 0.32\ M_\odot$ for $i = 15°$. The merging time is just above a Hubble time, $\tau_{\rm merge} < 20$ Gyr.

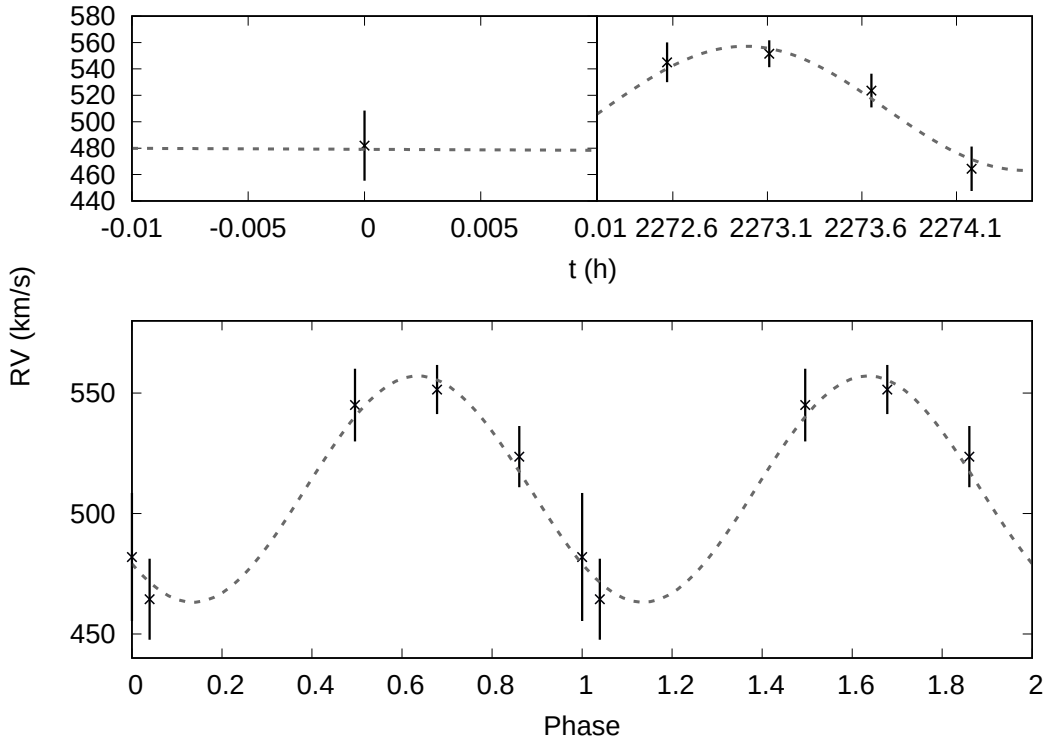

Figure 72 – Radial velocities (top) and best orbital solution (bottom) for SDSS J122911.49-003814.4. The systemic velocity of over 500 km/s might indicate that the semi-amplitude is much higher than the derived 47 km/s.

J233606.13-102551.5: J2336-1025 ($g = 19.34$) would be at a distance larger than 26 kpc if it had a main sequence radius. The GPS1 proper motion is not significant. We obtained $\log g = 5.72 \pm 0.15$, $T_{\rm eff} = 8\,330 \pm 39$ K, and $RV = 12$ km/s from its SDSS spectrum using our solar abundance models. This implies $M = 0.149 \pm 0.003\ M_\odot$ and $R = 0.088 \pm 0.02\ R_\odot$. I followed it up for three nights with Gemini South, obtaining six spectra. The RV estimates hint a period of 2.4 h, even though the variability could also be explained by Gaussian uncertainties. The best orbital solution ($R^2 = 0.92$) gives $K = 131$ km/s and is shown in Fig. 73. With these orbital parameters, I obtained $M_2 > 0.12\ M_\odot$ and $\tau_{\rm merge} < 3.73$ Gyr, shorter than a Hubble time.

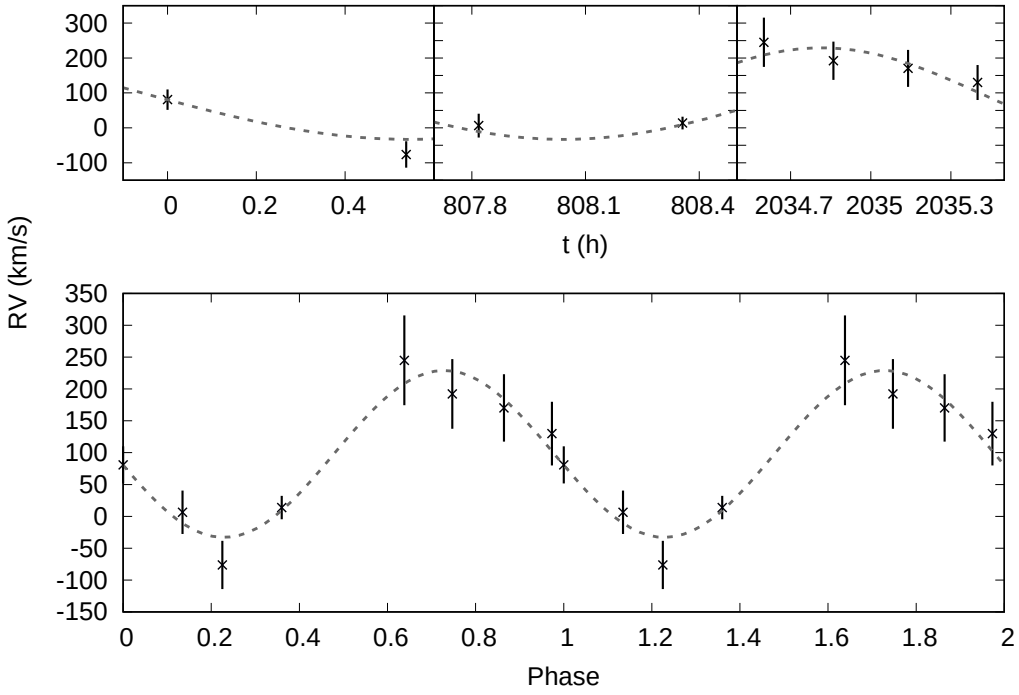

Figure 73 – Radial velocity estimates (top) and the best orbital solution (bottom) for SDSS J233606.13-102551.5.

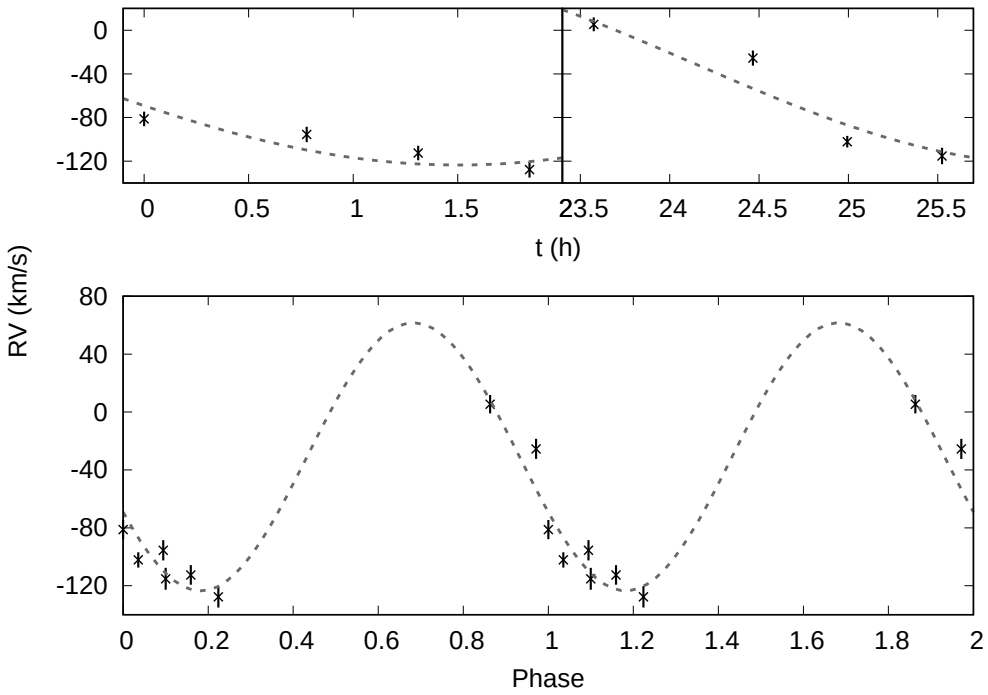

Figure 74 – The estimated RVs for SDSS J162624.91+162201.5 are shown in the top panel, while the bottom panel shows the velocities phase-folded to the 8.2 h period, together with the orbital solution.

J162624.91+162201.5: I obtained with the analysis in Section 4.2.5 that J1626+1622 ($g = 17.04$) was most likely a (pre-)ELM. It was followed-up for two nights at SOAR, when I obtained eight spectra. At a 90% confidence level, the detected RV variability cannot be explained by random uncertainty. I estimated a period of 8.2 ± 0.1 h and $K = 92.6 \pm 19.3$ km/s, obtaining an orbital solution with $R^2 = 0.88$, shown in Fig. 74.

However, J1626+1622 shows a low log $g = 3.83 \pm 0.03$, with $T_{\rm eff} = 7\,460 \pm 15$ K. With these parameters, we could only explain it as a pre-ELM in a CNO flash. The time scale of these flashes ranges from 10^5 to 10^6 years. The estimated physical parameters are consistent with the flashes of a $M = 0.34\ M_\odot$ model. Given the estimated orbital parameters, $M_2 > 0.20\ M_\odot$ and $\tau_{\rm merge} < 32$ Gyr.

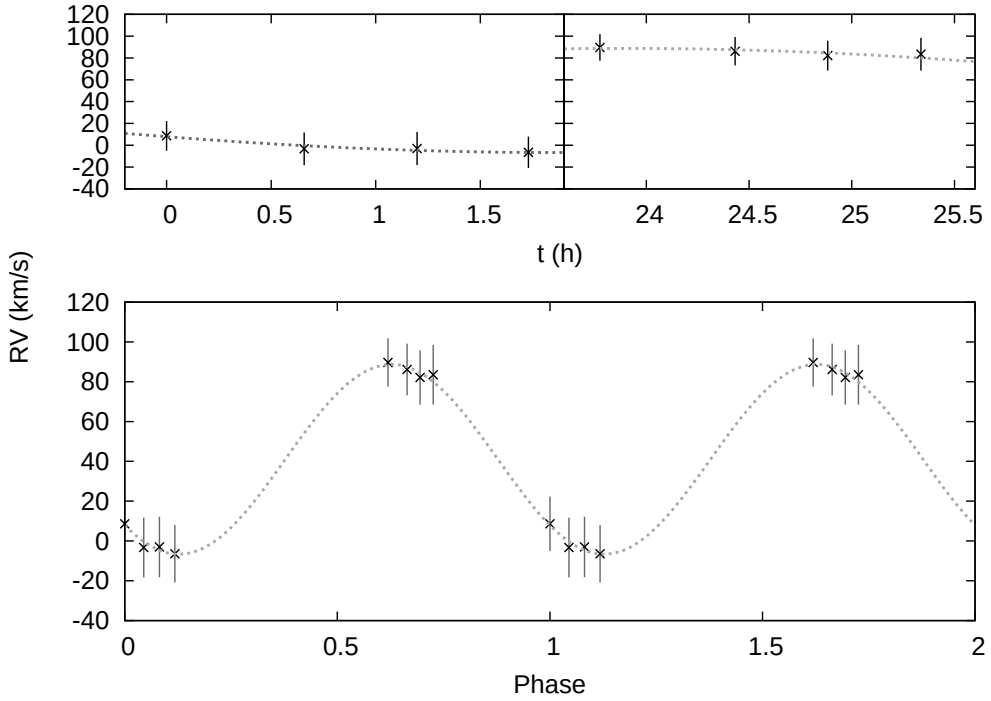

Figure 75 – The orbital solution for the SOAR data of SDSS J090410.00+034332.9, folded to the 14.7 h period (bottom), and the estimated RVs (top).

J090410.00+034332.9: I obtained eight spectra over two nights at SOAR for J0904+0343 ($g = 17.58$), given its RV variability in the SDSS subspectra. The normality test gave $p = 0.006$, confirming the variability. I estimated a period of 14.7 ± 0.3 h, with a low semi-amplitude of 47.7 ± 2.4 km/s, suggesting either a high-orbital inclination, or that the object is a main sequence binary. The orbital solution, shown in Fig. 75 gives $R^2 = 0.997$.

J0904+0343 spectra fits $T_{\rm eff} = 7\,680 \pm 20$ and $log\ g = 4.08 \pm 0.05$, assuming 0.1 $Z_\odot$. This is compatible with a pre-ELM of mass $0.18 \pm 0.05\ M_\odot$ given the models of Althaus, Miller Bertolami & Córsico (2013). However, it could also mean that the object is a binary metal poor F star in the halo. The estimated distance given a main sequence

radius is 9 kpc, and the proper motion is quite low (3.3 ± 3.1 mas yr^{-1}). The low detected semi-amplitude results on a low minimal mass of 0.08 $M_{\odot}$ assuming a pre-ELM primary, given that the orbit would probably not be edge-on. For a 15° inclination, the mass is about 1.05 $M_{\odot}$. The merging time would be up to 590 Gyr.

We will be able to estimate the distance for this star and others with the parallax to be released by Gaia, and therefore the difference between our preferred solution as a pre-ELM and a 9 kpc main sequence star will be clear.

4.2.8.3 No detected variation

Fig. 77 shows the RV estimates for the objects with no statistically significant RV variations, and no good orbital solutions in the probed ranges of periods, described below. We caution that periods as short as 12 min were observed for the known ELMs (Brown et al., 2011), and theoretical models predict periods up to several days (Sun; Arras, 2017).

J222009.74-092709.9 ($g = 15.81$) was found to be a photometric variable in OPD data (see Fig. 76), with periods 3591.244 ± 0.015 s (7.92 ± 0.7 mmag) and 2168.8 ± 0.6 s (3.94 ± 0.7 mmag).

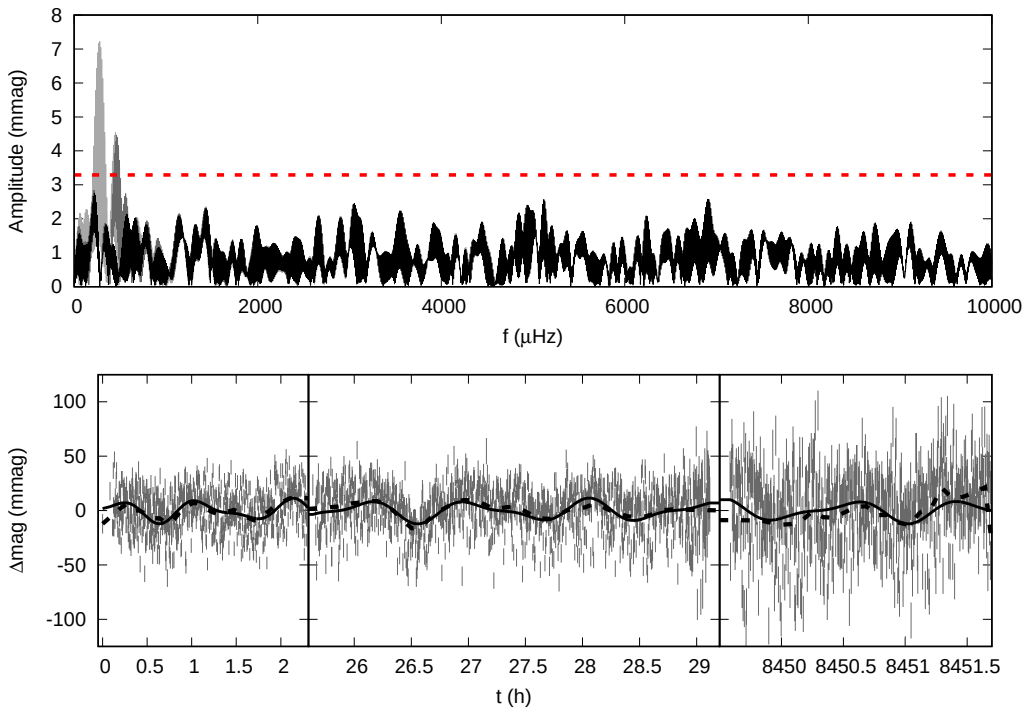

Figure 76 – OPD light curve for 222009.74-092709.9 (three bottom panels). Two periods were found above a detection limit of 4 ⟨A⟩ (red dashed line in the top panel), where ⟨A⟩ is the average amplitude of the Fourier transform. The fit to the light curve given these two periods is shown as continuous line. The dashed line shows the smoothed data.

Despite its reliable proper motion of $\mu = 9.6 \pm 1.6$ mas yr^{-1}, I did not find it to be most likely ELM in the analysis of Section 4.2.5 because of its colours. The spectroscopic follow-up revealed no orbital periods in the range ~ 20 min to ~ 200 days. However, we obtain $\log\ g = 6.10 \pm 0.02$ and $T_{\rm eff} = 8\,230 \pm 6$ K for the SOAR spectra of this object, which not only places it in the region of the known ELMs, but also within the instability strip given by (Tremblay et al., 2015), thus possibly justifying the observed photometric variability. Further monitoring of this object is required to probe shorter and longer orbital periods, as well as further time series photometry to allow an asteroseismological study.

J233403.21+153829.2, J223831.91+125318.3, and J155937.48+113721.9 also have reliable proper motion according to the criteria of outlined in Section 4.2.1 (39.1 ± 1.5, 13.6 ± 1.6, and 7.4 ± 1.8 mas yr^{-1}, respectively), yet they were not found to be most likely ELMs. J1559+1137 ($g = 17.22$) has not been previously studied in the literature. Our estimated physical parameters are close to the main sequence upper limit, $T_{\rm eff} = 11880 \pm 41$ K and $\log\ g = 4.83 \pm 0.01$. The lack of RV variation and periods in the range $\sim 1\ h$ to ~ 40 days suggests it is either an ELM with a period outside of the probed range, or possibly a halo blue straggler star.

J2343+1538 ($g = 16.34$) in particular was suggested to be an extremely-metal poor (EMP) star by Aoki et al. (2013). Their adopted physical parameters based on the SEGUE stellar parameter pipeline (SSPP, Lee et al., 2008), $T_{\rm eff} = 6\,500$ K and $\log\ g = 4.0$, agree within external uncertainties with the parameters we estimate from SOAR spectra, $T_{\rm eff} = 6\,710 \pm 17$ K and $\log\ g = 4.25 \pm 0.05$. No periods were found in the ~ 24 min to ~ 180 day range, thus the EMP explanation seems likely, although at odds with the high proper motion quoted above.

J2238+1253 ($g = 15.55$) was photometrically classified as a horizontal branch star by Xue et al. (2008). However, given our estimated physical parameters from its SOAR spectrum, $T_{\rm eff} = 7\,870 \pm 9$ K and $\log\ g = 5.17 \pm 0.05$, this classification seems unlikely, considering both the low temperature and high $\log\ g$. I found nonetheless no periods in the range ~ 20 min to ~ 180 days. The object could either be an EMP with an overestimated $\log\ g$, or a single ELM, formed through one of the alternative paths to binary evolution described in the Introduction. Gaia parallax will allow us to determine its nature.

J213428.63-011409.3 and J233708.62-094307.0 were both followed up considering the high proper motions (> 12 mas yr^{-1}) displayed in the catalogue of Munn et al. (2014). However, both values were actually unreliable due to the presence of nearby bright sources, and the proper motions given in the recent GPS1 catalogue (Tian et al., 2017) are much smaller and quite uncertain. For J2134-0114 ($g = 16.96$), not only no RV variation is found, but the fit to the SOAR spectrum suggests a relatively low $\log\ g = 3.76 \pm 0.02$, and $T_{\rm eff} = 12\,320 \pm 84$ K, placing it above the zero-age horizontal branch (ZAHB). It could thus be a HB star. We cannot, however, discard the possibility that it is a (pre-)ELM

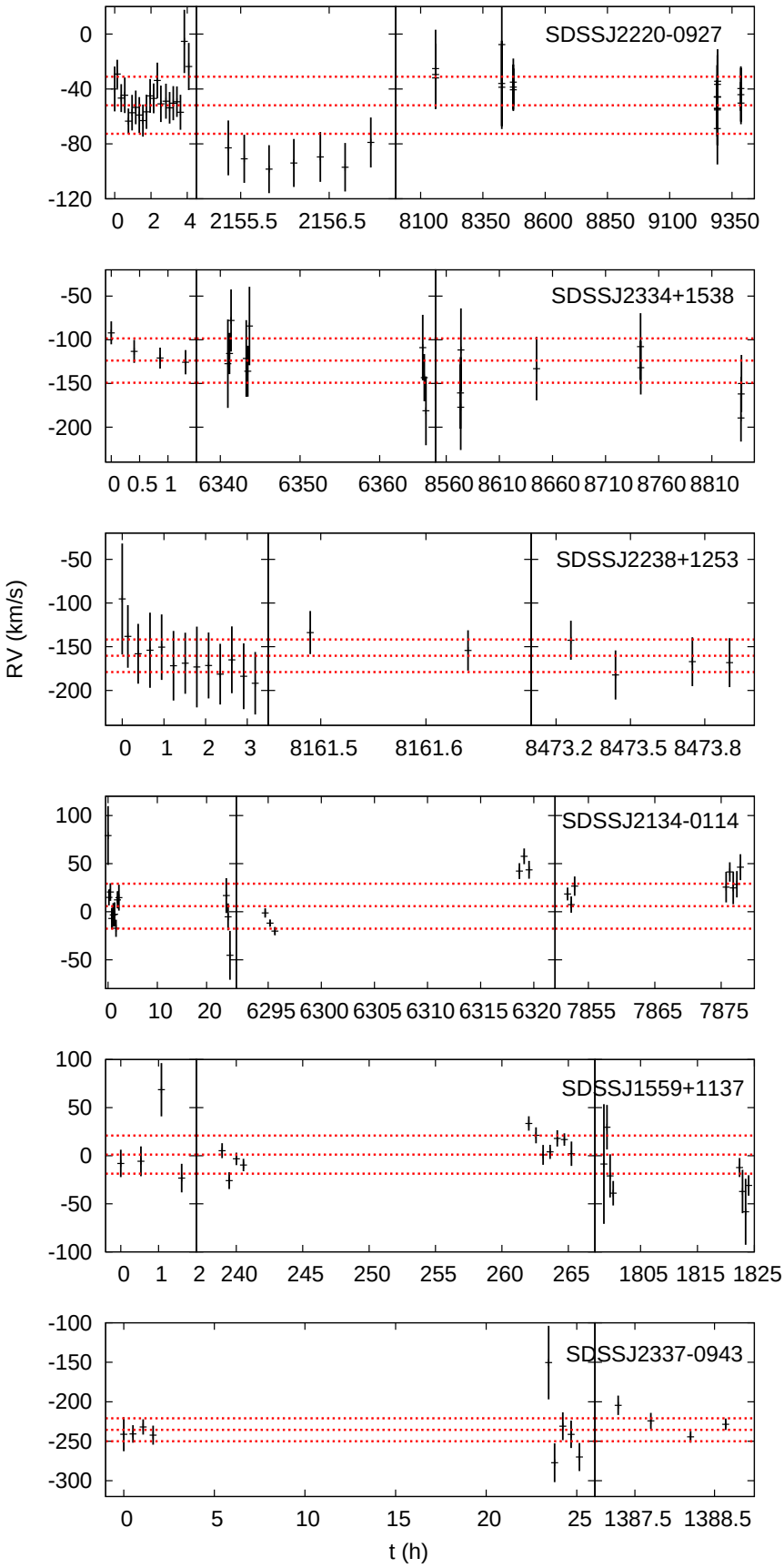

Figure 77 – Velocities for the six objects observed in multiple epochs, with no statistically detected variation. The dashed lines show the average velocity and ±1 σ limits.

in a CNO flash. J2337-0943 ($g = 17.90$), on the other hand, lies below the ZAHB, with $T_{\rm eff} = 8\,020 \pm 12$ K and $\log\ g = 4.59 \pm 0.06$. Such parameters are consistent with a $M = 0.160 \pm 0.004\ M_{\odot}$ pre-ELM, but the no detection of orbital periods in the range 1 h to 30 days and the lack of reliable ($> 3\sigma$) proper motion suggest it could be a halo metal-poor A/F star instead.

The five objects observed with X-shooter – J024932.84-010708.4, J101701.89+070806.8, J112620.47+090145.5, J112616.66-010140.7, and J233343.95-001502.0 – are shown in Figs. 78 to 82. Their physical properties as estimated from their X-shooter spectra are given in Table 13. Besides no RV variation, it can also be noted that they have no red companions. They all showed $\log g > 5.5$ in our fit to their SDSS spectra assuming solar abundances. Most show $\log\ g \gtrsim 5.5$ also when $Z = 0.1\ Z_{\odot}$ is assumed when fitting these spectra. Interestingly, the fit to the X-shooter spectra assuming $Z = 0.1\ Z_{\odot}$ suggests a $\log\ g$ lower by ~ 1 dex. Possible reasons are discussed in Section 4.2.8.5. The obtained parameters and the fact that none shows significant proper motion suggests they could all be metal-poor A/F stars. However, we caution that they are hotter and apparently less metallic than any known low-metallicity stars (e.g. those of Yong et al., 2013).

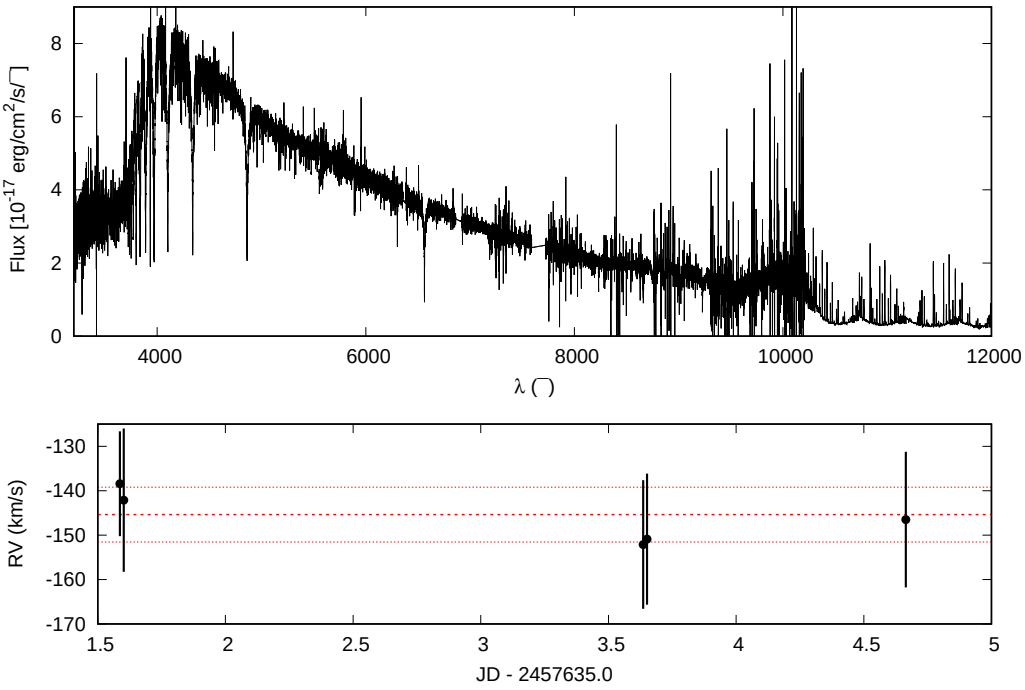

Figure 78 – The top panel shows the combined X-shooter spectrum for J024932.84-010708.4. No companion can be identified in the red. The bottom panel shows the RVs obtained for the spectra taken at three different nights. The dashed lines show the weighted mean and the $\pm 1\ \sigma$ values.

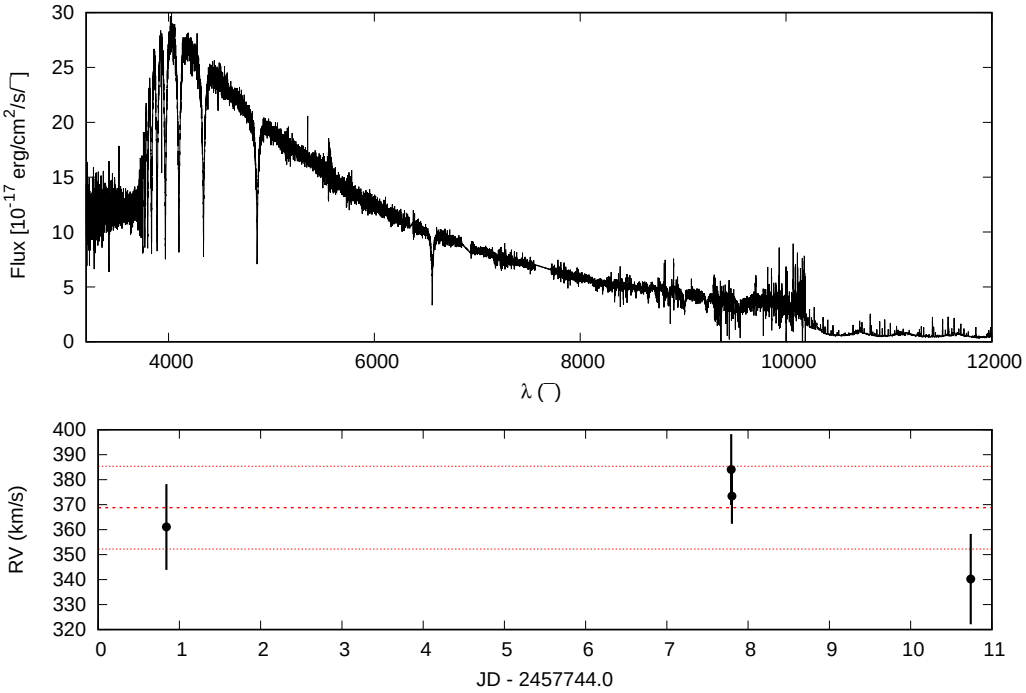

Figure 79 – Combined X-shooter spectrum for J101701.89+070806.8 (top), and the RVs obtained from each individual spectrum (bottom). The weighted mean and ± 1 σ values are indicated by the dashed lines.

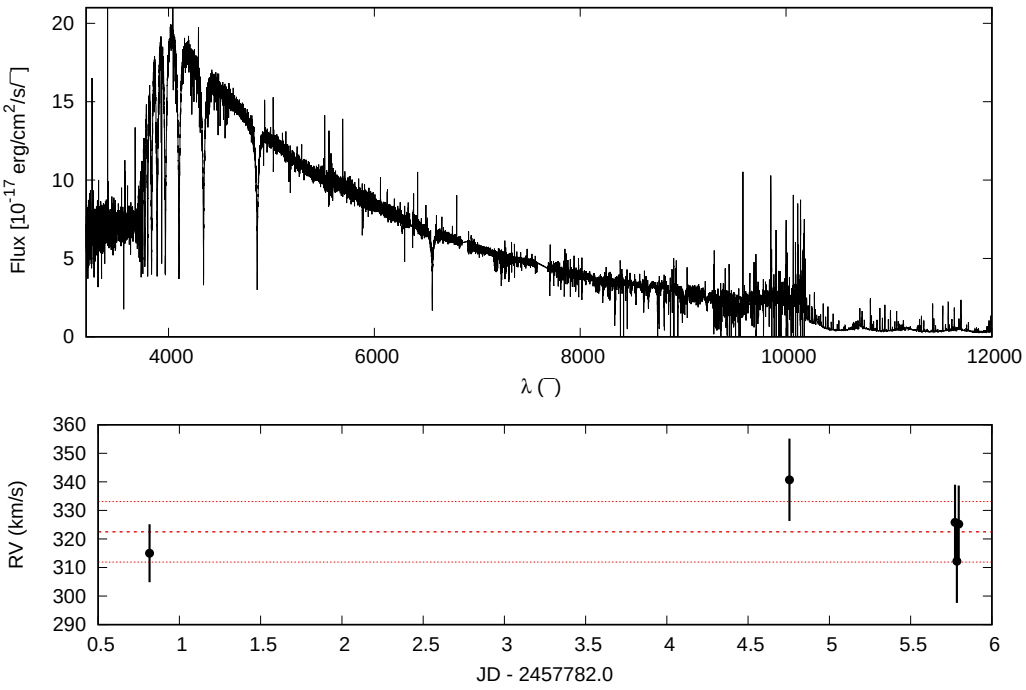

Figure 80 – The estimate RVs for J112620.47+090145.5 (bottom), obtained from the individual spectrum taken at three different nights. The Doppler-corrected combined spectrum is shown in the top panel.

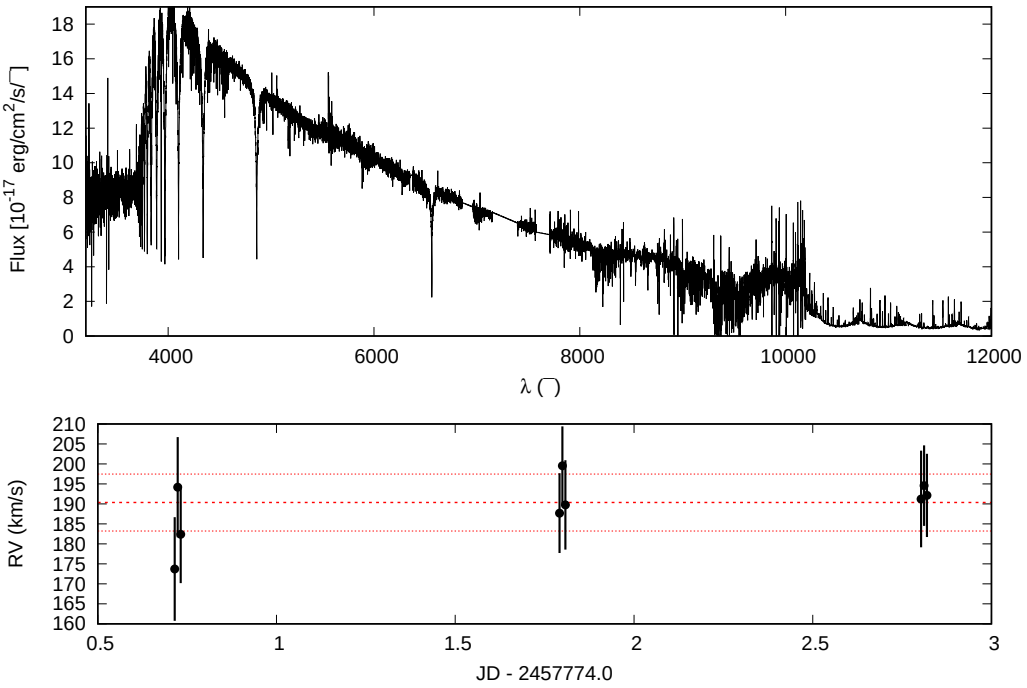

Figure 81 – X-shooter spectrum (top) and RV estimates (bottom) for J112616.66-010140.7. The RV estimates agree between the three nights.

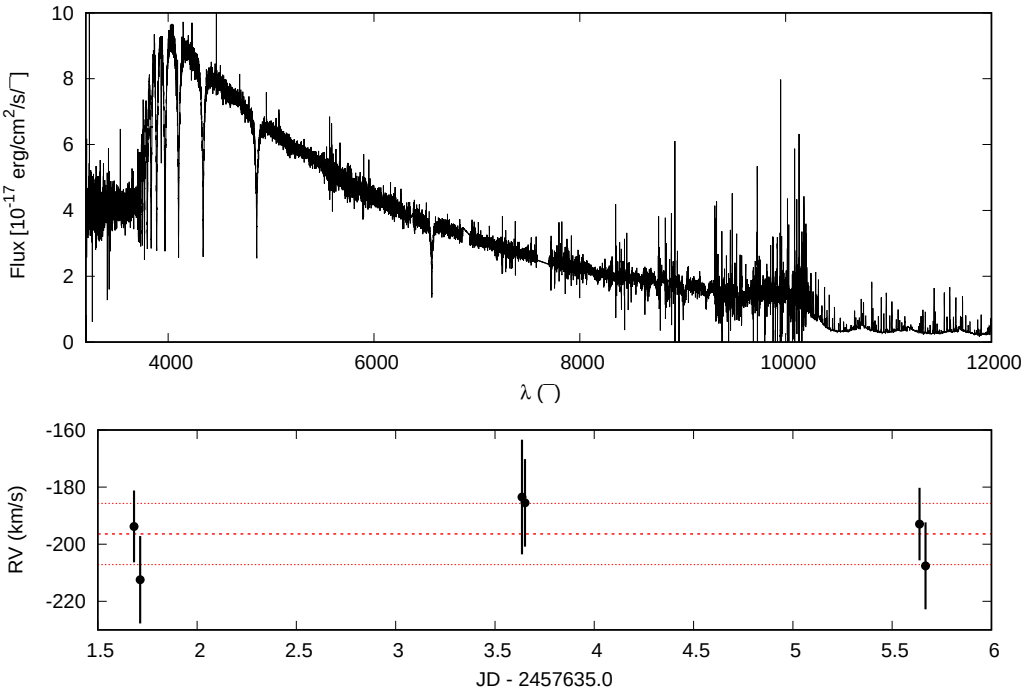

Figure 82 – Bottom panel shows the RV estimates for J233343.95-001502.0, and the top panels shows the combined Doppler-corrected spectrum for all epochs.

Table 13 – Physical properties derived for the objects observed with X-shooter.

SDSS J	g	$T_{\rm eff}$ (K)	$\log g$
024932.84-010708.4	19.44	8219(13)	4.775(0.044)
101701.89+070806.8	18.25	8746(6)	4.331(0.020)
112620.47+090145.5	18.85	8467(7)	4.640(0.021)
112616.66-010140.7	18.50	8073(8)	4.834(0.025)
233343.95-001502.0	19.32	8279(6)	4.410(0.016)

4.2.8.4 Eclipsing stars

Seven eclipsing systems identified by me in the CRTS data (Fig. 83) were observed for us by W. Brown with the 6.5 m telescope at the MMT Observatory (Mount Hopkins, USA) and the 1.5 m telescope at the Fred Lawrence Whipple Observatory (Cambridge, USA). These objects and their estimated properties, $T_{\rm eff}$, log g and period, are listed in Table 14. MMT spectra cover the range 3550-4500 Å at 1.0 Å resolution, while FLWO spectra cover 3500-5500 Å at 1.7 Å resolution.

Table 14 – Eclipsing objects whose follow-up time resolved spectroscopy was obtained by the collaborator W. Brown. We list their $T_{\rm eff}$, log g and the period estimated from the CRTS data.

Object (SDSS J)	g	$T_{\rm eff}$ (K)	log g	P (days)
075017.35+400441.2	18.32	8070 (400)	5.019(0.038)	1.2
074735.03+455420.0	17.58	7600 (380)	4.608(0.032)	0.5
080313.31+415740.4	18.42	8390 (420)	5.042(0.040)	1.3
075804.59+475406.3	16.40	7680 (380)	4.356 (0.021)	1.0
080205.90+433228.2	16.84	7710 (385)	4.564(0.025)	2.5
082328.31+373101.6	18.24	7720 (385)	4.572(0.056)	0.7
083238.89+135121.0	16.71	7275 (365)	4.246(0.034)	1.8

Radial velocities and orbital solutions were also obtained by W. Brown. The only object for which a significant orbital solution was obtained from the radial velocity data was SDSS J080313.31+415740.4 (Fig. 84). For the others, the radial velocity variations must be small, meaning that the objects are not in close binaries, and probably have a large orbital distance. The fitted $T_{\rm eff}$ and log g for SDSS J080313.31+415740.4, listed in Table 14, are consistent with a ELM. Using the models of Althaus, Miller Bertolami & Córsico (2013), we estimated a mass of 0.151 ± 0.001 $M_{\odot}$ and a radius of 0.19 ± 0.03 $R_{\odot}$. Eq. 1.3 gives the minimum mass of the companion as 0.14 $M_{\odot}$, and equal to 0.18 $M_{\odot}$ in case of

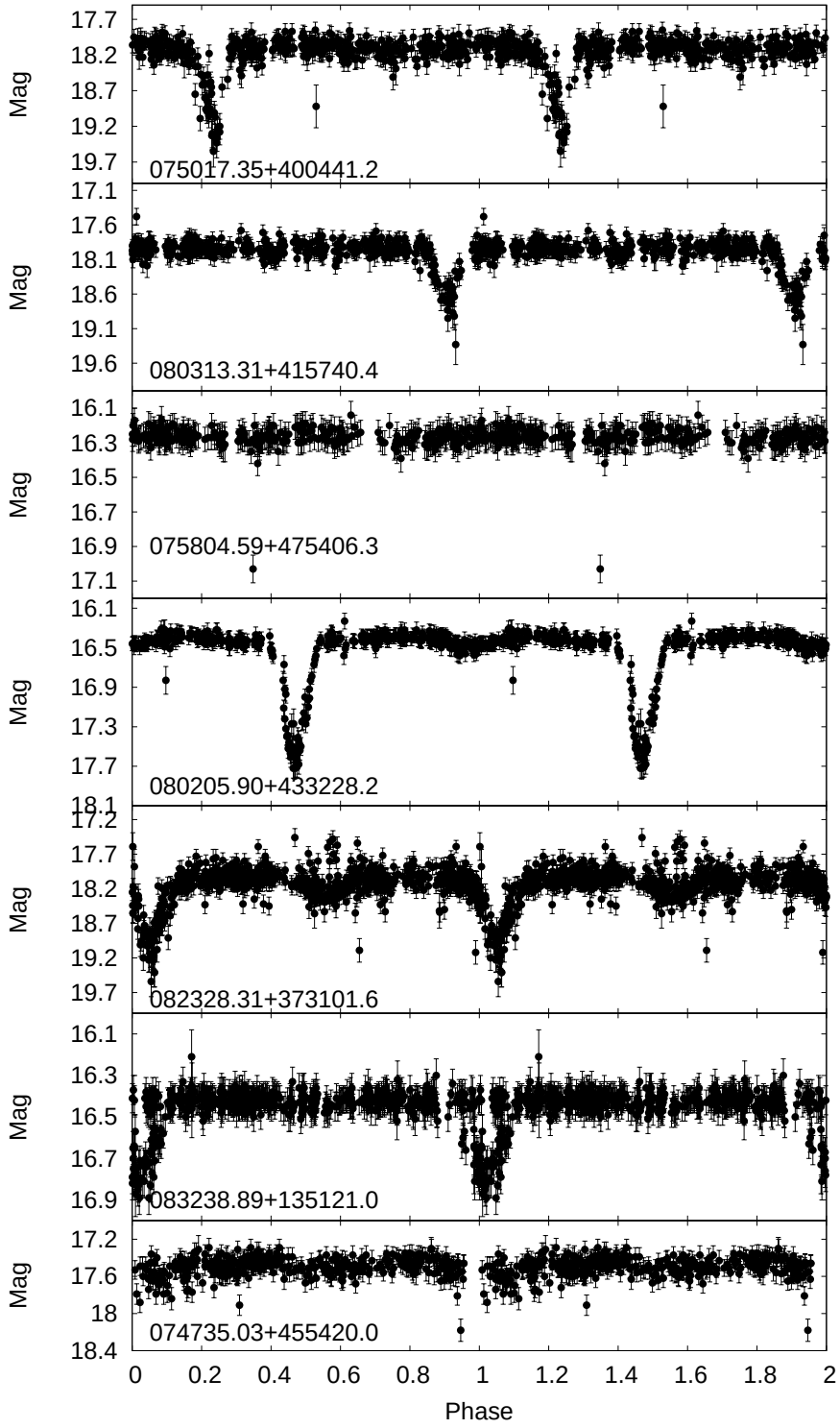

Figure 83 – Light curves, folded to the periods listed in Table 14, for the objects whose follow up spectroscopy was obtained at MMT and FLWO.

an inclination of 60°. This leads to merging times of the order of 10^3 Gyr, which are at least an order of magnitude higher than known ELMs, putting into question the nature of this object. In principle, as it has log $g > 5.0$ and it is confirmed to be in a close binary, it is classified as an ELM.

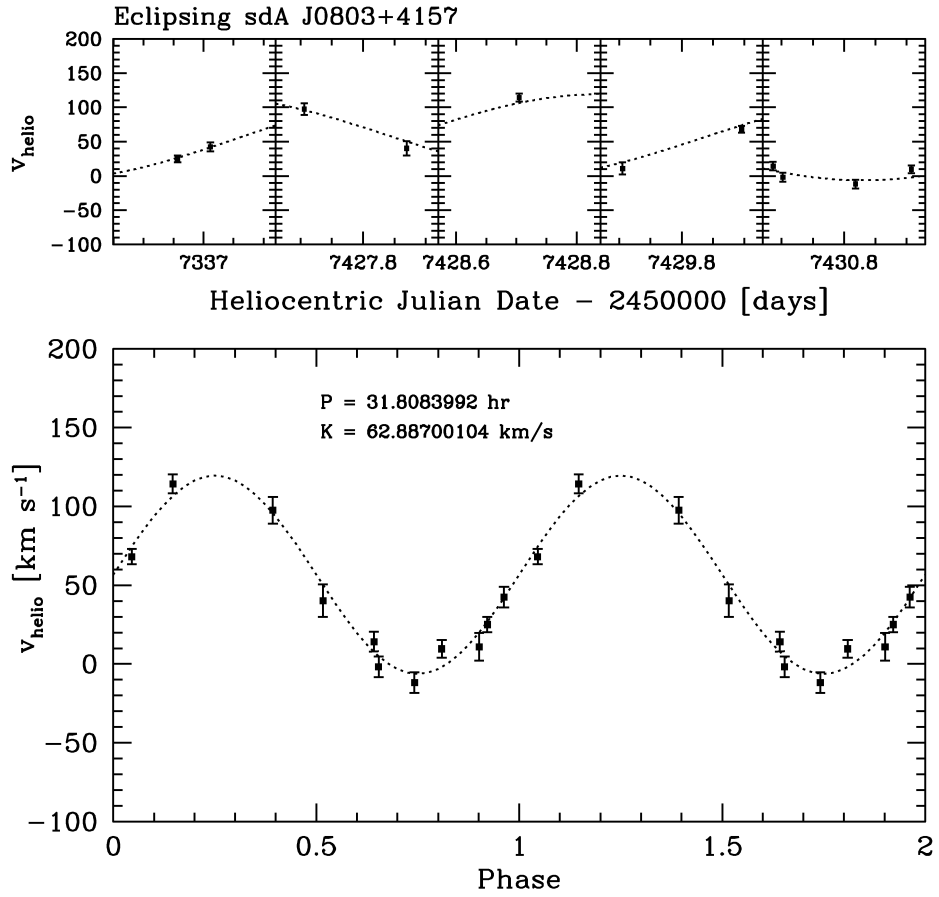

Figure 84 – Orbital solution obtained by W. Brown for the eclipsing sdA SDSS J080313.31+415740.4. The obtained period agrees with the one determined from the CRTS data.

4.2.8.5 Fits to followed-up spectra

Fig. 85 shows the comparison between our fit to SDSS spectra and to spectra obtained with SOAR or VLT as part of this work, with the same grid of models ($Z = 0.1$ $Z_\odot$). The effective temperature seems to agree remarkably well between spectra obtained with different facilities, with average differences of less than 2%. The log g, on the other hand, shows a larger spread. Considering the spectra obtained with SOAR, the average difference to SDSS, taking into account only objects whose fit is not at the border of our grid, is only about 0.08 dex, hence completely consistent with the uncertainties. However, comparing the four X-shooter spectra to SDSS, we obtain a large difference of −0.93 dex.

The grid of models is the same, so the difference cannot be explained by metallicity as suggested by Brown; Kilic; Gianninas (2017).

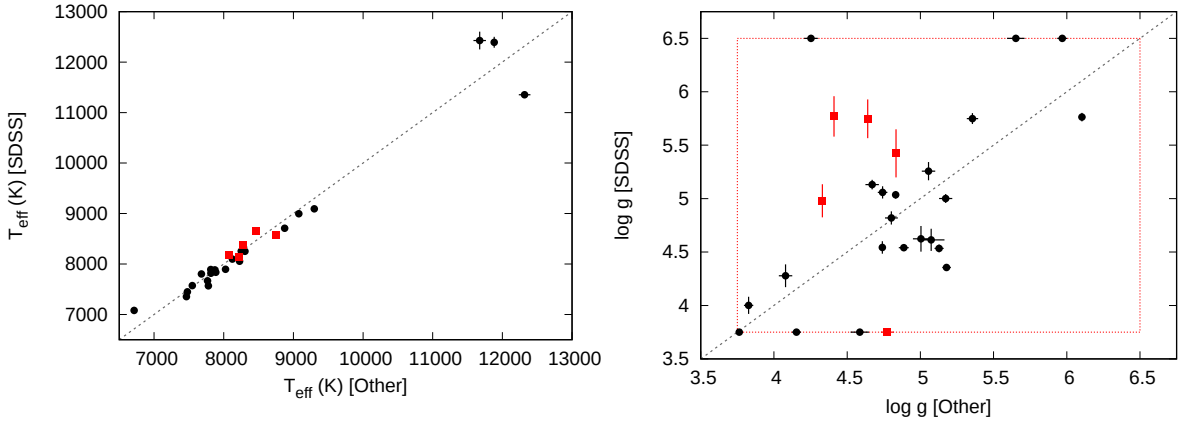

Figure 85 – Comparison between the physical parameters obtained by fitting SDSS spectra or SOAR/X-shooter spectra (labelled as other). The physical parameters derived from SOAR spectra are shown as black dots, while parameters derived from X-shooter spectra are shown as red squares. There is a very good agreement, to less than 2%, in $T_{\rm eff}$ (left). The dashed rectangle in the log g panel (right) indicates the border of the model grid. Considering objects within this limits, SOAR and SDSS log g show a low average difference of 0.08 dex. The X-shooter spectra suggest a log g lower by 0.93 dex, what could be due to the better resolution and larger spectral coverage provided by X-shooter, but could also be explained by statistical fluctuations, as detailed in the text.

The main differences between X-shooter and SDSS/SOAR spectra are the wavelength coverage and the spectral resolution. At low temperatures, the width of the lines is not very sensitive to log g, and the log g determination depends essentially on flux below 3700 Å. Spectra obtained with the SDSS spectrograph only cover above 3800 Å. More recent spectra obtained with BOSS extend the coverage down to 3600 Å, but usually with low-S/N in this wavelength range. This region is also very sensitive to flux calibration and extinction. Hence log g estimates with from SDSS spectra might be affected by these uncertainties. We had previously quoted an external 0.25 dex uncertainty, but it appears that it might be even larger, up to 0.50 dex. It is important to caution, however, that these four objects were selected on a very large sample, with tens of thousands of sdAs, hence we should expect to find several objects with errors of $2-3\ \sigma$. In short, we cannot assert that this difference between SDSS and X-shooter spectral fits is systematic, as it might result from statistical fluctuations.

The adopted physical parameters for our followed-up new and probable (pre-)ELMs are shown in Tables 15, and their estimated orbital parameters are in Table 16. Fig. 86 is similar to Fig. 5, including these new objects. These additions to the known sample of ELMs improve the comparison between model predictions and observed population,

by adding objects both to cool and to low-mass ends of the (pre-)ELM space of physical parameters.

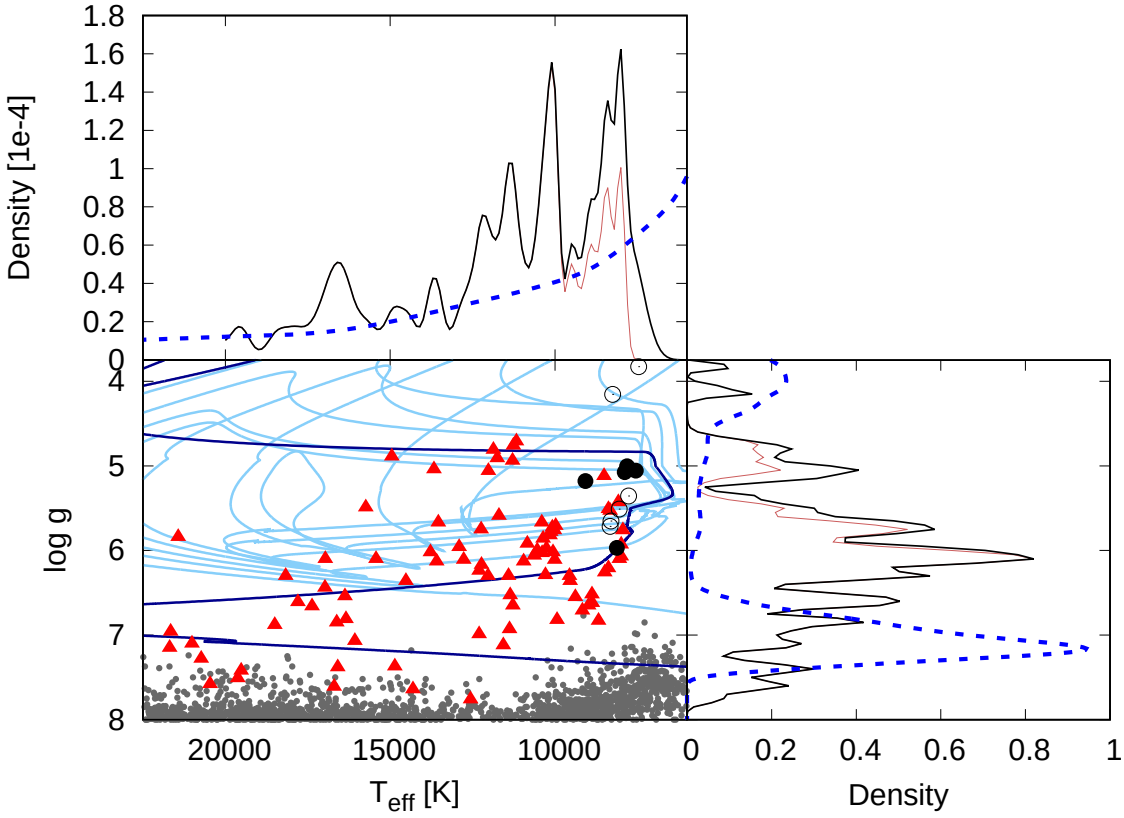

Figure 86 – Same as Fig. 5, adding the new (pre-)ELMs (filled black circles) and probable (pre-)ELMs (open black circles). The distributions with these added objects are shown in black. Especially in $T_{\rm eff}$, the population seems more similar to the predicted by the models, given the addition of objects to the $T_{\rm eff} < 9\,000$ K region. There are still missing (pre-)ELMs in the lower log g end.

4.2.8.6 Photometry

Besides J1343+0826 and J2220-0927 described in Sections 4.2.8.1 and 4.2.8.3, I found five other objects originally classified as sdAs to show variability. Two of them — J073958.57+175834.4 ($g = 14.75$) and J075519.92+091511.0 ($g = 15.32$) — show large amplitude variations with periods above 2 h. The estimated parameters from SDSS spectra assuming solar abundances are $T_{\rm eff} = 31\,700 \pm 111$ and log $g = 5.52 \pm 0.02$ for J0739+1758, and $T_{\rm eff} = 7\,470 \pm 5$ K and log $g = 4.50 \pm 0.04$ for J0755+0915. None shows significant proper motion. J0739+1758 was photometrically selected as a possible AM CVn binary by Carter et al. (2013). However, both the long period and the fact that the SDSS spectrum shows no emission or He lines seem to rule out this possibility. Its temperature places it within the region where subdwarfs stars show pulsations (see Fig. 90), hence it could be a new variable subdwarf star. J0755+0915 could be explained as a metal poor A/F star,

Table 15 – Estimated physical properties for the new and probable (pre-)ELMs, which are separated by a horizontal line, assuming $Z = 0.1\ Z_{\odot}$.

SDSS J	$T_{\rm eff}$ (K)	log g	M ($M_{\odot}$)
032914.77+003321.8	9077(10)	5.179(0.029)	0.1536(0.0006)
073934.37+172225.5	7548(12)	5.056(0.046)	0.1450(0.0011)
084034.83+045357.6	7886(32)	5.074(0.091)	0.1470(0.0022)
134336.44+082639.4	8123(10)	5.969(0.034)	0.1527(0.0011)
142421.30-021425.4	9299(11)	5.128(0.031)	0.1558(0.0008)
205120.67+014554.4	7813(12)	5.004(0.055)	0.1476(0.0014)
092056.09+013114.8	7478(13)	4.802(0.044)	0.1492(0.0014)
004227.73-010634.9	8051(24)	5.510(0.081)	0.1449(0.0003)
011508.65+005346.1	8673(24)	5.641(0.080)	0.1499(0.0011)
030608.92-001338.9	7768(10)	5.356(0.039)	0.1433(0.0004)
045515.00-043231.0	8251(8)	4.154(0.031)	0.1796(0.0014)
090410.00+034332.9	7680(20)	4.079(0.046)	0.1810(0.0488)
122911.49-003814.4	8305(21)	5.652(0.060)	0.1477(0.0009)
162624.91+162201.5	7464(15)	3.827(0.032)	0.3454(0.0127)
233606.13-102551.5	8328(39)	5.716(0.147)	0.1487(0.0030)

Table 16 – Estimated physical and orbital properties for the new and probable (pre-)ELMs, which are separated by a horizontal line. The secondary mass is the lower limit, and the time for merging is the upper limit. The uncertainties in P and K were calculated with a thousand Monte Carlo simulations in Period04.

SDSS J	$P_{\rm orb}$ (h)	K (km/s)	M_2 ($M_{\odot}$)	$\tau_{\rm merge}$ (Gyr)
032914.77+003321.8	20.0 ± 0.1	83 ± 22	0.17	765
073934.37+172225.5	6.64 ± 0.03	82.6 ± 6.8	0.10	68
084034.83+045357.6	8.13 ± 0.01	222 ± 13	0.59	28
134336.44+082639.4	21.39 ± 0.01	136.2 ± 7.0	0.43	449
142421.30-021425.4	6.3 ± 0.4	80 ± 22	0.09	57
205120.67+014554.4	22.9 ± 0.2	138 ± 14	0.45	533
092056.09+013114.8	15.742 ± 0.003	75.7 ± 8.1	0.09	50
004227.73-010634.9	1.52231 ± 0.00002	48.1 ± 1.6	0.14	4.2
011508.65+005346.1	1.678517 ± 0.000009	74.5 ± 5.5	0.05	3.1
030608.92-001338.9[a]	28.6 ± 1.1	186 ± 61	1.03	546
	13.5 ± 2.3	88 ± 19	0.15	320
045515.00-043231.0	4.1 ± 3.8	60 ± 23	0.06	25
090410.00+034332.9	14.7 ± 0.3	47.7 ± 2.4	0.08	590
122911.49-003814.4	2.96 ± 0.08	47 ± 5.0	0.04	20
162624.91+162201.5	8.2 ± 0.1	93 ± 19	0.20	32
233606.13-102551.5	2.38904 ± 0.0008	131 ± 11	0.12	3.7

[a] Two distinct periods are possible with the current data. Parameters for both are shown.

but we caution that there is at least one pre-ELM known to show RR Lyrae-pulsations (Pietrzyński et al., 2012a), given that during the CNO flashes the pre-ELM can reach the RR Lyrae instability strip.

For a third object, J075738.94+144827.5 ($g = 15.04$), we found four periods above the detection limit (see Fig. 87 and Table 17), which allows from a more detailed analysis in terms of the period spacing (Sánchez-Arias et al., submitted to A&A). Considering the period ranges of δ-Scuti and pre-ELMs, there are two possible scenarios: (i) the star could be a δ-Sctuti star with four p modes, or (ii) it could be a pre-ELMV star with three g modes and one p mode (803 s). If we assume that the periods between 2000 and 3000 s have consecutive radial orders, then the observed period difference is between 380 and 546 s. These values are similar to the period difference values corresponding to p-modes of δ-Scuti stars. The mean period spacing for a pre-ELM in the same range of periods is much lower, of only $\sim$ 80 s. Therefore it seems that J0757+1448 is more likely a δ-Scuti star, a result that should be confirmed by the parallax. The atmospheric parameters derived from the SDSS spectrum, $T_{\rm eff} = 8180 \pm 250$ K and log $g = 4.75 \pm 0.05$ are consistent with this possibility given the external uncertainties.

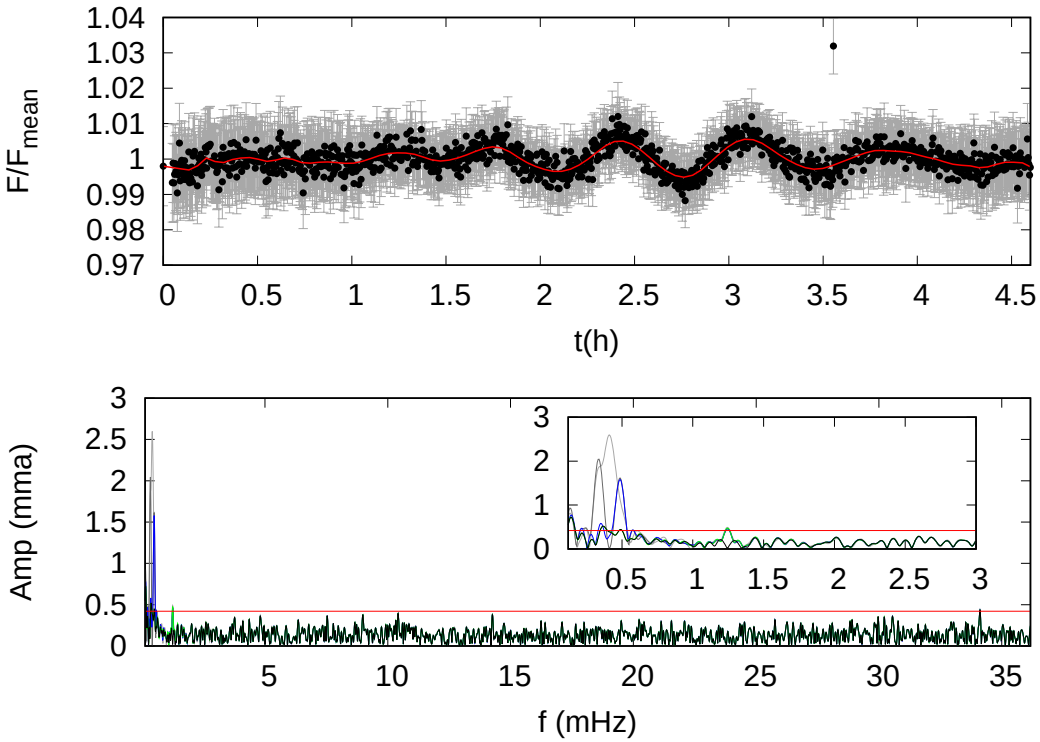

Figure 87 – Top panel shows the light curve for J075738.94+144827.5. Error bars are shown in grey and a smoothed light curve is shown in red. The bottom panel shows the original Fourier transform in grey, and the subsequent Fourier transforms, subtracting periods above a 3σ detection limit, in different colours. The final detection limit, above which no further periods were found, is shown in red.

Table 17 – Estimated period and amplitudes for J075738.94+144827.5.

P (s)	Amplitude (mmag)
2435 ± 107	2.5 ± 0.7
2981 ± 168	1.9 ± 0.7
2055 ± 173	1.2 ± 0.1
803 ± 4	0.5 ± 0.2

Two other new variables, J160040.95+102511.7 ($g = 15.00$) and J201757.29-125615.6 ($g = 17.07$), are shown in Figs. 88 and 89, respectively. The derived physical parameters for the SDSS spectrum of J1600+1025 assuming solar metallicity are $T_{\rm eff} = 8\,050 \pm 8$ K and $\log\ g = 5.59 \pm 0.03$, placing it within the instability strip of Tremblay et al. (2015). Its proper motion is 9.0 ± 0.4 mas/yr. For J2017-1256, the derived physical parameters from the SDSS spectrum assuming solar metallicity place it slightly above the instability strip, with $8\,240 \pm 9$ K and $\log\ g = 5.36 \pm 0.04$. The proper motion is smaller than 5 mas/yr, with an uncertainty of almost 2 mas/yr (Tian et al., 2017). The estimated $\log\ g$ of both objects is too high for δ-Scuti stars, which have similar spectral properties to (pre-)ELMs, but show $\log\ g < 4.4$ (e.g., Murphy et al., 2015). However, given the uncertainties in $\log\ g$ described in Section 4.2.8.5, the $\log\ g$ could be lower. We obtain a distances of over 3 kpc assuming a main sequence radius, and $z > 1$ kpc given their relatively high galactic latitude. Unfortunately, the number of periods is insufficient for an asteroseismological analysis, thus conclusions on the nature of these objects require more data.

I have also observed fourteen other objects for at least 2 h, and integration times shorter than 30 s, and found no pulsations. The observing time and obtained detection limits are shown in Table 18. They are shown in Fig. 90 as not observed to vary, but we caution that this does not mean they are not variables. Beating can cause destructive interference and essentially hide the pulsations for hours (Castanheira et al., 2007). Moreover, the objects can show pulsations below the detection limit or outside the probed periods.

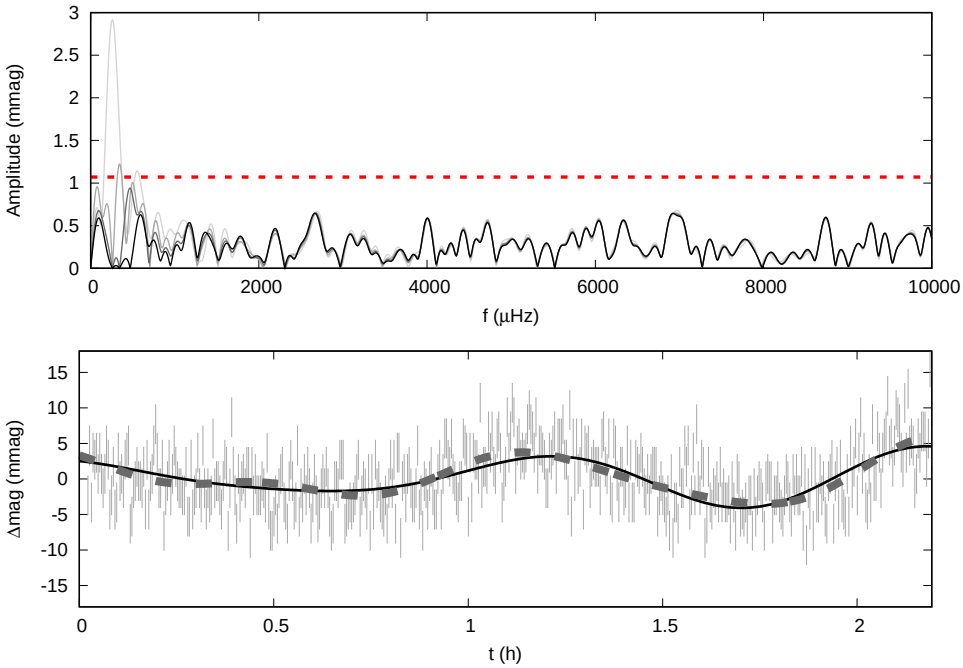

Figure 88 – The SOAR light curve for 160040.95+102511.7 is shown in the bottle panel. The grey continuous line is a fit considering the two periods above a 4 ⟨A⟩, 3849 ± 57 s with an amplitude of 3.1 ± 0.2 mmag, and 2923 ± 32 s with 1.4 ± 0.2 mmag. The dashed lined adds a third period, which shows an amplitude larger than 3.9 ⟨A⟩, 2133 ± 21 s with 1.0 ± 0.2 mmag. The Fourier transform is shown in the top panel; dark shades indicate the result after successive dominant periods were subtracted from the original light curve (lightest grey shade).

Table 18 – Objects not observed to vary. The physical parameters were estimated from the SDSS spectra assuming solar metallicity.

SDSS J	g	$T_{\rm eff}$ (K)	$\log g$	Telescope	Exposure time(h)	3 ⟨A⟩
092140.37+004347.9	18.39	7887(34)	5.687(0.116)	SOAR	4.0	5.0
143333.45+041000.8	18.31	8890(35)	4.729(0.119)	SOAR	1.8	7.0
233625.92+150259.6	17.18	8246(20)	6.207(0.061)	OPD	2.7	10.0
112058.97+042012.3	17.87	13840(265)	5.147(0.065)	SOAR	2.4	9.0
204038.41-010215.7	16.59	8028(15)	5.505(0.050)	SOAR	1.6	40.0
				OPD	2.2	6.0
163625.08+113312.4	17.24	8726(16)	3.967(0.035)	OPD	4.4	12.0
110338.46-160617.4	15.77	8350(9)	4.572(0.049)	OPD	5.9	10.0
140353.33+164208.1	16.20	8250(12)	6.178(0.036)	OPD	3.0	4.0
165700.89+130759.6	15.62	8381(11)	6.135(0.039)	SOAR	2.6	25.0
				OPD	5.3	10.0
075133.48+101809.4	17.40	13126(81)	3.853(0.023)	SOAR	2.2	1.5
045001.34-042712.9	19.07	7981(39)	5.320(0.162)	SOAR	3.2	8.0
104522.80-023735.6	19.28	7328(37)	4.226(0.136)	SOAR	2.1	7.0
094144.89+001233.8	19.28	7994(32)	4.914(0.102)	SOAR	2.9	6.0
111041.50+132354.3	18.28	7279(23)	4.300(0.074)	SOAR	3.2	6.0

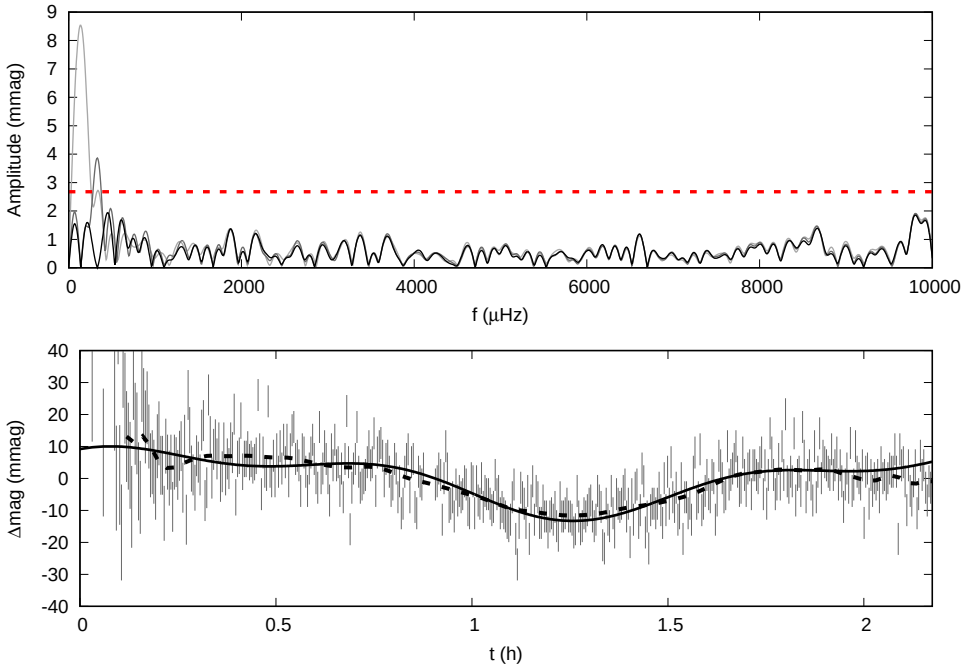

Figure 89 – Top panel shows the Fourier transform for the SOAR light curve of 201757.29-125615.6. As in the previous figure, darker shades indicate more subtractions. The light curve for and best fit (continuous line) are shown in the bottle panel. We find two periods, 7171 ± 49 s with and amplitude of 9.0 ± 0.5 mmag and 3011 ± 58 s and amplitude of 4.1 ± 0.5 mmag. Here the dashed line is a smoothing of the data.

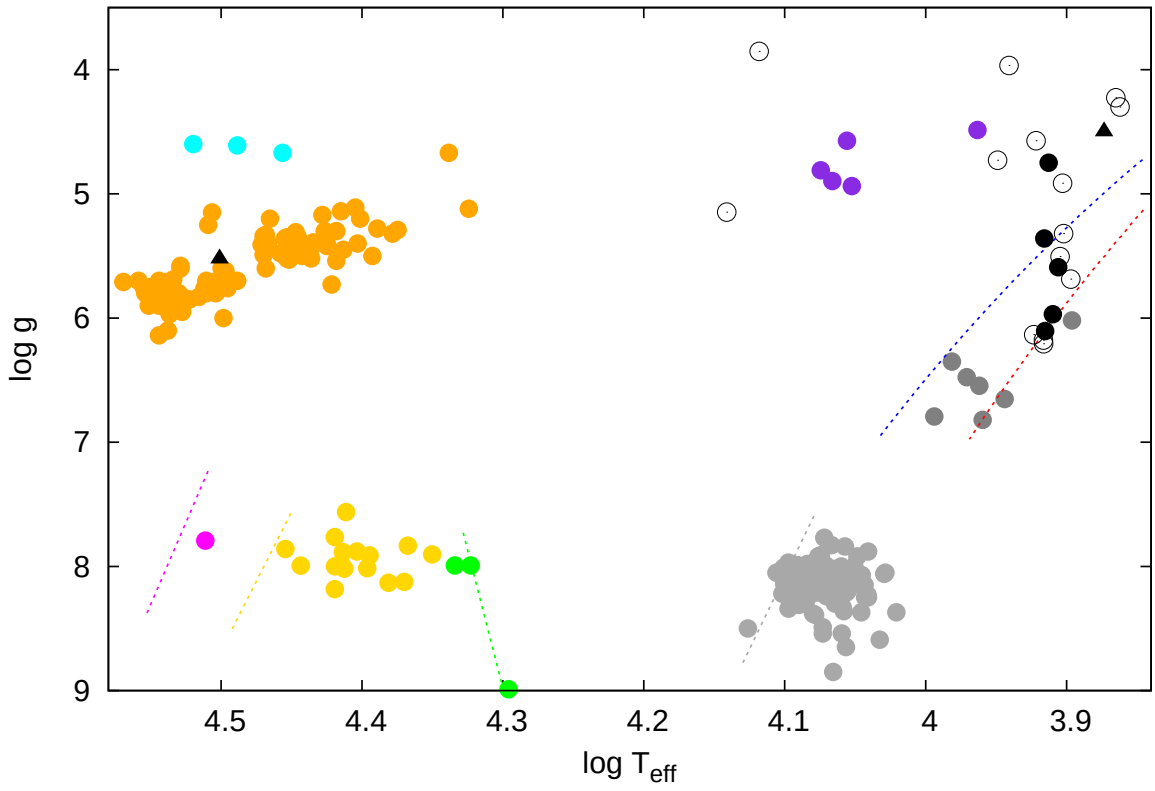

Figure 90 – Location of the newly detected variables (filled black symbols) in the $T_{\rm eff}$ – log g diagram. The triangles are the two objects with high amplitude pulsations. Open black circles are objects not observed to vary. The hot (blue line) and cool (red line) edges of the ELM instability strip shown as dotted lines were extracted from Tremblay et al. (2015). Other pulsating white dwarfs are shown as in fig. 1 of Córsico et al. (2016): pre-ELMVs (purple), ELMVs (dark grey), DAVs (light grey, bottom right), DQVs (green, at $\log T_{\rm eff} \sim 4.3$), DBVs (yellow), and the only known hot DAV (magenta, bottom left). We have also added the sdV stars from Holdsworth et al. (2017) (orange), and the newly discovered blue large amplitude pulsators (BLAPs, shown in cyan) from Pietrukowicz et al. (2017) as comparison.

5 Discussion & Conclusions

We have identified 3157 new white dwarf stars in the SDSS DR12 as part of this work, which represent a 10% increase in the known sample of spectroscopically confirmed white dwarfs. The resultant substantial increase in the number of spectroscopically confirmed white dwarfs contributes to works as those described in Section 2, and also allows the discovery of further rare objects like massive white dwarfs, magnetic white dwarfs, and He-dominated objects with oxygen lines (e.g Kepler; Koester; Ourique, 2016).

We estimated the masses for DAs and DBs given evolutionary models, and calculated the volume-corrected mass distributions. We found a mean mass for DAs which is significantly lower than previous estimates, but now agrees with the mean mass for the DB stars, as is expected from evolutionary models. The mass distributions for DAs and DBs, on the other hand, seem to be significantly different: the DAs show a much broader distribution, with a tail to higher masses, while the DB distribution is narrower and has a tail to lower masses. This suggests that the occurrence of late-thermal pulses leading to a DB star depends on the mass of the progenitor, which is not predicted by current evolutionary models. Hence, there might still be missing physics in these models.

We have also estimated the calcium abundance in polluted white dwarfs and the and carbon abundances in DQs. In both cases, we noted a correlation with $T_{\rm eff}$: the abundances get lower with decreasing temperature. This is probably related with the deepening of the convective layer as the star cools down, making the material more diluted.

We extended our white dwarf search to lower log g, including spectra identified by the SDSS pipeline as type O, B or A, and calculated a new model grid with solar abundances down to log $g = 3.5$ in order to identify ELM candidates, resulting from binary evolution. We analysed this sample of narrow-line hydrogen spectra using the new spectral models. Comparing these results to the previous pure-hydrogen models used in the DR12 analyses, we showed that there is a shift in $\log g$ when metals are added, yet it is not a constant as previously suggested by Brown, Kilic & Gianninas (2017), it rather depends on $\log g$. However, for objects with a pure-hydrogen log $g > 5.5$, as the objects analysed by Brown, Kilic & Gianninas (2017), the pure-hydrogen $\log g$ seems in fact to be about 1 dex higher than the solar abundance $\log g$.

With these new models, we have identified new ELM candidates in the range $5.0 \leq \log g \leq 7.0$ and $7\,000 \leq T_{\rm eff} < 20\,000$ K. We analysed the colours of the whole sample of narrow-line hydrogen spectra, obtaining that the spectroscopic log g does not seem to agree with the position of the objects in colour-colour diagrams. This might indicate that there is still missing physics in the models; the addition of metals alone

does not solve the discrepancy. Other missing opacities, such as molecular contributions, might be the explanation. However, the discrepancy could also be solved if the reddening is underestimated. One key-result obtained from the colour analysis is that the sdAs can not be explained as binaries of a hot subdwarf with a main sequence star, since they do not show significant flux in the UV. There is also no indication of infrared excess for over 98% of the sample.

Our most significant result is that the sdAs are clearly composed of two populations. One population contains the red objects, and it has no overlap with the known ELMs. These could be explained as cool late-type main sequence stars, when the velocities are consistent with the halo population. On the other extreme, there is a blue population, which does overlap with known ELMs, but contains cooler objects. Considering the existence of a missing cool ELM population to be found, which motivated this work, it is very likely that these objects belong to the blue population of sdAs.

Analysing the estimated distances and spatial velocities for the objects, we obtain that over 35% of them show too high velocities to belong to the halo when a main sequence radius is assumed. These objects cannot therefore be explained as simply metal-poor main sequence stars of type A–F. The discrepant velocities are solved when a (pre-)ELM radius is assumed for these objects, in which case their velocities become consistent with the disk distribution. Some percentage of these objects might be of binary stars, such as blue stragglers, in which case the velocities could be explained as orbital instead of spatial motion. A better sense of the nature of this population will be obtained when their parallax is released by Gaia.

We also compared our estimated values of $T_{\rm eff}$ and $\log\ g$ to evolutionary models, both single and binary. A very interesting result is that the parameters for the objects in our sample are consistent with those expected from binary evolution models. Considering the time spent in each bin of $\log g$ and the brightness at such phases, even pre-ELMs with $\log g < 4.0$ have considerable probability of being observed.

Taking into account the derived probabilities from the evolutionary models, combined with the probabilities given the colours and spatial velocities, we have estimated probabilities for each object with reliable proper motion to be either a main sequence star or a (pre-)ELM. As there is significant overlap between the parameters of each class, the probabilities do not sum up to one. Comparing the probabilities, we found that about 7% of the sdAs are better explained as (pre-)ELMs than as main sequence stars, a much larger percentage than the $\sim 1\%$ found by Brown, Kilic & Gianninas (2017) studying a small sample of eclipsing stars and not taking the (pre-)ELM phase into account. Considering the physical parameters of the objects with a higher probability of being (pre-)ELMs, our result is consistent with the existence of two times as many cool ELMs ($T_{\rm eff} < 8\,500$ K) as hot ELMs.

Analysing the SDSS radial velocities, we confirmed two new ELMs, SDSS J104826.86-000056.7 and SDSS J120616.93+115936.2. SDSS J120616.93+115936.2 also shows photometric variability with the same period as the orbital period. Two other objects are most likely ELMs. SDSS J171906.23+254142.3, although showing log $g < 5.0$, has an amplitude of almost 200 km/s in its best orbital fit. However, as only five subspectra are available, the period is not well constrained, and follow-up should be done to confirm the nature of this object. The SDSS subspectra of SDSS J122911.49-003814.4 did not allow the estimate of its period, but the high amplitude between its subspectra and its log g above the main sequence limit favoured the ELM classification, hence it was flagged for follow-up, which we obtained with SOAR. Finally, we also find SDSS J045947.40-040035.2 most likely to be a blue straggler star in the halo.

Following up on selected sdAs with properties consistent with ELMs, we have added twelve objects to the $T_{\rm eff} < 9000$ K range. With the three confirmed ELMs in this range given in Brown et al. (2016), we reach of total of fifteen objects, compared to 75 in the $T_{\rm eff} > 9000$ K range (73 confirmed binaries of Brown et al., 2016, plus J032914.77+003321.8 and J142421.30-021425.4, found in this work). This raises the fraction of cool ELMs from 4 to 20%, which is consistent with the predictions by evolutionary models, considering the uncertainties involving the residual burning.

All of our 15 discoveries show log $g < 6.0$. Combined with the 26 objects of the ELM Survey in this range, there are now 41 objects in the low-mass end of the ELM distribution. There are 50 objects with log $g > 6.0$. The fraction is thus close to 1:1; however, the brightness of the lower log g objects suggests the fraction could be as high as 100:1. Thus, as Fig. 86 already suggested, the population of low-mass objects seems to be missing still. As we considered the estimated log g as a selection criterion during most of our follow-up, preferring objects with log $g > 5.0$ or even > 5.5, the fact that this population is not unveiled by our work is not surprising, as there are still thousands of sdAs to be observed. With the upcoming data release 2 of the Gaia missing, finding this population will be a much easier task[1].

Out of the five observed objects we found to be most likely ELM in Section 4.2.5 (J0115+0053, J0306-0013, J1626+1622, J1343+0826, J0455-0432), one was confirmed as an ELM, and the remaining four were found to be probable ELMs. Four of the objects for which we found no RV variability were also in sample B, hence were part of the probability study, but a higher probability for the MS channel was obtained — consistent with the no detected variation. It seems that the probability criteria we calculated is a good indication of the nature of the probed sdAs. In addition, we confirmed 58% of the followed-up objects

[1] Preliminary analysis performed after the submission of this thesis shows that Gaia DR2 data are inconclusive for most ($> 90\%$) of the sdA sample, due to the large uncertainty in radii estimates. About 5% of our sample do seem to show radii smaller than main sequence, hence are likely (pre-)ELMs (see Pelisoli et al., 2018 for further discussion)

to be in binaries, a fraction close to the probability we estimated for a random sdA to be a (pre-)ELM. On the other hand, ten of the objects we followed up spectroscopically were flagged as possible ELMs given their log $g > 5.5$ estimated from SDSS spectra, but only one was confirmed as ELM (SDSSJ1343+0826), and two others were found to be possible ELMs (SDSSJ0042-0106 and SDSSJ0115+0053). This seems to suggest that the log g estimate, especially from SDSS spectra, is not a reliable criterion for selecting ELM candidates. This is in line with our findings described in Section 4.2.8.5. Spectral coverage of the $\lambda < 3700$ Å region with good S/N seems to be a requirement for a reliable estimate of the log g in this $T_{\rm eff}$ range. This might also explain the discrepancies found by Brown, Kilic & Gianninas (2017), but a study with a statistically significant sample is required to confirm this.

None of the newly discovered (pre-)ELMs has a orbital period short enough ($\lesssim 1$ h) to be above the predicted detection limit of the upcoming LISA gravitational wave detector. However, such short periods were not probed by our survey, given that most objects were observed with SOAR, a 4.1 m telescope, and required integration times close to 30 min to achieve $S/N \gtrsim 10$ in the individual spectra. Searching for this shorter periods might be interesting for the objects described Section 4.2.8.3, especially J2220-0927, which not only shows log $g > 6.0$ in our spectroscopic fit, but also photometric variability with periods in the ELM range.

The objects for which we found no RV variations could alternatively be metal-poor A/F stars in the halo, as already suggested by Brown, Kilic & Gianninas (2017) as a possible explanation for the sdAs. J2343+1538 in particular seems to be indeed an EMP star, as already suggested by Aoki et al. (2013). The five objects observed with X-shooter, which show no significant proper motion, could also be explained as such. J2134-0114 shows parameters consistent with an HB star, but the nature of the other objects remains puzzling. All show $g < 20.0$, therefore they should be included in the DR2 of Gaia, making it possible to constrain their radii and determine their nature with certainty. Follow up will still be required for the objects found to be ELMs in order to estimate their orbital parameters, given that Gaia will not be able to resolve binaries with separations below about 20 milliarcsec (~ 2 AU for a distance of 100 pc).

We have also found seven new photometrically variable stars in our follow-up. J1334+0826 was confirmed as a $M = 0.15\ M_{\odot}$ ELM with time-resolved spectroscopy, so its the eight member of the ELMV class, adding to the seven known pulsating ELMs (Hermes et al., 2012; Hermes et al., 2013; Hermes et al., 2013; Kilic et al., 2015; Bell et al., 2015). We found no RV variations for J2220-0927, but its estimated log g and temperature place it inside the instability strip, so it is possibily the ninth member of the class. Time-resolved spectroscopy with larger telescopes, allowing shorter integration times, should be done to probe shorter orbital periods for this object. Two other objects, J1600+1025 and

J2017-1256, are also found to show pulsations, and are within the instability ELMV strip given uncertainties. We have not obtained time resolved spectroscopy for them, therefore we make no claim about their nature given the uncertainties in the log g estimated from SDSS spectra. J0757+1448 seems to be a δ-Scuti star, given the spacing between the periods. One other variable, J0739 +1758, seems to be a sdBV, given the $T_{\rm eff} > 20\,000$ K. Finally, J0755+0915 shows high amplitude pulsations similar to RR Lyrae stars. The estimated physical parameters and the low proper motion (3.5 ± 1.7 mas/yr according to Tian et al., 2017) are consistent with a halo metal poor F star. We need extended observations for the pulsators to detected multiple periods and do asteroseismology. These might be facilitated by future missions such as PLAnetary Transits and Oscillations of stars (PLATO) and Transiting Exoplanet Survey Satellite (TESS).

Our effort shows that more than one evolutionary channel is definitely needed to explain the sdA population. For one, there are definitely He core objects such as pre-ELMs and ELMs in the sample. Even if only a small percentage of sdAs is confirmed as ELMs, the number would be high enough to significantly increase the number of known ELMs, especially at the cool end of the distribution. Our understanding of binary evolution, and especially of the common envelope phase that ELMs must experience, can be much improved if we have a sample covering all parameters predicted by these models. The sdA sample can provide that. Our understanding of the formation and evolution of the Galactic halo would also benefit from more detailed study of the sdAs. Many seem to be in the halo with ages and velocities not consistent with the halo population. It is possible that accreted stars from neighbouring dwarf galaxies might be among them. Those whose velocities are in fact consistent with the halo can in turn help us study its dynamics and possibly better constrain the gravitational potential of the halo. The final message of our results is that we should not overlook the complexity of the sdAs. They are of course not all pre-ELM or ELM stars, but they cannot be explained simply as main sequence metal-poor A–F stars. They are most likely products of binary evolution and as such are a valuable asset for improving our models.

Appendix

APPENDIX A – Comparison with parameters from the SDSS pipelines

The comparison between our estimated atmospheric parameters and those given by the SDSS pipelines is not straightforward, as the model grids do not cover the same range of $T_{\rm eff}$ and log g. We include this analysis here as an appendix to illustrate their differences. We do not, however, consider such comparison a valid test of our models, since the SDSS pipeline grids are strongly incomplete in terms of $T_{\rm eff}$ and $\log g$. Figs. 91 and 92 show the comparison between the $T_{\rm eff}$ and the $\log g$, respectively, that we obtained for the objects with a good fit (sample A) and the values given by two SDSS pipelines, the SEGUE Stellar Parameter Pipeline (SSPP, Lee et al., 2008) and the best match from the ELODIE stellar library (Prugniel; Soubiran, 2001). The two pipelines are also compared. We find good agreement ($\sim$ 5%) in $T_{\rm eff}$ between our fit and both pipelines. Our log g is 0.44 higher than the SSPP estimate, and 0.28 higher than the Elodie values, which is probably due to the difference in the extension of the grids. Note this average shift is not enough to raise the log g of a typical main sequence A star (log $g \sim 4.3$) to values above 5.0.

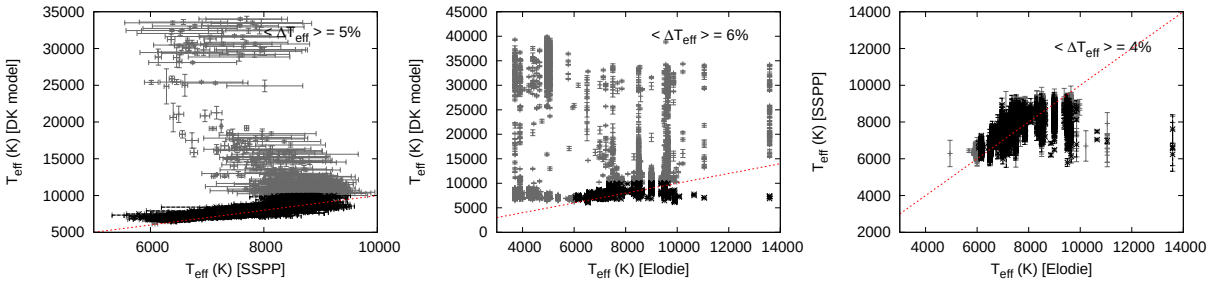

Figure 91 – Comparison between our estimate of $T_{\rm eff}$ (DK model) and both pipelines, as well as the comparison between the pipelines. Grey dots are outside of the area covered by SDSS grids, while black dots are within it. The red dashed line represents equality. The average difference for estimates within both grids is shown in each plot. It is clear that there is no discrepancy in the region covered by both grids. Our higher temperatures are backed up by both the GALEX ultraviolet flux, and the SDSS classification as type O and B, which is not coherent with their own estimated temperature.

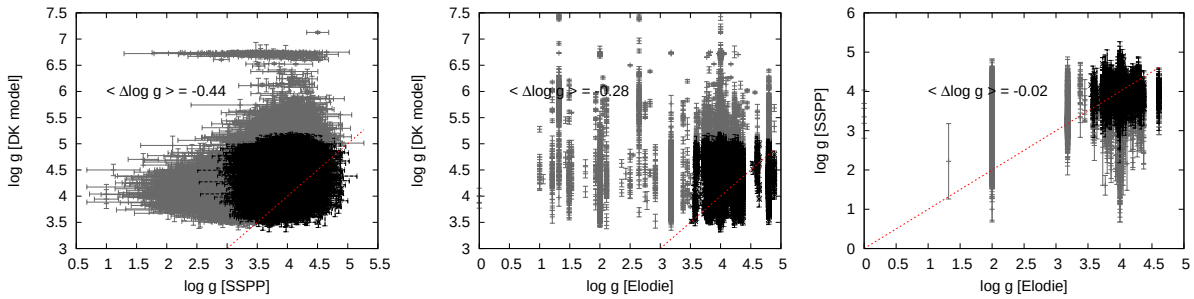

Figure 92 – Comparison between our log g and that of the pipelines. Colours are the same as in Fig. 91. The spread is larger and our fit favours, in average, slightly higher log g values, given the extension of our grid to higher values.

APPENDIX B – Further Kinematic Analyses of the sdAs

In many cases, the space motions of objects in the sample B of sdAs are dominated by the transversal velocity component, especially when a main sequence radius is assumed, as shown in Fig. 93. To verify this was not a consequence of outliers in the proper motion catalogue (such as found by e.g. Ziegerer et al., 2015), we cross-matched the GPS1 proper motions with both the Hot Stuff for One Year catalogue (HSOY, Altmann et al., 2017), and the proper motions given in the SDSS tables (Munn et al., 2004; Munn et al., 2014). Only 69 objects from sample B differ by more than 3-σ when comparing HSOY and GPS1 (see Fig. 94); 110 when we compare GPS1 to Munn et al. Such numbers are not of concern given the sample size, hence the objects were kept in the sample.

To work around possible effects risen by inaccuracy in the transversal velocity component, we have also performed a kinematic study relying on the radial velocity estimate alone. We have computed the Galactocentric distance (r) and the of line-of-sight velocities (v_{los}) in the Galactic standard of rest (GSR) frame following equations 4 and 5 of Xue et al. (2008). For the Galactocentric distance, we have assumed a MS radius. Fig. 95 shows v_{los} as a function of r, for both samples A and B, compared to the BHB stars of Xue et al. (2008). The unreliable proper motions of sample A result on unrealistic distance estimates, which are avoided by focusing on sample B, which shows similar distances to the halo BHBs. It is important to emphasise, however, that most sdAs show lower temperature than the ZAHB at their log g, as shown in Fig. 10. In Fig. 96, we show the distribution of v_{los} for both sample A and sample B, compared to a Gaussian of width $\sigma = 105$ km/s, as found by Xue et al. (2008) for BHB halo stars. There is no significant difference between the distributions of samples A and B. Moreover, both show a dispersion of the same order of the halo stars studied by Xue et al. (2008) when a main sequence radius is assumed, hence the conclusion that, if indeed main sequence stars, the sdAs would have to be in the halo is not dependent on the tangential velocity estimate.

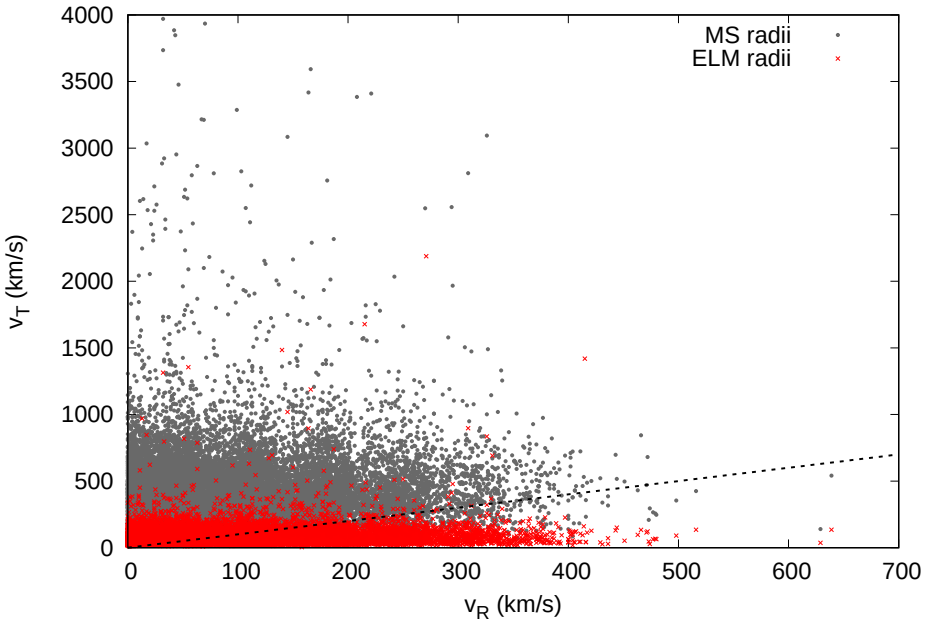

Figure 93 – Comparison between the radial velocity estimated from SDSS spectra (v_R), and the transversal velocity derived from the GPS1 proper motion given the estimated distance (v_T), both assuming a main sequence (grey dots) and an ELM radius (red crosses) for sample B only. The spatial motion is dominated by the tangential velocity if a main sequence radius is assumed, with many objects showing v_T much above the escape velocity. That does not happen when an ELM radius is assumed, with very few exceptions.

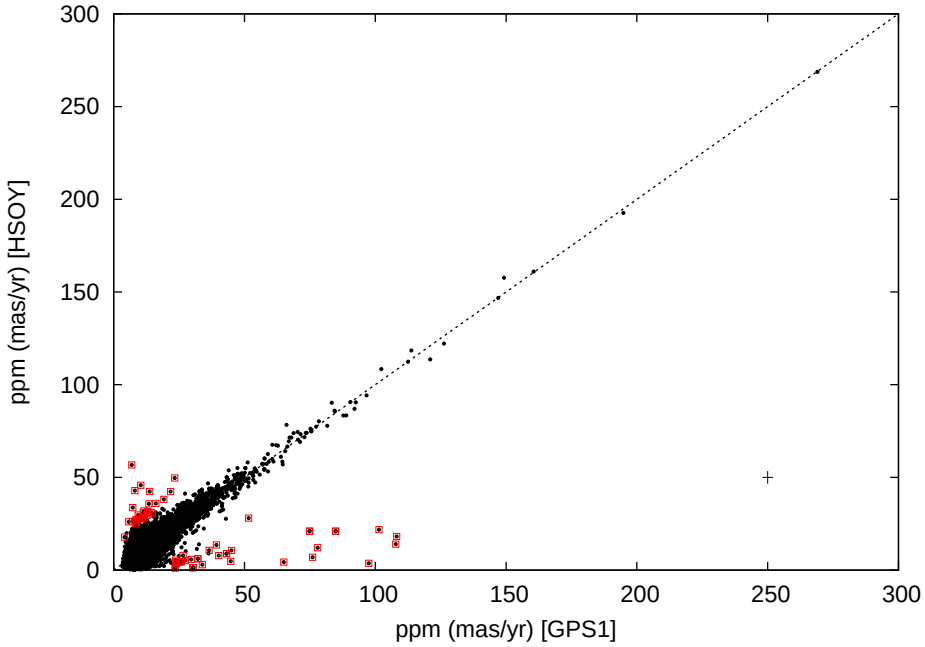

Figure 94 – Comparison between the GPS1 and HSOY proper motions. The outliers are marked with red squares. The dashed line represents equality between the two values. Average uncertainties are shown as a cross in the bottom right of the panel.

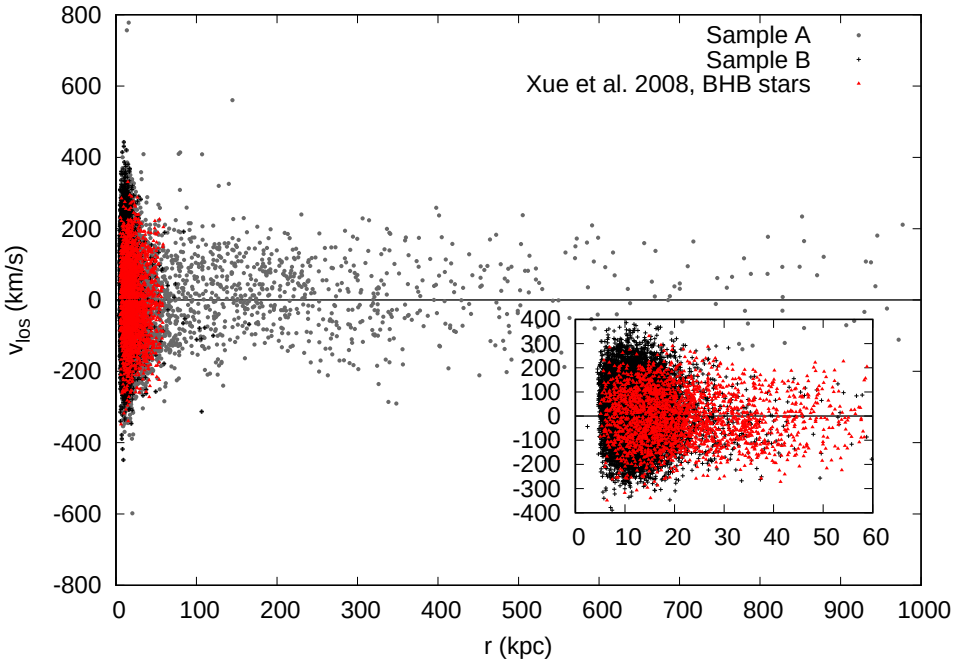

Figure 95 – Line-of-sight velocity in the GSR as a function of Galactocentric distance. Sample A (grey dots) and B (black crosses) are of course different, with the unreliable proper motion of sample A giving in some cases unrealistic values of distance. Focusing on sample B only (smaller overlay panel), distances and velocities are on a similar range as halo BHB stars (shown as red triangles for comparison), with slightly larger velocities giving a somewhat higher dispersion, as can be seen in Fig. 96.

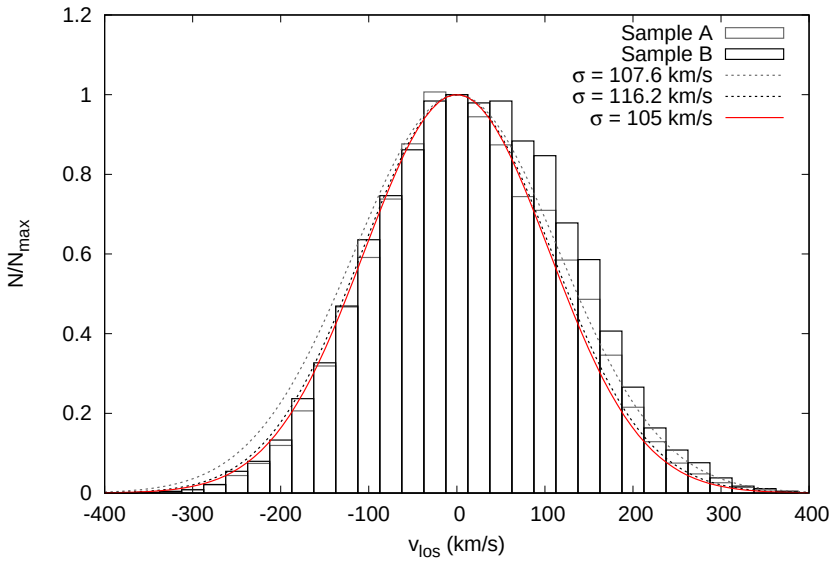

Figure 96 – Distribution of v_{los} for both samples A (black) and B (grey). The best fit Gaussian for each sample is shown as a dashed line of same colour. A Gaussian of width 105 km/s, similar to the value found by Xue et al. (2008) for halo BHB stars is shown in red for comparison. Samples A and B show very similar dispersions, which are consistent with the estimated for the Galactic halo.

APPENDIX C – Published papers

Monthly Notices of the ROYAL ASTRONOMICAL SOCIETY

MNRAS **455,** 3413–3423 (2016) doi:10.1093/mnras/stv2526

New white dwarf and subdwarf stars in the Sloan Digital Sky Survey Data Release 12

S. O. Kepler,[1⋆] I. Pelisoli,[1⋆] D. Koester,[2⋆] G. Ourique,[1] A. D. Romero,[1] N. Reindl,[3] S. J. Kleinman,[4] D. J. Eisenstein,[5] A. D. M. Valois[1] and L. A. Amaral[1]

[1]*Instituto de Física, Universidade Federal do Rio Grande do Sul, 91501-900 Porto-Alegre, RS, Brazil*
[2]*Institut für Theoretische Physik und Astrophysik, Universität Kiel, D-24098 Kiel, Germany*
[3]*Institute for Astronomy and Astrophysics, Kepler Center for Astro and Particle Physics, Eberhard Karls University, Sand 1, D-72076 Tübingen, Germany*
[4]*Gemini Observatory, Hilo, HI 96720, USA*
[5]*Harvard Smithsonian Center for Astrophysics, 60 Garden St., MS #20, Cambridge, MA 02138, USA*

Accepted 2015 October 27. Received 2015 October 26; in original form 2015 August 2

ABSTRACT

We report the discovery of 6576 new spectroscopically confirmed white dwarf and subdwarf stars in the Sloan Digital Sky Survey Data Release 12. We obtain $T_{\rm eff}$, log g and mass for hydrogen atmosphere white dwarf stars (DAs) and helium atmosphere white dwarf stars (DBs), estimate the calcium/helium abundances for the white dwarf stars with metallic lines (DZs) and carbon/helium for carbon-dominated spectra (DQs). We found one central star of a planetary nebula, one ultracompact helium binary (AM CVn), one oxygen line-dominated white dwarf, 15 hot DO/PG1159s, 12 new cataclysmic variables, 36 magnetic white dwarf stars, 54 DQs, 115 helium-dominated white dwarfs, 148 white dwarf + main-sequence star binaries, 236 metal-polluted white dwarfs, 300 continuum spectra DCs, 230 hot subdwarfs, 2936 new hydrogen-dominated white dwarf stars, and 2675 cool hydrogen-dominated subdwarf stars. We calculate the mass distribution of all 5883 DAs with S/N $\geq$ 15 in DR12, including the ones in DR7 and DR10, with an average S/N = 26, corrected to the 3D convection scale, and also the distribution after correcting for the observed volume, using $1/V_{\rm max}$.

Key words: catalogues – stars: magnetic field – subdwarfs – white dwarfs.

1 INTRODUCTION

White dwarf stars are the end product of evolution of all stars with progenitor masses below 7–10.6 $M_{\odot}$, depending on metallicity (e.g Ibeling & Heger 2013; Doherty et al. 2015; Woosley & Heger 2015), which corresponds to over 97 per cent of the total number of stars. Most white dwarfs do not generate energy from nuclear fusion, but radiate due to residual gravitational contraction. Because of the degenerate equation of state, this is accompanied by a loss of thermal energy instead of increase as in the case of ideal gases; the evolution of white dwarfs is therefore often simply described as cooling. The radius of a white dwarf star is of the same order of the Earth's radius, which implies that they have small surface area, resulting in very large cooling times (it takes approximately 10^{10} yr for the effective temperature of a normal mass white dwarf to decrease from 100 000 K to near 5000 K). Consequently, the cool ones are among the oldest objects in the Galaxy. Therefore, studying white dwarfs is extremely important to comprehend the processes of stellar formation and evolution in the Milky Way (e.g. Winget et al. 1987; Bergeron, Saffer & Liebert 1992; Liebert, Bergeron & Holberg 2005; Moehler & Bono 2008; Tremblay et al. 2014).

The number of known white dwarf stars is increasing fast thanks to the Sloan Digital Sky Survey (SDSS). The first full white dwarf catalogue from SDSS data (Kleinman et al. 2004) was based on SDSS Data Release 1 (DR1; Abazajian et al. 2003). Using data from the SDSS Data Release 4 (DR4; Adelman-McCarthy et al. 2006), Eisenstein et al. (2006) roughly doubled the number of spectroscopically confirmed white dwarf stars. In the white dwarf catalogue based on the SDSS Data Release 7 (DR7; Abazajian et al. 2009), Kleinman et al. (2013) increased the total number of white dwarf stars by more than a factor of 2 compared to the catalogue based on DR4 data. They also (re)analysed all stars from previous releases. Over 8000 new spectroscopically confirmed white dwarf stars were reported by Kepler et al. (2015) in the analysis of SDSS Data Release 10 (DR10; Ahn et al. 2014). They also improved the candidate selection compared to previous catalogues, implementing an automated search algorithm to search objects which were missed by the other selection criteria. It was also the first white dwarf catalogue based on SDSS data to fit not only DA and DB stars, but also DZ, DQ, and DA+MS pairs. We continue such detailed analysis

⋆ E-mail: kepler@if.ufrgs.br (SOK); ingrid.pelisoli@gmail.com (IP); koester@astrophysik.uni-kiel.de (DK)

Table 1. Number of objects and the main classifications in the previous white dwarf catalogues published based on SDSS data releases.

Catalogue	Objects	Main classifications
DR1[a]	2551 WDs	1888 DA
	240 sds	171 DB
DR4[b]	9316 WDs	8000 DA
	928 sds	731 DB
DR7[c]	19 713 WDs	12 831 DA
		922 DB
DR10[d]	8441 WDs	6887 DA
	647 sds	450 DB

Notes. [a]Kleinman et al. (2004).
[b]Eisenstein et al. (2006).
[c]Kleinman et al. (2013), includes the (re)analysis of stars from previous releases, but does not include subdwarfs.
[d]Kepler et al. (2015).

here with SDSS Data Release 12 (DR12; Alam et al. 2015). More details concerning the previous catalogues are presented in Table 1.

Although the SDSS increased the number of spectroscopically confirmed white dwarf stars more than an order of magnitude prior to the SDSS, the SDSS sample is far from complete. Target selection considerations of the original SDSS (up to DR8) implied that white dwarf selection for spectroscopy was incomplete (e.g. Gentile Fusillo, Gänsicke & Greiss 2015). In the SDSS DR12, the ancillary target programme 42 (Dawson et al. 2013) obtained the spectra of an additional 762 colour selected white dwarf candidates that were missed by prior SDSS spectroscopic surveys, i.e. up to DR10. Here, we report on our search for new white dwarfs from the SDSS DR12 (Alam et al. 2015), which in total observed photometrically one third of the celestial sphere and obtained 4.3 million useful optical spectra. Our catalogue does not include stars reported in the earlier catalogues, except for classification corrections.

2 TARGET SELECTION

Even though targeting in SDSS produced the largest spectroscopic sample of white dwarfs, much of SDSS I and II white dwarf targeting required that the objects be unblended, which caused many bright white dwarfs to be skipped (for a detailed discussion, see section 5.6 of Eisenstein et al. 2006). The Baryon Oscillation Spectroscopic Survey (BOSS) ancillary targeting programme (Dawson et al. 2013) relaxed this requirement and imposed colour cuts to focus on warm and hot white dwarfs. Importantly, the BOSS spectral range extends further into the ultraviolet, covering from 3610 to 10 140 Å, with spectral resolution 1560–2270 in the blue channel, and 1850–2650 in the red channel (Smee et al. 2013), allowing full coverage of the Balmer lines.

The targeted white dwarfs in SDSS-III were required to be point sources with clean photometry, and to have USNO-B Catalogue counterparts (Monet et al. 2003). They were also restricted to regions inside the DR7 imaging footprint and required to have colours within the ranges $g < 19.2$, $(u - r) < 0.4$, $-1 < (u - g) < 0.3$, $-1 < (g - r) < 0.5$, and to have low Galactic extinction $A_r < 0.5$ mag. Additionally, targets that did not have $(u - r) < -0.1$ and $(g - r) < -0.1$ were required to have USNO proper motions larger than 2 arcsec per century. Objects satisfying the selection criteria that had not been observed previously by the SDSS (ANC 42) were denoted by the WHITEDWARF_NEW target flag, while those with prior SDSS white dwarf photometric classification (ANC 43) are assigned the WHITEDWARF_SDSS flag. Some of the latter were re-observed with BOSS in order to obtain the extended wavelength coverage that the BOSS spectrograph offers. The targeting colour selection included DA stars with temperatures above ∼14 000 K, helium atmosphere white dwarfs above ∼8000 K, as well as many rarer classes of white dwarfs. Hot subdwarfs (sdB and sdO) were targeted as well.

Our selection of white dwarf candidates among DR12 objects was similar to that reported for DR10 (Kepler et al. 2015). We did not restrict our sample by magnitude, but by S/N ≥ 3. In addition to the 762 targeted white dwarf candidates after DR10 by ANC 42, we selected the spectra of any object classified by the ELODIE pipeline (Bolton et al. 2012) as a white dwarf, which returned 35 708 spectra, an O, B or A star, which returned another 144 471 spectra. Our general colour selection from Kleinman et al. (2013), which takes into account that SDSS multicolour imaging separates hot white dwarf and subdwarf stars from the bulk of the stellar and quasar loci in colour–colour space (Harris et al. 2003), returned 68 836 new spectra, from which we identified another 2092 white dwarfs, 79 subdwarfs, 36 cataclysmic variables (CVs), and 3 PG 1159. Most of these spectra were overlapping with the ELODIE selections.

We also used an automated search algorithm which assumes that the spectra of two objects with the same composition, effective temperature and surface gravity differ only in flux, due to different distances, and slope, because of reddening and calibration issues. This algorithm determines a polynomial of order between zero and two which minimizes the difference between each spectrum and a sample of models, allowing the determination of the most likely spectral class of each object. Running this search over the whole 4.5 million spectra from DR 12 recovered more than 80 per cent of our sample and found 400 white dwarf stars missed by previous searches.

3 DATA ANALYSIS

The data analysed here were reduced by the V5_0_7 spectroscopic reduction pipeline of Bolton et al. (2012). After visual identification of the spectra as a probable white dwarf, we fitted the optical spectra to DA and DB local thermodynamic equilibrium (LTE) grids of synthetic non-magnetic spectra derived from model atmospheres (Koester 2010). The DA model grid uses the ML2/$\alpha = 0.6$ approximation, and for the DBs we use the ML2/$\alpha = 1.25$ approximation, to be consistent with Kleinman et al. (2013) and Kepler et al. (2015). Our DA grid extends up to $T_{\rm eff} = 100\,000$ K, but non-local thermodynamic equilibrium (NLTE) effects are not included. Napiwotzki (1997) concluded pure hydrogen atmospheres of DA white dwarfs are well represented by LTE calculations for effective temperatures up to 80 000 K, but when traces of helium are present, NLTE effects on the Balmer lines occur, down to effective temperatures of 40 000 K. Napiwotzki (1997) concluded LTE models should exclude traces of helium for the analysis of DA white dwarfs. We fitted the spectral lines and photometry separately (Koester 2010), selecting between the hot and cool solutions using photometry as an indicator.

Of the 762 objects targeted specifically as new white dwarf spectra by BOSS as Ancillary Programme 42, 19 were not identified as white dwarfs or subdwarfs by us. Of the Ancillary Programme 43 of WHITEDWARF_SDSS already observed, 5 in 80 colour selected stars are in fact quasars. Gentile Fusillo et al. (2015) reports that only 40 per cent of their SDSS colour selected sample with high probability of being a white dwarf has spectra obtained by SDSS.

The SDSS spectra we classified as white dwarfs or subdwarfs have a g-band signal–to–noise ratio $85 \geq \mathrm{S/N}(g) \geq 3$, with an average of 12. The lowest S/N in the g-band occurs for stars cooler than 7000 K, but they have significant S/N in the red part of the spectrum.

We include in our tables the new proper motion determinations of Munn et al. (2014) and use them to separate DCs from BL Lac spectra. We applied complete, consistent human identifications of each candidate white dwarf spectrum.

3.1 Spectral classification

Because we are interested in obtaining accurate mass distributions for our DA and DB stars, we were conservative in labelling a spectrum as a clean DA or DB, adding additional subtypes and uncertainty notations (:) if we saw signs of other elements, companions, or magnetic fields in the spectra. While some of our mixed white dwarf subtypes would probably be identified as clean DAs or DBs with better signal-to-noise spectra, few of our identified clean DAs or DBs would likely be found to have additional spectral features within our detection limit.

We looked for the following features to aid in the classification for each specified white dwarf subtype.

(i) Balmer lines – normally broad and with a steep Balmer decrement (DA but also DAB, DBA, DZA, and subdwarfs).
(ii) He I 4 471 Å (DB, subdwarfs).
(iii) He II 4 686 Å (DO, PG1159, sdO).
(iv) C2 Swan band or atomic C I lines (DQ).
(v) Ca II H and K (DZ, DAZ, DBZ).
(vi) C II 4 367 Å (HotDQ)
(vii) Zeeman splitting (magnetic white dwarfs).
(viii) Featureless spectrum with significant proper motion (DC).
(ix) Flux increasing in the red (binary, most probably M companion).
(x) O I 6158 Å (Dox).

We also found eight of stars to have an extremely steep Balmer decrement (i.e. only a broad H α and sometimes H β is observed while the other lines are absent) that could not be fitted with a pure hydrogen grid, or indicated extremely high gravities. We find that these objects are best explained as helium-rich DAs, and denote them DA-He.

We finally note that the white dwarf colour space also contains many hot subdwarfs. It is difficult to distinguish a low-mass white dwarf from a subdwarf, as they are both dominated by hydrogen lines and the small differences in surface gravity cannot be spotted by visual inspection alone. We therefore extended the model grid to $\log g = 5.00$ for $T_{\rm eff} \geq 25\,000$ K, and $\log g = 3.75$ for $T_{\rm eff} < 25\,000$ K, to separate white dwarfs ($\log g \geq 6.5$), subdwarfs ($6.5 > \log g \geq 5.5$) and main-sequence stars ($\log g \leq 4.75$) (see Section 4.1 and 4.7), but we caution that the differences in the line widths for DAs cooler than $\simeq$8000 K and hotter than $\simeq$30 000 K are minor, with changing gravity. We use sdA to denote spectra with $6.5 > \log g \geq 5.5$ and $T_{\rm eff} \leq 20\,000$ K. Table 2 lists the number of each type of white dwarf and subdwarf stars we identified.

As an independent check, and to be consistent with the earlier SDSS white catalogues, we also fitted all DA and DB white dwarf spectra and colours with the AUTOFIT code described in Kleinman et al. (2004), Eisenstein et al. (2006) and Kleinman et al. (2013). AUTOFIT fits only clean DA and DB models. In addition to the best-fitting model parameters, it also outputs flags for other features noted in the spectrum, like a possible dM companion. These fits include SDSS imaging photometry and allow for refluxing of the models by a low-order polynomial to incorporate effects of unknown reddening and spectrophotometric flux calibration errors.

Table 2. Numbers of newly identified stars by type.

No. of stars	Type
2675	sdA
1964	DA[a]
300	DC
236	DZ
183	sdB
104	WD+MS[b]
66	DB
71	DAZ
54	DQ
47	sdO
27	DBA
28	DAH
14	DO/PG 1159
12	CV
7	DZH
6	DAO
3	DAB
2	DBH
1	DBZ
1	Dox
1	AM CVn (SDSS J131954.47+591514.84)
1	CSPN (SDSS J141621.94+135224.2

Notes. [a]Pure and certain DAs.
[b]These spectra show both a white dwarf star and a companion, non-white dwarf spectrum, usually a main-sequence M star.

4 RESULTS

4.1 Masses

Kleinman et al. (2013) limited the white dwarf classification to surface gravity $\log g \geq 6.5$. At the cool end of our sample, $\log g = 6.5$ corresponds to a mass around 0.2 $\mathrm{M}_{\odot}$, well below the single mass evolution in the lifetime of the Universe. The He-core white dwarf stars in the mass range 0.2–0.45 $\mathrm{M}_{\odot}$, referred to as low-mass white dwarfs, are usually found in close binaries, often double degenerate systems (Marsh, Dhillon & Duck 1995), being most likely a product of interacting binary stars evolution. More than 70 per cent of those studied by Kilic et al. (2011) with masses below 0.45 $\mathrm{M}_{\odot}$ and all but a few with masses below 0.3 $\mathrm{M}_{\odot}$ show velocity variations (Brown et al. 2013; Gianninas et al. 2014). Kilic, Stanek & Pinsonneault (2007) suggests single low-mass white dwarfs result from the evolution of old metal-rich stars that truncate evolution before the helium flash due to severe mass-loss. They also conclude all white dwarfs with masses below $\simeq$0.3 $\mathrm{M}_{\odot}$ must be a product of binary star evolution involving interaction between the components, otherwise the lifetime of the progenitor on the main sequence would be larger than the age of the Universe.

DA white dwarf stars with masses $M \leq 0.45\,\mathrm{M}_{\odot}$ and $T_{\rm eff} < 20\,000$ K are low mass and extremely low mass (ELM) as found by Brown et al. (2010), Kilic et al. (2011), Kilic et al. (2012), Brown et al. (2012), Brown et al. (2013), and Gianninas et al. (2014). Hermes et al. (2012), Hermes et al. (2013b), Hermes et al. (2013a), and Bell et al. (2015) found pulsations in six of these ELMs, similar to the pulsations seen in DAVs (ZZ Ceti stars), as described in Van Grootel et al. (2013). Maxted et al. (2014a) found

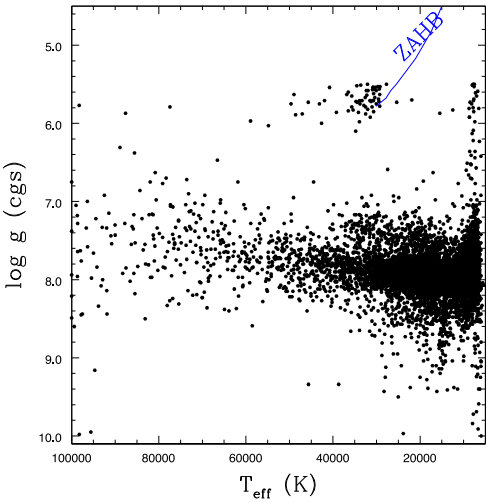

Figure 1. Surface gravity ($\log g$) and effective temperature ($T_{\rm eff}$) estimated for all DA white dwarf stars in DR7 to DR12 with spectral S/N$_g \geq 15$, after applying 3D convection atmospheric model corrections from Tremblay et al. (2013). The Zero Age Horizontal Branch (ZAHB) plotted was calculated with solar composition models. It indicates the highest possible surface gravity for a hot subdwarf. Stars with $T_{\rm eff} \leq 45\,000$ K and smaller surface gravities than the ZAHB are sdBs.

17 pre-ELMs, i.e. helium white dwarf precursors, and Maxted et al. (2014b) report pulsations in one of them. Pulsations are an important tool to study the stellar interior, and Córsico & Althaus (2014b), Córsico & Althaus (2014a), Córsico & Althaus (2015), Istrate et al. (2014a), and Istrate (2015) report on theoretical models and pulsations of ELMs.

We classified as DAs those with $\log g \geq 6.5$ as in Kleinman et al. (2013), and sdAs those with $6.5 > \log g \geq 5.5$ when $T_{\rm eff} \leq 20\,000$ K (see Section 4.7). Low metallicity main-sequence stars have an upper limit to $\log g \lesssim 4.75$. To select the low $\log g$ limit, we use an external, systematic uncertainty in our surface gravity determinations of $3\sigma(\log g) = 3 \times 0.25$, around 15× our average internal fitting uncertainty.

Fig. 1 shows surface gravity, $\log g$, as a function of the effective temperature $T_{\rm eff}$, estimated for all 5884 DAs spectroscopically identified in DR7 to DR12 with SDSS spectral S/N $\geq$ 15. We include corrections to $T_{\rm eff}$ and $\log g$ based on 3D convection calculations from Tremblay et al. (2013).

We use the mass–radius relations of Renedo et al. (2010) and Romero, Campos & Kepler (2015) for carbon–oxygen DA white dwarfs with solar metallicities to calculate the mass of our identified DA stars from the $T_{\rm eff}$ and $\log g$ values obtained from our fits, after correcting to 3D convection. These mass–radius relations are based on full evolutionary calculations appropriate for the study of hydrogen-rich DA white dwarfs that take into account the whole evolution of progenitor stars. The sequences are computed from the zero-age main sequence, through the hydrogen and helium central burning stages, thermal pulsations and mass-loss in the asymptotic giant branch phase and finally the planetary nebula domain. The white dwarf masses for the resulting sequences range from 0.525 to 1.024 M$_\odot$, covering the stellar mass range for C–O core DAs. For high-gravity white dwarf stars, we used the mass–radius relations for O–Ne core white dwarfs given in Althaus et al. (2005) in the mass range from 1.06 to 1.30 M$_\odot$ with a step of 0.02 M$_\odot$. For the low-gravity white dwarf and cool subdwarf stars, we used the evolutionary calculations of Althaus, Miller Bertolami & Córsico (2013) for helium-core white dwarfs with stellar mass between 0.155 and 0.435 M$_\odot$, supplemented by sequences of 0.452 and 0.521 M$_\odot$ calculated in Althaus et al. (2009a).

Table 3. Mean masses for all DAs, corrected to 3D convection.

S/N$_g$	N	$\langle M_{\rm DA}\rangle$ (M$_\odot$)
15	5884	0.608 ± 0.002
25	2591	0.620 ± 0.002
50	265	0.644 ± 0.008

The spectra we classified as DBs belong to 116 stars. 27 of these are DBAs, one is a DBZ (SDSS J122649.96+444513.59), and eight are DB+M. To calculate the DB white dwarf masses in the catalogue, we relied on the evolutionary calculations of hydrogen-deficient white dwarf stars with stellar masses between 0.515 and 0.870 M$_\odot$ computed by Althaus et al. (2009b). These sequences have been derived from the born-again episode responsible for the hydrogen-deficient white dwarfs. For high- and low-gravity DBs, we used the same O–Ne and helium evolutionary sequences described before.

To calculate a reliable mass distribution for DAs, we selected only the S/N $\geq$ 15 spectra with temperatures well fit by our models. Including the DAs from DR7 (Kleinman et al. 2013) and DR10 (Kepler et al. 2015), we classified a total of 5884 spectra as clean DAs with S/N $\geq$ 15, with a mean S/N $= 26 \pm 11$. Table 3 presents the mean masses for different signal-to-noise limits. Gianninas, Bergeron & Fontaine (2005) estimate the increase of the uncertainty in the surface gravity from $\Delta\log g \simeq$0.06 dex to $\Delta\log g \simeq$0.25 dex, when the S/N decreases from 50 to 15. Genest-Beaulieu & Bergeron (2014) conclude there appears to be a small residual zero-point offset in the absolute fluxes of SDSS spectra. If the differences in the mean masses with S/N are not due to systematic (not random) effects, it could be the reflection of different populations, as faint stars perpendicular to the disc of the Galaxy could have different metallicities, and therefore different star formation mass functions and different initial-to-final-mass relations (Romero et al. 2015). The mean masses estimated in our DR7 to DR12 sample are smaller than those obtained by Kepler et al. (2015), even with the use of the 3D corrections for the whole sample.

Fig. 2 shows the mass histogram for the 5884 DAs with S/N $\geq$ 15 and Fig. 3 shows the mass distribution after correcting by the observed volume, following Schmidt (1968, 1975), Green (1980), Stobie, Ishida & Peacock (1989), Liebert, Bergeron & Holberg (2003a), Kepler et al. (2007), Limoges & Bergeron (2010) and Rebassa-Mansergas et al. (2015). This correction takes into account the shape of the galactic disc, assuming a scaleheight of 250 pc, minimum ($g \simeq$14.5) and maximum ($g = 19$) magnitudes, for a complete sample. Green (1980) propose completeness can be estimated from $\langle V/V_{\rm max}\rangle$, which is equal to 0.48 in our sample, close to the expected value of 0.50.

Rebassa-Mansergas et al. (2015) limit their sample to bolometric magnitude $M_{\rm bol} \leq 13$, because Gentile Fusillo et al. (2015) estimates completeness of 40 per cent down to this magnitude. Such bolometric magnitude corresponds to $T_{\rm eff} \gtrsim 8500$ K around

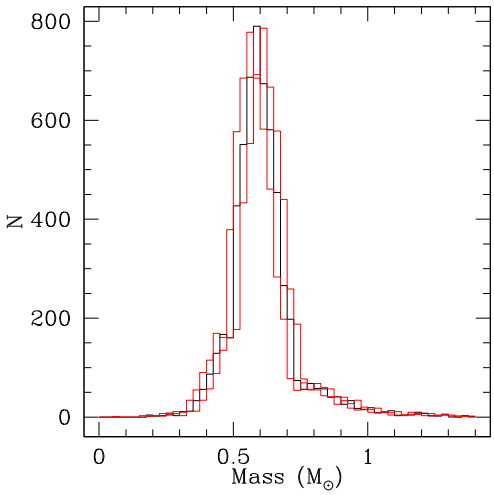

Figure 2. Histogram for the mass distribution of 5884 S/N ≥ 15 DAs versus mass, for log *g* corrected to 3D convection models using the corrections reported in Tremblay et al. (2013). The coloured lines show the -1σ and $+1\sigma$ uncertainties.

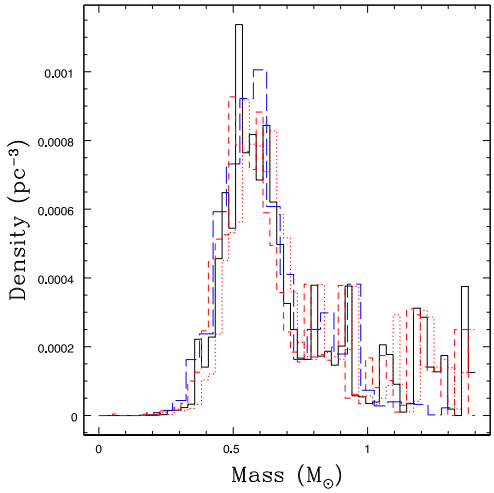

Figure 3. Histogram for the density distribution of S/N ≥ 15 DAs versus mass, for log *g* corrected to 3D convection models, after correcting by the observed volume and by 40 per cent completeness from Gentile Fusillo et al. (2015). The coloured lines show the -1σ and $+1\sigma$ uncertainties. The long dashed (blue) histogram is the one from Rebassa-Mansergas et al. (2015), limited to $M_{\rm bol} > 13$.

masses 0.6 $M_\odot$, and to $T_{\rm eff} \gtrsim 10\,000$ K around masses 1.0 $M_\odot$. We do not limit our sample to $M_{\rm bol} \leq 13$. We find 94 DA white dwarf stars with masses above 1.0 $M_\odot$ and S/N ≥ 15, and applying the volume correction to them, find a lower limit to their density of 0.000 026 $M_\odot$ pc^{-3}. 20 of these have $M_{\rm bol} > 13$. We did not apply any completeness correction by proper motion (e.g. Lam, Rowell & Hambly 2015) because we did not apply a consistent limit on the proper motion. The distribution for masses above the main peak around 0.6 $M_\odot$ is significantly uneven, possibly the outcome of distinct formation mechanisms, including single star formation, accretion, and mergers.

The DB mass distribution obtained from models including hydrogen contamination, is discussed in Koester & Kepler (2015). As our temperatures and surface gravities were estimated with pure DB models, while those of Koester & Kepler (2015) include hydrogen contamination, their values are more accurate.

4.2 Magnetic fields and Zeeman splittings

When examining each white dwarf candidate spectrum by eye, we found 36 stars with Zeeman splittings indicating magnetic fields above 2 MG – the limit where the line splitting becomes too small to be identified at the SDSS spectral resolution. This number is similar to our findings reported for DR7 in Kepler et al. (2013) and DR10 (Kepler et al. 2015).

If the line splitting and magnetic fields were not recognized, the spectral fittings of DA and DB models would have rendered too high log *g* determinations due to magnetic broadening being misinterpreted as pressure broadening.

We also identified seven cool DZH (Table 4), similar to those identified by Hollands, Gänsicke & Koester (2015).

We estimated the mean fields for the new DAHs following Külebi et al. (2009) as being from 3 to 80 MG. We caution that stars with large fields are difficult to identify because fields above around 30 MG, depending on effective temperature and signal-to-noise, intermixes subcomponents between different hydrogen series components so much that it becomes difficult to identify the star as containing hydrogen at all, and affect the colours significantly. Additionally, white dwarf stars with fields above 100 MG (see Fig. 4) represent the intermediate regime in which the spectra have very few features, except for a few stationary transitions that have similar wavelengths for a reasonable distribution of magnetic fields over the surface of the star.

In Kleinman et al. (2013) and Kepler et al. (2013), we misclassified SDSS J110539.77+250628.6, Plate–MJD–Fibre (P–M–F) = 2212–53789–0201 and SDSS J154012.08+290828.7, P–M–F = 4722–55735–0206 as magnetic, but they are in fact CVs. SDSS J110539.77+250628.6 was identified as an AM Her star by Liu et al. (2012). Here, we update the identification of SDSS J154012.08+290828.7 to a CV, with a period around 0.1 d based on data from the Catalina Sky Survey (CSS; Drake et al. 2009). We found another 14 CVs based on seeing hydrogen and/or helium lines in emission. Most are variable in the CSS.

Table 4. Magnetic field for DZHs.

SDSS J	Plate–MJD–Fibre	B (MG)	$\sigma(B)$ (MG)
003708.42−052532.80	7039–56572–0140	7.2	0.2
010728.47+265019.94	6255–56240–0896	3.4	0.1
110644.27+673708.64	7111–56741–0676	3.3	0.1
111330.27+275131.41	6435–56341–0036	3.0	0.1
114333.46+661532.01	7114–56748–0973	9.0	1.5
225448.83+303107.15	6507–56478–0276	2.5	0.1
233056.81+295652.68	6501–56563–0406	3.4	0.3

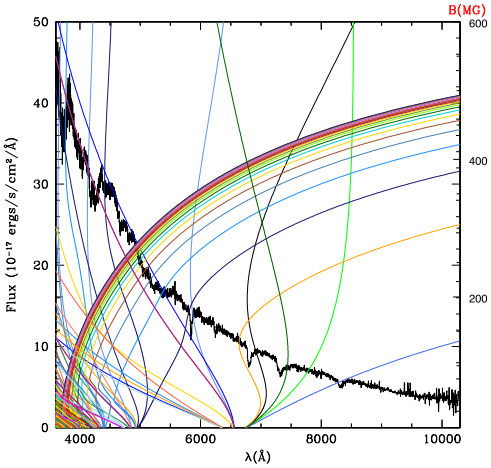

Figure 4. Observed spectrum of the DAH, SDSS J112148.77+103934.1 with $g = 17.98 \pm 0.03$ and $B \simeq 309$ MG. The coloured lines indicate the positions of each theoretical Zeeman split Balmer line subcomponent, assuming a dipole magnetic field of strength indicated in the right axis. Even low fields produce large splittings of the higher Balmer lines. The theoretical models are from Schimeczek et al. (2013), Schimeczek & Wunner (2014a) and Schimeczek & Wunner (2014b).

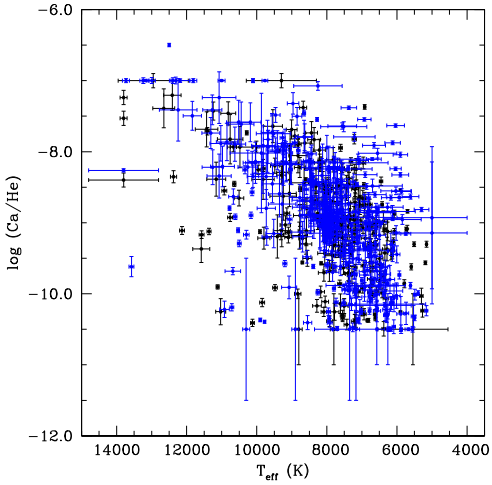

Figure 5. Calcium/Helium abundances estimated for DZs contained in DR7 to DR12.

4.3 DCs and BL Lac

Featureless optical spectra are the signature of DC white dwarfs, but also from extragalactic BL Lac objects. BL Lac objects are strong sources of radio emission, while non-interacting DCs are not. DCs, if bright enough to be detected in all images, generally have measurable proper motions, as their inherent dimness means they are relatively close to us. To separate DCs form BL Lacs, we searched for 1.4 GHz radio emission in the literature and looked for measured proper motions in Munn et al. (2014). We found 41 of our DC candidates were really BL Lac objects based on detectable radio emission. We discarded the objects with radio emission, as well as those with no radio emission and no proper motion.

4.4 DZs

Of the new white dwarfs in our sample, 3 per cent have spectra with metal lines, probably due to accretion of rocky material around the stars (e.g. Graham et al. 1990; Jura 2003; Koester, Gänsicke & Farihi 2014). Calcium and magnesium in general have the strongest lines for white dwarfs at these temperatures.

We identified two DBZs as having unusual oxygen lines. SDSS J124231.07+522626.6, P–M–F 6674–56416–0868, with $T_{\rm eff}$ = 13 000 K, was misclassified as an sdB from spectrum P–M–F 0885–52379–0112 in Eisenstein et al. (2006), and identified by us here as an oxygen-rich DBZ, possibly formed by accretion of an water-rich asteroid as suggested by Raddi et al. (2015) and Farihi, Gänsicke & Koester (2013). SDSS J123432.65+560643.1, spectrum P–M–F 6832–56426–0620, was identified as DBZA in Kleinman et al. (2013) from P–M–F 1020–52721–0540, but is a DBZ. We estimate $T_{\rm eff} = 12\,400 \pm 120$ K, $\log g = 8.135 \pm 0.065$.

We fit the spectra of each of the 236 stars classified as DZs to a grid of models with Mg, Ca and Fe ratios equal to the averages from the cool DZs in Koester et al. (2011), and Si added with the same abundance as Mg (Koester et al. 2014). These models have a fixed surface gravity of $\log g = 8.0$ as it is not possible to otherwise estimate it from the spectra. The absolute values for log Ca/He range from −7.25 to −10.50. Fig. 5 shows the calcium/helium abundance for the 246 DZs identified in DR12, in addition to those of DR7 and DR10. There seems to be a decrease of Ca/He abundances at lower temperatures. This trend might be explained if all stars had the same metal-rich material accretion rate, but the material becomes more diluted at cooler temperatures due to the increasing convection layer size.

4.5 DQs

Only 0.7 per cent of the newly identified spectra in our sample are dominated by carbon lines that are believed to be due to dredge-up of carbon from the underlying carbon–oxygen core through the expanding He convection zone (e.g. Koester, Weidemann & Zeidler 1982; Pelletier et al. 1986; Koester & Knist 2006; Dufour et al. 2007). These stars are in general cooler than $T_{\rm eff} = 12\,000$ K.

We fitted the spectra of the stars (classified as cool DQs) to a grid of models reported by Koester & Knist (2006). The models have a fixed surface gravity of $\log g = 8.0$ as it is not possible to otherwise estimate it from the spectra. The absolute values for log C/He range from −8 to −4, and effective temperatures vary from 13 000 K to 4400 K. Fig. 6 shows the carbon/helium abundance for the 54 new cool DQs identified here in addition to those from DR7 and DR10. There is a decrease of C/He abundances at lower temperatures, probably caused by the deepening of the convection zone, diluting any surface carbon.

4.6 White dwarf main-sequence binaries

We have identified 104 new white dwarfs that are part of apparent binary systems containing main-sequence companions (WD-MS binaries). The majority (96) of our new systems contain a DA white dwarf and an M dwarf secondary star (DA+M).

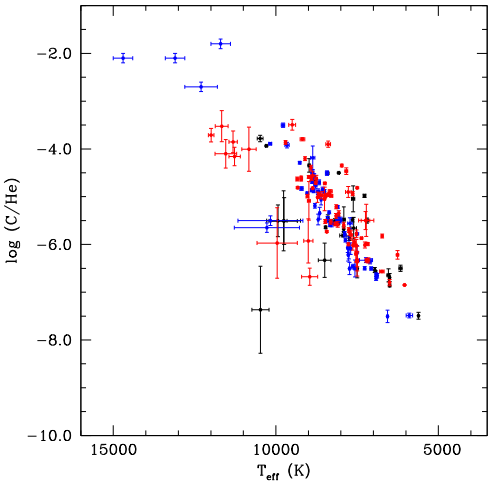

Figure 6. Carbon/Helium abundances estimated for DQs. The decrease with decreasing temperature comes from the increase in transparency and deepening convection zone. The darker points are the new DQs from DR12. The lighter (red and blue) points are the results of our fits with the same models for the cool DQs in Kleinman et al. (2013) and Kepler et al. (2015).

4.7 Subdwarfs

Hot subdwarfs are core He burning stars. Following Németh, Kawka & Vennes (2012), Drilling et al. (2013), Nemeth et al. (2014a), and Nemeth et al. (2014b), we have classified stars with $\log g < 6.5$ and $45\,000\,\mathrm{K} \geq T_{\rm eff} \geq 20\,000$ K as subdwarfs: sdOs if He II present and sdBs if not. Nemeth et al. (2014a) and Rauch et al. (2014) discuss how the He abundances typical for sdB stars affect the NLTE atmosphere structure. To a lower extent, CNO and Fe abundances are also important in deriving accurate temperatures and gravities. Our determinations of $T_{\rm eff}$ and $\log g$ do not include NLTE effects or mixed compositions, so they serve only as a rough estimate. We classified 47 new sdOs and 183 new sdBs.

The ELM white dwarf catalogue (Gianninas et al. 2015) lists 73 stars with $\log g \geq 4.8$, most with detected radial velocity variations demonstrating they are in binary system. We classified the hydrogen-dominated spectra with $6.5 > \log g_{\rm sdA} \geq 5.5$ and $T_{\rm eff} \leq 20\,000$ K as sdAs. These spectra look like main-sequence low metallicity A stars, but their estimated surface gravities with $\log g_{\rm sdA} \geq 5.5$ are at least 3σ (external) larger than those of main-sequence stars $\log g_{\rm MS} < 4.75$ (Heiter et al. 2015). We caution that the spectral lines and colours used in our analysis are weakly dependent on surface gravity for $T_{\rm eff} \leq 9000$ K. Even though a few of these stars have been classified previously as horizontal branch stars, to our knowledge, this is the first analysis with model spectra covering the range of surface gravities $3.75 \leq \log g \leq 10$. Of these sdAs, 1275 have estimated proper motions larger than 5 mas yr^{-1}, and 476 larger than 10 mas yr^{-1}. Because their spectra consists mainly of hydrogen lines, with cooler ones showing also Ca H and K, but no *G*- or CN-bands, we define their spectral types as sdA. We propose many of them are ELMs (Córsico & Althaus 2014b,a, 2015; Istrate et al. 2014a; Istrate, Tauris & Langer 2014b; Istrate 2015) but until their binarity can be established (e.g. Gianninas et al. 2015), we classify only their spectral type.

4.8 Noteworthy individual objects

Fig. 7 shows the spectrum of the AM CVn-type ultracompact double degenerate binary, SDSS J131954.47+591514.84, a new classification of a star with He-dominated atmosphere and He transfer. AM CVn objects are thought to be strong sources of gravitational waves (Nelemans 2005); however, only 43 such objects are known (Campbell et al. 2015; Levitan et al. 2015).

SDSS J141621.94+135224.20 (spectra with P–M–F 5458–56011–0636, Fig. 8) is a hot central star of a faint planetary nebula (CSPN) (PN G003.3+66.1) and was misclassified by

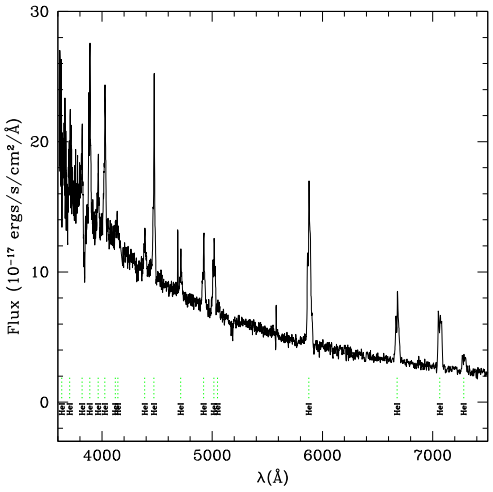

Figure 7. Spectra of the AM CVn double degenerate SDSS J131954.47+591514.84 ($g = 19.106 \pm 0.015$, proper motion = 33 mas yr^{-1}).

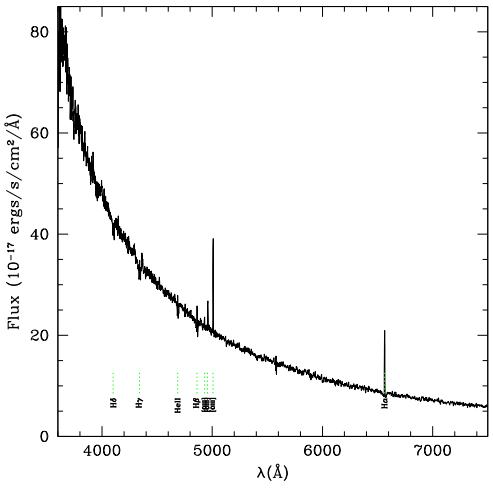

Figure 8. Spectra of the CSPN SDSS J141621.94+135224.20 ($g = 18.202 \pm 0.019$, proper motion = 12 mas yr^{-1}).

Gentile Fusillo et al. (2015) as a CV. It is listed in the Southern Hα Sky Survey Atlas; however, we could not detect any planetary nebula in either the SDSS image or wide-field infrared survey explorer images. Thanks to its higher S/N, the new SDSS spectrum reveals the nebular emission lines of [OIII] $\lambda\lambda$ 4931, 4956, 5007 Å, which we have now identified for the first time in this star. The lack of He I absorption lines indicates that the central star is hotter than 70 K. All photospheric absorption lines (Hδ, Hγ, Hβ, Hα as well as He II $\lambda\lambda$ 4686, 5412 Å) show central emissions. They are likely nebular lines, however a photospheric contribution cannot be excluded for very hot central stars.

SDSS J103455.90+240905.75 (P–M–F 6439–56358–0445) was classified by Girven et al. (2011) as DAB from spectra 2352–53770–0124, SDSS J100015.28+240724.60 (P–M–F 6459–56273–0598) was classified as DB from spectra 2344–53740–0137, and SDSS J101935.69+254103.04 (P–M–F 6465–56279–0808) was classified as DA from spectra 2349–53734–0523, but the new higher S/N spectra shows they are DOs.

Liebert et al. (2003b), Gänsicke et al. (2010), and Kepler et al. (2015) report on stars with spectra with strong oxygen lines that Kepler et al. (2015) designated as Dox. SDSS J124043.01+671034.68, on spectra P–M–F 7120–56720–0894, is a new Dox with $T_{\rm eff}$ $\simeq$22 000 K.

Table 5 lists the columns of data provided in our electronic catalogue file, Table 6.

Table 7 lists 409 new classifications of stars already in Simbad (Strasbourg Astronomical Data Center), but for which new higher S/N spectra lead us to a different classification.

5 CONCLUSIONS AND DISCUSSION

We have identified 6576 new white dwarf and subdwarf stars in the DR 12 of the SDSS, and estimated the masses for DAs and DBs, as well as the calcium contamination in DZs and carbon/helium abundances in DQs. We were able to extend our identifications down to $T_{\rm eff}$ = 5000 K, although these are certainly not complete, as we relied also on proper motion measurements to distinguish between cool DCs and BL Lac objects. Proper motions are typically incomplete below $g \simeq 21$. The resultant substantial increase in the number of spectroscopically confirmed white dwarfs is important because it allows the discovery of more rare objects like massive white dwarfs, magnetic white dwarfs, and He-dominated objects with oxygen lines. Extending the work of Kepler et al. (2007) and Rebassa-Mansergas et al. (2015), we find 94 white dwarf stars with masses above 1 $M_\odot$ and S/N $\geq$ 15. Their volume corrected distribution is inhomogeneous which, if confirmed, indicates multiple formation processes, including mergers. The volume-limited sample of white dwarfs within 40 pc by Limoges, Bergeron & Lépine (2015) finds 8 per cent (22/288) of the local sample of white dwarfs have masses $M > 1$ $M_\odot$.

Massive white dwarfs are relevant both to the lower limit of core collapse supernova (SN) and to white dwarf explosion or merger as SN Ia. Nomoto, Kobayashi & Tominaga (2013) estimates that the observed ^{64}Zn abundances provides an upper limit to the occurrence of exploding O–Ne–Mg cores at approximately 20 per cent of all core-collapse SNe. The existence of different types of SN Ia indicates different types of progenitors do exist.

Table 5. Columns provided in data table, Table 6.

Column no.	Heading	Description
1	Name	SDSS object name (SDSS 2000J+)
2	P–M–F	SDSS Plate number–Modified Julian date–Fibre
3	SN_g	SDSS g-band signal-to-noise ratio
4	u_psf	SDSS u-band PSF magnitude
5	u_err	SDSS u-band uncertainty
6	g_psf	SDSS g-band PSF magnitude
7	g_err	SDSS g-band uncertainty
8	r_psf	SDSS r-band PSF magnitude
9	r_err	SDSS r-band uncertainty
10	i_psf	SDSS i-band PSF magnitude
11	i_err	SDSS i-band uncertainty
12	z_psf	SDSS z-band PSF magnitude
13	z_err	SDSS z-band uncertainty
14	$E(B-V)$	Colour excess
15	PM	USNO proper motion (mas yr^{-1})
16	l	Galactic longitude (degrees)
17	b	Galactic latitude (degrees)
18	T_eff	$T_{\rm eff}$ (K)
19	T_err	$T_{\rm eff}$ uncertainty (K)
20	log_g	log g (cgs)
21	log_gerr	log g uncertainty (cgs)
22	humanID	Human classification
23	T_eff (3D)	$T_{\rm eff}$ for pure DAs and DBs or $-$log(Ca/He) for DZs or $-$log(C/He) for DQs[a]
24	T_err (3D)	$T_{\rm eff}$ uncertainty
25	log_g (3D)	log g
26	log_gerr (3D)	log g uncertainty
27	Mass	Calculated mass ($M_\odot$), corrected to 3D convection
28	Mass_err	Mass uncertainty ($M_\odot$), corrected to 3D convection

Notes. [a]The temperatures and surface gravities are corrected to the 3D convection models of Tremblay et al. (2013). The Ca/He and C/He abundances, calculated assuming log g = 8.0, are indicated by $-$log(Ca/He) or $-$log(C/He).

Table 6. New white dwarf stars. Notes: P–M–F are the Plate–Modified Julian Date–Fibre number that designates an SDSS spectrum. A: designates an uncertain classification. The columns are fully explained in Table 5. When $\sigma(\log g) = 0.000$, we have assumed $\log g = 8.0$, not fitted the surface gravity. The full table is available online at http://astro.if.ufrgs.br/keplerDR12.html.

#SDSSJ			*u*	s*u*	*g*	s*g*	*r*	s*r*	*i*	s*i*	*z*	s*z*	*E*(*B*−*V*)	ppm	long	lat	sp	$T_{\rm eff}$	sT	log *g*	*s*log *g*	$T_{\rm eff}$	$dT_{\rm eff}$	log *g*	*d*log *g*	Mass	*d*mass
#	P–M–F	S/N	(mag)	(mag)	(mag)	(mag)	(mag)	(mag)	(mag)	(mag)	(mag)	(mag)	(mag)	0.001 arcsec	(°)	(°)		(K)	(K)	(cgs)	(cgs)	(K)	(K)	(cgs)	(cgs)	($M_\odot$)	($M_\odot$)
000000.46+174808.91	6207–56239–0156	005	21.460	0.125	20.966	0.033	20.992	0.045	21.063	0.068	21.211	0.322	0.028	024.4	106.0	−43.4	DA	09 683	00 132	7.945	0.174	09 635	0132	7.680	0.170	0.459	0.067
000007.84+304606.35	7134–56566–0587	011	20.208	0.039	19.665	0.017	19.534	0.021	19.495	0.023	19.562	0.059	0.060	44.69	110.1	−30.8	DA:	07 545	00 064	7.616	0.117	07 566	0064	7.470	0.120	0.366	0.042
000013.17−102750.57	7167–56604–0281	006	21.356	0.146	20.583	0.035	20.548	0.039	20.556	0.053	20.940	0.310	0.050	07.58	084.6	−69.4	sdA:	07 836	00 119	5.520	0.376						
000035.88−024622.11	4354–55810–0305	011	20.979	0.081	19.803	0.019	19.666	0.027	19.650	0.023	19.591	0.063	0.037	007.5	094.2	−62.8	sdA	07 893	00 065	6.143	0.189	07 893	0065	5.940	0.190	0.153	0.0016
000043.52+351644.26	7145–56567–0818	006	21.132	0.112	20.585	0.030	20.531	0.040	20.534	0.051	20.477	0.175	0.071	015.3	111.4	−26.5	DA	09 208	00 104	8.095	0.149	09 178	0104	7.820	0.150	0.521	0.064
000049.03−105805.58	7167–56604–0202	010	20.992	0.104	20.036	0.032	19.768	0.027	19.774	0.032	19.717	0.116	0.036	002.0	084.1	−69.9	sdA	07 092	00 083	6.180	0.259	07 117	0083	6.003	0.260	0.149	0.0040
000052.60+265459.66	6511–56540–0042	017	19.480	0.044	18.577	0.022	18.258	0.015	18.174	0.017	18.129	0.028	0.046	005.7	109.2	−34.6	sdA	06 862	00 045	5.963	0.155	06 889	0045	5.804	0.150	0.147	0.0009
000100.52−100222.12	7167–56604–0234	005	21.850	0.308	20.956	0.088	20.953	0.071	21.108	0.094	21.952	0.858	0.036	000.0	085.7	−69.2	DA	08 977	00 131	8.292	0.164	08 969	0131	8.020	0.160	0.609	0.088
000110.91+285342.93	7134–56566–0368	004	21.433	0.116	21.032	0.041	20.916	0.045	20.958	0.069	20.535	0.172	0.068	00.00	109.9	−32.7	DA:	07 722	00 166	8.229	0.236	07 735	0166	8.090	0.240	0.646	0.135
000133.32+170237.76	6173–56238–0428	005	21.173	0.121	20.752	0.038	20.974	0.059	21.087	0.078	22.163	0.567	0.028	000.0	106.2	−44.2	DA	11 198	01 000	7.690	0.500	11 283	1000	7.540	0.500	0.409	0.176
000134.78+201514.44	6170–56240–0638	009	20.626	0.080	20.232	0.024	20.126	0.028	20.053	0.037	20.048	0.147	0.073	56.89	107.3	−41.1	DA	07 512	00 093	8.343	0.132	07 520	0093	8.230	0.130	0.726	0.080
000134.86+321616.24	6498–56565–0910	009	20.541	0.059	20.204	0.025	20.184	0.035	20.428	0.062	20.858	0.314	0.051	000.0	110.8	−29.4	DA	10 088	00 089	8.189	0.094	10 042	0089	7.920	0.090	0.558	0.041

Table 7. New classification of known white dwarf stars.

#SDSSJ			*u*	s*u*	*g*	s*g*	*r*	s*r*	*i*	s*i*	*z*	s*z*	*E*(*B*−*V*)	ppm	long	lat	sp	$T_{\rm eff}$	sT	log *g*	*s*log *g*	$T_{\rm eff}$	$dT_{\rm eff}$	log *g*	*d*log *g*	Mass	*d*mass
#	P–M–F	S/N	(mag)	(mag)	(mag)	(mag)	(mag)	(mag)	(mag)	(mag)	(mag)	(mag)	(mag)	0.001 arcsec	(°)	(°)		(K)	(K)	(cgs)	(cgs)	(K)	(K)	(cgs)	(cgs)	($M_\odot$)	($M_\odot$)
000054.40−090806.92	7167–56604–0806	022	19.317	0.042	18.997	0.033	18.952	0.019	19.030	0.029	19.094	0.061	0.050	53.63	087.0	−68.4	DQ	07 957	01 000	8.000	0.000	−log(C/He)	=	8.000	0.000		
000307.06+241211.68	6879–56539–0704	064	16.159	0.022	16.190	0.022	16.556	0.028	16.806	0.017	17.053	0.026	0.147	04.41	109.0	−37.4	sdB	28 566	00 099	5.503	0.017						
000309.26−060233.49	7147–56574–0956	007	20.571	0.058	20.065	0.021	19.970	0.020	19.966	0.027	19.926	0.074	0.041	054.6	092.2	−66.0	DA	08 264	00 097	7.157	0.218	08 259	0097	6.940	0.220	0.234	0.039
000309.26−060233.49	7148–56591–0586	008	20.571	0.058	20.065	0.021	19.970	0.020	19.966	0.027	19.926	0.074	0.041	054.6	092.2	−66.0	DA	08 489	00 099	8.164	0.162	08 500	0099	7.930	0.160	0.559	0.076
000321.60−015310.86	4365–55539–0502	015	19.232	0.028	19.216	0.027	19.294	0.020	19.498	0.025	19.728	0.072	0.041	053.8	096.4	−62.3	DA	06 126	00 103	9.320	0.214	06 110	0103	9.370	0.210	1.285	0.072

With our spectral model grid now extending from $3.75 \leq \log g \leq 10$, we identified 2675 stars with hydrogen-dominated spectra, and surface gravities 3σ–7σ larger than those of main-sequence stars. Time series spectroscopy is necessary to check if they are binaries, in order to establish what fraction of the sdA objects are ELM white dwarfs. If they were to have main-sequence radii, their distances would be tens of kiloparsecs outside the disc due to their distance moduli of $15 \leq m - M \leq 20$. The substantial fraction of these stars that have measured proper motions, if at large distances, would also be runaway stars or hypervelocity stars ($v > 600$ km s^{-1}; Brown 2015). The significant number of these stars probably indicates Population II formation lead to a considerable ratio of binary stars. De Rosa et al. (2014) determine that 69 ± 7 per cent of all A stars in the solar neighbourhood are in binaries. The pre-white dwarf ages of low metallicity stars with main-sequence masses $0.9\,M_{\odot}$ can amount to more than 8 Gyr, therefore white dwarfs originating from binary interactions of low mass, low metallicity stars should still be visible as ELM white dwarfs. If the stars we classified as sdAs are in fact A-type main-sequence stars, there is a large number of those at large distances from the galactic disc, and the galactic formation model would have to account for the continuous formation of low metallicity stars, perhaps from the continuous accretion of dwarf galaxies (Camargo et al. 2015; Drlica-Wagner et al. 2015). Our analysis of their spatial distribution shows no concentrations.

ACKNOWLEDGEMENTS

SOK, IP, GO, ADR, and ADMV are supported by CNPq-Brazil. DK received support from programme Science without Borders, MCIT/MEC-Brazil. NR is supported by the German Aerospace Center (DLR, grant 05 OR 1507). This research has made use of NASA's Astrophysics Data System.

Funding for SDSS-III has been provided by the Alfred P. Sloan Foundation, the Participating Institutions, the National Science Foundation, and the US Department of Energy Office of Science. The SDSS-III website is http://www.sdss3.org/.

SDSS-III is managed by the Astrophysical Research Consortium for the Participating Institutions of the SDSS-III Collaboration including the University of Arizona, the Brazilian Participation Group, Brookhaven National Laboratory, Carnegie Mellon University, University of Florida, the French Participation Group, the German Participation Group, Harvard University, the Instituto de Astrofisica de Canarias, the Michigan State/Notre Dame/JINA Participation Group, Johns Hopkins University, Lawrence Berkeley National Laboratory, Max Planck Institute for Astrophysics, Max Planck Institute for Extraterrestrial Physics, New Mexico State University, New York University, Ohio State University, Pennsylvania State University, University of Portsmouth, Princeton University, the Spanish Participation Group, University of Tokyo, University of Utah, Vanderbilt University, University of Virginia, University of Washington, and Yale University.

REFERENCES

Abazajian K. et al., 2003, AJ, 126, 2081
Abazajian K. N. et al., 2009, ApJS, 182, 543
Adelman-McCarthy J. K. et al., 2006, ApJS, 162, 38
Ahn C. P. et al., 2014, ApJS, 211, 17
Alam S. et al., 2015, ApJS, 219, 12
Althaus L. G., García-Berro E., Isern J., Córsico A. H., 2005, A&A, 441, 689
Althaus L. G., Panei J. A., Romero A. D., Rohrmann R. D., Córsico A. H., García–Berro E., Miller Bertolami M. M., 2009a, A&A, 502, 207
Althaus L. G., Panei J. A., Miller Bertolami M. M., García–Berro E., Córsico A. H., Romero A. D., Kepler S.O, Rohrmann R. D., 2009b, ApJ, 704, 1605
Althaus L. G., Miller Bertolami M. M., Córsico A. H., 2013, A&A, 557, A19
Bell K. J., Kepler S. O., Montgomery M. H., Hermes J. J., Harrold S. T., Winget D. E., 2015, in Dufour P., Bergeron P., Fontaine G., eds, ASP Conf. Ser. Vol. 493, SDSS J1618+3854: The Sixth Extremely Low-Mass White Dwarf Pulsator. Astron. Soc. Pac., San Francisco, p. 217
Bergeron P., Saffer R. A., Liebert J., 1992, ApJ, 394, 228
Bolton A. S. et al., 2012, AJ, 144, 144
Brown W. R., 2015, ARA&A, 53, 15
Brown W. R., Kilic M., Allende Prieto C., Kenyon S. J., 2010, ApJ, 723, 1072
Brown W. R., Kilic M., Allende Prieto C., Kenyon S. J., 2012, ApJ, 744, 142
Brown W. R., Kilic M., Allende Prieto C., Gianninas A., Kenyon S. J., 2013, ApJ, 769, 66
Camargo D., Bica E., Bonatto C., Salerno G., 2015, MNRAS, 448, 1930
Campbell H. C. et al., 2015, MNRAS, 452, 1060
Córsico A. H., Althaus L. G., 2014a, A&A, 569, A106
Córsico A. H., Althaus L. G., 2014b, ApJ, 793, L17
Córsico A. H., Althaus L. G., 2015, in Dufour P., Bergeron P., Fontaine G., eds, ASP Conf. Ser. Vol. 493, Theoretical Modeling of Pulsating Low-mass White Dwarfs. Astron. Soc. Pac., San Francisco, p. 221
Dawson K. S. et al., 2013, AJ, 145, 10
De Rosa R. J. et al., 2014, MNRAS, 437, 1216
Doherty C. L., Gil-Pons P., Siess L., Lattanzio J. C., Lau H. H. B., 2015, MNRAS, 446, 2599
Drake A. J. et al., 2009, ApJ, 696, 870
Drilling J. S., Jeffery C. S., Heber U., Moehler S., Napiwotzki R., 2013, A&A, 551, A31
Drlica-Wagner A. et al., 2015, ApJ, 813, 109
Dufour P., Liebert J., Fontaine G., Behara N., 2007, Nature, 450, 522
Eisenstein D. J. et al., 2006, ApJS, 167, 40
Farihi J., Gänsicke B. T., Koester D., 2013, Science, 342, 218
Gänsicke B. T., Koester D., Girven J., Marsh T. R., Steeghs D., 2010, Science, 327, 188
Genest-Beaulieu C., Bergeron P., 2014, ApJ, 796, 128
Gentile Fusillo N. P., Gänsicke B. T., Greiss S., 2015, MNRAS, 448, 2260
Gianninas A., Bergeron P., Fontaine G., 2005, ApJ, 631, 1100
Gianninas A., Dufour P., Kilic M., Brown W. R., Bergeron P., Hermes J. J., 2014, ApJ, 794, 35
Gianninas A., Kilic M., Brown W. R., Canton P., Kenyon S. J., 2015, AJ, 812, 167
Girven J., Gänsicke B. T., Steeghs D., Koester D., 2011, MNRAS, 417, 1210
Graham J. R., Matthews K., Neugebauer G., Soifer B. T., 1990, ApJ, 357, 216
Green R. F., 1980, ApJ, 238, 685
Harris H. C. et al., 2003, AJ, 126, 1023
Heiter U., Jofré P., Gustafsson B., Korn A. J., Soubiran C., Thévenin F., 2015, A&A, 582, A49
Hermes J. J., Montgomery M. H., Winget D. E., Brown W. R., Kilic M., Kenyon S. J., 2012, ApJ, 750, L28
Hermes J. J. et al., 2013a, MNRAS, 436, 3573
Hermes J. J. et al., 2013b, ApJ, 765, 102
Hollands M. A., Gänsicke B. T., Koester D., 2015, MNRAS, 450, 681
Ibeling D., Heger A., 2013, ApJ, 765, L43
Istrate A. G., 2015, in Dufour P., Bergeron P., Fontaine G., eds, ASP Conf. Ser. Vol. 493, The Formation of Low-mass Helium White Dwarfs in Close Binaries. Astron. Soc. Pac., San Francisco, p. 487
Istrate A. G., Tauris T. M., Langer N., Antoniadis J., 2014a, A&A, 571, L3
Istrate A. G., Tauris T. M., Langer N., 2014b, A&A, 571, A45
Jura M., 2003, ApJ, 584, L91
Kepler S. O., Kleinman S. J., Nitta A., Koester D., Castanheira B. G., Giovannini O., Costa A. F. M., Althaus L., 2007, MNRAS, 375, 1315

Kepler S. O. et al., 2013, MNRAS, 429, 2934
Kepler S. O. et al., 2015, MNRAS, 446, 4078
Kilic M., Stanek K. Z., Pinsonneault M. H., 2007, ApJ, 671, 761
Kilic M., Brown W. R., Allende Prieto C., Agüeros M. A., Heinke C., Kenyon S. J., 2011, ApJ, 727, 3
Kilic M., Brown W. R., Allende Prieto C., Kenyon S. J., Heinke C. O., Agüeros M. A., Kleinman S. J., 2012, ApJ, 751, 141
Kleinman S. J. et al., 2004, ApJ, 607, 426
Kleinman S. J. et al., 2013, ApJS, 204, 5
Koester D., 2010, Mem. Soc. Astron. Ital., 81, 921
Koester D., Kepler S. O., 2015, A&A, in press
Koester D., Knist S., 2006, A&A, 454, 951
Koester D., Weidemann V., Zeidler E.-M., 1982, A&A, 116, 147
Koester D., Girven J., Gänsicke B. T., Dufour P., 2011, A&A, 530, A114
Koester D., Gänsicke B. T., Farihi J., 2014, A&A, 566, A34
Külebi B., Jordan S., Euchner F., Gänsicke B. T., Hirsch H., 2009, A&A, 506, 1341
Lam M. C., Rowell N., Hambly N. C., 2015, MNRAS, 450, 4098
Levitan D., Groot P. J., Prince T. A., Kulkarni S. R., Laher R., Ofek E. O., Sesar B., Surace J., 2015, MNRAS, 446, 391
Liebert J., Bergeron P., Holberg J. B., 2003a, AJ, 125, 348
Liebert J. et al., 2003b, AJ, 126, 2521
Liebert J., Bergeron P., Holberg J. B., 2005, ApJS, 156, 47
Limoges M.-M., Bergeron P., 2010, ApJ, 714, 1037
Limoges M.-M., Bergeron P., Lépine S., 2015, ApJS, 219, 19
Liu C., Li L., Zhang F., Zhang Y., Jiang D., Liu J., 2012, MNRAS, 424, 1841
Marsh T. R., Dhillon V. S., Duck S. R., 1995, MNRAS, 275, 828
Maxted P. F. L. et al., 2014a, MNRAS, 437, 1681
Maxted P. F. L., Serenelli A. M., Marsh T. R., Catalán S., Mahtani D. P., Dhillon V. S., 2014b, MNRAS, 444, 208
Moehler S., Bono G., 2008, preprint (arXiv:0806.4456v3)
Monet D. G. et al., 2003, AJ, 125, 984
Munn J. A. et al., 2014, AJ, 148, 132
Napiwotzki R., 1997, A&A, 322, 256
Napiwotzki R., 2007, in Napiwotzki R., Burleigh M. R., eds, ASP Conf. Ser. Vol. 372, 15th European Workshop on White Dwarfs. Astron. Soc. Pac., San Francisco, p. 387
Nelemans G., 2005, in Hameury J. M., Lasota J.-P., eds, ASP Conf. Ser. Vol. 330, The Astrophysics of Cataclysmic Variables and Related Objects. Astron. Soc. Pac., San Francisco, p. 27
Németh P., Kawka A., Vennes S., 2012, MNRAS, 427, 2180
Nemeth P., Östensen R., Vos J., Kawka A., Vennes S., 2014a, in van Grootel V., Green E., Fontaine G., Charpinet S., eds, ASP Conf. Ser. Vol. 481, 6th Meeting on Hot Subdwarf Stars and Related Objects. Astron. Soc. Pac., San Francisco, p. 75
Nemeth P., Östensen R., Tremblay P., Hubeny I., 2014b, in van Grootel V., Green E., Fontaine G., Charpinet S., eds, ASP Conf. Ser. Vol. 481, 6th Meeting on Hot Subdwarf Stars and Related Objects. Astron. Soc. Pac., San Francisco, p. 95
Nomoto K., Kobayashi C., Tominaga N., 2013, ARA&A, 51, 457
Pelletier C., Fontaine G., Wesemael F., Michaud G., Wegner G., 1986, ApJ, 307, 242
Raddi R., Gänsicke B. T., Koester D., Farihi J., Hermes J. J., Scaringi S., Breedt E., Girven J., 2015, MNRAS, 450, 2083
Rauch T., Rudkowski A., Kampka D., Werner K., Kruk J. W., Moehler S., 2014, A&A, 566, A3
Rebassa-Mansergas A., Rybicka M., Liu X.-M., Han Z., García-Berro E., 2015, MNRAS, 452, 1637
Renedo I., Althaus L. G., Miller Bertolami M. M., Romero A. D., Córsico A. H., Rohrmann R. D., García–Berro E., 2010, ApJ, 717, 183
Romero A. D., Campos F., Kepler S. O., 2015, MNRAS, 450, 3708
Schimeczek C., Wunner G., 2014a, Comput. Phys. Commun., 185, 614
Schimeczek C., Wunner G., 2014b, ApJS, 212, 26
Schimeczek C., Boblest S., Meyer D., Wunner G., 2013, Phys. Rev. A, 88, 012509
Schmidt M., 1968, ApJ, 151, 393
Schmidt M., 1975, ApJ, 202, 22
Smee S. A. et al., 2013, AJ, 146, 32
Stobie R. S., Ishida K., Peacock J. A., 1989, MNRAS, 238, 709
Tremblay P.-E., Ludwig H.-G., Steffen M., Freytag B., 2013, A&A, 559, A104
Tremblay P.-E., Kalirai J. S., Soderblom D. R., Cignoni M., Cummings J., 2014, ApJ, 791, 92
Van Grootel V., Fontaine G., Brassard P., Dupret M.-A., 2013, ApJ, 762, 57
Winget D. E., Hansen C. J., Liebert J., van Horn H. M., Fontaine G., Nather R. E., Kepler S. O., Lamb D. Q., 1987, ApJ, 315, L77
Woosley S. E., Heger A., 2015, ApJ, 810, 34

This paper has been typeset from a TEX/LATEX file prepared by the author.

Monthly Notices of the ROYAL ASTRONOMICAL SOCIETY

MNRAS **475,** 2480–2495 (2018) doi:10.1093/mnras/sty011
Advance Access publication 2018 January 9

The sdA problem – I. Physical properties

Ingrid Pelisoli,[1,2]★ S. O. Kepler[1] and D. Koester[3]

[1] *Instituto de Física, Universidade Federal do Rio Grande do Sul, 91501-900 Porto-Alegre, RS, Brazil*
[2] *Department of Physics, University of Warwick, Coventry CV4 7AL, UK*
[3] *Institut für Theoretische Physik und Astrophysik, Universität Kiel, D-24098 Kiel, Germany*

Accepted 2017 December 22. Received 2017 December 21; in original form 2017 August 23

ABSTRACT

The so-called sdA stars are defined by having H-rich spectra and surface gravities similar to hot subdwarf stars, but effective temperature below the zero-age horizontal branch. Their evolutionary history is an enigma: their surface gravity is too high for main-sequence stars, but too low for single evolution white dwarfs. They are most likely byproducts of binary evolution, including blue-stragglers, extremely-low mass white dwarf stars (ELMs) and their precursors (pre-ELMs). A small number of ELMs with similar properties to sdAs is known. Other possibilities include metal-poor A/F dwarfs, second generation stars, or even stars accreted from dwarf galaxies. In this work, we analyse colours, proper motions, and spacial velocities of a sample of sdAs from the Sloan Digital Sky Survey to assess their nature and evolutionary origin. We define a probability of belonging to the main sequence and a probability of being a (pre-)ELM based on these properties. We find that 7 per cent of the sdAs are more likely to be (pre-)ELMs than main-sequence stars. However, the spacial velocity distribution suggests that over 35 per cent of them cannot be explained as single metal-poor A/F stars.

Key words: binaries: general – stars: evolution – stars: kinematics and dynamics – subdwarfs – white dwarfs.

1 INTRODUCTION

The evolution of single stars is a fairly well understood process. There are of course many uncertainties concerning specific phases (e.g. the asymptotic giant branch, Miller Bertolami 2016) and processes (e.g. convection, Bressan et al. 2013; Tremblay et al. 2013) throughout the evolution, but relating an initial mass and metallicity to a final outcome can be done with reasonable precision. Only a very small amount of objects, much less than 5 per cent of all stars in the Galaxy, will end their lives as neutron stars or black holes – those with initial masses larger than about 7–10.6 $M_\odot$ (e.g. Woosley & Heger 2015). The remaining over 95 per cent stars will become white dwarf stars, whose evolution can be approximated by a slow cooling process. Hence, as they are not only abundant but also long-lived, white dwarfs are very useful in obtaining information of all Galactic populations (Isern et al. 2001; Liebert et al. 2005; Bono et al. 2013; Tremblay et al. 2016; Cojocaru et al. 2017; Kilic et al. 2017).

White dwarf stars are also one possible result of binary evolution, both in binary systems (e.g. Rebassa-Mansergas et al. 2016) or as single stars resulting from merger events (Brown et al. 2016b). Of remarkable interest are the extremely low mass white dwarfs (ELMs, $M \lesssim 0.20$ $M_\odot$, see e.g. the ELM Survey: Brown et al. 2010; Kilic et al. 2011; Brown et al. 2012; Kilic et al. 2012b; Brown et al. 2013; Gianninas et al. 2015; Brown et al. 2016a), which can only be formed in interacting binary systems within a Hubble time. The evolution of single stars can lead to white dwarfs with masses down to 0.30–0.45 solar masses (Kilic et al. 2007), but main-sequence progenitors that would end up as lower mass white dwarfs have main-sequence lifetimes exceeding the age of the Universe. Objects with $0.30 < M < 0.45$ $M_\odot$ are usually referred to as low-mass white dwarfs. Their binary fraction is still high, about 30 per cent (Brown et al. 2011), because some form of enhanced mass-loss is needed to form them, and binarity is the easiest way to achieve this. Severe mass-loss in the first ascent giant branch, attributed to high metallicity (Hansen 2005), can also lead to single low-mass white dwarfs (Kilic et al. 2007). The binary fraction below 0.2–0.3 $M_\odot$, on the other hand, could be up to 100 per cent (Brown et al. 2016a), encompassing not only the ELMs but also the pre-ELMs, which still have not reached the white dwarf cooling track (Maxted et al. 2014).

Less than a hundred ELMs are known to date, making it difficult to test and improve theoretical models (Córsico & Althaus 2014, 2016; Istrate et al. 2016). White dwarf catalogues such as Kleinman et al. (2013), which relies on Sloan Digital Sky Survey (SDSS) data release (DR) 7, usually opt to remove any object with estimated surface gravity below 6.5, the single evolution limit, excluding the

★ E-mail: ingrid.pelisoli@gmail.com

ELMs and pre-ELMs from their analysis. This flaw motivated Kepler et al. (2016) to extend their catalogue down to $\log g = 5.5$, which unveiled thousands of objects in the ELM range of $\log g$ and $T_{\rm eff} \lesssim 20\,000$ K. As their nature as ELMs or pre-ELMs cannot be confirmed without probing their radius and verifying they are compact objects, they were dubbed *sdAs*, referring to their $\log g$ placing them below the main sequence as the subdwarfs, and their hydrogen-dominated A-type spectra. This, however, is merely a spectroscopic classification, saying nothing about the evolutionary nature of these objects, which remains a puzzle. They cannot be canonical He-core burning subdwarfs, which show $T_{\rm eff} \geq 20\,000$ K, lying above the zero-age horizontal branch (ZAHB). Their estimated $\log g$ suggests they are not H core main-sequence stars, seeing that evolutionary models indicate that the maximum $\log g$ of main-sequence A stars is around 4.75 (see Romero et al. 2015, and references therein).

Hermes et al. (2017) studied the sdAs published by Kepler et al. (2016), which were modelled with pure-H atmosphere models, using radial velocities obtained from SDSS subspectra, photometric colours, and reduced proper motions, and concluded that over 99 per cent of them are unlikely to be ELMs. Likewise, Brown et al. (2017) obtained follow-up time-resolved spectroscopy for five eclipsing systems and concluded they are not ELMs, but metal-poor $M \sim 1.2\,{\rm M}_{\odot}$ main-sequence stars with $M \sim 0.8\,{\rm M}_{\odot}$ companions. They suggest that the majority of sdAs are metal-poor A–F type stars. Considering their distance modulus $(m - M) > 14.5$ at the SDSS bright saturation, this puts them in the halo. Given a halo age of 11.5 Gyr (Kalirai 2012; Kilic et al. 2012a, 2017; Si et al. 2017), only objects with $M \lesssim 0.8\,{\rm M}_{\odot}$ should still be in the main sequence (e.g. as obtained with the LPCODE by Althaus et al. 2003), and that assuming a very low metallicity of $Z = 0.0001$, i.e. halo A-type stars should even have already evolved off the main sequence. For the same metallicity, main-sequence lifetimes of A-stars are between 0.5 and 1.5 Gyr. Models by Schneider et al. (2015) suggest that mass accretion can make a star appear up to 10 times younger than its parent population, what explains the so-called blue stragglers (first identified by Sandage 1953). The sdAs could be explained as blue stragglers, when the $\log g$ is not higher than the main-sequence limit.

Brown et al. (2017) state that the $\log g$ derived from pure hydrogen models for sdA stars suffers from a systematic overestimate of $\sim$1 dex on the surface gravities, likely explained by metal line blanketing below 9000 K. In this work we re-analyse the sdA sample selected in Kepler et al. (2016) in the light of new spectral models including metals in solar abundances, first reported in Pelisoli et al. (2017). We assess the changes in $\log g$ between the two models, analysing particularly the sdAs in Kepler et al. (2016), to understand why Hermes et al. (2017) and Brown et al. (2017) found only a small percentage of them to have ELM properties. We extend the analysis to other sdAs selected from the SDSS data base, identifying new pre-ELM and ELM candidates. Their colours, proper motions, and spacial velocities are studied in order to assess their possible nature. The physical parameters we obtained are compared to both single evolution and binary evolution models to assess if they can be explained by this scenario. Based on our findings, we estimate for each object in our sample a probability of being a (pre-)ELM and a probability of being a main sequence star. These probabilities can be used to guide future follow-up of these objects. More than one evolution channel will certainly be needed to explain the sdA population. The binaries within the sample can help us better understand binary stellar evolution and its possible outcomes, while the properties and dynamics of single stars contain insight on the formation and evolution of the Galactic halo.

1.1 Properties of possible evolutionary paths to sdAs

The sdAs where first unveiled when we mined the SDSS data release 12 (DR12) for pre-ELMs and ELMs, as described in Kepler et al. (2016). They were believed to belong to either of these classes because of the $\log g$ estimated from their SDSS spectra. ELMs show $\log g$ in the range $5.0 \leq \log g \leq 7.0$ and $T_{\rm eff} \leq 18\,000$–$20\,000$ (e.g. Brown et al. 2016a), filling in the region between the main sequence and the white dwarfs resulting from single evolution in a $T_{\rm eff}$–$\log g$ diagram. However, they also show other particular properties. While their colours might be similar to main-sequence stars, ELM radii are at least 10 times smaller, so they are significantly less luminous than main-sequence stars, and thus need to be nearer to be detected at same magnitude. As a consequence, they show higher proper motions than main-sequence stars with similar properties. Moreover, they are expected to be encountered still with the close binary companion which led to their mass-loss. Most will merge within a Hubble time (Brown et al. 2016b), implying high radial velocity variation (Brown et al. 2016a, e.g. found a median semi-amplitude of $220\,{\rm km\,s^{-1}}$) and somewhat low orbital periods, usually shorter than 1 d (Brown et al. 2016a).

The properties of the precursors of the ELMs, the pre-ELMs, are more difficult to establish, as they have not reached the white dwarf cooling branch yet. If the time-scale for mass-loss from the white dwarf progenitor is longer than the thermal time-scale, a thick layer of hydrogen will be surrounding the degenerate helium core. This can lead to residual p–p chain reaction H nuclear burning which can last for several million years (e.g. Maxted et al. 2014). Moreover, instead of a smooth transition from pre-ELM to ELM, the star can undergo episodes of unstable CNO burning, or shell flashes. These flashes can shorten the cooling time-scale, by reducing the hydrogen mass on the surface. Althaus et al. (2013) find that they occur when $M \leq 0.18\,{\rm M}_{\odot}$, while Istrate et al. (2016) find that the minimum mass at which flashes will occur depends on the metallicity of the progenitor. Importantly, these flashes significant alter the radius and effective temperature of a pre-ELM, making it very difficult to distinguish them from main-sequence or even giant branch stars. Pietrzyński et al. (2012), for example, found a $0.26\,{\rm M}_{\odot}$ pre-ELM showing RR Lyrae-type pulsations – the flashes caused the object to reach the RR Lyrae instability strip. Its identification was possible because the system is eclipsing, with an orbital period of 15.2 d, which allowed for an estimate of the mass. Greenstein (1973) and Schönberner (1978) discuss an interesting example of a post-common envelope binary mimicking a main-sequence B star. So pre-ELMs can show $\log g$, $T_{\rm eff}$, and colours in the same range as main-sequence or even giant stars, being even as bright as them. Their ages are more consistent with the halo population than single main-sequence stars of similar properties though, since they are at a later stage of evolution.

If found in the halo without a close binary companion inducing enhanced mass-loss, an sdA could also be explained as a metal-poor star of type A–F. This is the explanation suggested by Brown et al. (2017). They have, however, based this conclusion on the fact that their fit of pure hydrogen models to metal abundant models seemed to indicate an overestimate in $\log g$ of about 1 dex. As we will show, the change in $\log g$ with the addition of metals to the modelled spectra is actually *not* a constant. Moreover, they have overlooked the possibility that the sdAs are pre-ELMs, which do show $\log g$ in the same range as main sequence stars, but are older and thus should be found in abundance in the halo, whose age is over 10 Gyr – close to 10 times the expected lifetime in the main sequence of A stars. Main-sequence A stars in the halo can only be explained as

blue-stragglers, where mass transfer from a companion extends their life in the main sequence, or by rare events of star formation induced by matter accreted to the Galaxy (Lance 1988; Camargo et al. 2015). Main-sequence F stars might still be approaching the turn-off point in the halo, so these and other late-type main-sequence stars could explain cooler sdAs ($T_{\rm eff} \lesssim 8000$ K). A key-way to analyse the feasibility of this scenario is analysing the spacial velocities of the sdAs given a main-sequence radius, as we will show in Section 5.

Finally, another possibility that might explain some sdA is that they are binaries of a hot subdwarf with a main-sequence companion of type F, G, or K, as found by Barlow et al. (2012). In this kind of binary systems, the flux contribution of both components is similar, so the spectra appear to show only one object, with the lines of the main-sequence star broadened by the presence of the subdwarf, explaining the higher values of $\log g$ obtained. However, due to the presence of the subdwarf, which shows $T_{\rm eff} \geq 20\,000$ K, a higher flux contribution on the UV is expected when compared to main-sequence or ELM stars, allowing for telling these objects apart.

In summary, the sdAs physical properties are consistent with basically four different possibilities: (a) pre-ELMs or ELMs; (b) blue-stragglers; (c) metal-poor late-type main-sequence stars; (d) hot subdwarf plus main-sequence F, G, K binary. Estimated $\log g$ and $T_{\rm eff}$ should be similar between all possibilities. Colours are similar for pre-ELMs, ELMs, and metal-poor main-sequence stars, but hot subdwarfs with a main-sequence companion should have higher UV flux. ELMs and pre-ELMs should show a close binary companion leading to high radial velocity variations and orbital periods lower than 36 h, according to Brown et al. (2016a), or up to 100 d, according to Sun & Arras (2017). Main-sequence binaries showing physical parameters in the sdA range, on the other hand, should have periods above ∼9 h (Brown et al. 2017). ELMs and pre-ELMs have long evolutionary periods, so they can be detected with ages above 10 Gyr, while main-sequence stars of A-type have main-sequence lifetimes lower than 1.5 Gyr, although a companion might delay the evolution by transferring mass as occurs for blue straggler stars.

2 DATA SELECTION

We have selected all spectra in the SDSS DR12 (Alam et al. 2015) containing O, B, A, or WD in their classification with signal-to-noise ratio (S/N) at the g filter larger than 15. This resulted in 56 262 spectra. They were first fitted with spectral models derived from pure hydrogen atmosphere models calculated using an updated version of the code described in Koester (2010). Objects with $\log g \geq 5.5$ were published in the SDSS DR12 white dwarf catalogue by Kepler et al. (2016) and were the first to be called sdAs. Motivated by the fact that many objects showed metal lines in their spectra, we have calculated a new grid with metals added in solar abundances. The grid, whose physical input is discussed in Section 3.1, covers $6000\,{\rm K} \leq T_{\rm eff} \leq 40\,000$ K and $3.5 \leq \log g \leq 8.0$. With this grid, we were able to obtain a good fit to 39 756 spectra out of the initial sample. The remaining objects were mostly close to the border of the grid, either in $T_{\rm eff}$ or in $\log g$, and are probably giant stars. 723 objects fitted $T_{\rm eff} > 20\,000$ K and were excluded – 49 show $\log g > 6.5$ and are canonical mass white dwarfs, while 674 show $\log g < 6.5$ and are most likely hot subdwarfs. All the white dwarfs are known with the exception of two new DA white dwarfs (SDSS J152959.39+482242.4 and SDSS J223354.70+054706.6). Only 66 out of the 674 possible sdBs are not in the catalogue of Geier et al. (2017); they are listed in Table C1 in the Appendix, with the exception of SDSS J112711.70+325229.5, a known white dwarf with a composite spectrum that compromised the fit (Kleinman et al. 2013).

To choose between hot and cool solutions with similar χ^2, that arise given to the fact that these solutions give similar equivalent width for the lines, we have relied on SDSS *ugriz* photometry, and *GALEX fuv* and *nuv* magnitudes when available. Specifically, we have chosen the solution which gave a $T_{\rm eff}$ consistent with the one obtained from a fit to the spectral energy distributions when the $\log g$ was fixed at 4.5. Full reddening correction was applied following Schlegel et al. (1998) for the SDSS *ugriz* magnitudes. For *GALEX* magnitudes, extinction correction was applied using the $E(B-V)$ value given in the *GALEX* catalogue, which was derived from the dust maps of Schlegel et al. (1998), and the relative extinction of Yuan et al. (2013), $R_{fuv} = 4.89$ and $R_{nuv} = 7.24$, given that such values are not present in the catalogue of Schlegel et al. (1998). Yuan et al. (2013) caution, however, that the FUV and NUV coefficients have relatively large measurement uncertainties.

Next, we removed from the sample contaminations from other SDSS pipeline possible classifications that contained our keywords, such as G0V**a**, F8I**b**v**a**r, and Calcium**WD**. Those were only 182 objects, leaving a sample of 38 850 narrow hydrogen line objects with a good solar abundance fit and $T_{\rm eff} < 20\,000$ K. This sample will be referred to as *sample A* throughout the text.

When we rely on spacial velocity estimates to analyse our sample, only objects with a reliable proper motion are taken into account. Unfortunately, our objects are too faint to be featured in the DR1 of *Gaia*, so we used the proper motions of Tian et al. (2017), which combine *Gaia* DR1, Pan-STARRS1, SDSS, and 2MASS astrometry to obtain proper motions. To flag a proper motion as good, we required that the distance to nearest neighbour with $g > 22.0$ was larger than 5 arcsec, that the proper motion was at least three times larger than its uncertainty, and that the reduced χ-squared from the evaluation of proper motions in right ascension and declination was smaller than 5.0. This left 16 656 objects with a reliable proper motion, with an average uncertainty of 2.0 mas yr^{-1}, to be referred to as *sample B* in the text.

In order to estimate the contamination by outliers, we have compared GPS1 proper motions to both the Hot Stuff for One Year (HSOY, Altmann et al. 2017) catalogue and the catalogues by Munn et al. (2004, 2014), directly available at the SDSS tables. HSOY combines positions from *Gaia* DR1 and the PPXML catalogue (Roeser et al. 2010), while Munn et al. combine SDSS and USNO-B data. Hence they are not completely independent, but nevertheless useful to find possible outliers. We find only 69 objects whose proper motions differ by more than 3σ when comparing GPS1 and HSOY, and 110 objects when comparing to Munn et al. They represent less than 1 per cent of the sample, so we decided to keep them as part of sample B, since it does not affect the analysis, and GPS1 is regarded as the best proper motion catalogue available for our objects.

3 SPECTRAL ANALYSIS

3.1 The models

The code to calculate atmospheric models and synthetic spectra was originally developed for white dwarfs (Koester 2010). In that area it has been used and tested for decades and proven to be reliable (e.g. Kleinman et al. 2013; Kepler et al. 2015, 2016). It has also been used successfully for sdB stars with surface gravity around $\log g = 5.5$ (e.g. Kepler et al. 2016). The identification of sdA stars was a by-product of our study of white dwarfs in the SDSS DR12.

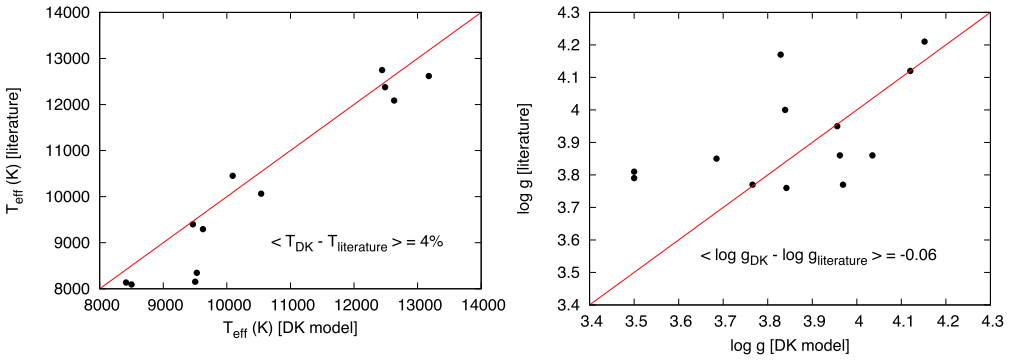

Figure 1. Left-hand panel shows the comparison between the $T_{\rm eff}$ obtained with our models (DK), and values from the literature. Right-hand panel shows the same comparison for $\log g$. The average difference is of about 4 per cent in $T_{\rm eff}$, and of -0.06 dex in $\log g$, which is even lower than the external error. The red line in both panels shows where both determinations would be equal.

We extended our grid to lower surface gravity in order to better identify and separate these sdAs from DAs and sdB. This extension is not meant to be used for a full-fledged analysis of main-sequence stars. It rather serves as an indicator of the luminosity class, given the external uncertainties of 5–10 per cent in $T_{\rm eff}$ and 0.25 dex in $\log g$.

To estimate internal uncertainties, we have compared our estimates for objects with duplicate spectra. We have found the average difference to be 0.55 per cent in $T_{\rm eff}$, with a standard deviation of 2.8 per cent, and of 0.047 dex in $\log g$, with a standard deviation of 0.133. Interestingly, these values are not significantly dependent on S/N for S/N $>$ 15. We have also found no variation in these internal uncertainties when excluding objects cooler than 8000 K from the sample. Hence the behaviour of the internal uncertainty does not seem to depend on either $T_{\rm eff}$ or S/N for the ranges considered here. The external uncertainty is higher for lower $T_{\rm eff}$, due to the decreasing strength of the lines, making them less sensitive as gravity indicators. That is, however, hard to quantify.

The models include metals up to $Z = 30$ with solar abundances in the equation of state, and include also the H_2 molecules. This ensures that the number densities of neutral and ionized particles are reasonable, which is important for the line broadening, in particular the Balmer lines. The tables of Tremblay & Bergeron (2009), which include non-ideal effects, are used to describe the Stark broadening of the Balmer lines. The occupation probability formalism of Hummer & Mihalas (1988) is taken into account for all levels of all elements. Absorption from metals is not included. We have tested that the addition of the photoionization cross-sections of metals with the highest abundances does not result in significant changes in the A star region. Line blanketing for the atmospheric structure uses only the hydrogen lines. The synthetic spectra, however, include approximately the 2400 strongest lines of all elements included in the range 1500–10 000 Å.

As a test for the validity of the models we have used a similar setup as for our sdA/ELM spectral fitting for a selection of known A stars. These include some of the objects with $\log g > 3.75$ from Allende Prieto & del Burgo (2016), as well as Vega from Bohlin (2007). As Fig. 1 shows, the average differences between our obtained values and the values from the literature are, in average, 4 per cent in $T_{\rm eff}$ and -0.06 dex in $\log g$, with no great discrepancies or systematic differences. This average difference can be easily explained by the dominant external errors. In Appendix A, we compare our estimates to those of the SDSS pipelines, whose grids have much smaller coverage than our own.

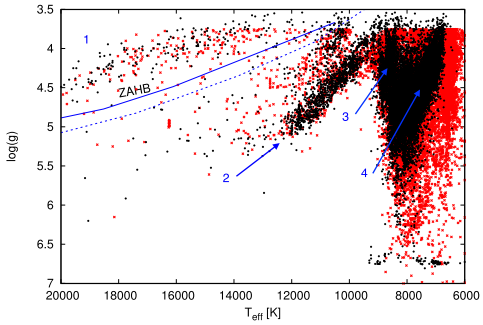

Figure 2. $T_{\rm eff}$–$\log g$ diagram showing the results of our pure hydrogen spectral fits as red crosses, and the updated result with metals added in solar abundance as black dots. The two distributions are shifted due to the changes in $T_{\rm eff}$ and $\log g$ for individual objects. The blue lines indicate the ZAHB, above which stars might be burning He in the core. Its position depends on metallicity; the continuous line assumes $Z = 0.0001$, the dashed line is for solar metallicity. Different sequences are labelled as 1, 2, 3, and 4. They reflect different temperature regimes described in the text.

3.2 Spectral fits

Fig. 2 shows the $T_{\rm eff}$–$\log g$ diagram with the values obtained from the two different models, pure hydrogen and solar abundance, for objects with good fit in both cases. It can be noted that the distribution shifts as a whole with the addition of metals to the models. Four sequences can be distinguished. At the hot low gravity end, some objects (labelled as sequence 1 in Fig. 2) are above the ZAHB; they could hence be blue horizontal branch stars. They are kept in the sample because, as we will show later, this region of the diagram can also be reached through binary evolution. There are a few hot objects between 10000 and 12000 K (sequence 2), and the bulk of the distribution is between 7 000 and 10 000 K. Careful inspection,

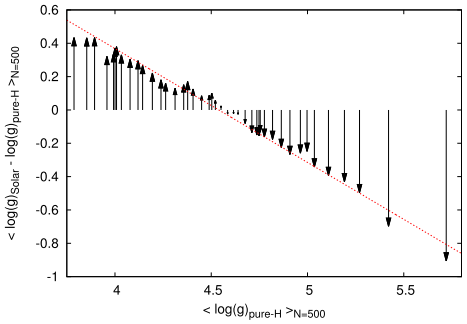

Figure 3. Shift in $\log g$ with the addition of metals in solar abundances as a function of the $\log g$ given by the pure-H models. Values were averaged over 500 objects sorted by $\log g$. The shifts are well described by a linear fit $\Delta\log g = -0.68\,(0.01)\log g_{\text{pure-H}} + 3.10\,(0.06)$ with the pure-H values being overestimated by almost 1.0 dex above $\log g = 5.5$. This is a similar result to the obtained by Brown et al. (2017) when fitting pure hydrogen model to synthetic main-sequence spectra.

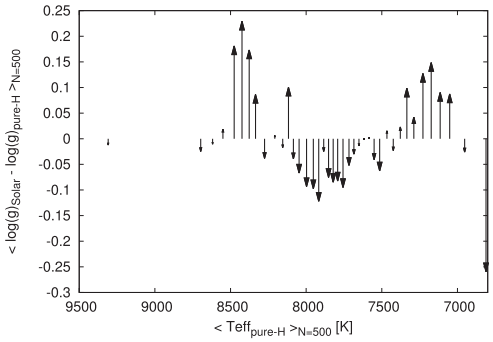

Figure 4. Change in $\log g$ when metals were added to the models as a function of the effective temperature of the pure-H models. The T_{eff} and the change in $\log g$ were averaged over 500 objects, sorted by T_{eff}. The systematic effect found as a function of $\log g_{\text{pure-H}}$ implies on a correlation also in T_{eff}, depending on how each range of $\log g$ is sampled in each bin of T_{eff}. Around 7000 K, for example, most objects have $\log g < 4.5$, where the shift in $\log g$ points upwards in Fig. 3, what is also seen here.

especially at the low $\log g$ end, suggests this region can also be split in two regimes around 8000 K (sequences 3 and 4).

We have analysed the change in $\log g$ for objects in sample A as a function of the pure hydrogen T_{eff} and $\log g$ values. We took into account only objects whose two estimated T_{eff} values differed by less than 500 K. We found a clear trend when plotting $\log g_{\text{Solar}}$–$\log g_{\text{pure-H}}$ as a function of $\log g_{\text{pure-H}}$, as can be seen in Fig. 3. The larger the $\log g_{\text{pure-H}}$, the smaller is the $\log g$ obtained from solar abundance models compared to pure hydrogen models. The shift, however, is not a constant value as suggested by Brown et al. (2017), but it rather behaves as a linear function of $\log g_{\text{pure-H}}$. Above $\log g \sim 5.5$, the solar abundance $\log g$ is in fact about 1 dex smaller than the value obtained from pure hydrogen models, as they have found. This explains their conclusion and that of Hermes et al. (2017) when analysing the $\log g \geq 5.5$ DR12 sdAs: they are exactly in this range where the difference between these two values is maximal. However, it is important to emphasize that the solar abundance model is not necessarily the correct one; while many sdAs do show clear signs of metals in their spectra, others seem to be almost free of metals.

This systematic trend also reflects on the dependence of the $\log g$ change with T_{eff}, shown in Fig. 4. At $T_{\text{eff}} \sim 8500$ K, there are objects spanning all the $\log g$ range (sequence 3 in Fig. 2), but a prevalence of objects with lower $\log g$, which have an upward correction. Hence the same upward correction is seen in this T_{eff} range. Between 7500 and 8000 K, a gap in the lower $\log g$ objects can be seen in Fig. 2, which moves the correction downwards. Finally, below $T_{\text{eff}} \sim 7500$ K (sequence 4), most objects show $\log g \leq 4.5$, so the correction moves upwards again. Close to the cool border of T_{eff}, most objects are also close to the lower border in $\log g$, which is 3.75 for the pure-hydrogen models and 3.5 for the solar abundance models, implying on an average difference of 0.25. There can of course be differences in metallicity and errors in the determination, so individual objects can somewhat obscure these trends.

The solar abundance solutions put most of the 2 443 sdAs published in by Kepler et al. (2016) in the main-sequence range, with the exception of 39 objects which still show $\log g \geq 5.0$. Only seven out of those maintain $\log g \geq 5.5$ in the solar abundance models. It is important to notice, however, that these higher values of $\log g$ can rise from statistics alone given an external uncertainty of about 0.25 even if the correct $\log g$ for these objects is about 4.5, so these objects should be analysed with caution.

Two of the $\log g > 5.0$ objects were published in the ELM Survey, SDSS J074615.83+392203.1 (Brown et al. 2012), and SDSS J091709.55+463821.7 (Gianninas et al. 2015). SDSS J0746+3922 was not confirmed as a binary; the published solution of $T_{\text{eff}} = 12\,130 \pm 400$ K and $\log g = 5.98 \pm 0.12$ agrees in $\log g$ with our pure hydrogen solution, $T_{\text{eff}} = 8300$ K and $\log g = 5.85$, but there is a discrepancy in T_{eff}. The UV colours favour the hotter solution. Our solar metallicity solution gives a slightly lower $\log g$ of 5.481 ± 0.017 and $T_{\text{eff}} = 8326 \pm 9$ K.[1] SDSS J0917+4638 was confirmed as a binary with period of 7.6 h and amplitude of 150 km s^{-1}. The solution published in Gianninas et al. (2015), $T_{\text{eff}} = 12240 \pm 180$ K and $\log g = 5.75 \pm 0.04$, agrees with our solar metallicity values of $T_{\text{eff}} = 12\,958 \pm 111$ K and $\log g = 5.842 \pm 0.029$. Our pure hydrogen fit indicates $T_{\text{eff}} = 9600$ K and $\log g = 5.00$.

Another object which maintained $\log g > 5.0$ is SDSS J075017.35+400441.2, an eclipsing binary analysed in Brown et al. (2017). Our solar metallicity fit gives $T_{\text{eff}} = 8071 \pm 15$ K and $\log g = 5.019 \pm 0.038$, a $\log g$ significantly lower than the pure hydrogen value of 5.619. Brown et al. (2017) points out that the SEGUE stellar parameter pipeline (SSPP) gives a much lower $\log g$ of 4.229 ± 0.155. However, the SSPP grid has no model above $\log g = 5.0$. The obtained period from their radial velocity orbital fit agrees with the photometric period of 28 h. They obtain a radial velocity amplitude of 36.2 km s^{-1} and conclude the star is best explained by a metal-poor main-sequence binary, which is consistent with our solar metallicity solution given the external uncertainties. The star's detected proper motion is not significant (2.03 ± 1.96 mas yr^{-1}), but the distance obtained from its distance modulus is over 14 kpc – in the Galactic halo. If indeed a main-sequence A

[1] Quoted uncertainties in our values of T_{eff} and $\log g$ are formal fit errors. The external uncertainties in the models are much larger, as discussed in Section 3.1.

Table 1. Obtained values of $T_{\rm eff}$ and $\log g$ for the 408 analysed SDSS objects in the range $5.5 \leq \log g < 7.0$ and $7000 \leq T_{\rm eff} \leq 20\,000$ K. The quoted uncertainties are formal fitting errors; external uncertainties in the models are 5–10 per cent in $T_{\rm eff}$ and 0.25 dex in $\log g$. The plate-modified Julian date-fibre, or P-M-F, identifies the SDSS spectrum for the object from which the solution was obtained. The S/N of the spectrum is given at the g band. The full table can be found in the on-line version of this paper.

SDSS J	P-M-F	S/N_g	$T_{\rm eff}$ (K)	$\log g$
112616.66−010140.7	0281-51614-0243	14.72	8312 (46)	5.624 (0.170)
113704.83+011203.6	0282-51658-0565	44.29	8122 (11)	5.544 (0.040)
130149.63+003823.8	0293-51689-0581	19.07	7150 (37)	6.724 (0.004)
130717.12−002639.4	0294-51986-0174	21.25	8167 (36)	5.572 (0.134)
134428.86+002820.4	0300-51666-0342	51.18	7246 (11)	6.704 (0.001)
135042.43−002004.7	0300-51943-0102	17.84	8582 (36)	5.606 (0.150)
140114.04−003553.6	0301-51641-0104	16.31	7403 (40)	6.747 (0.006)
140126.86+003156.3	0301-51641-0584	14.50	8040 (41)	5.728 (0.135)
121715.08−000928.3	0324-51666-0039	16.94	8358 (38)	5.533 (0.142)
162220.66−002000.4	0364-52000-0272	35.80	8242 (20)	5.672 (0.082)

star, it can only be explained as blue straggler whose main-sequence lifetime was significantly extended due to mass accreted from the companion.

SDSS J014442.66−003741.7, which was classified as δ-Scuti by Bhatti et al. (2010) given its Stripe 82 SDSS data, also has $\log g > 5.0$ in both our models. Bhatti et al. (2010) obtained a period of 1.5 h, which could also be explained as a g-mode pulsation of a pre-ELM star, given our solar metallicity fit of $T_{\rm eff} = 7\,949 \pm 35$ K and $\log g = 5.18 \pm 0.11$. The object's proper motion in the GPS1 proper motion table, 8.48 ± 3.59 mas yr^{-1} has too high uncertainty to allow any further conclusions on the object's nature. The object is relatively faint, $g = 19.8$, so the SDSS subspectra have too low SNR to allow good estimates of radial velocity. Better data are needed in order to establish the nature of this star. As discussed in Sánchez-Arias et al. (submitted to A&A), period spacing and rate of period change can be used to tell pre-ELMs and δ-Scuti stars apart.

Given that the changes in $\log g$ and $T_{\rm eff}$ can go up or down, many other objects are raised above the main-sequence $\log g$ limit. Table 1 lists the 408 objects with $5.5 \leq \log g < 7.0$ and $7000 \leq T_{\rm eff} \leq 20\,000$ K. Other 82 objects with $\log g$ in this range but $T_{\rm eff} < 7000$ K are omitted because we believe our models to be unreliable below this limit. The general weakness of the lines and the uncertainty of neutral line broadening at these temperatures make the $\log g$ difficult to estimate.

4 COLOURS

While spectra are considered the most reliable way to estimate the physical properties of a star, the colours of an object alone can still tell us something about its nature and be used as a complement to spectral results, especially when the colours include the ultraviolet region, not included in most spectra. Girven et al. (2011), for example, used colour–colour cuts in the SDSS photometry to identify DA white dwarfs with an efficiency of returning a true DA of 62 per cent, obtaining a 95 per cent complete sample. This type of approach was also used by Kleinman et al. (2013), Kepler et al. (2015), and Kepler et al. (2016) to select white dwarf candidates in the SDSS data base. This method relies notably on the $(u - g) \times (g - r)$ diagram, where models are significantly dependent on $\log g$. However, for pre-ELMs and ELMs, the lower $\log g$ gives them colours more similar to main-sequence stars, making this method less effective.

In Fig. 5 we show the $(u - g)_0 \times (g - r)_0$ diagram for samples A and B. Full reddening correction is applied following Schlegel et al. (1998). For comparison, we also show the confirmed ELMs from

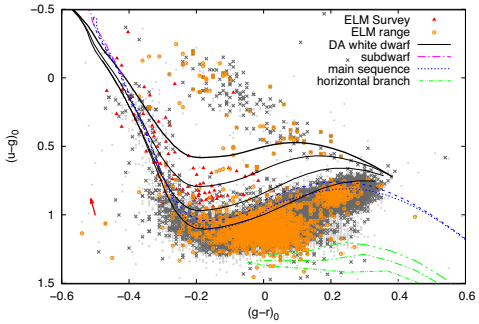

Figure 5. Colour–colour diagram showing sample A as dots in light grey, sample B as dark grey crosses, and the known ELMs from Brown et al. (2016a) as red triangles. Objects whose obtained spectral fit places them in the ELM range $T_{\rm eff} \leq 20\,000$ K and $5.0 \leq \log g \leq 7.0$ are marked with orange circles. The red arrow indicates the average vector of the reddening correction. Some theoretical models are included to guide the eye; the increasing thickness of the lines reflects an increasing $\log g$. The DA white dwarf models in black are obtained from our pure-hydrogen spectral models by convolving them with the SDSS filters. They span $\log g$ 4.0–7.0 in steps of 1.0 from bottom to top. Subdwarf, main-sequence, and horizontal branch models are from Lenz et al. (1998). The subdwarf model assumes $\log g = 5.00$ and [M/H] = 0.0, and covers $20\,000$ K $\leq T_{\rm eff} \leq 50\,000$ K. The selected main-sequence models have fixed [M/H] = −5.0, with $\log g = 4.0$, 4.5 and 4250 K $\leq T_{\rm eff} \leq 40\,000$ K. Finally, horizontal branch models have [M/H] = −1.0, $\log g = 1.0$, 1.5, 2.0 and span 3500 K $\leq T_{\rm eff} \leq 26\,000$ K.

the ELM Survey as published in Brown et al. (2016a). Objects that were placed in the ELM range, $T_{\rm eff} \leq 20\,000$ K and $5.0 \leq \log g \leq 7.0$, when fitted with our solar metallicity models, are marked with orange circles. They could be interpreted as extending the ELM strip to cooler temperature, but remarkably most of them lie below the $\log g = 5.0$ model line in this colour–colour diagram, despite the fact that spectroscopy indicates $\log g > 5.0$. This might suggest that there is still some missing physics in our spectral models: the addition of metals alone does not solve the discrepancy. Possibly some opacity included in the models needs better calculations, as might the case for broadening of the Balmer lines by neutral hydrogen atoms. He contamination through deep convection may also play a role. A possibility that cannot be discarded is that the extinction correction

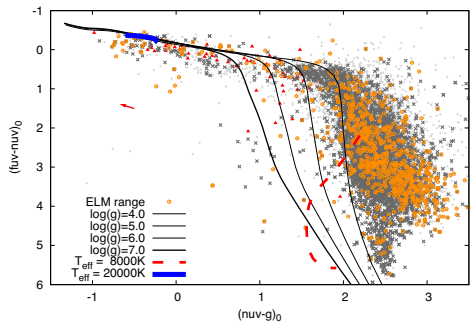

Figure 6. Diagram showing the $(fuv - nuv)_0$ and $(nuv - g)_0$ colours. The colours of each sample are the same as in Fig. 5. The red arrow indicates the average reddening correction vector. The indicated models were obtained from our pure-hydrogen spectral models. Despite the reddening correction, the data still seem dislocated in relation to the models, suggesting this correction might be underestimated.

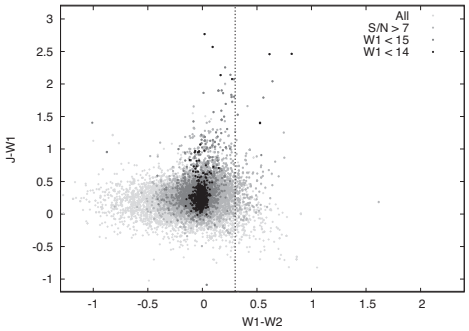

Figure 7. $(J - W1) \times (W1 - W2)$ colour–colour diagram for sample A. The whole sample is shown as light grey crosses, objects with S/N > 7 at both $W1$ and $W2$ filters are shown as grey dots. The dark grey dots indicate objects brighter than $W1 = 15$, and the black dots are those brighter than $W1 = 14$. The dashed vertical line is the $(W1 - W2) = 0.3$ limit, above which the objects might have infrared excess as suggested by Hoard et al. (2013).

is not accurate due to reasons such as variations on dust type and size, or the object being within the Galactic disc.

We have also analysed the *GALEX* UV magnitudes, far-ultraviolet (*fuv*), and near-ultraviolet (*nuv*), when available. Fig. 6 shows a $(fuv - nuv)_0 \times (nuv - g)_0$ diagram for samples A and B; the objects for which we have obtained $T_{\rm eff} \leq 20\,000$ K and $5.0 \leq \log g \leq 7.0$ are marked as orange circles. Extinction correction was applied using the $E(B - V)$ value given in the *GALEX* catalogue, $R_{fuv} = 4.89$ and $R_{nuv} = 7.24$ (Yuan et al. 2013). The colours suggest again $\log g$ lower than the estimated spectroscopically. However, extinction correction is even more uncertain in the ultraviolet than in the visible region, so again it should not be discarded that the correction is underestimated.

This diagram is especially useful in identifying sdB + FGK binaries, which should have significant flux in the UV due to the hot subdwarf component showing $T_{\rm eff} \gtrsim 20\,000$ K. In Fig. 6, there is a clustering of objects with $(nuv - g)_0 < -0.4$; many of them show radial velocity differences larger than 100 km s^{-1} in the SDSS subspectra that compose the final spectrum. About half of the sdBs are found to be in close binary systems (e.g. Heber 2016), with many showing radial velocity amplitudes in this range (e.g. Copperwheat et al. 2011). This considered, we suggest that sdAs showing $(nuv - g)_0 < -0.4$ – about 0.5 per cent – can be explained as sdB + FGK binaries.

Notably, two published ELMs are in this colour range: SDSS J234536.46−010204.9 and SDSS J162542.10+363219.1. SDSS J2345−0102 was analysed in Kilic et al. (2011). They obtained $T_{\rm eff} = 33\,130 \pm 450$ and $\log g = 7.20 \pm 0.04$ and found no evidence of radial velocity variations, suggesting this object is 0.42 $M_\odot$ white dwarf – therefore a low-mass white dwarf, which are often found to be single, rather than an ELM. The obtained $T_{\rm eff} > 20\,000$ K and $\log g > 7.0$ make it easier to distinguish this object from the sdAs, so it is not affected by our $(nuv - g)_0 < -0.4$ criterion. On the other hand, SDSS J1625+3632 which was also analysed in Kilic et al. (2011), has its estimated parameters, $T_{\rm eff} = 23\,570 \pm 440$ and $\log g = 6.12 \pm 0.03$, close to the range where we put the sdAs. Kilic et al. (2011) found it to present a small semi-amplitude of $K = 58.4$ km s^{-1} and a period of 5.6 h, suggesting it to be a 0.20 $M_\odot$ white dwarf with most likely another white dwarf as a companion. However, they point out that their obtained physical parameters are very similar to the sdB star HD 188112 (Heber et al. 2003), and mention that the 4471 Å line, a common feature of sdB stars, can be detected on the spectrum of the object. All this combined suggests that this object is rather an sdB than an ELM, fitting the $(nuv - g)_0 < -0.4$ criterion.

Finally, we searched for infrared excess due to a cool companion star using data from the Wide-field Infrared Survey (Wright et al. 2010) and the Two Micron All Sky Survey (2MASS, Skrutskie et al. 2006). We follow the approach of Hoard et al. (2013), who searched for candidate white dwarfs with infrared excess by examining a $(J - W1) \times (W1 - W2)$ diagram, suggesting $(W1 - W2) > 0.3$ as an indication of possible excess. As both white dwarfs and sdAs show hydrogen-dominated spectra, with very few lines in the infrared, the infrared flux in both cases depends basically on $T_{\rm eff}$, thus the method is suitable for analysing the sdAs. Hoard et al. (2013) restrict their analysis to objects with S/N > 7 at both $W1$ and $W2$. Using this same criterion, we find only about 1.3 per cent of the sample to possibly show infrared excess. The percentage is similar when we consider only objects brighter than $W1 = 14$ or than $W1 = 15$, as illustrated in Fig. 7.

5 DISTANCE AND MOTION IN THE GALAXY

One further step in the separation of white dwarfs from main-sequence objects is taking into account measured proper motions (e.g. Gentile Fusillo et al. 2015). As white dwarfs are compact objects, they have smaller radius and therefore are fainter than main-sequence stars with same temperature. Due to their degenerate nuclei, white dwarfs have a mass–radius relationship $R \sim M^{-1/3}$, implying that the smaller the mass, the larger the radius. Thus ELMs have larger radius and are brighter than common mass white dwarfs. Still, their radii are of the order of 0.1 $R_\odot$, so they should be about 10 times closer than main-sequence stars with similar $T_{\rm eff}$ to be seen at similar apparent magnitude, showing higher proper motion. The picture is more complicated when the pre-ELMs are considered. Mostly because of the CNO flashes, they can be as bright as main-sequence stars, so proper motion cannot be used as a criterion to tell these objects apart. Fig. 8 shows a reduced proper motion (H_g) versus $(g - z)_0$ diagram. Only sample B, containing objects

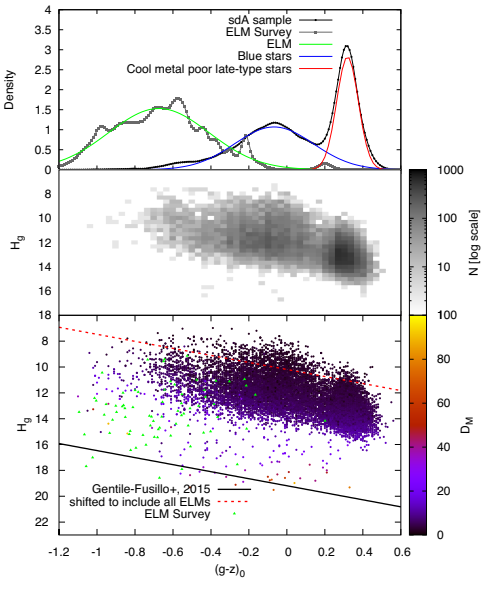

Figure 8. The bottom panel shows the $H_g \times (g-z)_0$ diagram (see e.g. Gentile Fusillo et al. 2015), with the objects in sample B colour coded according to their Mahalonobis distance to the halo given a main-sequence radius. Known ELMs are shown as green triangles for comparison. Middle panel shows the same diagram as a bidimensional histogram. The top panel shows the densities assuming each object as a Gaussian to account for the uncertainty; it becomes clear that there are two populations of objects within the sdA sample. The suggested limit for white dwarf detection with probability equal to 1.0 given by Gentile Fusillo et al. (2015) is indicated as a black solid line. Most known ELMs, due to their larger radius implying a smaller reduced proper motion, since they can be detected at larger distances, are not below the white dwarf limit. A reference line, defined arbitrarily shifting the estimate of Gentile Fusillo et al. (2015) to include all known ELMs is shown as a red dashed line. Most sdAs are also below such line.

with reliable proper motion, is taken into account. Here the reduced proper motion is evaluated as

$$H_g = g_0 + 5\log(\mu[\mathrm{arcsec\,yr^{-1}}]) + 5. \quad (1)$$

It can be interpreted as a proxy for the absolute magnitude: the higher the reduced proper motion, the fainter the object.

The objects are colour coded by their Mahalonobis distance D_M (e.g. Kilic et al. 2012b) to the halo when a main-sequence radius is assumed. The Mahalonobis distance is given by

$$D_M = \sqrt{\frac{(U-\langle U\rangle)^2}{\sigma_U^2} + \frac{(V-\langle V\rangle)^2}{\sigma_V^2} + \frac{(W-\langle W\rangle)^2}{\sigma_W^2}}, \quad (2)$$

where we have assumed the values of Kordopatis et al. (2011) for the halo mean velocities and dispersions. The Mahalonobis distance measures the distance from the centre of the distributions in units of standard deviations; hence considering the size of our sample and assuming a Gaussian behaviour, all objects should show $D_M < 4.0$. None the less, when a main-sequence radius is assumed, about 74 per cent of the objects show $D_M > 4.0$. When we assume an ELM radius for these objects, this number falls to less than 2 per cent.

Fig. 8 suggests that most of the objects with $T_{\rm eff}$ and $\log g$ in the ELM range have, in average, H_g lower than the estimated value for known ELMs. This, combined with the fact that they seem to be in the same region of the diagram as the $\log g < 5.0$ objects, could again be seem as an indication of missing physics in the models leading to an overestimate of the $\log g$. However, their reduced proper motion is consistent with a tentative limit based on Gentile Fusillo et al. (2015), but including all ELMs. This limit is given by

$$H_g = 2.72(g-z)_0 + 16.09. \quad (3)$$

The diagram in Fig. 8 is very enlightening when we look at the density of objects. It is evident that there are two different populations within the sdAs: one to the red limit of the diagram and another in an intermediary region. While the distribution of the red population has no intersection with the known ELMs, the distribution resulting from the blue population shares colour properties with the known ELMs. Most of the ELMs in the blue distribution show $T_{\rm eff} > 8000$ K (comprising sequences 1, 2, and 3 from Fig. 2), while the red distribution contains objects mainly cooler than that (sequence 4 in Fig. 2), explaining the two regimes which could be glimpsed in Fig. 2. These distributions will be used to study the nature of these objects in terms of probabilities in Section 7. We believe the red distribution is dominated by main-sequence late-type stars, which can be found in the halo, with some possible contamination of cooler (pre-)ELMs, since there is an intersection with the blue distribution. The blue distribution, on the other hand, should contain the missing cool (pre-)ELM population, which is under-represented in the literature. Evolutionary models predict that ELMs spend about the same amount of time above and below $T_{\rm eff} = 8500$ K, although the occurrence or not of shell flashes, which is still under discussion, can alter the time-scales by even a factor of two. Either way, 20–50 per cent of the ELMs should show $T_{\rm eff} < 8500$ K (Pelisoli et al. 2017); however, as a systematic effect of the search criterion, only 4 per cent of the published ELMs are in this range.

One of the outputs of our photometric fit, obtained by comparing the observed flux with the intensity given by the model, is the observed solid angle, related to the ratio between the radius R of the object and its distance d. So assuming a radius, we can estimate the distance for the objects in our sample. We estimated the radii assuming both a main-sequence radius, interpolated from a table with solar metallicity values given the estimated $T_{\rm eff}$, and a (pre-)ELM radius interpolating evolutionary models. Fig. 9 shows an Aitoff projection of the position of the objects in sample A with colour-coded distance for both cases. About 2000 objects have estimated distances larger than 20 kpc when a main-sequence radius is assumed; if indeed main-sequence stars, it is unlikely they were formed within the Galactic disc, since there would not be enough time for them to migrate there within their evolutionary time. They could be accreted stars from neighbouring dwarf galaxies, but we have found no evidence of streams to support that. An alternative is that they are (pre-)ELMs white dwarfs. Most objects are contained within 3.0 kpc in this scenario.

Combining these distances with the reliable proper motions, and with radial velocities estimated from our spectral fit, we estimated the Galactic velocities U, V, and W (Johnson & Soderblom 1987) given the main sequence or the ELM radius for sample B. The results are shown in Fig. 10 for a main-sequence radius and in Fig. 11 for a (pre-)ELM radius. About 38 per cent of the objects show velocities more than 3σ above the halo mean velocity dispersion when a main-sequence radius is assumed – implying a 1 per cent chance that they actually belong to the halo. Such high velocities also imply that the population cannot be related to blue

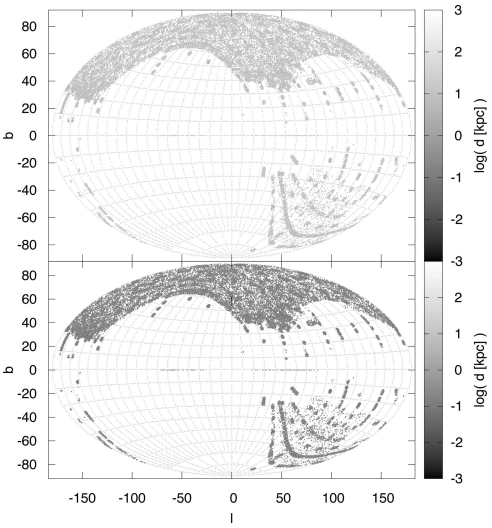

Figure 9. Aitoff projection showing the Galactic latitude (b) and longitude (l) for all analysed objects. The grey-scale indicates the estimated distance assuming either a main-sequence radius (top panel) or a (pre-)ELM (bottom panel). There are no apparent streams, with the objects appearing to be distributed all over the SDSS footprint.

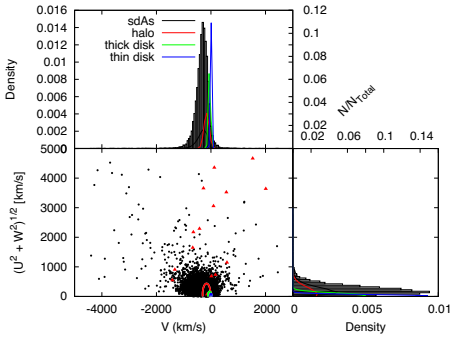

Figure 10. Toomre diagram of the objects in sample B, assuming a main-sequence radius. Density plots are shown to left and on top. The ellipses indicate the 3σ values for halo (red), thick disc (green), and thin disc (blue) according to Kordopatis et al. (2011).

horizontal-branch stars such as those studied by e.g. Xue et al. (2008). When the (pre-)ELM radius is assumed, on the other hand, the objects show a distribution consistent with a disc population. Further kinematic analysis, relying solely on the radial velocity component, can be found in Appendix B.

6 EVOLUTIONARY MODELS

We have also compared our obtained values of $T_{\rm eff}$ and $\log g$ to predictions from evolutionary models, both to single and binary evolution, as shown in Fig. 12. Single evolution models were taken from

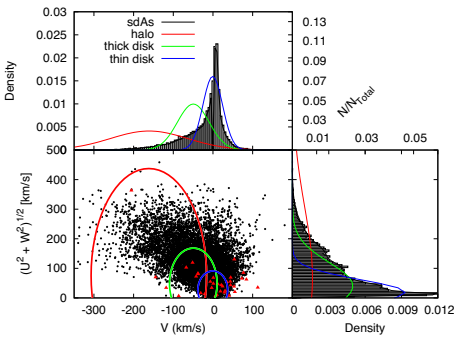

Figure 11. Same as Fig. 10, but assuming a (pre-)ELM radius.

Bertelli et al. (2008, 2009). The plotted models are for $Z = 0.0001$, since the sdAs, if main-sequence objects, should be in the halo, where the metallicity is low. We have used the binary evolution models of Istrate et al. (2016), the only ones to take rotation into account. The main panel in Fig. 12 shows that the values given by our solar metallicity fits are completely consistent with predictions from binary evolution models. Thus, given the values of $T_{\rm eff}$ and $\log g$ alone, the sdAs could be explained as (pre-)ELMs.

Using both single and binary evolution models, we have also obtained two probability distributions for the $\log g$ given each evolutionary path. Our approach was to evaluate the time spent in each bin of $\log g$, $T_{\log g}$, for all single or binary models, over the total evolutionary time, $T_{\rm evol}$, to obtain a probability $p_{\log g} = T_{\log g}/T_{\rm evol}$ that an object resulting from single, or binary, evolution shows $\log g$ in the given bin.

To take into account the fact that brighter objects are more easily observable, even if short lived, this probability was combined with a volume correction assuming, by simplicity, spherical symmetry. Considering that a main-sequence radius puts most of our objects in the halo, this approximation should hold. We have evaluated the observable volume $V_{\log g}$ of each bin of $\log g$ by summing up the volumes $V_{\rm obs}$ of all models with $\log g$ in said bin, where the volume was calculated using the M_v magnitude of each model, and assuming a saturation limit of $V = 14.5$ and a detection threshold of $V = 20.0$, so that

$$V_{\rm obs} = \frac{4\pi}{3}\left\{\left[10^{(14.5-M_V+5)/5}\right]^3 - \left[10^{(20.0-M_V+5)/5}\right]^3\right\}. \quad (4)$$

For each bin, we calculated the fraction of observable volume compared to the total volume throughout the evolutionary path, obtaining a probability of observing an object with the given $\log g$ during its evolution $p_{\rm obs} = V_{\log g}/\sum V_{\log g}$. To obtain our final probability distribution, we have combined both probabilities in $1.0 - (1.0 - p_{\log g}) \times (1.0 - p_{\rm obs})$. The resulting distributions are shown in red for the main-sequence models and in blue for the binary evolution models in Fig. 12.

7 A WAY-OUT: PROBABILITIES

Considering our previous analysis, it is clear that the observable properties of the sdAs are consistent with more than one evolutionary channel, since there is overlap between evolutionary paths. The

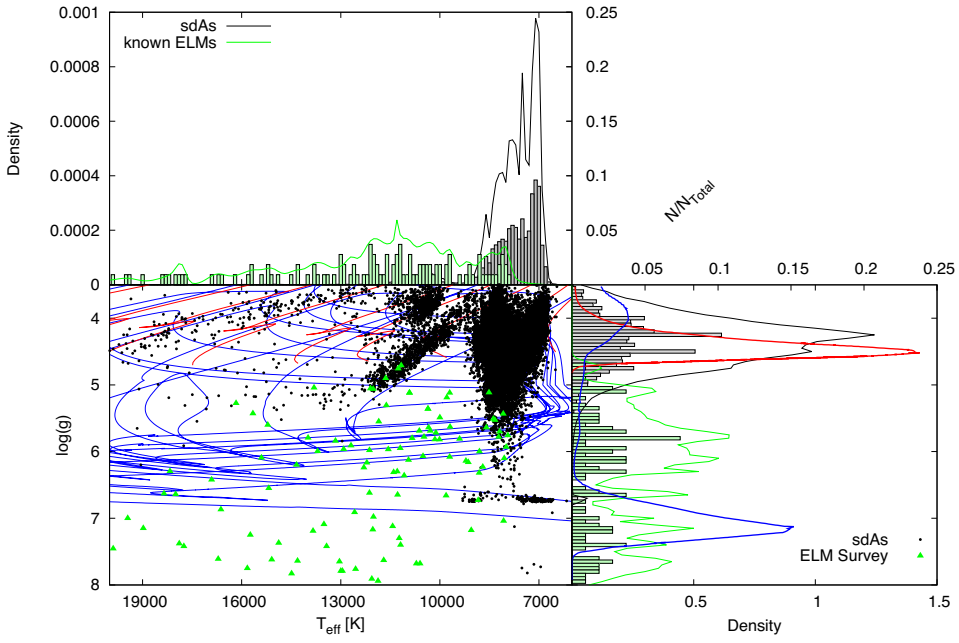

Figure 12. Bottom-left panel shows the $T_{\rm eff}$–$\log g$ diagram for objects in sample A, shown as black dots, and known ELMs, shown as green triangles, compared to single evolution models of Bertelli et al. (2008, 2009) (red), and binary evolution models of Istrate et al. (2016) (blue). For $\log g \gtrsim 5.0$, the objects can only be explained by binary evolution tracks. The top panel shows the distributions in $T_{\rm eff}$, while the bottom-right panel shows the distributions in $\log g$. The obtained probability distributions in $\log g$ for single (red) and binary evolution models (blue) are also shown. Note that there is significant overlap especially around $\log g \sim 4.5$. A colour version of this figure is available at the online version of the paper.

only physical parameter that would allow an unique classification for the sdAs would be the radius, which, combined with $\log g$ estimates, would allow us to tell whether the objects have a degenerate nucleus. As there is no parallax measured for the sdAs, this will not be possible at least until *Gaia*'s data release 2, scheduled for April 2018. High proper motion objects might not be in the data release 2, so the wait might be even longer. In the meantime, we can analyse the sdAs in terms of probability: do they have a higher probability of belonging to the main sequence, or can they be more easily explained by (pre-)ELMs?

Based on the estimated $\log g$ compared to evolutionary models, on the reduced proper motion diagram distributions, and on the spacial velocities given either a (pre-)ELM radius or a main-sequence radius, we have estimated for each object in sample B a probability of belonging to the main sequence and a probability of being a (pre-)ELM star. Our intention is to provide a basis for future follow-up projects, such as time resolved spectroscopy, impossible with the present size of the samples, and to understand the sdA population as a whole.

The main-sequence probability was evaluated taking into account three probabilities:

i) probability of being explained by a single-evolution model (Fig. 12) given the estimated solar abundance $\log g$: $p_{\rm MS1}$;

ii) probability of belonging to the red distribution in Fig. 8 given the $(g-z)_0$ colour: $p_{\rm MS2}$;

iii) probability of belonging to the halo, thick or thin disc of the Galaxy given the U, V, W velocities estimated with a main-sequence radius: $p_{\rm MS3}$.

The final probability was calculated as the complementary probability of the object *not* belonging to the main sequence, assuming the intermediary probabilities listed above are independent:

$$p_{\rm MS} = 1 - (1 - p_{\rm MS1}) \times (1 - p_{\rm MS2}) \times (1 - p_{\rm MS3}). \quad (5)$$

The (pre-)ELM probability on the other hand takes into account:

i) probability of being explained by binary evolution models (Fig. 12) given their estimated solar abundance $\log g$: $p_{\rm ELM1}$;

ii) probability of belonging to the blue distribution in Fig. 8 given the $(g-z)_0$ colour: $p_{\rm ELM2}$;

iii) probability of belonging to the halo, thick or thin disc of the Galaxy given the U, V, W velocities estimated with a (pre-)ELM radius: $p_{\rm ELM3}$.

This gives a final probability, again assuming the intermediary probabilities are independent, of

$$p_{\rm ELM} = 1-(1-p_{\rm ELM1}) \times (1-p_{\rm ELM2}) \times (1-p_{\rm ELM3}). \quad (6)$$

As previously mentioned, there are intersections between the properties of the two populations, therefore the two probabilities are not independent and *do not* sum up to one. Fig. 13 shows the obtained results for the objects in sample B. If we analyse these results in terms of an average, a random sdA has 68 per cent

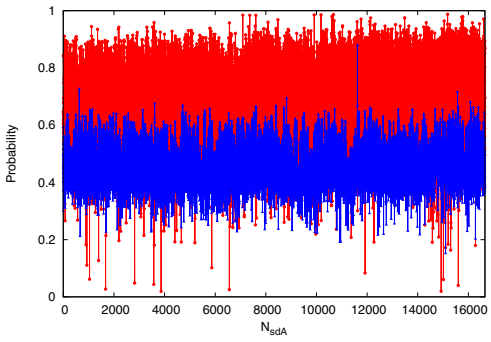

Figure 13. Circles in red show the probability of belonging to the main sequence, while triangles in blue show the resulting probability of being a (pre-)ELM object according to our evaluated distributions. The *x*-axis is simply a count of sdAs in sample B.

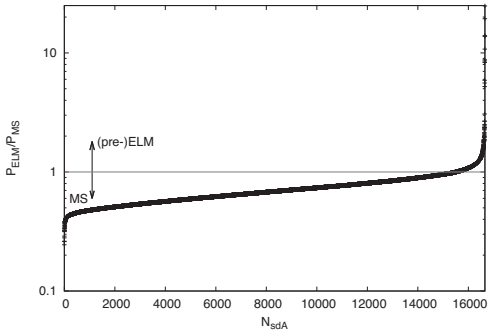

Figure 14. Probability of (pre-)ELM over probability of main sequence, ordered from smallest to largest. The *y*-axis is shown in log scale. Most objects do show a larger probability of belonging to the main sequence, but 1 150 objects in sample B (about 7 per cent) are most probably (pre-)ELMs.

probability of belonging to the main sequence, and a 46 per cent probability of being a (pre-)ELM. Doing the ratio between the two probabilities, we can obtain the objects which are more likely (pre-)ELMs in the sample. Fig. 14 shows the (pre-)ELM probability over the main-sequence probability. 1 150 objects in sample B, or 7 per cent, have a higher probability of being (pre-)ELMs. They are listed in Table 2. 170 of these objects show $\log g > 5.0$ – implying they would be ELMs rather than pre-ELMs. Out of those, 146 also show $T_{\rm eff} < 8\,500$ K.

Assuming all these objects have their nature correctly predicted, this would raise the number of ELMs with $T_{\rm eff} > 8\,500$ K in the SDSS footprint to 97 (73 confirmed binaries of Brown et al. (2016a) in this range + 24 sdAs), while the number of objects with $T_{\rm eff} < 8500$ K would be 149 [three confirmed binaries of Brown et al. (2016a) in this range + 146 sdAs], making the cool ELM population about 50 per cent larger. The evolutionary models predict the same amount of time to be spent in both ranges, but shell flashes can reduce the hydrogen in the atmosphere, speeding up the cooling process and making it possible that the time spent at lower temperatures be higher by a factor of two, as found here. However, the circumstances where these shell flashes occur are still unclear. Follow-up of these objects to detect the true cool ELMs, allowing for an observational estimate of the rate of objects in the two $T_{\rm eff}$ ranges, should be acquired to help calibrate the evolutionary models. We will discuss the current state of our follow-up in upcoming papers.

8 SUMMARY AND CONCLUSIONS

We have analysed a sample of narrow-line hydrogen spectra identified in the SDSS, estimating $T_{\rm eff}$ and $\log g$ from their spectra using new spectral models derived from solar abundance atmospheric models. Comparing these results to previous pure-hydrogen models by Kepler et al. (2016), we showed that the shift in $\log g$ when metals are added is not a constant, but depends on $\log g$, unlike what was suggested by Brown et al. (2017). For objects with a pure-hydrogen $\log g > 5.5$ though, as the objects analysed by Brown et al. (2017), the pure-hydrogen $\log g$ seems in fact to be about 1 dex higher than the solar abundance $\log g$.

With these new models, we have identified new sdAs in the range $5.0 \leq \log g \leq 7.0$ and $7000\,{\rm K} \leq T_{\rm eff} < 20\,000$ K. We analyse the colours of the whole sample of narrow-line hydrogen spectra, obtaining that the spectroscopic $\log g$ does not seem to agree with the position of the objects in colour–colour diagrams. This might indicate that there is still missing physics in the models; the addition of metals alone does not solve the discrepancy. Other missing opacities, such as molecular contributions, might be the explanation. However, the discrepancy could also be solved if the reddening is underestimated. Although out of the scope of this work, we consider that both possibilities should be investigated. One key-result obtained from the colour analysis is that the sdAs cannot

Table 2. Objects with a higher probability of being (pre-)ELM compared to main sequence. We show the obtained physical parameters, and the P-M-F of the spectrum from which they were derived, as well as the obtained probabilities for each case. The full table can be found in the on-line version of this paper.

SDSS J	P-M-F	$T_{\rm eff}$ (K)	$\log g$	$p_{\rm MS}$	$p_{\rm ELM}$
101053.89−004218.1	0270-51909-0161	7451 (21)	4.356 (0.139)	0.56	0.53
105752.38+001326.3	0276-51909-0599	6804 (35)	3.764 (0.097)	0.52	0.50
112941.67+000545.2	0281-51614-0117	7708 (37)	4.338 (0.157)	0.56	0.55
113704.83+011203.6	0282-51630-0561	8137 (13)	5.277 (0.056)	0.33	0.32
113704.83+011203.6	0282-51658-0565	8122 (11)	5.544 (0.040)	0.31	0.27
121213.83−003046.8	0287-52023-0240	7280 (31)	4.772 (0.135)	0.54	0.51
120811.97−004230.4	0287-52023-0311	8275 (10)	5.050 (0.042)	0.52	0.51
122000.93−005556.5	0288-52000-0100	7898 (22)	4.856 (0.111)	0.56	0.39
121715.08−000928.3	0288-52000-0234	8481 (26)	5.097 (0.105)	0.52	0.40
123222.47−001222.6	0289-51990-0028	7598 (40)	5.235 (0.138)	0.55	0.54

be explained as binaries of a hot subdwarf with a main-sequence star, since they do not show significant flux in the UV. There is also no indication of infrared excess for over 98 per cent of the sample.

The most significant result is, though, that the sdAs are clearly composed of two populations. One population contains the red objects, and it has no overlap with the known ELMs. These could be explained as cool late-type main-sequence stars, when the velocities are consistent with the halo population. On the other extreme, there is a blue population, which does overlap with known ELMs, but contains cooler objects. Considering that there is still a missing cool ELM population to be found, given the predictions of evolutionary models, it is very likely that these objects belong to the blue population of sdAs.

Analysing the estimated distances and spacial velocities for the objects, we obtain that over 35 per cent of them show too high velocities to belong to the halo when a main-sequence radius is assumed. These objects cannot therefore be explained as simply metal-poor main-sequence stars of types A–F. The discrepant velocities are solved when a (pre-)ELM radius is assumed for these objects, in which case their velocities become consistent with the disc distribution. Some percentage of these objects might be of binary stars, such as blue stragglers, in which case the velocities could be explained as orbital instead of spacial motion. A better sense of the nature of this population will be obtained when their parallax is released by *Gaia*. What we should keep in mind is that, given their apparent extreme velocities and distances, they certainly can help us study the dynamics of the halo.

We have also compared our estimated values of $T_{\rm eff}$ and $\log g$ to evolutionary models, both single and binary. A very interesting result is that the parameters for the objects in our sample are consistent with those expected from binary evolution models. Considering the time spent in each bin of $\log g$ and the brightness at such phases, even pre-ELMs with $\log g < 4.0$ have considerable probability of being observed.

Taking into account the derived probabilities from the evolutionary models, combined with the probabilities given the colours and spacial velocities, we have estimated probabilities for each object to be either a main-sequence star or a (pre-)ELM. As there are significant overlap between the parameters of each class, the probabilities do not sum up to one. Comparing the probabilities, we find that about 7 per cent of the sdAs are better explained as (pre-)ELMs than as main-sequence stars, a much larger percentage than found by Brown et al. (2017) studying a small sample of eclipsing stars. Considering the physical parameters of the objects with a higher probability of being (pre-)ELMs, our result is consistent with the existence of two times as many cool ELMs ($T_{\rm eff} < 8\,500$ K) as hot ELMs. However, as in many cases the probability of being ELM is only marginally larger than of belonging to the main sequence, this result should be confirmed by follow-up of these objects, as we will discuss in upcoming papers.

Even if only a small percentage of the sdAs is composed by (pre-)ELMs, the number is high enough to potentially double the number of known ELMs. The cool ELM population, in particular, seems to be within the sdAs. As our models for this kind of object are still under development, monitoring of the sdAs is essential to find this missing population. Tables 1 and 2 published here are a valuable asset to guide this monitoring. Our understanding of binary evolution, and especially of the common envelope phase that ELMs must experience, can be much improved if we have a sample covering all parameters predicted by these models. The sdA sample provides that.

Our understanding of the formation and evolution of the Galactic halo would also benefit from more detailed study of the sdAs. Many seem to be in the halo with ages and velocities not consistent with the halo population. It is possible that accreted stars from neighbouring dwarf galaxies might be among them. Those whose velocities are in fact consistent with the halo can in turn help us study its dynamics and possibly better constrain the gravitational potential of the halo. Comparing the numbers of both populations, we can obtain clues of how different formation scenarios, namely accretion and formation in locus, contributed to the halo.

The key message of our results is that we should not overlook the complexity of the sdAs. They are of course not all pre-ELM or ELM stars, but they cannot be explained simply as main-sequence metal-poor A–F stars. They are most likely products of binary evolution and as such are a valuable asset for improving our models.

ACKNOWLEDGEMENTS

IP and SOK acknowledge support from Conselho Nacional de Desenvolvimento Científico e Tecnológico (CNPq-Brazil). IP was also supported by Coordenação de Aperfeicoamento de Pessoal de Nível Superior (CAPES-Brazil) under grant 88881.134990/2016-01. DK received support from programme Science without Borders, MCIT/MEC-Brazil. We thank Thomas G. Wilson for useful discussions on IR-excess, Alejandra D. Romero for providing ZAHB tables, and the anonymous referee for their helpful comments and suggestions.

This research has made extensive use of NASA's Astrophysics Data System.

Funding for the Sloan Digital Sky Survey IV has been provided by the Alfred P. Sloan Foundation, the U.S. Department of Energy Office of Science, and the Participating Institutions. SDSS-IV acknowledges support and resources from the Center for High-Performance Computing at the University of Utah. The SDSS web site is www.sdss.org.

SDSS-IV is managed by the Astrophysical Research Consortium for the Participating Institutions of the SDSS Collaboration including the Brazilian Participation Group, the Carnegie Institution for Science, Carnegie Mellon University, the Chilean Participation Group, the French Participation Group, Harvard-Smithsonian Center for Astrophysics, Instituto de Astrofísica de Canarias, The Johns Hopkins University, Kavli Institute for the Physics and Mathematics of the Universe (IPMU) / University of Tokyo, Lawrence Berkeley National Laboratory, Leibniz Institut für Astrophysik Potsdam (AIP), Max-Planck-Institut für Astronomie (MPIA Heidelberg), Max-Planck-Institut für Astrophysik (MPA Garching), Max-Planck-Institut für Extraterrestrische Physik (MPE), National Astronomical Observatories of China, New Mexico State University, New York University, University of Notre Dame, Observatário Nacional / MCTI, The Ohio State University, Pennsylvania State University, Shanghai Astronomical Observatory, United Kingdom Participation Group, Universidad Nacional Autónoma de México, University of Arizona, University of Colorado Boulder, University of Oxford, University of Portsmouth, University of Utah, University of Virginia, University of Washington, University of Wisconsin, Vanderbilt University, and Yale University.

REFERENCES

Alam S. et al., 2015, ApJS, 219, 12
Allende Prieto C., del Burgo C., 2016, MNRAS, 455, 3864

Althaus L. G., Serenelli A. M., Córsico A. H., Montgomery M. H., 2003, A&A, 404, 593
Althaus L. G., Miller Bertolami M. M., Córsico A. H., 2013, A&A, 557, A19
Altmann M., Roeser S., Demleitner M., Bastian U., Schilbach E., 2017, A&A, 600, L4
Barlow B. N., Wade R. A., Liss S. E., Østensen R. H., Van Winckel H., 2012, ApJ, 758, 58
Bertelli G., Girardi L., Marigo P., Nasi E., 2008, A&A, 484, 815
Bertelli G., Nasi E., Girardi L., Marigo P., 2009, A&A, 508, 355
Bhatti W. A., Richmond M. W., Ford H. C., Petro L. D., 2010, ApJS, 186, 233
Bohlin R. C., 2007, in Sterken C., ed., ASP Conf. Ser. Vol. 364, The Future of Photometric, Spectrophotometric and Polarimetric Standardization. Astron. Soc. Pac., San Francisco, p. 315
Bono G., Salaris M., Gilmozzi R., 2013, A&A, 549, A102
Bressan A., Marigo P., Girardi L., Nanni A., Rubele S., 2013, in EPJ Web Conf., 43, 03001
Brown W. R., Kilic M., Allende Prieto C., Kenyon S. J., 2010, ApJ, 723, 1072
Brown J. M., Kilic M., Brown W. R., Kenyon S. J., 2011, ApJ, 730, 67
Brown W. R., Kilic M., Allende Prieto C., Kenyon S. J., 2012, ApJ, 744, 142
Brown W. R., Kilic M., Allende Prieto C., Gianninas A., Kenyon S. J., 2013, ApJ, 769, 66
Brown W. R., Gianninas A., Kilic M., Kenyon S. J., Allende Prieto C., 2016a, ApJ, 818, 155
Brown W. R., Kilic M., Kenyon S. J., Gianninas A., 2016b, ApJ, 824, 46
Brown W. R., Kilic M., Gianninas A., 2017, ApJ, 839, 23
Camargo D., Bica E., Bonatto C., Salerno G., 2015, MNRAS, 448, 1930
Cojocaru R., Rebassa-Mansergas A., Torres S., Garcia-Berro E., 2017, MNRAS, 470, 1442
Copperwheat C. M., Morales-Rueda L., Marsh T. R., Maxted P. F. L., Heber U., 2011, MNRAS, 415, 1381
Córsico A. H., Althaus L. G., 2014, A&A, 569, A106
Córsico A. H., Althaus L. G., 2016, A&A, 585, A1
Geier S., Østensen R. H., Nemeth P., Gentile Fusillo N. P., Gänsicke B. T., Telting J. H., Green E. M., Schaffenroth J., 2017, A&A, 600, A50
Gentile Fusillo N. P., Gänsicke B. T., Greiss S., 2015, MNRAS, 448, 2260
Gianninas A., Kilic M., Brown W. R., Canton P., Kenyon S. J., 2015, ApJ, 812, 167
Girven J., Gänsicke B. T., Steeghs D., Koester D., 2011, MNRAS, 417, 1210
Greenstein J. L., 1973, A&A, 23, 1
Hansen B. M. S., 2005, ApJ, 635, 522
Heber U., 2016, PASP, 128, 082001
Heber U., Edelmann H., Lisker T., Napiwotzki R., 2003, A&A, 411, L477
Hermes J. J., Gänsicke B. T., Breedt E., 2017, in Tremblay P.-E., Gaensicke B., Marsh T., eds, ASP Conf. Ser. Vol. 509, 20th European White Dwarf Workshop. Astron. Soc. Pac., San Francisco, p. 453
Hoard D. W., Debes J. H., Wachter S., Leisawitz D. T., Cohen M., 2013, ApJ, 770, 21
Hummer D. G., Mihalas D., 1988, ApJ, 331, 794
Isern J., García-Berro E., Salaris M., 2001, in von Hippel T., Simpson C., Manset N., eds, ASP Conf. Ser. Vol. 245, Astrophysical Ages and Times Scales. Astron. Soc. Pac., San Francisco, p. 328
Istrate A. G., Marchant P., Tauris T. M., Langer N., Stancliffe R. J., Grassitelli L., 2016, A&A, 595, A35
Johnson D. R. H., Soderblom D. R., 1987, AJ, 93, 864
Kalirai J. S., 2012, Nature, 486, 90
Kepler S. O. et al., 2015, MNRAS, 446, 4078
Kepler S. O. et al., 2016, MNRAS, 455, 3413
Kilic M., Stanek K. Z., Pinsonneault M. H., 2007, ApJ, 671, 761
Kilic M., Brown W. R., Allende Prieto C., Agüeros M. A., Heinke C., Kenyon S. J., 2011, ApJ, 727, 3
Kilic M., Thorstensen J. R., Kowalski P. M., Andrews J., 2012a, MNRAS, 423, L132
Kilic M., Brown W. R., Allende Prieto C., Kenyon S. J., Heinke C. O., Agüeros M. A., Kleinman S. J., 2012b, ApJ, 751, 141
Kilic M., Munn J. A., Harris H. C., von Hippel T., Liebert J. W., Williams K. A., Jeffery E., DeGennaro S., 2017, ApJ, 837, 162
Kleinman S. J. et al., 2013, ApJS, 204, 5
Koester D., 2010, Mem. Soc. Astron. Italiana, 81, 921
Kordopatis G. et al., 2011, A&A, 535, A107
Lance C. M., 1988, ApJ, 334, 927
Lee Y. S. et al., 2008, AJ, 136, 2022
Lenz D. D., Newberg J., Rosner R., Richards G. T., Stoughton C., 1998, ApJS, 119, 121
Liebert J., Bergeron P., Holberg J. B., 2005, ApJS, 156, 47
Maxted P. F. L. et al., 2014, MNRAS, 437, 1681
Miller Bertolami M. M., 2016, A&A, 588, A25
Munn J. A. et al., 2004, AJ, 127, 3034
Munn J. A. et al., 2014, AJ, 148, 132
Pelisoli I., Kepler S. O., Koester D., Romero A. D., 2017, in Tremblay P.-E., Gaensicke B., Marsh T., eds, ASP Conf. Ser. Vol. 509, 20th European White Dwarf Workshop. Astron. Soc. Pac., San Francisco, p. 447
Pietrzyński G. et al., 2012, Nature, 484, 75
Prugniel P., Soubiran C., 2001, A&A, 369, 1048
Rebassa-Mansergas A., Ren J. J., Parsons S. G., Gänsicke B. T., Schreiber M. R., García-Berro E., Liu X.-W., Koester D., 2016, MNRAS, 458, 3808
Roeser S., Demleitner M., Schilbach E., 2010, AJ, 139, 2440
Romero A. D., Campos F., Kepler S. O., 2015, MNRAS, 450, 3708
Sandage A. R., 1953, AJ, 58, 61
Schlegel D. J., Finkbeiner D. P., Davis M., 1998, ApJ, 500, 525
Schneider F. R. N., Izzard R. G., Langer N., de Mink S. E., 2015, ApJ, 805, 20
Schönberner D., 1978, A&A, 70, 451
Si S., van Dyk D. A., von Hippel T., Robinson E., Webster A., Stenning D., 2017, MNRAS, 468, 4374
Skrutskie M. F. et al., 2006, AJ, 131, 1163
Sun M., Arras P., 2017, preprint (arXiv:1703.01648)
Tian H.-J. et al., 2017, ApJS, 232, 4
Tremblay P.-E., Bergeron P., 2009, ApJ, 696, 1755
Tremblay P.-E., Ludwig H.-G., Steffen M., Freytag B., 2013, A&A, 552, A13
Tremblay P.-E., Cummings J., Kalirai J. S., Gänsicke B. T., Gentile-Fusillo N., Raddi R., 2016, MNRAS, 461, 2100
Woosley S. E., Heger A., 2015, ApJ, 810, 34
Wright E. L. et al., 2010, AJ, 140, 1868
Xue X. X. et al., 2008, ApJ, 684, 1143
Yuan H. B., Liu X. W., Xiang M. S., 2013, MNRAS, 430, 2188
Ziegerer E., Volkert M., Heber U., Irrgang A., Gänsicke B. T., Geier S., 2015, A&A, 576, L14

SUPPORTING INFORMATION

Supplementary data are available at *MNRAS* online.

most_likely_ELM.dat
ELM2016_20160513_log55.dat

Please note: Oxford University Press is not responsible for the content or functionality of any supporting materials supplied by the authors. Any queries (other than missing material) should be directed to the corresponding author for the article.

APPENDIX A: COMPARISON WITH PARAMETERS FROM THE SDSS PIPELINES

The comparison between our estimated parameters and those given by the SDSS pipelines is not straightforward, as the model grids do not cover the same range of $T_{\rm eff}$ and $\log g$. We include this analysis here as an appendix to illustrate their differences. We do not, however, consider such comparison a valid test of our models, since the SDSS pipeline grids are strongly incomplete in terms of

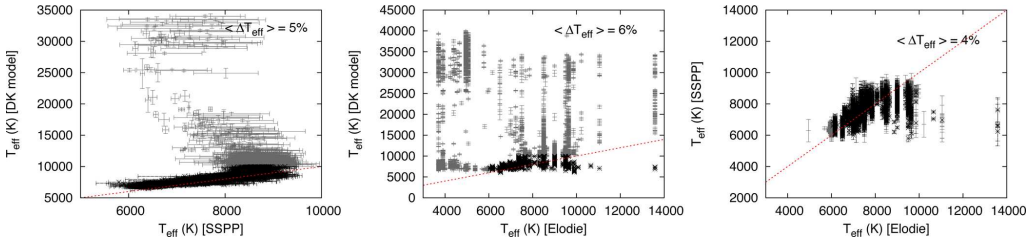

Figure A1. Comparison between our estimate of $T_{\rm eff}$ (DK model) and both pipelines, as well as the comparison between the pipelines. Grey dots are outside of the area covered by SDSS grids, while black dots are within it. The red dashed line represents equality. The average difference for estimates within both grids is shown in each plot. It is clear that there is no discrepancy in the region covered by both grids. Our higher temperatures are backed up by both the *GALEX* ultraviolet flux, and the SDSS classification as type O and B, which is not coherent with their own estimated temperature.

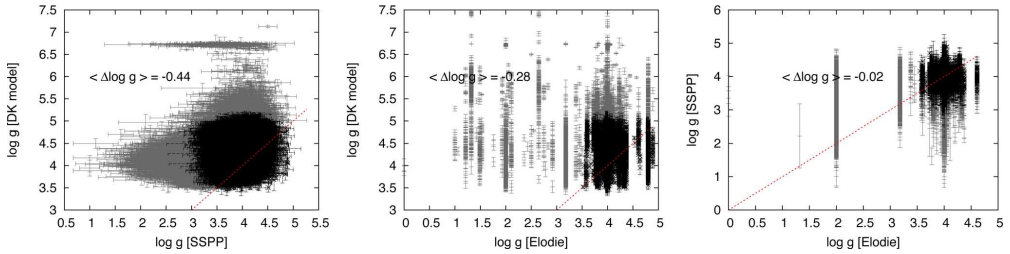

Figure A2. Comparison between our log g and that of the pipelines. Colours are the same as in Fig. A1. The spread is larger and our fit favours, in average, slightly higher log g values, given the extension of our grid to higher values.

$T_{\rm eff}$ and log g. Figs A1 and A2 show the comparison between the $T_{\rm eff}$ and the log g, respectively, that we obtained for the objects with a good fit (sample A) and the values given by two SDSS pipelines, the SSPP (Lee et al. 2008) and the best match from the ELODIE stellar library (Prugniel & Soubiran 2001). The two pipelines are also compared. We find good agreement (∼5 per cent) in $T_{\rm eff}$ between our fit and both pipelines. Our log g is, in average, 0.44 dex higher than the SSPP estimate, and 0.28 dex higher than the Elodie values, which is probably due to the difference in the extension of the grids. Moreover, this average shift is not enough to raise the log g of a typical main-sequence A star (log $g \sim 4.3$) to values above 5.0.

We have also performed an analysis to estimate whether the metallicity would play a significant role in the gravity estimate. In order to do that, we verified if the difference in log g between our determination and that of SSPP was dependent on the value of [Fe/H] given by SSPP. There are 10 120 objects in sample A with SSPP determinations. We ordered them by [Fe/H], and calculated the average of the absolute difference in log g, $\sqrt{(\log g_{\rm DK} - \log g_{\rm SSPP})^2}$, as well as the standard deviation of this average, every 100 points. Fig. A3 suggests that the metallicity is not a dominant uncertainty factor in the gravity estimate, since there is no dependence of the difference between determinations on [Fe/H].

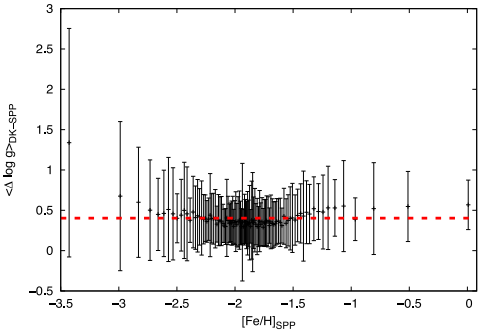

Figure A3. Absolute difference in log g between our models and the SSPP determination, averaged every 100 points, as a function of the metallicity [Fe/H] given by SSPP. The red dashed line shows the overall average. There seems to be no strong dependence of the difference between surface gravity on the metallicity.

APPENDIX B: FURTHER KINEMATIC ANALYSES

In many cases, the space motions of objects in sample B are dominated by the transversal velocity component, especially when a main-sequence radius is assumed, as shown in Fig. B1. To verify this was not a consequence of outliers in the proper motion catalogue (such as found by e.g. Ziegerer et al. 2015), we cross-matched the GPS1 proper motions with both the HSOY catalogue (Altmann et al. 2017), and the proper motions given in the SDSS tables (Munn et al. 2004, 2014). Only 69 objects from sample B differ by more than 3σ when comparing HSOY and GPS1 (see Fig. B2); 110 when we compare GPS1 to Munn et al. Such numbers are not of concern given the sample size, hence the objects were kept in the sample.

To work around possible effects raised by inaccuracy in the transversal velocity component, we have also performed a kinematic study relying on the radial velocity estimate alone. We

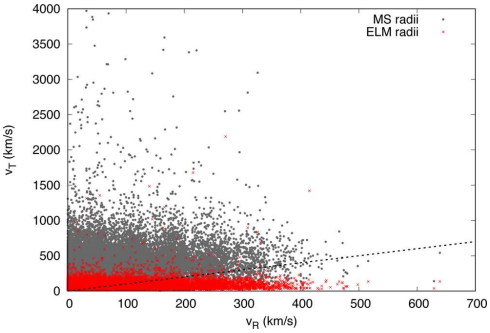

Figure B1. Comparison between the radial velocity estimated from SDSS spectra (v_R), and the transversal velocity derived from the GPS1 proper motion given the estimated distance (v_T), both assuming a main-sequence (grey dots) and an ELM radius (red crosses) for sample B only. The spacial motion is dominated by the tangential velocity if a main-sequence radius is assumed, with many objects showing v_T much above the escape velocity. That does not happen when an ELM radius is assumed, with very few exceptions.

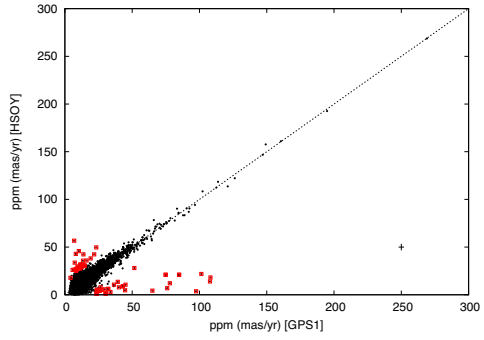

Figure B2. Comparison between the GPS1 and HSOY proper motions. The outliers are marked with red squares. The dashed line represents equality between the two values. Average uncertainties are shown as a cross in the bottom right of the panel.

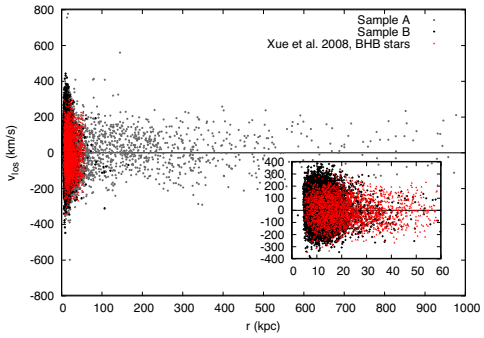

Figure B3. Line-of-sight velocity in the GSR as a function of Galactocentric distance. Sample A (grey dots) and B (black crosses) are of course different, with the unreliable proper motion of sample A giving in some cases unrealistic values of distance. Focusing on sample B only (smaller overlay panel), distances and velocities are on a similar range as halo BHB stars (shown as red triangles for comparison), with slightly larger velocities giving a somewhat higher dispersion, as can be seen in Fig. B4.

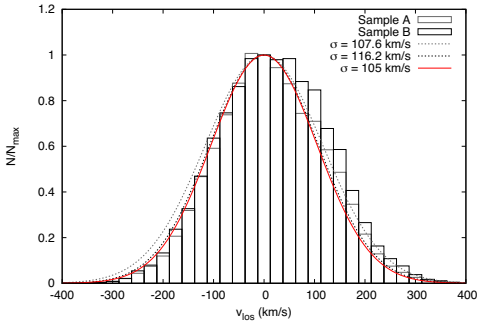

Figure B4. Distribution of v_{los} for both samples A (black) and B (grey). The best-fitting Gaussian for each sample is shown as a dashed line of same colour. A Gaussian of width 105 km s^{-1}, similar to the value found by Xue et al. (2008) for halo BHB stars is shown in red for comparison. Samples A and B show very similar dispersions, which are consistent with the estimated for the Galactic halo.

have computed the Galactocentric distance (r) and the of line-of-sight velocities (v_{los}) in the Galactic standard of rest (GSR) frame following equations 4 and 5 of Xue et al. (2008). For the Galactocentric distance, we have assumed a main sequence radius. Fig. B3 shows v_{los} as a function of r, for both samples A and B, compared to the BHB stars of Xue et al. (2008). The unreliable proper motions of sample A result on unrealistic distance estimates, which are avoided by focusing on sample B, which shows similar distances to the halo BHBs. It is important to emphasize, however, that most sdAs show lower temperature than the ZAHB at their $\log g$, as shown in Fig. 1. In Fig. B4, we show the distribution of v_{los} for both sample A and sample B, compared to a Gaussian of width $\sigma = 105$ km s^{-1}, as found by Xue et al. (2008) for BHB halo stars. There is no significant difference between the distributions of samples A and B. Moreover, both show a dispersion of the same order of the halo stars studied by Xue et al. (2008) when a main-sequence radius is assumed, hence the conclusion that, if indeed main-sequence stars,

the sdAs would have to be in the halo is not dependent on the tangential velocity estimate.

APPENDIX C: LIST OF POSSIBLE HOT SUBDWARFS

Table C1. Objects for which our fit indicated $T_{\rm eff} > 20\,000$ K and $\log g < 6.5$, which are possible hot subdwarfs not listed in Geier et al. (2017).

SDSS J	P-M-F
000138.22+282731.9	2824-54452-0443
003739.05+000842.3	3588-55184-0616
013940.56+003626.6	1907-53265-0339,1907-53315-0335
021419.64−084505.3	4395-55828-0478
062336.21+642730.0	2301-53712-0627
063659.39+832025.0	2548-54152-0076
064846.81+373614.3	2700-54417-0079
073225.82+153729.7	2713-54400-0172
073546.72+410350.5	2701-54154-0541
073654.60+280923.4	4456-55537-0728
075029.26+181749.5	2729-54419-0428
075640.08+071806.6	4843-55860-0525
080520.22+000944.5	4745-55892-0147
081544.25+230904.7	4469-55863-0004
082606.25+113913.8	4508-55600-0855
083830.10+135117.6	4500-55543-0263
090141.48+345924.4	4645-55623-0456
091301.01+305119.8	2401-53768-0389
091721.87+283656.0	5797-56273-0546
091914.64+480306.0	5813-56363-0709
093946.04+065209.4	1234-52724-0304
100233.49+164500.5	5326-56002-0106
100442.16+132711.6	5328-55982-0828
104159.64+192254.5	5886-56034-0628
104437.73+145213.3	5350-56009-0768
105847.65+203917.4	5876-56042-0729
111917.41+050617.3	4769-55931-0682
112121.98+453955.5	6648-56383-0750
113312.12+010824.8	2877-54523-0369
121123.36+611203.8	0954-52405-0567,6972-56426-0278
121910.44+230020.7	5979-56329-0474
132138.31+133200.1	5427-56001-0746
132210.94+421216.9	6622-56365-0473
133540.82+014725.2	4045-55622-0014
134531.00−005314.4	4043-55630-0180
140603.27+374216.6	4711-55737-0208
141055.68+374340.6	4712-55738-0466
141810.60−020038.8	4032-55333-0532,4035-55383-0990
150421.06−005613.8	4020-55332-0950
151404.97+065352.7	2927-54621-0268
151940.51+014457.1	4011-55635-0310
152729.40+222448.5	3954-55680-0244
153049.60+321425.4	4723-56033-0639
155105.64+452134.0	3454-55003-0204
155241.28+045428.7	4877-55707-0254
160612.98+521919.3	2187-54270-0224
161430.90+041843.4	2189-54624-0633
164014.57+320325.2	5202-55824-0900
165237.92+240302.8	4181-55685-0236
165406.79+271117.7	4185-55469-0985
165634.74+231256.4	3290-54941-0378
170126.69+204620.5	4175-55680-0810
172037.66+534009.3	0359-51821-0273
191837.28+370917.5	2821-54393-0203
204403.97-051135.6	0635-52145-0360
204802.45+002753.1	1116-52932-0512
211716.97-005401.6	4192-55469-0376
213301.81-004914.7	4194-55450-0178
215014.24+233039.1	5953-56092-0185
224145.04+292426.0	6585-56479-0883
225654.02+074449.8	2325-54082-0376
232810.27-084156.3	3145-54801-0371

This paper has been typeset from a TEX/LATEX file prepared by the author.

APPENDIX D – Conference Proceedings

20th European White Dwarf Workshop
ASP Conference Series, Vol. 509
Tremblay, Gänsicke, and Marsh, eds.

What's the Nature of sdA Stars?

Ingrid Pelisoli,[1] S. O. Kepler,[1] D. Koester,[2] and A. D. Romero[1]

[1]*Instituto de Física, Universidade Federal do Rio Grande do Sul, 91501-900 Porto Alegre, RS, Brazil;* ingrid.pelisoli@ufrgs.br

[2]*Institut für Theoretische Physik und Astrophysik, Universität Kiel, 24098 Kiel, Germany*

Abstract. White dwarfs with log g lower than 7.0 are called Extremely Low Mass white dwarfs (ELMs). They were first found as companions to pulsars, then to other white dwarfs and main sequence stars (The ELM Survey: 2010 to 2016), and can only be formed in interacting binaries in the age of the Universe. In our SDSS DR12 white dwarf catalog (Kepler et al. 2016), we found a few thousand stars in the effective temperature and surface gravity ranges attributed to ELMs. We have called these objects sdAs, alluding to their narrow hydrogen line spectra showing sub-main sequence log g. One possible explanation for the sdAs is that they are ELMs. Increasing the ELMs sample would help constrain the number of close binaries in the Galaxy. Interestingly, if they turn out to be A stars with an overestimated log g, the distance modulus would put these young stars in the Galaxy's halo.

1. Introduction

White dwarf stars are the final evolutionary state of stars with initial masses up to 8.5–10.6 $M_\odot$ (Woosley & Heger 2015), corresponding to at least 95% of all stars. For the evolution of single stars, the minimum mass of a white dwarf is around 0.30–0.45 $M_\odot$ (e.g. Kilic et al. 2007), because progenitors that would become lower mass white dwarfs have main sequence evolution time larger than the age of the Universe. Such masses correspond, considering the mass-radius relation of white dwarfs, to a minimal log g of around 6.5. On the other hand, evolutionary models (see Romero et al. 2015, and references therein) indicate that the maximum log g of main sequence A stars, which have similar optical spectra to DA white dwarfs, is 4.75, even for very low metallicity.

Objects with $4.75 < \log\ g < 6.50$ can result from binary evolution. Hot subdwarf stars are one example: binary interaction strips away the star's outer layers during core He burn, leaving a hot ($T_{\rm eff} > 20\,000$ K) lower mass ($M \sim 0.45\ M_\odot$) object. However, for low-mass progenitors ($M \lesssim 2.0\ M_\odot$), the temperature for burning He is only reached after it has become degenerate. Therefore, if the outer layers of a low-mass progenitor are stripped away before the He burning starts, a degenerate He core with a hydrogen atmosphere will be left: a white dwarf. Because the mass of the white dwarfs resulting from this channel can be much lower than the single star evolution limit ($M \lesssim 0.3\ M_\odot$), they are known as extremely-low mass white dwarfs, or ELMs (see the ELM Survey: Brown et al. 2010; Kilic et al. 2011; Brown et al. 2012; Kilic et al. 2012; Brown et al. 2013; Gianninas et al. 2015; Brown et al. 2016a).

2. Data Analysis

Mining the Data Release 12 of the Sloan Digital Sky Survey (SDSS DR12, Alam et al. 2015) for white dwarfs, we found thousands of objects with hydrogen atmospheres showing $4.75 \leq \log\ g \leq 6.5$. These objects were classified as type O, B, A, or white dwarf by the SDSS pipeline. Canonical mass white dwarfs were analyzed and published in Kepler et al. (2016). The remaining objects with signal-to-noise ratio larger than 15 were fitted to a grid of hydrogen-dominated atmosphere models, with metals added in solar abundances, covering $6\,000\ \mathrm{K} \leq T_{\mathrm{eff}} \leq 40\,000\ \mathrm{K}$ and $3.5 \leq \log\ g \leq 8.0$. To choose between hot and cool solutions, we relied on the photometric results using the SDSS *ugriz* magnitudes and also the Galaxy Evolution Explorer (GALEX, Bianchi et al. 2014) *fuv* and *nuv* magnitudes, when available. This is the first time a fit with such large coverage in T_{eff} and $\log g$ is done to these spectra, to our knowledge.

This selection left 1010 objects with $8\,000\ \mathrm{K} \leq T_{\mathrm{eff}} \leq 20\,000\ \mathrm{K}$ and $5.00 \leq \log\ g \leq 6.5$. About a hundred of them have proper motion higher than 10 mas/yr, most showing also galactic latitude larger than 30°, indicating they may be outside the disk, since they are all fainter than $g = 14$. As the nature of these objects is not yet fully understood, we have called them sdAs, referring to their narrow hydrogen line spectra (A-type) and their sub-main sequence $\log g$. If these objects are indeed main sequence A stars ($M_g \simeq 0$) with an overestimated $\log\ g$, some could be explained as relatively young high velocity or runaway stars. Only one high-velocity (Brown et al. 2009) and no runaway A stars are known to date. Moreover, their temperatures put them below the zero-age horizontal branch (ZAHB), so they cannot be explained as conventional He core burning subdwarfs, unless they are in binary systems as found by Barlow et al. (2012). In these sdB+FGK binary systems, the flux contribution of both components is similar, so the spectra appear to show only one object, with the lines of the main sequence star broadened by the presence of the subdwarf. The other possible explanation for these objects is that they are ELMs or pre-ELMs (Maxted et al. 2014b,a).

3. Properties of sdA Stars

In an attempt to understand the nature of the sdAs, we have studied properties such as colors, proper motion, and velocities, comparing them to models and to the known ELMs listed in Brown et al. (2016a). Fig. 1 shows the $(u-g)_0 \times (g-r)_0$ color-color diagram, where u_0, g_0 and r_0 are SDSS magnitudes with full extinction correction following Schlegel et al. (1998). The sdAs do not show the same colors as the known ELMs, but rather seem to extend the ELM branch to cooler temperatures. Evolutionary models (e.g. Córsico & Althaus 2014, 2016) indicate that the time spent with $7\,500\ \mathrm{K} \leq T_{\mathrm{eff}} \leq 8\,500\ \mathrm{K}$ is about the same as the time spent with $8\,500\ \mathrm{K} \leq T_{\mathrm{eff}} \leq 22\,000\ \mathrm{K}$. Less than 10% of the known ELMs show $T_{\mathrm{eff}} \leq 8500\ \mathrm{K}$ (Brown et al. 2016a), indicating that there's still a cool ELM population to be discovered, which is probably within the sdA sample. Curiously, despite the fact that the $\log g$ obtained from spectroscopy is above five, most sdAs lie below the model indicating $\log\ g = 5$ in this color-color diagram. This might indicate that spectroscopic $\log\ g$ is overestimated. Another possibility is that the extinction correction is not accurate for these objects.

On Fig. 2, a color-color diagram using GALEX colors for the objects available in this database is shown. Extinction correction was applied using the $E(B-V)$ given

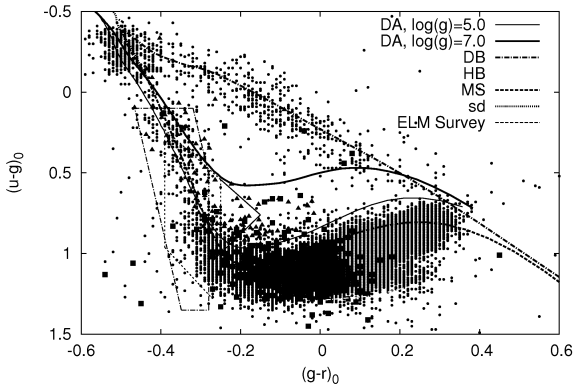

Figure 1. $(u-g)_0 \times (g-r)_0$ color-color diagram, showing the sdAs (squares, dark gray), the known ELMs (triangles, red), and the objects for which we obtained a log $g < 5.0$ (dots, light gray) for comparison. The original color selection in the ELM Survey is shown in red, depending on magnitude: $15 < g_0 < 17$ dot-dashed line, $17 < g_0 < 19.5$ dashed line, and $19.5 < g_0 < 20.5$ continuous line. Theoretical models with fixed log g and metallicity are also plotted to guide the eye. Subdwarf (sd, magenta dotted line), main sequence (MS, blue dashed line), and horizontal branch (HB, green dotted-dashed line) models were calculated by Lenz et al. (1998). DB models (black dotted-dashed line) are from Bergeron et al. (2011). The DA models shown in black and labeled by log g were obtained from our grid of models.

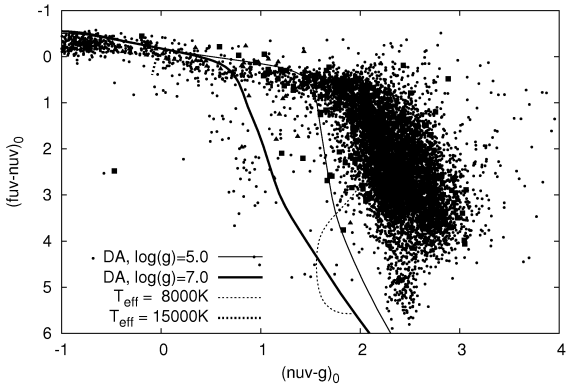

Figure 2. GALEX colors of the sdAs (squares, dark gray), the known ELMs (triangles, red), and the objects for which we obtained a log $g < 5.0$ (dots, light gray) for comparison. Some DA models, both for fixed $T_{\rm eff}$ and fixed log g, are also shown on the plot.

in the catalog, $R_{fuv} = 8.24$ and $R_{nuv} = 8.20$ (Wyder et al. 2007). The picture here is the same as for the SDSS colors: the sdAs seem to be a cooler extension of the ELM branch. The fact that this stands for the UV colors is a strong suggestion that the sdB+FGK main sequence star hypothesis doesn't hold, because the sdB would have a strong contribution to the UV flux, which is not detected in most cases.

Finally, by comparing the observed flux with the intensity given by the model, we obtained the observed solid angle, related to the ratio between the object's radius R and its distance d. Assuming either a main sequence or an ELM radius for the sdAs, we estimated two possible values for d. Combining these distances with the measured proper motions obtained from USNO-B and SDSS data (Munn et al. 2004), we estimated their galactic velocities U, V, and W (e.g Johnson & Soderblom 1987) given the main sequence or the ELM radius. The results are shown on Fig. 3, together with the 3σ ellipses for halo, thin, and thick disk as obtained by Kordopatis et al. (2011). When a main sequence radius is assumed, many objects show velocities considerably outside the halo distribution. Considering that main sequence A stars have typical lifetimes around 1–2 Gyr, they are expected to be found within the disk, so these velocities are highly unexpected. Some objects might be explained as relatively young high velocity (ejected by the Galaxy's central black hole) or runaway (ejected due to interaction in multiple systems) stars, but velocities higher than 1000 km/s cannot be explained by any of those mechanisms. Only one high-velocity (Brown et al. 2009) and no runaway A stars are known to date. The other possible explanation for these objects is that they are ELMs. When we assume an ELM radius, the objects have velocities consistent with a disk and halo distribution.

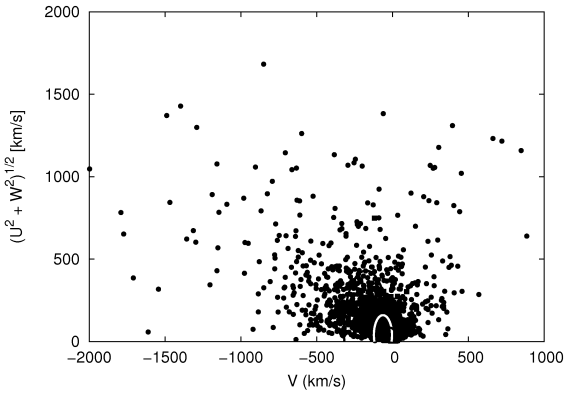

Figure 3. Estimated velocities for all sdAs assuming either a main sequence radius (dots, gray) or a ELM radius (squares, black). The ellipses show the 3 σ limit for the halo (red), the thick disk (green), and the thin disk (blue), as given by Kordopatis et al. (2011).

4. Discussion

There are three possible explanations for the nature of the sdAs: binaries of a subdwarf and a main sequence object of type FGK, main sequence A stars with an overestimated log g, or ELMs. The first option is ruled out for most objects, because no significant flux in the ultraviolet, as would be expected from the subdwarf, is detected (Fig. 2). Some objects do show UV flux [$(nuv - g)_0 \leq 1.5$, $(fuv - nuv)_0 \sim 0$], and thus might be explained as this kind of system. This can be verified with time-resolved spectroscopy to measure radial velocity variations. These systems have relatively long periods, of the order 3–4 years, showing radial velocity variations with a semi-amplitude typically smaller than 50 km/s (Barlow et al. 2012). In contrast, ELMs, which are typically found in close binaries, have a median semi-amplitude of 220 km/s (Brown et al. 2016a).

The main sequence A star hypothesis is strongly suggested by the colors shown by the sdAs. Both in the $(u - g)_0 \times (g - r)_0$ and the $(fuv - nuv)_0 \times (nuv - g)_0$ diagrams, the sdAs lie on cool regions, populated by low-log g objects, in spite of the log $g > 5.0$ determined spectroscopically. As mentioned above, our models assume solar abundances for these objects, which is an overestimate considering the calcium abundances we have estimated from their spectra. Moreover, helium abundances were not taken into account. Finally, at the cool temperatures estimated for the sdAs, collisional effects between neutral hydrogen atoms should have a significant effect. There is no rigorous calculation of the line broadening caused by this effect in the literature yet, so it is also not properly accounted for. In short, there are many factors to be improved in the models, so we cannot rule out that the log g is not well determined. However, when we assume main sequence radii for the sdAs, the obtained distances and velocities are not consistent to what is expected for a population of young objects: they seem to be scattered through the halo, some with considerably high velocities which couldn't be explained even by black hole acceleration.

If the proper motion given in the SDSS tables are correct, hypothesis we tested by verifying they are similar to those given in the APOP catalog (Qi et al. 2015), the only way to avoid having this scenario is if, instead of having a main sequence radius, these objects are actually ELMs, with a radius about twenty times smaller. This leads to a lower luminosity, in such a way that much smaller distances are needed to explain the observed flux. This also leads to much more reasonable velocities, within the thin and thick disk distributions, with very few objects appearing to be in the halo. The cooler colors presented by the sdAs when compared to the ELMs might be easily explained if they are a cooler ELM population, predicted by evolutionary models but sill underrepresented in the literature. The main issue with this hypothesis is that most sdAs do not show significant radial velocity variations between their SDSS subspectra. This might be explained if they are ELMs which already underwent a merging event. According to Brown et al. (2016b), most double degenerate white dwarfs will merge within a Hubble time, so ELMs resulting from mergers are expected to exist. The known ELMs which shown no radial velocity are possibly explained as face-on systems. These two factors might explain the lack of variability to some objects, but is highly unlike that all the cool ELMs are either merged or in face-on systems. As the SDSS subspectra are usually of low-signal to noise and cover less than one hour, this can likely explain the no detection of variation to many objects. Therefore more observations are needed in order to understand the true nature of the sdA population.

Acknowledgments. IP, SOK, and ADR are supported by CNPq-Brazil. DK received support from program Science without Borders, MCIT/MEC-Brazil. This research has made use of NASA's Astrophysics Data System and of the cross-match service provided by CDS, Strasbourg. Funding for the Sloan Digital Sky Survey IV has been provided by the Alfred P. Sloan Foundation, the U.S. Department of Energy Office of Science, and the Participating Institutions. SDSS-IV acknowledges support and resources from the Center for High-Performance Computing at the University of Utah. The SDSS web site is `www.sdss.org`.

References

Alam, S., Albareti, F. D., Allende Prieto, C., et al. 2015, ApJS, 219, 12
Barlow, B. N., Wade, R. A., Liss, S. E., Østensen, R. H., & Van Winckel, H. 2012, ApJ, 758, 58
Bergeron, P., Wesemael, F., Dufour, P., et al. 2011, ApJ, 737, 28
Bianchi, L., Conti, A., & Shiao, B. 2014, Advances in Space Research, 53, 900
Brown, W. R., Geller, M. J., & Kenyon, S. J. 2009, ApJ, 690, 1639
Brown, W. R., Gianninas, A., Kilic, M., Kenyon, S. J., & Allende Prieto, C. 2016a, ApJ, 818, 155
Brown, W. R., Kilic, M., Allende Prieto, C., Gianninas, A., & Kenyon, S. J. 2013, ApJ, 769, 66
Brown, W. R., Kilic, M., Allende Prieto, C., & Kenyon, S. J. 2010, ApJ, 723, 1072
Brown, W. R., Kilic, M., Allende Prieto, C., & Kenyon, S. J. 2012, ApJ, 744, 142
Brown, W. R., Kilic, M., Kenyon, S. J., & Gianninas, A. 2016b, ApJ, 824, 46
Córsico, A. H., & Althaus, L. G. 2014, A&A, 569, A106
Córsico, A. H., & Althaus, L. G. 2016, A&A, 585, A1
Gianninas, A., Kilic, M., Brown, W. R., Canton, P., & Kenyon, S. J. 2015, ApJ, 812, 167
Johnson, D. R. H., & Soderblom, D. R. 1987, AJ, 93, 864
Kepler, S. O., Pelisoli, I., Koester, D., et al. 2016, MNRAS, 455, 3413
Kilic, M., Brown, W. R., Allende Prieto, C., et al. 2011, ApJ, 727, 3
Kilic, M., Brown, W. R., Allende Prieto, C., et al. 2012, ApJ, 751, 141
Kilic, M., Stanek, K. Z., & Pinsonneault, M. H. 2007, ApJ, 671, 761
Kordopatis, G., Recio-Blanco, A., de Laverny, P., et al. 2011, A&A, 535, A107
Lenz, D. D., Newberg, J., Rosner, R., Richards, G. T., & Stoughton, C. 1998, ApJS, 119, 121
Maxted, P. F. L., Bloemen, S., Heber, U., et al. 2014a, MNRAS, 437, 1681
Maxted, P. F. L., Serenelli, A. M., Marsh, T. R., et al. 2014b, MNRAS, 444, 208
Munn, J. A., Monet, D. G., Levine, S. E., et al. 2004, AJ, 127, 3034
Qi, Z., Yu, Y., Bucciarelli, B., et al. 2015, AJ, 150, 137
Romero, A. D., Campos, F., & Kepler, S. O. 2015, MNRAS, 3708
Schlegel, D. J., Finkbeiner, D. P., & Davis, M. 1998, ApJ, 500, 525
Woosley, S. E., & Heger, A. 2015, ApJ, 810, 34
Wyder, T. K., Martin, D. C., Schiminovich, D., et al. 2007, ApJS, 173, 293

DE GRUYTER OPEN Open Astron. 2017; 26: 169–178

Research Article

Ingrid Pelisoli*, S. O. Kepler, and Detlev Koester

Are sdAs helium core stars?

https://doi.org/10.1515/astro-2017-0433
Received Sep 30, 2017; accepted Oct 23, 2017

Abstract: Evolved stars with a helium core can be formed by non-conservative mass exchange interaction with a companion or by strong mass loss. Their masses are smaller than 0.5 $M_\odot$. In the database of the Sloan Digital Sky Survey (SDSS), there are several thousand stars which were classified by the pipeline as dwarf O, B and A stars. Considering the lifetimes of these classes on the main sequence, and their distance modulus at the SDSS bright saturation, if these were common main sequence stars, there would be a considerable population of young stars very far from the galactic disk. Their spectra are dominated by Balmer lines which suggest effective temperatures around 8 000–10 000 K. Several thousand have significant proper motions, indicative of distances smaller than 1 kpc. Many show surface gravity in intermediate values between main sequence and white dwarf, $4.75 < \log g < 6.5$, hence they have been called sdA stars. Their physical nature and evolutionary history remains a puzzle. We propose they are not H-core main sequence stars, but helium core stars and the outcomes of binary evolution. We report the discovery of two new extremely-low mass white dwarfs among the sdAs to support this statement.

Keywords: white dwarfs, subdwarfs, binaries

1 Introduction

The physical properties of main sequence stars can be reasonably inferred from their spectral type. The spectral classes from A to M show an increase in molecular bands, with hydrogen becoming less prominent, reflecting a decrease in effective temperature ($T_{\rm eff}$). Similarly, the mass also decreases. As mass is the determinant factor on the lifetime of a star, hydrogen abundant main sequence stars (early-type) are short lived compared to cool, late-type stars. Dwarf A stars, in particular, have a main sequence lifetime shorter than 2 Gyr. Consequently, stars of type A and earlier should not be found in the Galactic halo, which is at least 10 Gyr old, unless they were accreted or recently formed.

Mining the Sloan Digital Sky Survey (SDSS), we were surprised to encounter thousands of objects classified by the pipeline as of type O, B and A. The SDSS bright saturation is about $g = 14.5$, while the absolute magnitude of a dwarf A star is $M_g = 0$; thus, if indeed in the main sequence, these objects would mostly have to be in the halo, given their distance modulus $(g - M_g) > 14.5$ implying $d \gtrsim 8$ kpc and the fact that the SDSS operates mostly outside the disk ($b > 30^\circ$).

In Kepler *et al.* (2016), we fitted the spectra of these objects to spectral models derived from pure-hydrogen atmosphere models, and found thousands to show surface gravity with $\log g > 5.5$. Given the properties of a dwarf A star, its maximal $\log g$ is about 4.75 (see Romero *et al.* 2015 and references therein). White dwarfs resulting from single evolution, on the other hand, have a lower limit in $\log g$ of about 6.5–7.0 (*e.g.* Kilic *et al.* 2007). Objects with $4.5 < \log g < 6.5$ can result from binary evolution, as the hot subdwarf stars: binary interaction strips away the star's outer layers during core He burn, leaving a hot ($T_{\rm eff}$ >20 000 K) lower mass (M∼0.45 $M_\odot$) object. However, we found the objects to have $T_{\rm eff} < 20\,000$ K, therefore they should not be core helium burning objects as the hot subdwarfs. We have dubbed this type of object subdwarf A stars (sdAs), referring to their sub-main sequence surface gravity and A-star-like spectra. This is nonetheless merely a spectroscopic classification: Their physical nature and evolutionary history remains an embarrassing puzzle.

A promising possibility was that these objects were new extremely-low mass white dwarfs (ELMs, $M \lesssim 0.3\ M_\odot$). For low-mass progenitors ($M \lesssim 2.0\ M_\odot$), the temperature for burning He is only reached after it has become degenerate. Therefore, if the outer layers of a low-mass star are stripped

Corresponding Author: I. Pelisoli *et al.*: Instituto de Física, Universidade Federal do Rio Grande do Sul, Porto Alegre, Rio Grande do Sul, 91501-900, Brazil; Email: ingrid.pelisoli@ufrgs.br
S. O. Kepler: Instituto de Física, Universidade Federal do Rio Grande do Sul, Porto Alegre, Rio Grande do Sul, 91501-900, Brazil; Email: kepler@if.ufrgs.br
Detlev Koester: Institut für Theoretische Physik und Astrophysik, Kiel, Schleswig-Holstein, 24098, Germany; Email: koester@astrophysik.uni-kiel.de

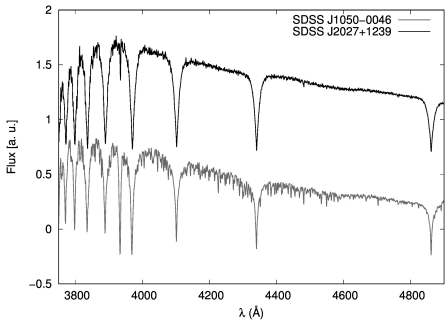

Figure 1. Two sdA stars, SDSS J105025.94-004655.5 (bottom) and SDSS J202721.77+123942.7 (top). While SDSS J1050-0046 shows lots of metallic lines, SDSS J2027+1239 appears to have only a small amount of Ca and Mg.

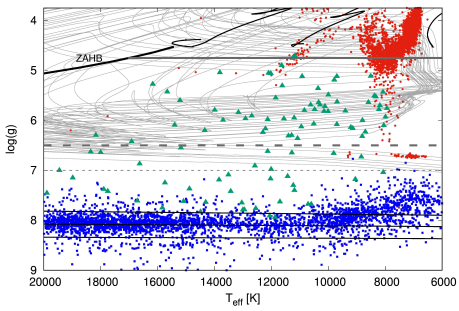

Figure 2. Red dots show the fitted O, B, A type objects. The white dwarfs of Kepler *et al.* (2016) are shown as blue squares, and the known ELMs as green triangles for comparison. The zero-age horizontal branch (ZAHB), above which stars are burning He in the core, is indicated. The remaining black lines are single evolution models for 1.0, 2.0 and 3.0 $M_\odot$ and Z=0.004 calculated with the LPCODE (see Althaus *et al.* 2003 and references therein). The horizontal lines indicate the upper limit in log g for main sequence A stars (4.75) and the lower limit for white dwarf stars (6.5–7.0). The grey lines are the binary evolution models of Istrate *et al.* (2016), taking into account stellar rotation. Both the ELMs and the sdAs can be explained by these models.

away before the He burning starts, a degenerate He core with a hydrogen atmosphere will be left: an ELM (see the ELM Survey: Brown *et al.* 2010; Kilic *et al.* 2011; Brown *et al.* 2012; Kilic *et al.* 2012; Brown *et al.* 2013; Gianninas *et al.* 2015; Brown *et al.* 2016).

Hermes *et al.* (2017) studied the sdAs that we published in Kepler *et al.* (2016), using radial velocity limits obtained from SDSS subspectra, photometric colours, and reduced proper motions, and concluded that over 99 per cent of them are unlikely to be ELMs. Likewise, Brown *et al.* 2017 obtained follow-up time-resolved spectroscopy for five eclipsing systems and concluded they are not ELMs. They proposed these objects are metal-poor $M \sim 1.2$ $M_\odot$ main sequence stars with $M \sim 0.8$ $M_\odot$ companions, and suggested that the majority of sdAs are metal-poor A–F type stars. They argued that the log g of the sdAs was overestimated by ~ 1 dex on the surface gravities derived from pure hydrogen models, which is likely explained by metal line blanketing below 9000 K. As illustrated in Figure 1, some sdAs do show significant amount of metals in their spectra; however, the metals are almost undetectable in others. Brown *et al.* (2017) gives no explanation as to why or how these early-type stars are found in the halo.

An alternative that was overlooked by Brown *et al.* (2017) is that these objects are He-core stars and byproducts of binary interaction, including not only the ELMs, but the pre-ELMs, which have not reached the white dwarf cooling track yet, and blue straggler stars. Although stellar multiplicity is a function of mass, increasing from about 46 per cent for G-stars (Tokovinin 2014) to over 70 per cent for A stars (De Rosa *et al.* 2014), most stars with initial mass larger than 1.0 $M_\odot$ are in multiple systems (Duchêne & Kraus 2013), making this alternative very attractive. As shown in Figure 2, the estimated $T_{\rm eff}$ and log g of the sdAs are consistent with binary evolution models. Even though the time spent with log $g = 5-6$ is ten times smaller than with log $g = 6-7$ in the models of Istrate *et al.* (2016), the average luminosity is about a hundred times higher in the log $= 5-6$ range, hence the objects are five magnitudes brighter. Assuming a spherical distribution, and limiting magnitudes of $g = 14.5$ (bright saturation in the SDSS) and $g = 20$ (faint limit detection), the detection volume for log $= 5-6$ is a thousand times larger than the volume for log $= 6-7$. Combining these two factors, one should expect to find a hundred objects with log $g = 5-6$ for each object with log $g = 6-7$ in a magnitude-limited survey. Table 5 of Brown *et al.* (2016) lists 31 objects with log $g = 6-7$, but only 44 with log $g = 5-6$, about 85 per cent less than our estimate predicts, which is a consequence of their selection criteria.

Still, low ionisation potential metals can in fact contribute significantly to the electron pressure, so the issue raised by Brown *et al.* (2017) concerning the possible overestimate on the log g deserves attention. In Pelisoli *et al.* (2017), we have presented a brief analysis of the sdA population using a grid of solar metallicity models to account for the metal effect. In this work, we further analyse the sdA sample in the light of these new spectral models.

Colours, proper motions, and galactic velocities are studied in order to access their possible nature. Analysing the SDSS subspectra, we find five new probable ELMs, two of which we confirm with our analysis of the SDSS radial velocities, and one also shows photometric variability in the Catalina Sky Survey (CSS) data. It seems that more than one evolution channel is needed to explain the sdA population. A definitive explanation of their nature and origin will help us to better understand not only stellar evolution, but also the formation of the halo.

2 Methods

The 55 000+ spectra of automatically classified O, B, A and white dwarf stars retrieved from the SDSS database were first fitted with a grid of spectral models derived from pure hydrogen atmosphere models calculated using an updated version of the code described in Koester (2010). Objects with $\log g \geq 5.5$ were published in the SDSS DR12 white dwarf catalogue by Kepler *et al.* (2016) and were the first to be called sdAs. Both Hermes *et al.* (2017) and Brown *et al.* (2017) studied this DR12 sample reaching the conclusion that they are overwhelmingly not ELMs. The explanation of Brown *et al.* (2017) was an overestimate in $\log g$ resulting from the fact that pure hydrogen models ignore the effect of metal line blanketing. To account for that, we added metals, in solar abundances for simplicity, to our model atmosphere and synthetic spectra. Our grid covers $6\,000\ \mathrm{K} \leq T_{\mathrm{eff}} \leq 40\,000\ \mathrm{K}$ and $3.5 \leq \log g \leq 8.0$. The objects were fitted with this new grid first reported in Pelisoli *et al.* (2017).

While spectra are the most reliable way to estimate the physical properties of a star, the colours of an object alone can still be used as a complement and tell us something about its nature. The ultraviolet magnitudes, in particular, are very useful in identifying if the T_{eff} of an object is high enough for it to be burning helium. We retrieved the far- and near-ultraviolet (*fuv* and *nuv*) magnitudes from the Galaxy Evolution Explorer (GALEX) when available. Extinction correction was applied using the $E(B-V)$ value given on the GALEX catalogue, $R_{fuv} = 4.89$ and $R_{nuv} = 7.24$ (Yuan *et al.* 2013).

Assuming the objects were main sequence stars, we estimated their distances d by assuming a radius interpolated from solar-abundance values given the T_{eff} of the object. The distance was calculated from the solid angle, which is estimated in a photometric fit to the SDSS *ugriz* magnitudes and the GALEX *fuv* and *nuv* magnitudes. Given the galactic latitude b, we estimated the distance from the disk Z as $d \sin(b)$.

We studied the proper motion of the O, B, A type objects using a reduced proper motion diagram (*e.g.* Gentile-Fusillo *et al.* 2015), where the reduced proper motion is given by:

$$H_g = g_0 + 5\log(\mu[''/yr]) + 5. \quad (1)$$

It can be interpreted as a proxy for the absolute magnitude: the higher the reduced proper motion, the fainter the object. We used the proper motions of Munn *et al.* (2004) and Munn *et al.* (2014), given in the SDSS tables. They were obtained combining the data from the U.S. Naval Observatory (USNO) and the SDSS. We only show in the plot objects with reliable proper motion, namely with the following characteristics:

- proper motion $> 3\sigma_{\mathrm{ppm}}$;
- distance to nearest neighbour with $g > 22.0$ larger than 5";
- only one matched object in the USNO catalogue;
- at least four detections in the USNO catalogue plates;
- RMS residual for the proper motion fit in right ascension smaller than 500.0;
- RMS residual for the proper motion fit in declination smaller than 500.0.

Typical errors for the whole sample are 2–4 mas/yr; for the reliable proper motion sample this goes down to 0.5 mas/yr. For objects with a good proper motion, we have also evaluated the galactic velocities U, V, and W following Johnson and Soderblom (1987), with the radial velocities we derived from the spectra, assuming both a main sequence and an ELM radius.

To search for binaries in the sample, we have used the SDSS subspectra. Each final SDSS spectrum is composed by multiple spectra, usually three, with $\sim$ 15 min exposure time. The signal-to-noise ration (S/R) of the subspectra is almost always below ten, so while conclusions can hardly be made based solely on the SDSS subspectra, they can be used to probe for possible variations suggesting the need for a follow-up. Our approach is similar to that of Badenes & Maoz (2012) and Hermes *et al.* (2017). We normalise each subspectrum by the continuum, which is estimated by fitting a linear function between each of the Balmer lines, and then fit each of the lines (up to H8) to a Gaussian profile. The obtained redshift to the line centre is used to estimate a radial velocity for each line. The final radial velocity for the given subspectrum is assumed to be the average velocity, with the error estimated by the standard deviation.

We were able to obtain a fit to 80 per cent of the spectra in the O, B, A sample. We then evaluated the ΔV between the maximal and the minimal estimated radial velocities, considering only estimates with an error smaller than 100 km/s. Badenes & Maoz (2012) suggest that follow-up is needed to reach conclusions on objects that show $\Delta V < 200$ km/s, so we restrict further analysis to 14 objects showing $\Delta V > 200$ km/s. We used the Period04 software (Lenz & Breger 2005) to estimate the orbital period by doing a Fourier transform and finding the orbital solution with the smallest residuals.

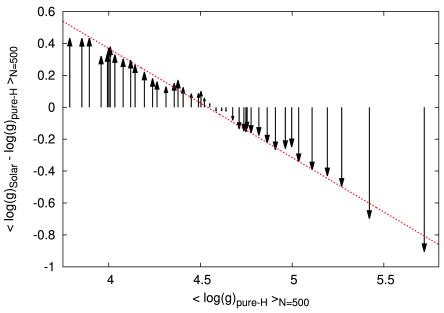

Figure 3. Shift in log g with the addition of metals in solar abundances as a function of the log g given by the pure-H models. Values were averaged over 500 objects sorted by log g. The shifts are well described by a linear fit $\Delta \log g = -0.68(0.01) \log g_{\text{pure-H}} + 3.10(0.06)$, shown as a red dashed line. The pure-H values are almost 1.0 dex higher than the solar abundance values above log $g = 5.5$. This is a similar result to the obtained by Brown *et al.* (2017) when when fitting pure hydrogen model to synthetic main-sequence spectra.

3 Results

3.1 Spectral fits

The shifts in $\log g$ and in T_{eff} when going from a pure-hydrogen model to a solar abundance model are shown in Figures 3 and 4. They were averaged between 500 objects, with the sample sorted according to $\log g$ or T_{eff}, respectively. Only objects with T_{eff} differing by less than 500 K were taken into account, to avoid contamination by objects suffering from hot-cool solution degeneracy. We find that the addition of metals does not cause a constant shift in $\log g$ as suggested by Brown *et al.* (2017). The shift behaves linearly, with $\log g < 4.5$ objects showing an upward correction and $\log g > 4.5$ showing a downward correction. Above $\log g = 5.5$, where the sdAs of Kepler *et al.* (2016) are, about −1.0 dex is indeed the shift, as found by Brown *et al.* (2017). However, as the shift can go either way, even though the addition of metals solves the $\log g$ discrepancy for a few objects, others are raised above the $\log = 5.0$ limit, and still can not be explained by single evolution, even when metals are taken into account.

This systematic trend also reflects on the dependence of the $\log g$ change with T_{eff}, shown on Figure 4. At $T_{\text{eff}} \sim 8\,500$ K, there are objects spanning all the $\log g$ range (see Figure 2), but a prevalence of objects with lower $\log g$, which have an upward correction. Hence the same upward correction is seen in this T_{eff} range. Between 7 500 – 8 000 K, a gap in the lower $\log g$ objects can be seen on Figure 2, which moves the correction downwards. Finally, below $T_{\text{eff}} \sim 7\,500$ K, most objects show $\log g \lesssim 4.5$, so the correction moves upwards again. Close to the cool border of T_{eff}, most objects are also close to the lower border in $\log g$, which is 3.75 for the pure-hydrogen models and 3.5 for the solar abundance models, implying on an average difference of 0.25. There can of course be differences in

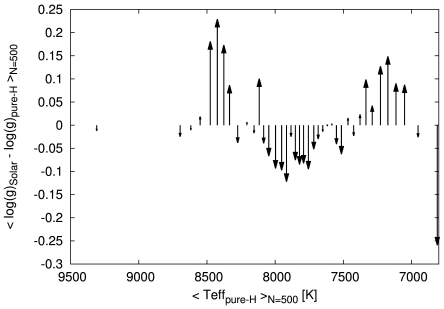

Figure 4. Change in log g when metals were added to the models as a function of the effective temperature of the pure-H models. The T_{eff} and the change in log g were averaged over 500 objects, sorted by T_{eff}. The apparent puzzling behaviour is a consequence of the systematic effect found for as a function of log $g_{\text{pure-H}}$, which implies a correlation also in T_{eff}, depending on how each range of $\log g$ is sampled in each bin of T_{eff}, as discussed in the text.

metallicity and errors in the determination, so individual objects can somewhat obscure these trends.

The solar abundance solutions put most of the 2 443 sdAs published in by Kepler *et al.* (2016) in the main sequence range, with the exception of 39 objects with still show $\log g \geq 5.0$. Only seven out of those maintain $\log g \geq 5.5$ in the solar abundance models, two of them were published on the ELM Survey, (SDSS J074615.83+392203.1 in

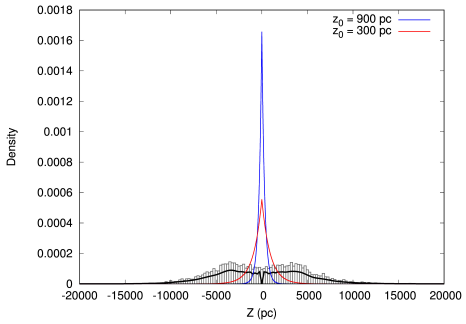

Figure 5. The distance to the disk of the stars classified as O, B and A, assuming a main sequence radius. The histogram is given as $N/N_{\rm total}$; the solid black line is calculated assuming each point as a Gaussian with standard deviation of 0.1 Z. The red line is an exponential thin disk model assuming $Z_0 = 300$ pc, while the blue line is a thick disk model with $Z_0 = 900$ pc. All functions are normalised. It is clear that, if indeed main sequence objects, these stars are not consistent with a disk distribution, but would rather have to be in the halo.

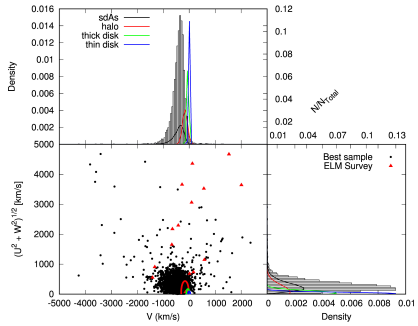

Figure 6. Toomre diagram of the objects in our sample, assuming a main sequence radius. The velocities the objects in the ELM survey would have if main sequence radii were assumed are shown for comparison. Density plots are shown to left and on top. The ellipses indicate the 3-σ values for halo (red), thick disk (green) and thin disk (blue) according to Kordopatis *et al.* (2011).

Brown *et al.* 2012, and SDSS J091709.55+463821.7 in Gianninas *et al.* 2015). However, given that the change in $\log g$ can also be upward, other objects are raised above the main sequence $\log g$ limit. We find 1 952 objects to show $5.0 \leq \log(g) < 7.0$ and $T_{\rm eff} < 20\,000$ K; out of those, 492 show $\log g > 5.5$.

3.2 Distance and Velocities

Figure 5 shows a histogram of the density $N/N_{\rm total}$ given the estimated distances from the disk for the sample of O, B and A stars assuming they have main sequence radii. Exponential functions describing a thin and thick disk with the scaleheights given by Bland-Hawthorn & Gerhard (2016) are shown as a comparison. It is clear that, when a main sequence radius is assumed, the sdA distribution extends much further than the disk, to distances up to 10 kpc.

A similar result occurs when the Galactic velocities U, V, W are estimated. Figure 6 shows the velocities estimated assuming the main sequence radius. Ellipses with the 3-σ value for the thin disk, thick disk and halo, according to Kordopatis *et al.* (2011), are shown as a comparison. Again, the objects seem to reach velocities much higher than the disk distribution, and even than the halo distribution. In fact, over 30 per cent of the stars have velocities more than 4-σ above the halo mean velocity dispersion when a main sequence radius is assumed. Even if we assume the distance is systematically 10 per cent smaller than our estimate, over 20 per cent of the objects show velocities above 4-σ. The statistical uncertainty is however set to zero when calculating the tangential velocities, so the identification of individual significant outliers requires caution. Considering the sample as whole though, it follows that metal-poor A–F main sequence is probably a too simplistic explanation for these objects. At the very least, they must be in a binary to account for the high velocities, which could be due to orbital motion rather than Galactic motion.

3.3 Reduced proper motion

The reduced proper motion for the O, B, and A stars is shown in Figure 7. It suggests that most of these objects have, in average, H_g lower than the estimated for known ELMs. However, their reduced proper motion is mostly consistent with a tentative limit based on Gentile-Fusillo *et al.* (2015), but dislocated to include all ELMs, suggesting the objects might have similar absolute magnitude, and thus similar radii, to the known ELMs. This limit is given by

$$H_g = 2.72(g-z)_0 + 16.09. \quad (2)$$

The objects are colour coded by their Mahalonobis distance D_M to the halo when a main sequence radius is assumed. The Mahalonobis distance is given by

$$D_M = \sqrt{\frac{(U-\langle U\rangle)^2}{\sigma_U^2} + \frac{(V-\langle V\rangle)^2}{\sigma_V^2} + \frac{(W-\langle W\rangle)^2}{\sigma_W^2}}, \quad (3)$$

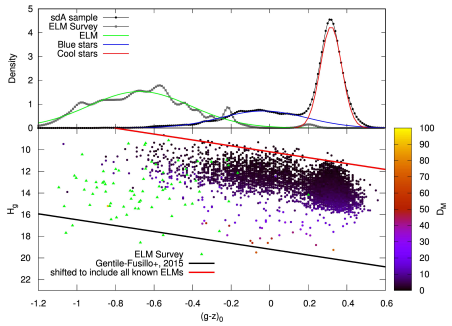

Figure 7. $H_g \times (g-z)_0$ diagram (see *e.g.* Gentile-Fusillo *et al.* 2015), with the objects in sample B colour coded according to their Mahalonobis distance to the halo given a main sequence radius. Known ELMs are shown as green triangles for comparison. The top plot shows the densities assuming each object as a Gaussian to account for the uncertainty; it becomes clear that there are two populations of objects within the sdA sample. The suggested limit for white dwarf detection with probability equal to 1.0 given by Gentile-Fusillo *et al.* (2015) is indicated as a black solid line. Most known ELMs, due to their larger radius implying a smaller reduced proper motion, since they can be detected at larger distances, are not below the white dwarf limit. A reference line, dislocating the white dwarf limit to include all known ELMs is shown as a red dashed line. Most O, B and A stars are also below such line.

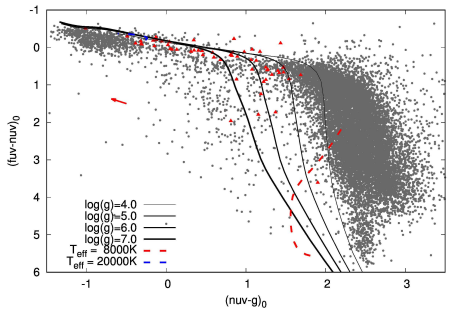

Figure 8. Diagram showing the $(fuv-nuv)_0$ and $(nuv-g)_0$ colours. Grey dots are the O, B, and A objects, and red triangles are the known ELMs shown for comparison. The red arrow indicates the average reddening correction vector. The indicated models were obtained from our pure-hydrogen spectral models.

where we have assumed the values of Kordopatis *et al.* (2011) for the halo mean velocities and dispersions.

This diagram is very enlightening when we look at the $(g-z)_0$ colour in terms of density. It is evident that there are two different populations within the sample: one to the red limit of the diagram and another in an intermediary region. While the distribution of the red population has no intersection with the known ELMs, the distribution resulting from the blue population shares colour properties with the known ELMs. This is a clear indication that more than one evolutionary channel is needed to explain the nature of these objects. The red distribution contains about 60 per cent of the sample. Most of these objects ($\sim$ 97 per cent) are cooler than 8 000 K and show $\log g < 4.75$, implying they may be low metallicity F stars or other late-type objects, which can be found in the halo. The blue population, on the other hand, contains about 40 per cent of the sample and most of the objects hotter than 8 000 K (A-type and earlier) and with higher $\log g$. These early-type stars can not easily be explained as halo objects, since their life time in the main sequence is much smaller than the age of the halo. This population probably consists of binaries, such as blue stragglers, and He-core objects, such as blue horizontal-branch stars (BHBs), as previous studies in the literature have found (*e.g.* Preston *et al.* 1994; Clewley *et al.* 2004; Brown *et al.* 2008; Xue *et al.* 2008), or pre-ELMs, and ELMs. However, there can also be a contribution from extragalactic stars accreted onto our Galaxy, as previously suggested by *e.g.* Rodgers *et al.* (1981); Lance (1988), and Preston *et al.* (1994).

3.4 UV colours

Figure 8 shows a $(fuv-nuv)_0 \times (nuv-g)_0$ for the O, B, and A stars and known ELMs for comparison. This diagram is especially useful in identifying if the objects can be hot subdwarfs in binaries. Hot subdwarf stars have similar flux in the optical region to main sequence stars of type F, G, and K, so that if they are in a binary with one of these types of stars, the combined spectrum will appear to have an intermediary $\log g$, but a lower temperature, similar to what is found for the sdAs. We find that almost all the objects, with a 0.5 per cent exception, do not have significant flux in the UV, showing $(nuv-g)_0 < -0.4$, which rules out that these objects can be explained as sdOB + FGK binaries.

3.5 SDSS Radial Velocities

Figure 9 shows a histogram of the estimated radial velocity amplitude ΔV from the SDSS subspectra. Most spectra show $\Delta V < 100$ km/s, with 334 having $\Delta V > 100$ km/s. Out of those, 14 show $\Delta V > 200$ km/s. Two of these objects were previously published in the ELM Survey, namely SDSS J123800.09+194631.4 (Brown *et al.* 2013)

Table 1. Atmospheric and orbital parameters obtained for the objects shown in Figures 10 and 11, assuming the solar abundance models. Quoted uncertainties in our values of $T_{\rm eff}$ and $\log g$ are formal fit errors. The external uncertainties in the models are much larger, of about 5–10 per cent in $T_{\rm eff}$ and 0.25 dex in $\log g$. The orbital parameters are for the best solution, but some objects might need follow-up (see text for discussion). The secondary mass M_2 is the minimal mass assuming an edge-on orbit.

	SDSS J	g	$T_{\rm eff}$	$\log(g)$	P (h)	K (km/s)	R^2	M_2 ($M_\odot$)	$\Upsilon_{\rm merge}$ (Gyr)
(a)	104826.86-000056.7	18.39	8 508(17)	5.861(0.068)	2.9	246	0.88	0.32	2.7
(b)	120616.93+115936.2	17.37	8 869(12)	5.092(0.050)	6.4	220	1.00	0.50	16
(c)	045947.40-040035.2	19.62	8 182(21)	4.804(0.113)	61	53	0.82	0.18	11280
(d)	171906.23+254142.3	19.13	8 566(41)	4.126(0.128)	13	197	1.00	0.75	69
(e)	122911.49-003814.4	18.27	8 020(22)	4.657(0.128)	-	-	-	-	-

Table 2. Pure-hydrogen atmosphere spectral parameters for the objects shown in Table 1. As before, the uncertainties are of about 5–10 per cent in $T_{\rm eff}$ and 0.25 dex in $\log g$.

	SDSS J	$T_{\rm eff}$	$\log(g)$
(a)	104826.86-000056.7	8571	6.269
(b)	120616.93+115936.2	8861	5.308
(c)	045947.40-040035.2	8153	4.815
(d)	171906.23+254142.3	11288	4.500
(e)	122911.49-003814.4	8083	5.339

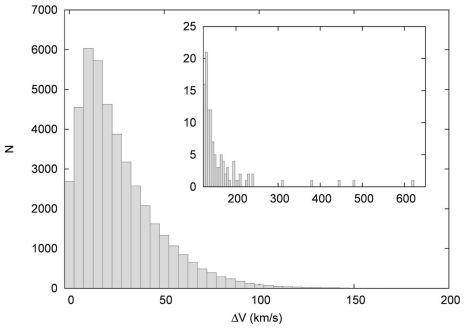

Figure 9. Histogram showing the obtained amplitude for all analysed SDSS spectra. Most show no significant amplitude, but over 300 indicate an amplitude between subspectra larger than 100 km/s, 14 larger than 200 km/s.

and SDSS J082511.90+115236.4 (Kilic *et al.* 2012). Three are hot subdwarf stars showing $T_{\rm eff} > 20\,000$ K, which are also commonly found in binaries (SDSS J141558.19-022714.3, SDSS J163205.75+172241.3, and SDSS J211651.95-003328.5). Two show $\log g > 7.0$ and are probably double degenerate systems (SDSS J095157.78+290341.5 and SDSS J132232.12+641545.8). One is a known CV (SDSS J152020.40-000948.3) identified by its colours by Gentile-Fusillo *et al.* (2015). The remaining six spectra belong to five objects. The spectra are shown in Figure 10. Their atmospheric parameters are shown in Table 1, for solar abundance models, and in Table 2, for pure-hydrogen atmosphere.

Using the radial velocities estimated from the SDSS spectra of these objects, we attempted to obtain their orbital parameters. The best obtained results are shown on Table 1. The best orbital solutions are shown on Figure 11. SDSS J104826.86-000056.7 has nineteen subspectra, which were enough to constrain the period and obtain a good orbital solution. SDSS J120616.93+115936.2 has only seven subspectra, but its light curve on the Catalina Sky Survey (CSS) shows variability with a period which was consistent with the highest peak on the Fourier transform of the velocities. The phase-folded light curve is shown in Figure 12. SDSS J045947.40-040035.2 has ten subspectra, but the spacing is such that many aliases arise in the Fourier transform, and in fact periods ranging from 10 h to 60 h had orbital solutions with similar residuals. As previously stated, follow-up is definitely needed to study the nature of this object. SDSS J171906.23+254142.3 has five subspectra, but less aliasing than SDSS J045947.40-040035.2, suggesting a period between 8 h and 14 h. We were not able to find a good solution for SDSS J122911.49-003814.4, which has six subspectra, therefore follow-up is required to probe its nature.

Out of these five objects, we conclude that SDSS J104826.86-000056.7 and SDSS J120616.93+115936.2 are unarguably new ELMs, given that both their atmospheric and orbital parameters are consistent with the class. The three remaining objects show the solar abundance $\log g < 5.0$. SDSS J122911.49-003814.4, however, has $\log g > 5.0$ when the pure-hydrogen models are used. Its spectra does not show strong metal lines, so it is a good ELM candidate. The confirmation of its nature is pending on follow-up studies that can allow the determination of its orbital parameters. SDSS J171906.23+254142.3 still shows $\log g < 5.0$ on the pure-hydrogen models, but the obtained radial velocity amplitude (197 km/s) can only be

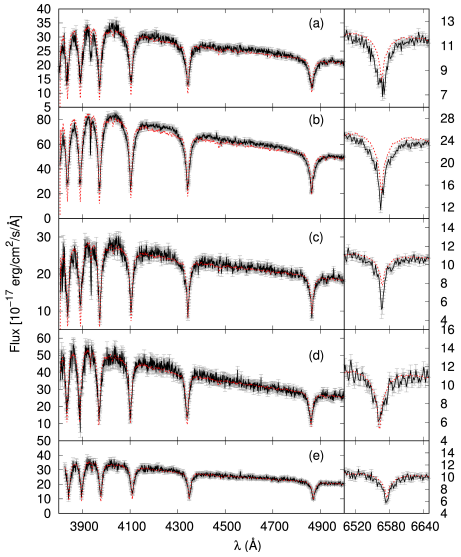

Figure 10. Spectra for the five objects showing $\Delta V > 200$ km/s (solid black line). The SDSS template is shown as a dashed red line for comparison. For the object with two spectra, the highest S/R spectrum is shown.

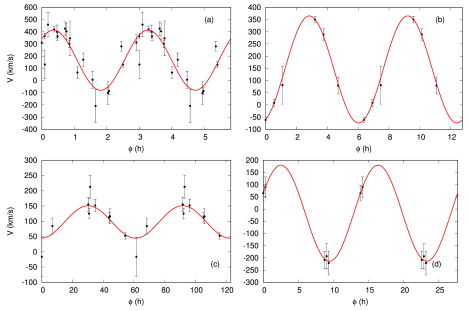

Figure 11. Best orbital solutions for the four objects for which we were able to constrain the period.

explained if the object is in a close binary, requiring it to be compact, therefore it is most likely an ELM. The most uncertain object is SDSS J045947.40-040035.2, which has $\log g$ in the threshold between main sequence and ELM assuming both models. The estimated distance assuming a main sequence radius is 16 kpc, and its velocities are consistent with the halo. The obtained period and amplitude are also consistent with a main sequence object.

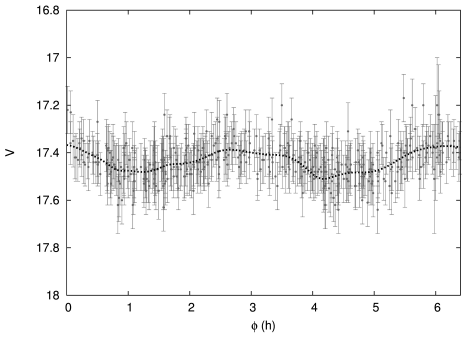

Figure 12. CSS light curve for SDSS J120616.93+115936.2, phase-folded to the 6.4 h, which is the same obtained analysing the velocities, suggesting the variability is due to either eclipses or ellipsoidal variation.

Given all that, SDSS J045947.40-040035.2 is probably a blue straggler star in the halo.

4 Discussion

We analysed O, B and A type stars identified by the SDSS pipeline, and estimated their $T_{\rm eff}$ and $\log g$ from their spectra, using spectral models derived from solar abundance atmospheric models. Comparing the results to our pure-hydrogen solutions published in Kepler *et al.* (2016), we showed that the addition of metals causes a shift in $\log g$ that is downwards for objects with $\log g > 4.5$, but upwards for objects with $\log g < 4.5$. No general conclusion can be made as to whether the pure-hydrogen models are in fact overestimating the $\log g$, as was suggested by Brown *et al.* (2017), since the correction depends on the $\log g$. Moreover, although some objects do show many metallic lines in their spectra, others are restricted to Ca and Mg, which are also seen in the known ELMs, due to the fact that rotation has the power to counteract the gravitational settling (Istrate *et al.* 2016). It is clear from these studies that neither of these two grid of models are in fact adequate, they provide only rough estimates on the parameters, which are dependent on the metallicity. These spectra need to be analysed with more general grids, spanning different metallicities.

Independent of the estimated $\log g$, the magnitudes of the objects suggest that they can not simply be main sequence objects. Assuming a main sequence radius, we estimate distances which are not consistent with a disk dis-

tribution. The velocities are also not consistent with the disk and not even with the halo, with over 30 per cent of the O, B and A objects showing velocities more than 4-σ above the halo mean velocity. The most probable reason is that the radius estimate — assuming that the objects have main sequence radius — is wrong. If we assume they are He core objects, pre-ELMs and ELMs, they show a distribution consistent with the disk. Another possibility is that the high proper motion and estimated high radial velocity, leading to high spatial velocities, are actually due to orbital motion. They could be blue stragglers in the halo. Models by Schneider *et al.* (2015) suggest that mass accretion can make a star appear up to 10 times younger than its parent population, which would be sufficient to make an A star survive long enough in the halo. This is in agreement with previous studies in the literature, which find that $\sim$ 50 per cent of stars with A-type spectra in the halo are presumably blue stragglers (*e.g.* Norris & Hawkins 1991; Kinman *et al.* 1994; Preston *et al.* 1994; Clewley *et al.* 2004; Brown *et al.* 2008; Xue *et al.* 2008). The remaining objects are mostly explained as BHBs, hence He-core stars. Some authors suggest that a few could in fact be main sequence stars with an extragalactic origin to explain their young ages (*e.g.* Preston *et al.* 1994). The (pre-)ELM explanation is mostly ignored by these studies, since this is a relatively new class. The sdAs could also be binaries of a hot subdwarf with a main sequence star, but the UV colours suggest that this is not the case, since they do not show significant flux in the UV.

Our most significant result is that the sdAs are clearly composed of two populations. One population contains the red objects, and it has no overlap with the known ELMs. On the other extreme, there is a blue population, which does overlap with known ELMs, but contains cooler objects. The red distribution is possibly dominated by metal-poor main sequence late-type stars, which can be found in the halo, with contamination of cooler pre-ELMs and ELMs, since there is an intersection with the blue distribution. The blue distribution, on the other hand, should contain the missing cool pre-ELM and ELM population, which is under-represented in the literature. Evolutionary models predict that ELMs spend about the same amount of time above and below $T_{\rm eff}$ = 8 500 K; however, their cooling time-scale is dictated by residual burning. On one hand, this time-scale can be prolonged if mass loss is not effective, so that the star is left with a thick hydrogen atmosphere, where burning via $p-p$ chain reaction will occur (*e.g.* Maxted *et al.* 2014). On the other hand, instead of a smooth transition from pre-ELM to ELM, the star can undergo episodes of unstable CNO burning, or shell flashes, that shorten the cooling time-scale by reducing the hydrogen mass on the surface (Althaus *et al.* 2013; Istrate *et al.* 2016). As there are many uncertainties in the models, concerning *e.g.* assumptions on element diffusion, progenitor initial mass and metallicity, and rotation, the cooling time scale between models can vary by more than a factor of two. Brown *et al.* (2017) estimated a 1:2 ratio of ELMs in the ranges 6500 < $T_{\rm eff}$ < 9000 K to 10 000 < $T_{\rm eff}$ < 15 000 K. Propagating the factor of two uncertainty in the cooling time scale, these ratio can be from 1:4 to 1:1, so 20–50 per cent of the ELMs should show $T_{\rm eff}$ < 9 000 K; however, as a systematic effect of the search criterion, less than 5 per cent of the published ELMs are in this range. Moreover, the ratio of $\log g = 6-7$ to $\log g = 5-6$ is about 3:4 in the ELM survey, totally dominated by selection effects, while the brightness difference suggests it should be 1:100.

Analysing the SDSS radial velocities, we confirm two new ELMs, SDSS J104826.86-000056.7 and SDSS J120616.93+115936.2. SDSS J120616.93+115936.2 also shows photometric variability with the same period as the orbital period. Two other objects are most likely ELMs. SDSS J171906.23+254142.3, although showing $\log g < 5.0$, has an amplitude of almost 200 km/s in its best orbital fit. However, as only five subspectra are available, the period is not well constrained, and follow-up should be done to confirm the nature of this object. The SDSS subspectra of SDSS J122911.49-003814.4 did not allow the estimate of its period, but the high amplitude between its subspectra and its $\log g$ above the main sequence limit favour the ELM classification. All of these objects show $T_{\rm eff}$ < 9000 K. There are only six confirmed ELMs in close binaries in this range (Brown *et al.* 2016), reflecting the lack of effort to find ELMs in the cool end of the distribution, hence the importance of further studying the objects found here. Finally, we also find SDSS J045947.40-040035.2 most likely to be a blue straggler star in the halo.

Our effort shows that more than one evolutionary channel is definitely needed to explain the sdA population. For one, there are definitely He core objects such as pre-ELMs and ELMs in the sample. Even if only a small percentage of sdAs is confirmed as ELMs, the number would be high enough to significantly increase the number of known ELMs, especially at the cool end of the distribution. Our understanding of binary evolution, and especially of the common envelope phase that ELMs must experience, can be much improved if we have a sample covering all parameters predicted by these models. The sdA sample can provide that. Our understanding of the formation and evolution of the Galactic halo would also benefit from more detailed study of the sdAs. Many seem to be in the halo with ages and velocities not consistent with the halo population. It is possible that accreted stars from neighbouring

dwarf galaxies might be among them. Those whose velocities are in fact consistent with the halo can in turn help us study its dynamics and possibly better constrain the gravitational potential of the halo. The key message of our results is that we should not overlook the complexity of the sdAs. They are of course not all pre-ELM or ELM stars, but they cannot be explained simply as main sequence metal-poor A–F stars. They are most likely products of binary evolution and as such are a valuable asset for improving our models.

References

Althaus, L. G., Miller Bertolami, M. M., Córsico, A. H. 2013, A&A, 557, A19.

Althaus, L. G., Serenelli, A. M., Córsico, A. H., Montgomery, M. H. 2003, A&A, 404, 593–609.

Badenes, C., Maoz, D. 2012, ApJ, 749, L11.

Bland-Hawthorn, J., Gerhard, O. 2016, Annual Review of Astronomy and Astrophysics, 54, 529–596.

Brown, W. R., Beers, T. C., Wilhelm, R., Allende-Prieto, C., Geller, M. J., Kenyon, S. J., et al. 2008, ApJ, 135, 564–574.

Brown, W. R., Gianninas, A., Kilic, M., Kenyon, S. J., Allende Prieto, C. 2016, ApJ, 818, 155.

Brown, W. R., Kilic, M., Allende Prieto, C., Gianninas, A., Kenyon, S. J. 2013, ApJ, 769, 66.

Brown, W. R., Kilic, M., Allende Prieto, C., Kenyon, S. J. 2010, ApJ, 723, 1072–1081.

Brown, W. R., Kilic, M., Allende Prieto, C., Kenyon, Scott J. 2012, ApJ, 744, 142.

Brown, W. R., Kilic, M., Gianninas, A. 2017, ApJ, 839, 23.

Clewley, L., Warren, S. J., Hewett, P. C., Norris, J. E., Evans, N. W. 2004, MNRAS, 352, 285–298.

De Rosa, R. J., Patience, J., Wilson, P. A., Schneider, A., Wiktorowicz, S. J., Vigan, A. 2014, MNRAS, 437, 1216–1240.

Duchêne G., Kraus A. 2013, ARA&A, 51, 269–310.

Gentile-Fusillo, N. P., Gaensicke, B. T., Greiss, S. 2015, MNRAS, 448, 2260–2274.

Gianninas, A., Kilic, M., Brown, W. R., Canton, P., Kenyon, S. J. 2015, ApJ, 812, 167.

Hermes, J. J., G$^{\acute{a}}$nsicke, B. T., Breedt, E. 2017, In: P.-E. Tremblay, B. Gaensicke, T. Marsh (Ed.), Proceedings of 20th European White Dwarf Workshop (25-29 July 2016, Coventry, UK), ASP Conference Series, 509, 453–459.

Istrate, A. G., Marchant, P., Tauris, T. M., Langer, N., Stancliffe, R. J., Grassitelli, L. 2016, A&A, 595, A35.

Johnson, D. R. H. and Soderblom, D. R. 1987, AJ, 93, 864–867.

Kepler, S. O., Pelisoli, I., Koester, D., Ourique, G., Romero, A. D., Reindl, N. et al. 2016, MNRAS, 455, 3413–3423.

Kilic, M., Brown, W. R., Allende Prieto, C., Ag$^{\acute{u}}$eros, M. A., Heinke, C., Kenyon, S. J. 2011, ApJ, 727, 3.

Kilic, M., Brown, W. R., Allende Prieto, C., Kenyon, S. J., Heinke, C. O., Ag$^{\acute{u}}$eros, M. A., et al. 2012, ApJ, 751, 141.

Kilic, M., Stanek, K. Z., Pinsonneault, M. H. 2007, ApJ, 671, 761–766.

Kinman, T. D., Suntzeff, N. B., Kraft, R. P. 1994, AJ, 108, 1722–1772.

Koester, D. 2010, MmSAI, 81, 921–931.

Kordopatis, G., Recio-Blanco, A., de Laverny, P., Gilmore, G., Hill, V., Wyse, R. F. G. 2011, A&A, 535, A107.

Lance, C. M. 1988, AJ, 334, 927–946.

Lenz, P., Breger, M. 2005, Communications in Asteroseismology, 46, 53–136.

Maxted, P. F. L., Bloemen, S., Heber, U., Geier, S., Wheatley, P. J., Marsh, T. R. et al. 2014, MNRAS, 437, 1681–1697.

Munn, J. A., Monet, D. G., Levine, S. E., Canzian, B., Pier, J. R., Harris, H. C. et al. 2004, AJ, 127, 3034–3042.

Munn, J. A., Harris, H. C., von Hippel, T., Kilic, M., Liebert, J. W., Williams, K. A. et al. 2014, AJ, 148, 132.

Norris, J.E. & Hawkins, M.R.S. 1991, 380, 104–115.

Pelisoli, I., Kepler, S. O., Koester, D., Romero, A. D. 2017, In: P.-E. Tremblay, B. Gaensicke, T. Marsh (Ed.), Proceedings of 20th European White Dwarf Workshop (25-29 July 2016, Coventry, UK), ASP Conference Series, 509, 447–452.

Preston, G. W., Beers, T. C., Shectman, S. A. 1994, AJ, 108, 538–554.

Rodgers, A. W., Harding, P., Sadler, E. 1981, AJ, 244, 912–918.

Romero, A. D., Campos, F., Kepler, S. O. 2015, MNRAS, 450, 3708–3723.

Schneider, F. R. N., Izzard, R. G., Langer, N., de Mink, S. E. 2015, ApJ, 805, 20.

Tokovinin A. 2014, AJ, 147, 87.

Xue, X. X., Rix, H. W., Zhao, G., Re Fiorentin, P., Naab, T., Steinmetz, M. et al. 2008, ApJ, 684, 1143–1158.

Yuan, H. B., Liu, X. W., Xiang, M. S. 2013, MNRAS, 430, 2188–2199.

Bibliography

Abazajian, K. et al. The First Data Release of the Sloan Digital Sky Survey. *The Astronomical Journal*, v. 126, p. 2081–2086, 2003.

Abazajian, K. N. et al. The Seventh Data Release of the Sloan Digital Sky Survey. *ApJS*, v. 182, p. 543–558, 2009.

Adelman-McCarthy, J. K. et al. The Fourth Data Release of the Sloan Digital Sky Survey. *ApJS*, v. 162, p. 38–48, 2006.

Adelman-McCarthy, J. K. et al. The Sixth Data Release of the Sloan Digital Sky Survey. *ApJS*, v. 175, p. 297–313, 2008.

Ahn, C. P. et al. The Tenth Data Release of the Sloan Digital Sky Survey: First Spectroscopic Data from the SDSS-III Apache Point Observatory Galactic Evolution Experiment. *ApJS*, v. 211, p. 17, 2014.

Allen, C.; Santillan, A. An improved model of the galactic mass distribution for orbit computations. *Revista Mexicana de Astronomia y Astrofisica*, v. 22, p. 255–263, out. 1991.

Allende Prieto, C.; del Burgo, C. New bright optical spectrophotometric standards: A-type stars from the STIS Next Generation Spectral Library. *MNRAS*, v. 455, p. 3864–3870, fev. 2016.

Althaus, L. G. et al. White dwarf evolutionary sequences for low-metallicity progenitors: The impact of third dredge-up. *A&A*, v. 576, p. A9, 2015.

Althaus, L. G.; Miller Bertolami, M. M.; Córsico, A. H. New evolutionary sequences for extremely low-mass white dwarfs. Homogeneous mass and age determinations and asteroseismic prospects. *A&A*, v. 557, p. A19, 2013.

Althaus, L. G. et al. New Evolutionary Sequences for Hot H-Deficient White Dwarfs on the Basis of a Full Account of Progenitor Evolution. *ApJ*, v. 704, p. 1605–1615, 2009.

Althaus, L. G. et al. Evolution and colors of helium-core white dwarf stars with high-metallicity progenitors. *A&A*, v. 502, 2009.

Althaus, L. G.; Serenelli, A. M.; Benvenuto, O. G. Diffusion and the occurrence of hydrogen-shell flashes in helium white dwarf stars. *MNRAS*, v. 323, p. 471–483, 2001.

Althaus, L. G. et al. New evolutionary models for massive ZZ Ceti stars. I. First results for their pulsational properties. *A&A*, v. 404, p. 593–609, jun. 2003.

Altmann, M. et al. Hot Stuff for One Year (HSOY). A 583 million star proper motion catalogue derived from Gaia DR1 and PPMXL. *A&A*, v. 600, p. L4, abr. 2017.

Andrews, J. J. et al. Constraints on the Initial-Final Mass Relation from Wide Double White Dwarfs. *ApJ*, v. 815, p. 63, 2015.

Aoki, W. et al. High-resolution Spectroscopy of Extremely Metal-poor Stars from SDSS/SEGUE. I. Atmospheric Parameters and Chemical Compositions. *AJ*, v. 145, p. 13, jan. 2013.

Avvakumova, E. A.; Malkov, O. Y.; Kniazev, A. Y. Eclipsing variables: Catalogue and classification. *Astronomische Nachrichten*, v. 334, p. 860, out. 2013.

Badenes, C.; Maoz, D. The Merger Rate of Binary White Dwarfs in the Galactic Disk. *ApJL*, v. 749, p. L11, abr. 2012.

Bainbridge, M. et al. Probing the Gravitational Dependence of the Fine-Structure Constant from Observations of White Dwarf Stars. *Universe*, v. 3, p. 32, mar. 2017.

Barlow, B. N. et al. A Radial Velocity Study of Composite-spectra Hot Subdwarf Stars with the Hobby-Eberly Telescope. *ApJ*, v. 758, p. 58, 2012.

Bell, K. J. et al. Outbursts in two new cool pulsating DA white dwarfs. *arXi:1607.01392*, 2016.

Bell, K. J. et al. SDSS J1618+3854: The Sixth Extremely Low-Mass White Dwarf Pulsator. In: Dufour, P.; Bergeron, P.; Fontaine, G. (Ed.). *19th European Workshop on White Dwarfs*. [S.l.: s.n.], 2015. (Astronomical Society of the Pacific Conference Series, v. 493), p. 217.

Bergeron, P.; Saffer, R. A.; Liebert, J. A spectroscopic determination of the mass distribution of DA white dwarfs. *ApJ*, v. 394, p. 228–247, 1992.

Bergeron, P. et al. A Comprehensive Spectroscopic Analysis of DB White Dwarfs. *ApJ*, v. 737, p. 28, 2011.

Bhatti, W. A. et al. Variable Point Sources in Sloan Digital Sky Survey Stripe 82. I. Project Description and Initial Catalog (0 hr $< \alpha <$ 4 hr). *ApJS*, v. 186, p. 233–258, fev. 2010.

Binnendijk, L. The orbital elements of W Ursae Majoris systems. *Vistas in Astronomy*, v. 12, p. 217–256, 1970.

Bland-Hawthorn, J.; Gerhard, O. The Galaxy in Context: Structural, Kinematic, and Integrated Properties. *Annual Review of Astronomy and Astrophysics*, v. 54, p. 529–596, set. 2016.

Bohlin, R. C. HST Stellar Standards with 1% Accuracy in Absolute Flux. In: Sterken, C. (Ed.). *The Future of Photometric, Spectrophotometric and Polarimetric Standardization*. [S.l.: s.n.], 2007. (Astronomical Society of the Pacific Conference Series, v. 364), p. 315.

Brown, J. M. et al. The Binary Fraction of Low-mass White Dwarfs. *ApJ*, v. 730, p. 67, abr. 2011.

Brown, W. R.; Geller, M. J.; Kenyon, S. J. MMT Hypervelocity Star Survey. *ApJ*, v. 690, p. 1639–1647, jan. 2009.

Brown, W. R.; Geller, M. J.; Kenyon, S. J. MMT Hypervelocity Star Survey. II. Five New Unbound Stars. *ApJ*, v. 751, p. 55, maio 2012.

Brown, W. R.; Geller, M. J.; Kenyon, S. J. MMT Hypervelocity Star Survey. III. The Complete Survey. *ApJ*, v. 787, p. 89, maio 2014.

Brown, W. R. et al. The ELM Survey. VII. Orbital Properties of Low-Mass White Dwarf Binaries. *ApJ*, v. 818, p. 155, 2016.

Brown, W. R. et al. The ELM Survey. I. A Complete Sample of Extremely Low-mass White Dwarfs. *ApJ*, v. 723, p. 1072–1081, 2010.

Brown, W. R. et al. The ELM Survey. III. A Successful Targeted Survey for Extremely Low Mass White Dwarfs. *ApJ*, v. 744, p. 142, 2012.

Brown, W. R. et al. The ELM Survey. V. Merging Massive White Dwarf Binaries. *ApJ*, v. 769, p. 66, 2013.

Brown, W. R.; Kilic, M.; Gianninas, A. The Physical Nature of Subdwarf A Stars: White Dwarf Impostors. *ApJ*, v. 839, p. 23, abr. 2017.

Brown, W. R. et al. A 12 Minute Orbital Period Detached White Dwarf Eclipsing Binary. *ApJL*, v. 737, p. L23, ago. 2011.

Brown, W. R. et al. Most Double Degenerate Low-mass White Dwarf Binaries Merge. *ApJ*, v. 824, p. 46, jun. 2016.

Camargo, D. et al. Discovery of two embedded clusters with WISE in the high Galactic latitude cloud HRK 81.4-77.8. *MNRAS*, v. 448, p. 1930–1936, abr. 2015.

Campos, F. et al. A comparative analysis of the observed white dwarf cooling sequence from globular clusters. *MNRAS*, v. 456, p. 3729–3742, mar. 2016.

Carter, P. J. et al. A search for the hidden population of AM CVn binaries in the Sloan Digital Sky Survey. *MNRAS*, v. 429, p. 2143–2160, mar. 2013.

Castanheira, B. G. et al. Towards a pure ZZ Ceti instability strip. *A&A*, v. 462, p. 989–993, fev. 2007.

Clayton, G. C. The R Coronae Borealis Stars. *Publications of the Astronomical Society of the Pacific*, v. 108, p. 225, mar. 1996.

Clemens, J. C.; Crain, J. A.; Anderson, R. The Goodman spectrograph. In: Moorwood, A. F. M.; Iye, M. (Ed.). *Ground-based Instrumentation for Astronomy*. [S.l.: s.n.], 2004. (SPIE, v. 5492), p. 331–340.

Copperwheat, C. M. et al. Radial-velocity measurements of subdwarf B stars. *MNRAS*, v. 415, p. 1381–1395, ago. 2011.

Córsico, A. H.; Althaus, L. G. Pulsating low-mass white dwarfs in the frame of new evolutionary sequences. I. Adiabatic properties. *A&A*, v. 569, p. A106, 2014.

Córsico, A. H.; Althaus, L. G. Pulsating low-mass white dwarfs in the frame of new evolutionary sequences. II. Nonadiabatic analysis. *A&A*, v. 585, p. A1, jan. 2016.

Córsico, A. H. et al. The rate of cooling of the pulsating white dwarf star G117-B15A: a new asteroseismological inference of the axion mass. *MNRAS*, v. 424, p. 2792–2799, ago. 2012.

Córsico, A. H. et al. Pulsating low-mass white dwarfs in the frame of new evolutionary sequences. III. The pre-ELM white dwarf instability strip. *A&A*, v. 588, p. A74, 2016.

Cummings, J. D. et al. Two Massive White Dwarfs from NGC 2323 and the Initial-Final Mass Relation for Progenitors of 4 to 6.5 M. *ApJ*, v. 818, p. 84, fev. 2016.

D'Cruz, N. L. et al. The Origin of Extreme Horizontal Branch Stars. *ApJ*, v. 466, p. 359, jul. 1996.

De Rosa, R. J. et al. The VAST Survey - III. The multiplicity of A-type stars within 75 pc. *MNRAS*, v. 437, p. 1216–1240, jan. 2014.

Drake, A. J. et al. First Results from the Catalina Real-Time Transient Survey. *ApJ*, v. 696, p. 870–884, 2009.

Drake, A. J. et al. The Catalina Surveys Periodic Variable Star Catalog. *ApJS*, v. 213, p. 9, 2014.

Drilling, J. S. et al. An MK-like system of spectral classification for hot subdwarfs. *A&A*, v. 551, p. A31, 2013.

Duchêne, G.; Kraus, A. Stellar Multiplicity. *Annual Review of Astronomy and Astrophysics*, v. 51, p. 269–310, ago. 2013.

Dufour, P. et al. White dwarf stars with carbon atmospheres. *Nature*, v. 450, p. 522–524, 2007.

Dufour, P. et al. Hot DQ White Dwarf Stars: A New Challenge to Stellar Evolution. In: Werner, A.; Rauch, T. (Ed.). *Hydrogen-Deficient Stars*. [S.l.: s.n.], 2008. (Astronomical Society of the Pacific Conference Series, v. 391), p. 241.

Eisenstein, D. J. et al. A Catalog of Spectroscopically Confirmed White Dwarfs from the Sloan Digital Sky Survey Data Release 4. *APJS*, v. 167, p. 40–58, 2006.

Falcon, R. E. et al. A Gravitational Redshift Determination of the Mean Mass of White Dwarfs. DA Stars. *ApJ*, v. 712, p. 585–595, 2010.

Falcon, R. E. et al. A Gravitational Redshift Determination of the Mean Mass of White Dwarfs: DBA and DB Stars. *ApJ*, v. 757, p. 116, 2012.

Fontaine, G.; Brassard, P.; Bergeron, P. The Potential of White Dwarf Cosmochronology. *Publications of the Astronomical Society of the Pacific*, v. 113, p. 409–435, 2001.

Foss, D.; Wade, R. A.; Green, R. F. Limits on the space density of double degenerates as type IA supernova progenitors. *ApJ*, v. 374, p. 281–287, 1991.

Fouesneau, M. et al. Precise Ages of Field Stars from White Dwarf Companions. *arXiv:1802.06663*, fev. 2018.

Gänsicke, B. T. et al. The chemical diversity of exo-terrestrial planetary debris around white dwarfs. *MNRAS*, v. 424, p. 333–347, jul. 2012.

Geier, S. et al. The population of hot subdwarf stars studied with Gaia. I. The catalog of known hot subdwarf stars. *A&A*, v. 600, p. A50, abr. 2017.

Gentile Fusillo, N. P.; Gänsicke, B. T.; Greiss, S. A photometric selection of white dwarf candidates in Sloan Digital Sky Survey Data Release 10. *MNRAS*, v. 448, p. 2260–2274, 2015.

Gianninas, A. et al. The ELM Survey. VI. Eleven New Double Degenerates. *ApJ*, v. 812, p. 167, 2015.

Gimeno, G. et al. On-sky commissioning of Hamamatsu CCDs in GMOS-S. In: *Ground-based and Airborne Instrumentation for Astronomy VI*. [S.l.: s.n.], 2016. (SPIE, v. 9908), p. 99082S.

Girven, J. et al. DA white dwarfs in Sloan Digital Sky Survey Data Release 7 and a search for infrared excess emission. *MNRAS*, v. 417, p. 1210–1235, 2011.

Graham, J. R. et al. The infrared excess of G29-38 - A brown dwarf or dust? *ApJ*, v. 357, p. 216–223, 1990.

Green, R. F. The luminosity function of hot white dwarfs. *ApJ*, v. 238, p. 685–698, 1980.

Greenstein, J. L. A highly evolved, low-mass binary, HZ 22. *A&A*, v. 23, p. 1–7, fev. 1973.

Guan, X. Oscillator strength spectrum of hydrogen in strong magnetic and electric fields with arbitrary mutual orientation. *PRA*, v. 74, n. 2, p. 023413, ago. 2006.

Hayashi, C. Stellar evolution in early phases of gravitational contraction. *Publications of the Astronomical Society of Japan*, v. 13, p. 450–452, 1961.

Hayashi, C.; Hoshi, R. The Outer Envelope of Giant Stars with Surface Convection Zone. *Publications of the Astronomical Society of Japan*, v. 13, p. 442–449, 1961.

Heber, U. Hot Subluminous Stars. *Publications of the Astronomical Society of the Pacific*, v. 128, n. 8, p. 082001, ago. 2016.

Heber, U. et al. Discovery of a helium-core white dwarf progenitor. *A&A*, v. 411, p. L477–L480, dez. 2003.

Hermes, J. J. et al. Precision Asteroseismology of the Pulsating White Dwarf GD 1212 Using a Two-wheel-controlled Kepler Spacecraft. *ApJ*, v. 789, p. 85, 2014.

Hermes, J. J.; Gänsicke, B. T.; Breedt, E. sdA in SDSS DR12 are Overwhelmingly Not Extremely Low-Mass (ELM) White Dwarfs. In: Tremblay, P.-E.; Gaensicke, B.; Marsh, T. (Ed.). *20th European White Dwarf Workshop*. [S.l.: s.n.], 2017. (Astronomical Society of the Pacific Conference Series, v. 509), p. 453.

Hermes, J. J. et al. A Second Case of Outbursts in a Pulsating White Dwarf Observed by Kepler. *ApJL*, v. 810, p. L5, 2015.

Hermes, J. J. et al. A new class of pulsating white dwarf of extremely low mass: the fourth and fifth members. *MNRAS*, v. 436, p. 3573–3580, 2013.

Hermes, J. J. et al. SDSS J184037.78+642312.3: The First Pulsating Extremely Low Mass White Dwarf. *ApJL*, v. 750, p. L28, 2012.

Hermes, J. J. et al. Discovery of Pulsations, Including Possible Pressure Modes, in Two New Extremely Low Mass, He-core White Dwarfs. *ApJ*, v. 765, p. 102, 2013.

Hoard, D. W. et al. The WIRED Survey. IV. New Dust Disks from the McCook & Sion White Dwarf Catalog. *ApJ*, v. 770, p. 21, jun. 2013.

Holdsworth, D. L. et al. Three new pulsating sdB stars discovered with SuperWASP. *MNRAS*, v. 466, p. 5020–5032, abr. 2017.

Hollands, M. A.; Gänsicke, B. T.; Koester, D. The incidence of magnetic fields in cool DZ white dwarfs. *MNRAS*, v. 450, p. 681–690, 2015.

Hook, I. M. et al. The Gemini-North Multi-Object Spectrograph: Performance in Imaging, Long-Slit, and Multi-Object Spectroscopic Modes. *The Publications of the Astronomical Society of the Pacific*, v. 116, p. 425–440, maio 2004.

Hummer, D. G.; Mihalas, D. The equation of state for stellar envelopes. I - an occupation probability formalism for the truncation of internal partition functions. *ApJ*, v. 331, p. 794–814, ago. 1988.

Iben, I.; Livio, M. Common envelopes in binary star evolution. *Astronomical Society of the Pacific, Publications*, v. 105, p. 1373–1406, 1993.

Istrate, A. et al. Models of low-mass helium white dwarfs including gravitational settling, thermal and chemical diffusion, and rotational mixing. *arXiv:1606.04947*, 2016.

Istrate, A. G. et al. The timescale of low-mass proto-helium white dwarf evolution. *A&A*, v. 571, p. L3, 2014.

Jeffery, C. S.; Saio, H. Radial pulsation as a function of hydrogen abundance. *MNRAS*, v. 458, p. 1352–1373, 2016.

Johnson, D. R. H.; Soderblom, D. R. Calculating galactic space velocities and their uncertainties, with an application to the Ursa Major group. *Astronomical Journal*, v. 93, p. 864–867, 1987.

Jura, M. A Tidally Disrupted Asteroid around the White Dwarf G29-38. *ApJL*, v. 584, p. L91–L94, 2003.

Jura, M. Pollution of Single White Dwarfs by Accretion of Many Small Asteroids. *AJ*, v. 135, p. 1785–1792, maio 2008.

Jura, M. et al. Two Extrasolar Asteroids with Low Volatile-element Mass Fractions. *ApJ*, v. 750, p. 69, 2012.

Kalirai, J. S. et al. The Space Motion of the Globular Cluster NGC 6397. *ApJL*, v. 657, p. L93–L96, mar. 2007.

Kepler, S. O. et al. White dwarf mass distribution in the SDSS. *MNRAS*, v. 375, p. 1315–1324, 2007.

Kepler, S. O.; Koester, D.; Ourique, G. A white dwarf with an oxygen atmosphere. *Science*, v. 352, p. 67–69, abr. 2016.

Kepler, S. O. et al. Magnetic white dwarf stars in the Sloan Digital Sky Survey. *MNRAS*, v. 429, p. 2934–2944, 2013.

Kepler, S. O. et al. New white dwarf stars in the Sloan Digital Sky Survey Data Release 10. *MNRAS*, v. 446, p. 4078–4087, 2015.

Kepler, S. O. et al. New white dwarf and subdwarf stars in the Sloan Digital Sky Survey Data Release 12. *MNRAS*, v. 455, p. 3413–3423, 2016.

Kilic, M. et al. Habitable Planets Around White Dwarfs: an Alternate Mission for the Kepler Spacecraft. *ArXiv e-prints*, 2013.

Kilic, M. et al. The ELM Survey. II. Twelve Binary White Dwarf Merger Systems. *ApJ*, v. 727, p. 3, 2011.

Kilic, M. et al. The ELM Survey. IV. 24 White Dwarf Merger Systems. *ApJ*, v. 751, p. 141, 2012.

Kilic, M. et al. Gaia Reveals Evidence for Merged White Dwarfs. *ArXiv e-prints*, maio 2018.

Kilic, M. et al. PSR J1738+0333: the first millisecond pulsar + pulsating white dwarf binary*. *MNRAS*, v. 446, p. L26–L30, 2015.

Kilic, M.; Stanek, K. Z.; Pinsonneault, M. H. The Future Is Now: The Formation of Single Low-Mass White Dwarfs in the Solar Neighborhood. *ApJ*, v. 671, p. 761–766, 2007.

Kleinman, S. J. et al. A Catalog of Spectroscopically Identified White Dwarf Stars in the First Data Release of the Sloan Digital Sky Survey. *ApJ*, v. 607, p. 426–444, 2004.

Kleinman, S. J. et al. SDSS DR7 White Dwarf Catalog. *ApJS*, v. 204, p. 5, 2013.

Koester, D. White dwarf spectra and atmosphere models . *MmSAI*, v. 81, p. 921–931, 2010.

Koester, D.; Gänsicke, B. T.; Farihi, J. The frequency of planetary debris around young white dwarfs. *A&A*, v. 566, p. A34, 2014.

Koester, D. et al. Cool DZ white dwarfs in the SDSS. *A&A*, v. 530, p. A114, 2011.

Koester, D.; Kepler, S. O. DB white dwarfs in the Sloan Digital Sky Survey data release 10 and 12. *A&A*, v. 583, p. A86, 2015.

Koester, D.; Knist, S. New DQ white dwarfs in the Sloan Digital Sky Survey DR4: confirmation of two sequences. *A&A*, v. 454, p. 951–956, 2006.

Koester, D.; Weidemann, V.; Zeidler, E.-M. Atmospheric parameters and carbon abundance of white dwarfs of spectral types C2 and DC. *A&A*, v. 116, p. 147–157, 1982.

Kordopatis, G. et al. A spectroscopic survey of thick disc stars outside the solar neighbourhood. *A&A*, v. 535, p. A107, nov. 2011.

Kowalski, P. M. On the Dissociation Equilibrium of H_2 in Very Cool, Helium-rich White Dwarf Atmospheres. *ApJ*, v. 641, p. 488–493, abr. 2006.

Kraft, R. P.; Mathews, J.; Greenstein, J. L. Binary Stars among Cataclysmic Variables. II. Nova WZ Sagittae: a Possible Radiator of Gravitational Waves. *ApJ*, v. 136, p. 312–315, jul. 1962.

Krauss, L. M.; Chaboyer, B. Age Estimates of Globular Clusters in the Milky Way: Constraints on Cosmology. *Science*, v. 299, p. 65–70, 2003.

Külebi, B. et al. Analysis of hydrogen-rich magnetic white dwarfs detected in the Sloan Digital Sky Survey. *A&A*, v. 506, p. 1341–1350, 2009.

Kurtz, M. J.; Mink, D. J. RVSAO 2.0: Digital Redshifts and Radial Velocities. *The Publications of the Astronomical Society of the Pacific*, v. 110, p. 934–977, ago. 1998.

Lance, C. M. Young, high-velocity a stars. II - Misidentified, ejected, or unique? *ApJ*, v. 334, p. 927–946, nov. 1988.

Landau, L.; Lifshitz, E. *The Theory of Classical Fields*. Oxford: Pergamon Press, 1958.

Latour, M. et al. Quantitative spectral analysis of the sdB star HD 188112: A helium-core white dwarf progenitor. *A&A*, v. 585, p. A115, jan. 2016.

Law, N. M. et al. The Palomar Transient Factory: System Overview, Performance, and First Results. *PASP*, v. 121, p. 1395–1408, 2009.

Lee, Y. S. et al. The SEGUE Stellar Parameter Pipeline. I. Description and Comparison of Individual Methods. *AJ*, v. 136, p. 2022–2049, nov. 2008.

Lenz, D. D. et al. Photometric Separation of Stellar Properties Using SDSS Filters. *ApJS*, v. 119, p. 121–140, 1998.

Lenz, P.; Breger, M. Period04 User Guide. *Communications in Asteroseismology*, v. 146, p. 53–136, jun. 2005.

Liebert, J.; Bergeron, P.; Holberg, J. B. The Formation Rate and Mass and Luminosity Functions of DA White Dwarfs from the Palomar Green Survey. *ApJS*, v. 156, p. 47–68, 2005.

Limoges, M.-M.; Bergeron, P. A Spectroscopic Analysis of White Dwarfs in the Kiso Survey. *ApJ*, v. 714, p. 1037–1051, 2010.

Lomb, N. R. Least-squares frequency analysis of unequally spaced data. *Astrophysics and Space Science*, v. 39, p. 447–462, fev. 1976.

Marsh, T. R.; Dhillon, V. S.; Duck, S. R. Low-Mass White Dwarfs Need Friends - Five New Double-Degenerate Close Binary Stars. *MNRAS*, v. 275, p. 828, 1995.

Martin, D. C. et al. The Galaxy Evolution Explorer: A Space Ultraviolet Survey Mission. *ApJL*, v. 619, p. L1–L6, jan. 2005.

Maxted, P. F. L. et al. Discovery of a stripped red giant core in a bright eclipsing binary system. *MNRAS*, v. 418, p. 1156–1164, dez. 2011.

Maxted, P. F. L. et al. WASP 1628+10 - an EL CVn-type binary with a very low mass stripped red giant star and multiperiodic pulsations. *MNRAS*, v. 444, p. 208–216, out. 2014.

Maxted, P. F. L. et al. Multi-periodic pulsations of a stripped red-giant star in an eclipsing binary system. *Nature*, v. 498, p. 463–465, jun. 2013.

Moehler, S.; Bono, G. White Dwarfs in Globular Clusters. *ArXiv e-prints*, 2008.

Munn, J. A. et al. A Deep Proper Motion Catalog Within the Sloan Digital Sky Survey Footprint. *AJ*, v. 148, p. 132, dez. 2014.

Munn, J. A. et al. An Improved Proper-Motion Catalog Combining USNO-B and the Sloan Digital Sky Survey. *Astronomical Journal*, v. 127, p. 3034–3042, 2004.

Murphy, S. J. et al. A search for non-pulsating, chemically normal stars in the δ Scuti instability strip using Kepler data. *MNRAS*, v. 447, p. 3948–3959, mar. 2015.

Napiwotzki, R. LTE or NLTE for the analysis of hot white dwarf and subdwarf B stars? *A&A*, v. 322, p. 256–265, 1997.

Nelemans, G. The Galactic gravitational wave foreground. *Classical and Quantum Gravity*, v. 26, n. 9, p. 094030, maio 2009.

Nelemans, G.; Tauris, T. M. Formation of undermassive single white dwarfs and the influence of planets on late stellar evolution. *A&A*, v. 335, p. L85–L88, jul. 1998.

Nelemans, G.; Yungelson, L. R.; Portegies Zwart, S. F. The gravitational wave signal from the Galactic disk population of binaries containing two compact objects. *A&A*, v. 375, p. 890–898, set. 2001.

Németh, P.; Kawka, A.; Vennes, S. A selection of hot subluminous stars in the GALEX survey - II. Subdwarf atmospheric parameters. *MNRAS*, v. 427, p. 2180–2211, 2012.

Nemeth, P. et al. Synthetic Spectra for O and B Type Subdwarf Stars. In: van Grootel, V. et al. (Ed.). *6th Meeting on Hot Subdwarf Stars and Related Objects*. [S.l.: s.n.], 2014. (Astronomical Society of the Pacific Conference Series, v. 481), p. 95.

Nemeth, P. et al. SD1000 Collaboration: Hunting down the Subdwarf Populations. In: van Grootel, V. et al. (Ed.). *6th Meeting on Hot Subdwarf Stars and Related Objects*. [S.l.: s.n.], 2014. (Astronomical Society of the Pacific Conference Series), p. 75.

Paczyński, B. Evolutionary Processes in Close Binary Systems. *Annual Review of Astronomy and Astrophysics*, v. 9, p. 183, 1971.

Palaversa, L. et al. Exploring the Variable Sky with LINEAR. III. Classification of Periodic Light Curves. *AJ*, v. 146, p. 101, out. 2013.

Panei, J. A. et al. Full evolution of low-mass white dwarfs with helium and oxygen cores. *MNRAS*, v. 382, p. 779–792, 2007.

Pelisoli, I. et al. The sdA problem - III. Hundreds of new extremely low-mass white dwarfs and their precursors from Gaia astrometry. *ArXiv e-prints*, maio 2018.

Pelletier, C. et al. Carbon pollution in helium-rich white dwarf atmospheres Time-dependent calculations of the dredge-up process. *ApJ*, v. 307, p. 242–252, 1986.

Pietrukowicz, P. et al. Blue large-amplitude pulsators as a new class of variable stars. *Nature Astronomy*, v. 1, p. 0166, ago. 2017.

Pietrzyński, G. et al. RR-Lyrae-type pulsations from a 0.26-solar-mass star in a binary system. *Nature*, v. 484, p. 75–77, abr. 2012.

Pietrzyński, G. et al. RR-Lyrae-type pulsations from a 0.26-solar-mass star in a binary system. *Naure*, v. 484, p. 75–77, 2012.

Podsiadlowski, P. The Evolution of Close Binaries. In: Evans, A. et al. (Ed.). *RS Ophiuchi (2006) and the Recurrent Nova Phenomenon*. [S.l.: s.n.], 2008. (Astronomical Society of the Pacific Conference Series, v. 401), p. 63.

Prugniel, P.; Soubiran, C. A database of high and medium-resolution stellar spectra. *A&A*, v. 369, p. 1048–1057, abr. 2001.

Rau, A. et al. Exploring the Optical Transient Sky with the Palomar Transient Factory. *PASP*, v. 121, p. 1334–1351, 2009.

Rauch, T. et al. The virtual observatory service TheoSSA: Establishing a database of synthetic stellar flux standards . II. NLTE spectral analysis of the OB-type subdwarf Feige 110. *A&A*, v. 566, p. A3, 2014.

Razali, N.; Wah, Y. B. Power comparisons of Shapiro-Wilk, Kolmogorov-Smirnov, Lilliefors and Anderson-Darling tests. *Journal of Statistical Modeling and Analytics*, v. 2, n. 1, jun. 2011.

Rebassa-Mansergas, A. et al. The mass function of hydrogen-rich white dwarfs: robust observational evidence for a distinctive high-mass excess near 1 $M_{\odot}$. *MNRAS*, v. 452, p. 1637–1642, 2015.

Reid, I. N.; Liebert, J.; Schmidt, G. D. Discovery of a Magnetic DZ White Dwarf with Zeeman-Split Lines of Heavy Elements. *ApJL*, v. 550, p. L61–L63, 2001.

Renedo, I. et al. New Cooling Sequences for Old White Dwarfs. *ApJ*, v. 717, p. 183–195, 2010.

Robinson, E. L.; Shafter, A. W. An Upper Limit to the Space Density of Short-period Noninteracting Binary White Dwarfs. *ApJ*, v. 322, p. 296, 1987.

Roeser, S.; Demleitner, M.; Schilbach, E. The PPMXL Catalog of Positions and Proper Motions on the ICRS. Combining USNO-B1.0 and the Two Micron All Sky Survey (2MASS). *AJ*, v. 139, p. 2440–2447, jun. 2010.

Romero, A. D.; Campos, F.; Kepler, S. O. The age-metallicity dependence for white dwarf stars. *MNRAS*, p. 3708–3723, jul. 2015.

Romero, A. D. et al. Toward ensemble asteroseismology of ZZ Ceti stars with fully evolutionary models. *MNRAS*, v. 420, p. 1462–1480, 2012.

Rueda, J. A. et al. GRB 170817A-GW170817-AT 2017gfo and the observations of NS-NS and NS-WD mergers. *arXiv:1802.10027*, fev. 2018.

Salpeter, E. E. The Luminosity Function and Stellar Evolution. *ApJ*, v. 121, p. 161, 1955.

Saltas, I. D.; Sawicki, I.; Lopes, I. White dwarfs and revelations. *arXiv:1803.00541*, mar. 2018.

Scargle, J. D. Studies in astronomical time series analysis. II - Statistical aspects of spectral analysis of unevenly spaced data. *ApJ*, v. 263, p. 835–853, dez. 1982.

Schimeczek, C. et al. Atomic ground states in strong magnetic fields: Electron configurations and energy levels. *Phys. Rev. A*, v. 88, n. 1, p. 012509, 2013.

Schimeczek, C.; Wunner, G. Accurate 2d finite element calculations for hydrogen in magnetic fields of arbitrary strength. *Computer Physics Communications*, v. 185, p. 614–621, 2014.

Schimeczek, C.; Wunner, G. Atomic Data for the Spectral Analysis of Magnetic DA White Dwarfs in the SDSS. *ApJS*, v. 212, p. 26, 2014.

Schlegel, D. J.; Finkbeiner, D. P.; Davis, M. Maps of Dust Infrared Emission for Use in Estimation of Reddening and Cosmic Microwave Background Radiation Foregrounds. *ApJ*, v. 500, p. 525–553, 1998.

Schmidt, M. Space Distribution and Luminosity Functions of Quasi-Stellar Radio Sources. *ApJ*, v. 151, p. 393, 1968.

Schmidt, M. The mass of the galactic halo derived from the luminosity function of high-velocity stars. *ApJ*, v. 202, p. 22–29, 1975.

Schneider, F. R. N. et al. Evolution of Mass Functions of Coeval Stars through Wind Mass Loss and Binary Interactions. *ApJ*, v. 805, p. 20, maio 2015.

Schönberg, M.; Chandrasekhar, S. On the Evolution of the Main-Sequence Stars. *ApJ*, v. 96, p. 161, set. 1942.

Schönberner, D. The mass of HZ 22. *A&A*, v. 70, p. 451–452, nov. 1978.

Shapiro, S. S.; Wilk, M. B. An analysis of variance test for normality (complete samples)†. *Biometrika*, v. 52, n. 3-4, p. 591–611, 1965.

Silvotti, R. et al. Orbital properties of an unusually low-mass sdB star in a close binary system with a white dwarf. *MNRAS*, v. 424, p. 1752–1761, 2012.

Skrutskie, M. F. et al. The Two Micron All Sky Survey (2MASS). *AJ*, v. 131, p. 1163–1183, fev. 2006.

Solheim, J.-E. AM CVn Stars: Status and Challenges. *Publications of the Astronomical Society of Pacific*, v. 122, p. 1133–1163, 2010.

Southworth, J.; Maxted, P. F. L.; Smalley, B. Eclipsing binaries in open clusters - II. V453 Cyg in NGC 6871. *MNRAS*, v. 351, p. 1277–1289, jul. 2004.

Stobie, R. S.; Ishida, K.; Peacock, J. A. Distance errors and the stellar luminosity function. *MNRAS*, v. 238, p. 709–727, 1989.

Stokes, G. H. et al. Lincoln Near-Earth Asteroid Program (LINEAR). *Icarus*, v. 148, p. 21–28, 2000.

Sun, M.; Arras, P. Formation of Extremely Low-mass White Dwarfs Binaries. mar. 2017.

Tauris, T. M.; Langer, N.; Podsiadlowski, P. Ultra-stripped supernovae: progenitors and fate. *MNRAS*, v. 451, p. 2123–2144, 2015.

Thévenin, F. et al. VLT observations of turnoff stars in the globular cluster NGC 6397. *A&A*, v. 373, p. 905–915, jul. 2001.

Tian, H.-J. et al. A Gaia-PS1-SDSS (GPS1) Proper Motion Catalog Covering 3/4 of the Sky. *ApJS*, v. 232, p. 4, set. 2017.

Tokovinin, A. From Binaries to Multiples. II. Hierarchical Multiplicity of F and G Dwarfs. *AJ*, v. 147, p. 87, abr. 2014.

Toonen, S. et al. The binarity of the local white dwarf population. *A&A*, v. 602, p. A16, jun. 2017.

Tremblay, P.-E.; Bergeron, P. Spectroscopic Analysis of DA White Dwarfs: Stark Broadening of Hydrogen Lines Including Nonideal Effects. *ApJ*, v. 696, p. 1755–1770, maio 2009.

Tremblay, P.-E. et al. 3D Model Atmospheres for Extremely Low-mass White Dwarfs. *ApJ*, v. 809, p. 148, ago. 2015.

Tremblay, P.-E. et al. White Dwarf Cosmochronology in the Solar Neighborhood. *ApJ*, v. 791, p. 92, 2014.

Tremblay, P.-E. et al. Spectroscopic analysis of DA white dwarfs with 3D model atmospheres. *A&A*, v. 559, p. A104, 2013.

Van Grootel, V. et al. The Newly Discovered Pulsating Low-mass White Dwarfs: An Extension of the ZZ Ceti Instability Strip. *ApJ*, v. 762, p. 57, 2013.

Vernet, J. et al. X-shooter, the new wide band intermediate resolution spectrograph at the ESO Very Large Telescope. *A&A*, v. 536, p. A105, dez. 2011.

Vivas, A. K. et al. The QUEST RR Lyrae Survey. I. The First Catalog. *The Astronomical Journal*, v. 127, p. 1158–1175, 2004.

Wang, B.; Han, Z. Companion stars of type Ia supernovae and hypervelocity stars. *A&A*, v. 508, p. L27–L30, dez. 2009.

Werner, K. et al. PG 1159 stars. In: Jeffery, C. S.; Heber, U. (Ed.). *Hydrogen Deficient Stars*. [S.l.: s.n.], 1996. (Astronomical Society of the Pacific Conference Series, v. 96), p. 267.

Willems, B.; Kolb, U. Detached white dwarf main-sequence star binaries. *A&A*, v. 419, p. 1057–1076, jun. 2004.

Winget, D. E. et al. An independent method for determining the age of the universe. *ApJL*, v. 315, p. L77–L81, 1987.

Winget, D. E. et al. The Physics of Crystallization From Globular Cluster White Dwarf Stars in NGC 6397. *ApJL*, v. 693, p. L6–L10, mar. 2009.

Woosley, S. E.; Heger, A. The Remarkable Deaths of 9-11 Solar Mass Stars. *ApJ*, v. 810, p. 34, 2015.

Wright, E. L. et al. The Wide-field Infrared Survey Explorer (WISE): Mission Description and Initial On-orbit Performance. *AJ*, v. 140, p. 1868–1881, dez. 2010.

Xue, X. X. et al. The Milky Way's Circular Velocity Curve to 60 kpc and an Estimate of the Dark Matter Halo Mass from the Kinematics of ˜2400 SDSS Blue Horizontal-Branch Stars. *ApJ*, v. 684, p. 1143–1158, set. 2008.

Yong, D. et al. The Most Metal-poor Stars. II. Chemical Abundances of 190 Metal-poor Stars Including 10 New Stars with [Fe/H] < -3.5. *ApJ*, v. 762, p. 26, jan. 2013.

Yuan, H. B.; Liu, X. W.; Xiang, M. S. Empirical extinction coefficients for the GALEX, SDSS, 2MASS and WISE passbands. *MNRAS*, v. 430, p. 2188–2199, abr. 2013.

Zhang, X. et al. Evolution Models of Helium White Dwarf-Main-sequence Star Merger Remnants. *ApJ*, v. 835, p. 242, fev. 2017.

Zhang, X.; Jeffery, C. S. Evolutionary models for double helium white dwarf mergers and the formation of helium-rich hot subdwarfs. *MNRAS*, v. 419, p. 452–464, jan. 2012.

Ziegerer, E. et al. Candidate hypervelocity stars of spectral type G and K revisited. *A&A*, v. 576, p. L14, abr. 2015.

Zorotovic, M. et al. Post-common-envelope binaries from SDSS. IX: Constraining the common-envelope efficiency. *A&A*, v. 520, p. A86, set. 2010.